The Effect of Principal Elements on Defect Evolution in Single-Phase Solid Solution Ni Alloys

by

Tai Ni Yang

A dissertation submitted in partial fulfillment
of the requirements for the degree of
Doctor of Philosophy
(Nuclear Engineering and Radiological Sciences)
in the University of Michigan
2019

Doctoral Committee:

Professor Lumin Wang, Chair
Professor Fei Gao
Professor Amit Misra
Professor Gary S. Was

Tai Ni Yang
taiyang@umich.edu
ORCID iD: 0000-0002-4386-7400

To my family and friends

ACKNOWLEDGEMENTS

I would like to express my gratitude to the following people and organizations. This work would not be possible without the help and collaboration of many people.

The first person I would like to thank is my adviser, Lumin Wang, for providing the opportunity to pursue my passion in science at the next level and providing guidance, support and assistance along the way. I would also like to thank my committee members, Dr. Fei Gao and Dr. Amit Misra for their input to improve the quality of this thesis. Especially, I would like to thank Dr. Gary Was for his guidance on the stress corrosion project and the opportunity of attending group meetings throughout these years.

I would also like to express my gratitude to all my lab members in both Wang and Was research group, Dr. Chenyang Lu, Dr. Kale Stephenson, Dr. Stephen Raiman, Dr. Shyam Dwaraknath, Dr. Elizabeth Getto, Dr. George Jiao, Dr. Peng Wang, Dr. Miao Song, Dr. Mi Wang, Dr. Wenjun Kuang, Dr. Donghai Du, Alex Flick, Dr. Calvin Lear, Pengyuan Xiu, Justin Hesterberg, Gerrit VanCoevering, Drew Johnson, Rigel Hanbury, Samara Levine, Katey Thomas and Nanjun Chen. The scientific discussions, advice and countless board game nights will always be a part of my cherish memory.

Thank you to the MIBL Staff, Dr. Ovidiu Toader, Dr. Fabian Naab, Dr. Ethan Uberseder, Thomas Kubley and Dr. Prabir Roy, for their great help on irradiation experiments. I would like to thank the members of Energy Dissipation to Defect Evolution, Dr. Yanwen Zhang, Dr. Willian J. Weber, Dr. Hongbin Bei, Dr. Ke Jin, Dr. Gihan Velisa, Dr. Shi Shi, Dr. Shijun Zhao, Dr. Yang

Tong for their great help in the preparation of single crystal materials, performing ion irradiations, suggestions on choosing experimental conditions and discussions on the results. Thank you to the $(MC)^2$ staff for their professional training with FIB and TEM, especially Dr. Kai Sun, who was always patient and willing to pass on his knowledge of the microscopes.

To my family in Taiwan, especially my parents Lien-Chuan Yang and Li-Yun Lu, thank you for supporting me to pursue my dream, providing suggestions but always respecting my decisions. To my family in the U.S., thank you for your encouragement and cheers on this journey.

Lastly, to my husband Anthony Monterrosa, thank you for always being there to cheer me on and provide the much-needed fun when things are moving slow. Taking on the journey of getting a Ph.D degree can be quite a daunting thought sometimes, but luckily I had you to walk this adventure with me and showed me how it is being done.

This work has been supported by an EFRC grant of DOE BES on Energy Dissipation to Defect Evolution.

TABLE OF CONTENTS

LIST OF FIGURES

LIST OF TABLES

LIST OF PUBLICATIONS

(1) **T. Yang,** C. Lu, G. Velisa, K. Jin, P. Xiu, Y. Zhang, H. Bei and L. Wang, "Influence of irradiation temperature on void swelling in NiCoFeCrMn and NiCoFeCrPd" Scr. Mater., 158 (2019) 57-61.

(2) **T. Yang,** C. Lu, G. Velisa, K. Jin, P. Xiu, M. Crespillo, Y. Zhang, H. Bei and L. Wang, "Effect of alloying elements on defect evolution in Ni-20X binary alloys" Acta Mater., 151 (2018) 159-168.

(3) C. Lu, **T. Yang**, K. Jin, G. Velisa, P. Xiu, M. Song, Q. Peng, F. Gao, Y. Zhang, H. Bei, W.J. Weber, L. Wang, "Enhanced void swelling in NiCoFeCrPd high-entropy alloy by indentation-induced dislocations" Mater. Res. Lett. 6 (2018) 10, 584-591.

(4) C. Lu, **T. Yang**, L. Niu, Q. Peng, Ke. Jin, M. Crespillo, G. Velisa, H. Xue, F. Zhang, P. Xiu, Y. Zhang, F. Gao, H. Bei, W.J. Weber, L. Wang, "Interstitial migration behavior and defect evolution in ion irradiated pure nickel and Ni-xFe binary alloys" J. Nucl. Mater. 509 (2018) 237-244.

(5) Y. Tong, G. Velisa, S. Zhao, W. Guo, **T. Yang**, K. Jin, C. Lu, H. Bei, J.Y.P. Ko, D. C. Pagan, Y. Zhang, L. Wang, F. X. Zhang, "Effect of atomic size mismatch on radiation damage in medium- and high- entropy alloys" Materialia 2 (2018).

(6) **T. Yang,** C. Lu, K. Jin, M. Crespillo, Y. Zhang, H. Bei and L. Wang, "The effect of injected interstitials on void formation in self-ion irradiated nickel containing concentrated solid solution alloys" J. Nucl. Mater.,488 (2017) 328-337.

(7) C. Lu**, T. Yang**, K. Jin, N. Gao, P. Xiu, Y. Zhang, F. Gao, H. Bei, W.J. Weber, K. Sun, Y. Dong, L. Wang, "Radiation-induced segregation on defect clusters in single-phase concentrated solid-solution alloys"Acta Mater.,127 (2017) 98-107.

(8) C. Lu, L. Niu, N. Chen, K. Jin, **T. Yang**, P. Xiu, Y. Zhang, F. Gao, H. Bei, S. Shi, M. He, I. Robertson, W.J. Weber, L. Wang, "Enhancing radiation tolerance by controlling defect mobility and migration pathways in multicomponent single-phase alloys" Nature Communications,7 (2016)13564.

(9) C. Lu, K. Jin, L.K. Beland, F. Zhang, **T. Yang**, Y. Zhang, H. Bei, R. Stoller, L. Wang, "Observation on defect structure, range and evolution in ion irradiated single crystal Ni and Ni binary alloys" Scientific Reports, 6 (2016) 19994**.**

ABSTRACT

The objectives of this thesis are: firstly, to investigate the effect of increasing chemical complexity on radiation-induced defect evolution (both in voids and dislocation loops) in Ni based single-phased concentrated solid solution alloys (SP-CSAs). SP-CSAs typically contain two to five elements in high or equiatomic concentrations. The compositionally complex but structurally simple features of SP-CSAs make them great candidates in studying irradiation-induced defect interactions. This was done by first performing a study on SP-CSAs in a single elevated irradiation temperature, and followed by testing the dose and temperature dependence of radiation tolerance of these alloys. Secondly, to understand the role of increasing alloy concentrations on defect migration mechanisms with Ni-xFe (x=up to 35%) binary alloys. Thirdly, to understand the effect of alloying elements on radiation-induced microstructural evolution with pure Ni and Ni-20X (X=Fe, Cr, Mn and Pd) binary alloys. Most of the tested samples were irradiated with 3.0 MeV Ni^{2+} ions at 500℃ up to damage levels of 60 dpa at peak dose. A combination of Transmission electron microscopy (TEM) was used to characterize the microstructure evolution of irradiated CSA samples, emphasizing void swelling and dislocation loop formation.

As a result, void swelling decreased while the growth of dislocation loops was suppressed with increasing chemical complexity of an alloy in general. The exceptions were attributed to the difference in CSAs melting temperature. Two interstitial migration mechanisms; 1D and 3D mode, were proposed to explain the qualitative observation of defect distributions throughout the irradiation depth. The suppression on void swelling and delay of dislocation loop growth were attributed to the relatively localized 3D migration mode, which enhanced defect recombination in the main irradiated region. The transition of 1D to 3D mode for interstitials was quantitatively analyzed in Ni-xFe binary alloys using the mean free path of interstitial clusters.

In the study of varying irradiation temperatures, the equiatomic Ni-based high entropy alloys (HEAs) have demonstrated superior swelling resistance than Ni-based medium entropy alloys (MEAs) over three homologous temperatures of irradiation. In NiCoFeCrMn, an order of magnitude increase on swelling was observed with increasing temperature, but the swelling performance was still comparable to ferritic steels. Between the two HEAs studied, alloying with Pd was found to have a stronger suppression effect on void and dislocation loop growth than alloying with Mn. This was attributed to the higher lattice distortion observed in NiCoFeCrPd than in NiCoFeCrMn. No significant increase was observed on the equilibrium vacancy concentration as the number of alloying components increased.

In the study of Ni-20X, it was found that the average size of defect clusters decreased as the solute atomic volume size factor increased. Oversized magnetic solutes can act as strong trapping sites for interstitials and suppress the growth of dislocation loops. The average dislocation loop size in Ni-20Fe was four times larger than Ni-20Pd (atomic volume factor is 10.6% and 41.3%) but an order of magnitude lower in density. Overall, the alloying effect on defects is more significant in concentrated binary alloys than in dilute binary alloys, due to the concentration difference of alloying atoms and the interstitial dominant migration mechanisms in the main irradiated region. Furthermore, this study demonstrated that similar results on swelling resistance can be achieved in HEAs and well-designed binary alloys with increased concentration or atomic volume factor of alloying elements.

Chapter 1-Introduction and Objective

1.1 Introduction

Traditionally, the development of metallic alloys and their applications have been limited on conventional alloys based on one principal element or two major elements. The improvement of material performance has taken different forms but can be roughly categorized as follows. Adding minor alloy elements in low concentrations, creating multiple phases inside the material structure, applying nano-technology, either through adding nanosized features into the material, modifying grain size to maximize grain boundaries or creating precipitates, etc. Despite taken different approaches, the main goal is to increase the microstructure complexity of materials and improve their performance in extreme environments.

Contrary to the conventional alloys, the development of concentrated solid solution alloys (CSAs) has adopted a different approach. Instead of creating a material with complex microstructure, it aims to modify the chemical complexity of materials while keeping a simple microstructure, such as face centered cubic (fcc) or body centered cubic (bcc). CSAs typically consist of two to five (Ni, Co, Fe, Cr, Mn, Pd) elemental species all at high concentrations, or near equiatomic composition. Such material systems have emerged recently and quickly attracted research interests due to their excellent mechanical properties, including high tensile strength, ductility, good thermal stability, and fracture toughness [1-3]

The simple microstructure and excellent mechanical properties make nickel and various single-phase nickel alloys perfect candidates in studying the alloying effects in radiation-induced defect evolution. In addition, the combination of high concentration alloying elements provides a unique way to understand the correlation between intrinsic properties and defect dynamics at an atomic scale, and to further bridge the knowledge gap between dilute and concentrated alloys.

Ion irradiations have the advantages of achieving high damage dose rate at a relatively short time and within a reasonable cost compared to neutron irradiations. Therefore, the use of ion beams in studying irradiation effect on materials has become popular due to its time and cost efficiency. The ion beams studies have shown great success in replicating comparable radiation damage effects as neutrons [4-6]. However, there are several drawbacks one must consider when using ion irradiations. For instance, a relatively shallow penetration depth, changing damage dose and injected interstitial concentration as a function of depth [7-8]. These limitations can be either compensated with appropriate characterization techniques or be included in the discussion of results.

1.2 Objective

The objectives of this thesis are: first, to investigate the effect of increasing chemical complexity on radiation-induced defect evolution (both in voids and dislocation loops) in Ni based SP-CSAs. The first objective was achieved by initially studying SP-CSAs in a single elevated irradiation temperature, and followed by testing the dose and temperature dependence of radiation tolerance of these alloys. Secondly, to understand the role of increasing alloy concentrations on defect migration mechanisms with Ni-xFe binary alloys. Thirdly, to understand the effect of alloying elements on radiation-induced microstructural evolution with pure Ni and Ni-20X (X=Fe, Cr, Mn and Pd) binary alloys. The motivation for these studies is elaborated as follows.

Effect of increasing chemical complexity on irradiated Ni SP-CSAs

This thesis work is one of its first in studying irradiation effect on Ni SP-CSAs. Since there was scarce reference to predict the irradiation performance of Ni SP-CSAs, a systematic study with a constant irradiation condition was needed. A hypothesis for the behavior of void swelling is presented as follows:

Addition of small amounts of principal elements into metallic solid solutions is known to strongly influence the development of defect structures during irradiation. Ion-irradiated Ni SP-CSAs will exhibit less void swelling as chemical complexity is increased. This is due to the severe

lattice distortion from different neighboring atoms, which also leads to higher defect recombination.

Furthermore, the presence of various sized alloy elements will further suppress void swelling and growth of dislocation loops by trapping point defects. The substantially increased thermodynamic vacancy concentration in HEAs will also increase the swelling resistance of the material when compared to materials with less principal elements.

To achieve the main objective, self-ion irradiations were conducted using 3 MeV Ni^{2+} ions at 500℃ to a fluence of $5.0 \times 10^{16} ion/cm^2$. Systematic characterization methods were also established while performing the analysis from the first objective, and were detailed in Chapter 3 Experimental Procedure.

The first step was to establish a general understanding of irradiation performance. To this end, a single irradiation temperature and a single damage dose were selected. However, the defect evolution between SP-CSAs may vary with irradiation damages, and the variance in melting temperature can inevitably shift the swelling peak of SP-CSAs. Therefore, Ni, NiCo, NiFe, and NiCoFeCr were selected to perform a damage dose dependent test, and to observe the trend of defect evolution.

To investigate the effect on swelling, NiCoCr, NiCoFeCr, NiCoFeCrMn and NiCoFeCrPd were selected to irradiate at three elevated temperatures, 420℃, 500℃ and 580℃ to a fluence of $5.0 \times 10^{16} ion/cm^2$. The only difference was the irradiated temperature while keeping the rest of the parameters constant. The results were compared in both homologous temperature and absolute temperature to determine the effect of irradiation temperature on swelling behavior in SP-CSAs. The systematic study validated that HEAs indeed have better swelling resistance than medium entropy alloys, and it also helped to estimate the swelling peak range for tested Ni-SPCSAs.

Effect of increasing iron concentration on defect migration mechanisms in Ni-xFe

The first objective required determining what happened to the irradiation behavior as the composition of Ni SP-CSAs varied. Two sub-objectives further studied the defect evolution as a function of damage dose and irradiation temperature. Two interstitial migration mechanisms were proposed from the first objective based on qualitative defect distributions. To provide a quantitative analysis, Ni-Fe binary alloys were chosen to determine the transition of interstitial migration mechanisms as a function of iron concentration. The self-ion irradiations were conducted using 3 MeV Ni^{2+} ions at 500℃ to a fluence of $5.0 \times 10^{16} ion/cm^2$. The irradiation temperature was chosen to remain constant due to small variations (less than 10 K) in the melting temperature of Ni-xFe binary alloys.

This second objective was accomplished by a detailed analysis of depth-dependent void/dislocation loop distributions, and the ratio of faulted to perfect loops. The results observed from experimental work were compared to MD simulation results, which introduced the concept of mean free path to define the average length of an interstitial cluster traveled before changing its directions. This analysis provided the much-needed quantitative insight into the changes in interstitial migration mode due to increase chemical complexity.

Effect of alloying elements on defect evolution in Ni-20X binary alloys

To investigate the individual effect of alloy elements on defect evolution, concentrated Ni binary alloys will serve as the best material, as Fe, Cr, Mn and Pd all have different atomic volume factors than Ni [9]. The results were compared with the well-studied dilute Ni binary alloys in the past [10-14]. A general threshold categorizes binary alloys with less than 10at% of solutes as dilute alloys, while higher than 10at% as concentrated alloys. The main goal of this objective was to study the influence on defect evolution from the perspective of increasing alloy concentration, increasing the size of minor alloy elements and to understand the dominating interstitial migration mechanism.

Single crystal nickel and concentrated nickel binary alloys, which contain 20at% of Fe,

Cr, Mn or Pd as solute atoms were investigated for this objective. These individual alloying elements were chosen since they are the main composition of NiCoFeCrMn and NiCoFeCrPd, which alloying together show great swelling resistance at elevated temperatures [15-17]. The element Co was excluded due to a similar atomic volume compared with Ni. In order to maintain a face-centered cubic (fcc) crystal structure, a composition of 80 % Ni versus 20% other alloying elements was chosen. The decision was made considering Ni-Cr does not hold fcc single-phase at 500℃ once the Cr concentration exceeds 22 at%, according to the ASTM phase diagrams.

The as-grown Ni, Ni-20Fe and Ni-20Cr rods were confirmed as single-crystals, while the Ni-20Mn and Ni-20Pd were large-grain polycrystals with average grain size of 100-200 um. These polycrystal samples have grain sizes large enough that no grain boundaries were appeared in the entire regime of interest, and interaction of defects with grain boundaries was negligible inside grains [18]. By choosing a consistent alloy concentration and irradiating these binary alloys at homologous temperature, the effect of specific alloy element on defect evolution were studied systematically.

Chapter 2-Background

A review of the published literature and fundamental theories relevant to this work is presented in this chapter. The main purpose is to provide a better understanding on the objectives, goals and outcomes of this thesis. Section 2.1-2.2 present the general properties of materials used in this dissertation, Ni-based concentrated solid solution alloys. Section 2.3 provides an overview of the radiation-induced damage on materials. Section 2.4 discusses parameters that can affect irradiation-induced defects evolution and supporting literature review. Section 2.5 briefly discusses two common changes on material properties due to irradiation.

2.1 Metallurgy and Microstructure of Concentrated Solid Solution Alloys

Addition of small amounts of principal elements into metallic solid solutions is known to strongly influence the development of defect structures during irradiation, and has been widely used in material fabrication to achieve optimum performance. Conventionally, the alloy design has been limited to one or two principal elements to modify its material properties. The concept of high-entropy alloys (HEA) was proposed by Yeh *et al.* [19-21] to fundamentally change the concept of materials design. In a general sense, the HEAs are preferentially defined as those alloys with at least five principal elements, each with atomic percentage between 5% and 35% [21], and can be considered as a type of concentrated solid solution alloys. The basic principle behind HEAs is that solid-solution phases are relatively stabilized by their significantly high entropy of mixing compared to intermetallic compounds. Among the entropy terms contributing to total mixing entropy, the configurational entropy is commonly agreed to be the dominant one over entropy contribution from vibrational, magnetic dipole and electronic randomness.

The alloy world can be divided into three categories based on the number of major elements involved: high-entropy alloys (HEAs), medium-entropy alloys and low-entropy alloys. The configurational entropy per mole can be calculated using Boltzmann's hypothesis:

$$\Delta S_{conf} = -k \ln w = -R(\frac{1}{n}\ln\frac{1}{n} + \frac{1}{n}\ln\frac{1}{n} + \cdots + \frac{1}{n}\ln\frac{1}{n}) = -R\ln\frac{1}{n} = R\ln n$$

where R is gas constant, 8.314 J/Kmol, and n is the number of elements. Table 2.1 lists the configurational entropies of equimolar alloys in terms of the gas constant R. In general, the entropy increases as the number of elements increases. The limit for HEAs is 1.5R, while those between 1R and 1.5R are medium-entropy alloys, and those smaller than 1R are low-entropy alloys. Table 2.2 lists some configurational entropies of traditional alloys for comparison.

2.1.1 Physical Metallurgy

The materials studied in this thesis are all Ni-based single-phase concentrated solid solution alloys (SP-CSAs), which possess complex chemical composition but simple face-centered cubic crystal structure. Two to five principal elements (Ni, Co, Fe, Cr, Mn and Pd) have been developed and fabricated in the form of single-phase single crystals or large grain polycrystals, with completely random atomic distributions. The atomic radius of each principal element respective to Ni is listed in Table 2.3. SP-CSAs contain five or more alloying elements are also referred to be HEAs. The elemental metals Ni, Co, Fe, Cr, Mn and Pd (> 99.9% pure) were carefully weighted and mixed by arc melting. The arc-melted buttons were flipped and re-melted at least five times before drop casting to ensure homogeneous mixing. The single crystals were then grown from the polycrystalline ingots using a high temperature optical floating-zone directional solidification method, as shown in Figure 2.1.

Since there are more than one SP-CSAs being studied in this thesis work, the preparation detail of each material may vary slightly. Figure 2.2 shows the general process of sample preparation and its corresponding grain structure. The polycrystalline ingots were homogenized for ~24 hours at 1200 °C, and then rolled at room temperature in steps to a final thickness of ~1.8 mm. The rolled specimens were then annealed at 1170 °C for several days. Alloys with polycrystals structure have an average grain size of 100-200 μm to ensure minimum influence from grain boundaries.

The formation of single phase was examined both in X-ray powder diffraction (XRD) and under scanning electron microscope (SEM), while the material composition was carefully

measured by Energy-dispersive X-ray spectroscopy (EDS/EDX). Figure 2.3 shows the composition, crystal structure of NiCoFeCrPd examined by these techniques as an example. The sub-system SP-CSAs of the most studied HEA, NiCoFeCrMn, are highlighted in red in Figure 2.4. The concentration limit of principal elements in Ni SP-CSAs to maintain fcc single phase structure are listed in Table 2.4. The high concentration of alloying elements and the simple fcc structure make SP-CSAs unique materials to study the compositional effect on ideal model systems under irradiation damage.

2.1.2 Four Core Effects of HEAs

The high concentration of alloying elements and randomized atomic configuration in concentrated solid solutions have a large effect on microstructure, physical and mechanical properties. Among these properties, four core effects proposed in 2006 [22] are summarized here: high-entropy effect for thermodynamics, severe lattice distortion effect for material structure, sluggish diffusion effect for kinetics and cocktail effect for material properties. (1) The high entropy effect reduces the number of phases in HEAs, and prevents it from forming complex microstructure of intermetallic compounds. (2) With the high concentration of principal elements, the atoms in HEAs are surrounded by different kinds of neighboring atoms, and thus create lattice strain and stress from atomic size difference, as shown in Figure 2.5. The severe lattice distortion can significantly reduce the electrical and thermal conductivities due to stronger electron and phonon scattering. (3) From the different localized atomic configuration, HEAs can have larger fluctuation of lattice potential energy between lattice sites. These sites can serve as traps to hinder atomic diffusion and leads to slower atom diffusion rates and higher activation energies. The changes in atomic movement can result in different defect clusters interactions. (4) The cocktail effect summarizes the overall contribution of the constituent phases in HEAs. This effect not only considers the basic properties of individual elements, but also taken the mutual interaction between elements and the resulting severe lattice distortion into consideration.

Jin and Bei [23] reviewed and summarized the electrical and thermal transport properties of SP-CSAs that have been tested, as shown in Figure 2.6. It is found that the addition of Cr has the most significant impact on the electrical resistivity, with the alloys containing Cr having one order higher of resistivity than the ones without. The thermal conductivity of NiCoFeCr-based

HEAs and its sub-systems is presented in Figure 2.7. Similar to the electrical resistivity, the thermal conductivity can be separated into two groups based on the composition contains Cr or not. The group of SP-CSAs with Cr shows lower thermal conductivity in general. However, no definite correlation is found between electrical and thermal conductivities and the number of alloying elements in SP-CSAs.

The hindered atomic movement, or "sluggish diffusion" as it is frequently addressed in HEAs was proposed to explain the thermal stability at high temperature. The comparison of normalized diffusion activation energy in Ni-containing CSAs is presented in Figure 2.8. To be noted, the comparisons here were made with respect to the homologous temperature to normalize the difference in their melting temperature. The measure of using homologous temperature when analyzing the correlation between thermal diffusivity and number of elements in CSAs has been supported by several measurements [24-27], where the diffusion coefficient of HEAs may not always be lower than non-HEAs if compared in absolute temperatures.

2.2 Thermodynamics of Point Defect Formation

Before discussing the irradiation damage on materials and the following irradiation-induced defect evolution, it is worthwhile to examine the intrinsic point defects generated in materials naturally. If a crystal has n defects with N available sites, the increase of free energy can be expressed as:

$$\Delta \mathrm{G} = G^n - G^0 = \Delta H_f - T\Delta S^n$$

where G represents the free energy, ΔH_f is the increase in enthalpy from the formation of n defects, ΔS^n is the change in total entropy. The changes of enthalpy and entropy can be further expanded as:

$$\Delta H_f = n\Delta h_f$$

$$\Delta S^n = \Delta S_c^n + \Delta S_v^n = \Delta S_c^n + n\Delta S_v$$

h_f represents the increase of enthalpy from the formation of individual defect, S_v represents the vibrational entropy, which is associated with lattice vibrations, S_c^n represents the configurational entropy and can be considered in terms of the number of ways in which atoms can be distributed

in space. Using the expanded equation, the increase of free energy can be rewritten as:

$$\Delta \mathrm{G} = n\left(\Delta h_f - T\Delta S_v\right) - T\Delta S_c^n$$

and $\Delta S_c^n = k \ln \Omega_n = k \ln[N!/n!\,(N-n)!]$.

Equilibrium vacancy concentration can be found when $\partial \Delta \mathrm{G}/\partial \mathrm{n} = 0$

$$\partial \Delta G/\partial n = \frac{\partial}{\partial n}\left[n\left(\Delta h_f - T\Delta S_v\right) - T\Delta S_c^n\right] = \Delta h_f - T\Delta S_v + kT\, ln(\frac{n_{eq}}{N}) = 0$$

$$\text{where } \frac{\partial \Delta S_c^n}{\partial n} = k\frac{\partial}{\partial n}\{ln\,(\Omega_n)\} = k\frac{\partial}{\partial n}\{ln[N!/n!\,(N-n)!]\}$$

$$= k\,\frac{\partial}{\partial n}\{ln(N!) - ln(n!) - ln(N-n)\,!\}$$

$$\approx \mathrm{k}\,\frac{\partial}{\partial n}\{\mathrm{N}\ln(\mathrm{N}) - \mathrm{N} - \mathrm{n}\ln(\mathrm{n}) + \mathrm{n} - (\mathrm{N}-\mathrm{n})\ln(\mathrm{N}-\mathrm{n}) + (\mathrm{N}-\mathrm{n})\}$$

$$= k\,\frac{\partial}{\partial n}\{\,N\,ln(N) - n\,ln(n) - (\mathrm{N}-\mathrm{n})\ln(\mathrm{N}-\mathrm{n})\}$$

$$= k\,\frac{\partial}{\partial n}\left(\frac{N-n}{n}\right) \approx -k\,\frac{\partial}{\partial n}\left(\frac{n}{N}\right)$$

By applying the statistical thermodynamics, the concentration of intrinsic point defects can be expressed as:

$$C_x = \frac{n_{eq}}{N} = \exp\left(\frac{\Delta S_v^x}{k}\right)\exp\left(\frac{-\Delta h_f^x}{kT}\right) = \exp(\frac{-\Delta G_f^x}{kT})$$

where C represents the concentration of a certain type of point defects, x can represent either vacancies or interstitials, n represents the number of defects generated, N represents the number of available sites for defects to form, the subscript f represents the formation of defects, ΔS_v^x represents the change in vibrational entropy when certain defects are formed, Δh_f^x represents the total enthalpy change due to the formation of certain defects, ΔG_f^x represents the change of free energy due to the formation of intrinsic defects, k is the Blotzmann constant and T is the temperature. For actual applications, $\Delta S_v^x = S_f^x$, the formation entropy of the defect; and $\Delta h_f^x = E_f^x$, the formation energy of the defect. The formation energy of interstitials is about four times

higher than for vacancies [28], hence for the equilibrium concentration $C_v \gg C_i$.

To consider the effect of high concentration alloying elements on thermodynamic defect concentrations, some assumptions were proposed by Wang *et al.* [29] in an attempt to draw a correlation between number of alloying elements involved and changes on C_v. First, since the formation entropy of defects is hard to measure directly, the term $\exp(S_f^x/k)$ is assumed to equal to 1, and the equilibrium concentration of vacancy is assumed to be proportional to the formation energy only, which can be rewritten as:

$$C_v \approx \exp\left(\frac{-E_f^v}{kT}\right)$$

In an equiatomic multicomponent solid solution alloys, the equilibrium concentration of vacancy can be written as:

$$C_{v,m} = \frac{\exp(m - 1 - E_f^v/kT)}{m + \exp(m - 1 - E_f^v/kT)}$$

where m represents the alloying number of elements in the solid solution alloy. The detailed derivation can be referred to Wang *et al.* [29]. To simplify the derivation, they further assumed the formation energy of a vacancy do not change as the alloying number increases and derived the variation of vacancy concentration as:

$$C_{v,m}/C_{v,1} = \frac{\exp(m-1)}{m + \exp(m - 1 - E_f^v/kT)} \approx \frac{\exp(m-1)}{m}$$

The correlation between vacancy concentration and the number of alloying elements in solid solution alloys is shown in Figure 2.9. The component number is represented by m here in the derivation to avoid confusion on symbols. Form the derivation, the equilibrium concentration of vacancy increases with the number of alloying elements involved in equiatomic solid solution alloys.

2.3 Radiation Damage in Crystalline Metallic Materials

The concept of interaction of radiation with materials is addressed here to provide background necessary to analyze result of this thesis. During irradiation, high energy particles injected into materials will collide and transfer energy to lattice atoms to displace them. The produced vacancy-interstitial pairs are called Frenkel pairs, and these point defects can migrate to recombine, form clusters or being absorbed by sinks. These defect interaction mechanisms are illustrated in Figure 2.10 for pure metal and HEA, respectively. HEAs have the same defect interaction mechanisms as pure metal, but have much more combination of different interstitials and vacancies due to their high concentration of alloying elements and various surrounding atoms.

The concentration of radiation-induced vacancy and interstitial can be written as a net result of the local production rate, reaction with other species, and diffusion into or out of the local volume [28]. These competing processes can be expressed by the point defect balance equations:

$$\frac{dC_v}{dt} = K_0 - K_{iv}C_iC_v - \sum K_{vs}C_vC_s$$

$$\frac{dC_i}{dt} = K_0 - K_{iv}C_iC_v - \sum K_{is}C_iC_s$$

where C_v represents vacancy concentration, C_i represents interstitial concentration, K_0 represents the defect production rate, K_{iv} is the vacancy-interstitial recombination rate coefficient, K_{vs} is the vacancy-sink reaction rate coefficient and K_{is} is the interstitial-sink reaction rate coefficient.

In the past decades, several approaches have been developed to reduce residual defect concentrations from the perspective of increasing sink densities. The development of nano-crystalline metals [30-31], oxide-dispersion-strengthened (ODS) steels [32-33] represent some of the most well-known examples. Although great progress has been made, there are still challenges in material processing, such as alloy homogeneity and batch to batch reliability [33] waiting to be resolved. On the other hand, the development of Ni-containing SP-CSAs focuses on the primary defect generation stage, which emphasizes on understanding the defect migration

mechanism, enhancing defect recombination and minimizing the influence from defect sinks (grain boundaries, pre-existing dislocation lines, precipitates etc.).

The degradation of irradiated materials is usually due to the formation, growth and dissolution of defect aggregates such as voids, dislocation loops and lines. Defect evolution- defined here as the progression of vacancy and interstitial clusters generated during irradiation, is very sensitive to changes in material composition (including number and type of alloying elements) and irradiation temperature. In the following sections, mechanism of void swelling, dislocation microstructure, factors that can influence defect evolution, special considerations for ion irradiation and available literature results will be presented.

2.3.1 Mechanisms of Void Swelling

Void formation can have profound influence on material properties due to the induced volumetric changes on material. The driving force of void formation is the supersaturation of vacancies (C_v/C_v^0), where C_v is the concentration of vacancies in the material and C_v^0 represents the thermal equilibrium concentration of vacancies [28]. Voids are the result of vacancy agglomeration, where a net influx of vacancies can increase the size of voids. The critical number of vacancies to form a stable void embryo can be expressed by the following expression:

$$\Delta G = -nkT \ln S_V + (36\pi\Omega^2)^{1/3}\gamma n^{2/3}$$

where ΔG is the free energy change in the material, n is the number of vacancies, k is the Boltzmann's constant, T is the temperature, S_V is the vacancy supersaturation, Ω is the atomic volume, and γ is the surface energy. The illustration of free energy change and its relationship with the critical number of vacancies is presented in Figure 2.11. Some other factors that can affect the formation of void embryo are also listed here. (1) Thermal fluctuations can increase the critical size of void embryo, making the formation of stable void harder. (2) The presence of interstitials will decrease the net flow of vacancies to the embryo, and lead to higher free energy changes and would require more vacancies in order to reach critical embryo size.

As these embryos stabilize, the continuous vacancy accumulation can help voids grow in

size. In short, the equation for void growth can be expressed as:

$$dV/dt = 4\pi R\Omega[D_V(C_V - C_V^V) - D_i C_i]$$

where D_V and D_i are the diffusion coefficients for vacancies and interstitials, respectively. C_V and C_i are the concentration for vacancies and interstitials, respectively. R is the void radius, and C_V^V is the vacancy concentration at the void surface. The void growth process can be separated into three regions depending on the dominating mechanism: the nucleation region, the transition region, and the growth-dominated region. In the nucleation region, void embryos nucleate in the matrix and absorb most of the excess vacancies generated during irradiation, leaving few vacancies for void growth. On the contrary, in the growth-dominated region, existing voids become the dominating sites in absorbing excess vacancies generated, and pushing the growth of void size. The transition region falls between the nucleation and growth-dominated region.

2.3.2 Dislocation Microstructure

The dislocation loop/line feature is another irradiation defect that has profound influence on the microstructure development. In addition to its bias characteristic for interstitials, dislocation loops interact with each other and other microstructure features through their stress fields. Similar to voids, dislocation loops grow by the absorption/influx of interstitials while shrink by the annihilation with vacancies or absorb by sinks. Once they reach a critical size, the loops become stable and will keep growing until they unfault by interaction with other loops, or with the network dislocation [28].

Dislocation movement in fcc structure alloys occurs on {111} planes and in the <110> direction. With increasing doses, faulted loops can transform into unfaulted/perfect loops according to the reaction:

$$(a/3)\langle 111\rangle + (a/6)\langle 112\rangle = (a/2)\langle 110\rangle$$

where elliptical Frank loops have Burgers vector b= <111>/3, rhombus perfect loops have Burgers vector b= <110>/2, and Shockley partials have Burgers vector b= <112>/6. When the

vacancy shell collapse (condense) onto a close-packed plane, it produces an intrinsic faulted loop, while an extrinsic faulted loop is produced when condense of interstitial shell happens. Theoretically, both type of loops can be observed in fcc alloys; however, all dislocation loops examined in Ni SP-CSAs are all of interstitial-type [15, 34-35].

Stacking fault tetrahedron (SFT) is another unique dislocation configuration that can form during irradiation process. A SFT has a three-dimantional configuration and is in the shape of a tetrahedron, with stacking faults as sides and stair-rod dislocations as edges, as illustrated in Figure 2.12.

Stacking fault energy (SFE) measures the differences in deformation behavior of fcc alloys and has been used as one of the indicators to quantify chemical complexity. The term chemical complexity is used here to summarize the changes of chemical and physical properties arise from the alteration of element composition on atomic level. Alloys with low SFEs tend to deform through twinning while alloys with high SFEs tend to undergo dislocation-medicated slip. In low SFE materials, deform by dissociation into partial dislocations is more energetically favorable, and the spacing between the partial dislocations (the width of the stacking fault) is larger. As the spacing increases, cross-slip and climb becomes more difficult, increasing the strength of the material.

Zaddach *et al.* [36] measured the changes in SFEs from Ni to ternary HEA-Mn with increase number of alloys elements. It is found that the SFE decreased from over 120 mJ/m^2 in pure Ni to ~20 mJ/m^2 in equiatomic HEA-Mn, as shown in Figure 2.13. The greatest decrease in SFE was achieved by increasing Cr and decreasing Ni with the result that non-equiatomic $Ni_{14}Fe_{20}Cr_{26}Co_{20}Mn_{20}$ had a measured SFE of only 3.5. However, in this thesis work, only equiatomic HEAs are studied.

Zhao *et al.* [37] investigated the temperature dependent SFEs for a series of CSAs using first principles calculations. The negative SFEs observed at low temperatures indicated that hexagonal close-pack (hcp) is more energy favorable than fcc structure. The transition from hcp to fcc structure with increasing temperature can be attributed to intrinsic vibrational entropy.

And the coupling between different alloying elements can determine the magnitude of SFE and its temperature dependence. Figure 2.14 shows the calculated SFEs of CSAs, most of them are also being studied in this dissertation, expect NiCoFeMn.

2.4 Factors Affecting Defect Evolution

2.4.1 Temperature Effect

Temperature Effect on Voids

The temperature effect on defect evolution can be separated into two main parts, the first one is the effect on voids, and the second is its effect on dislocation loops. The first part of the discussion will be focused on voids. As previously mentioned, the formation and growth of voids or bubbles is one of the most severe material degradations in radiation environment at elevated temperatures. Voids are formed when materials undergo volumetric swelling, with an optimum formation temperature ranges between 0.3 to 0.6 T_m (melting temperature of the material).

Void nucleation is highly dependent on the vacancy super-saturation, which is also temperature sensitive and can be expressed as follows:

$$n = \frac{32\pi\gamma^3\Omega^2}{3(kT)^3[\ln(\frac{B_v(n) - B_i(n+1)}{B_v^0(n)})]^3}$$

where γ is the surface energy, Ω is the atomic volume, k is the Boltzmann's constant, T is the temperature, and $\frac{B_v(n)-B_i(n+1)}{B_v^0(n)}$ represents the vacancy supersaturation. At relatively high temperature, the nucleation rate decreases due to a higher emission rate of vacancies and a dramatically increased vacancy saturation concentration (very large n). At relatively low temperature, the low diffusivities of point defects lead to few vacancies available (small vacancy supersaturation) for void formation. Furthermore, vacancies have higher migration barriers at low temperatures and tend to annihilate with interstitials than clustering into voids. These decreases of swelling at both ends of temperature spectrum lead to a bell-curve temperature

dependence on void swelling [28].

Sprague *et al.*[38] performed studies on temperature dependence of void and dislocation structures in high-purity nickel using 3 mm TEM disks. The irradiation was done using 2.8 MeV $^{58}Ni^{+}$ ions irradiated to 13 dpa at a displacement rate of $7 \times 10^{-2}\ dpa/sec$ over the temperature range of 325 to 625 ℃. The irradiation-induced features were summarized in Table 2.5. The TEM images of voids and dislocations observed at three temperatures were shown in Figure 2.15. The features were shown in separate images due to the difference in optimum contrast imaging condition. The general trend showed that voids and dislocation structures both grow larger and have lower defect density as temperature increased.

Ryan [39] studied the void microstructure developed in the temperature range from 525℃ to 675 ℃ to various damage doses with different irradiation ions. The data suggests that the peak swelling temperature for pure Ni irradiated using $^{58}Ni^{+}$at a dose rate of $4 \times 10^{-3}\ dpa/sec$ falls between 600℃ and 625℃, or about 0.5 T_m of Ni, while the swelling peak shifted to 500-550 ℃ for neutron-irradiated Ni. The peak temperature shift can be attributed to higher displacement rates associated with ion irradiation, which results in higher point defect recombination and lower ratio of net in-flux vacancies for void growth.

Since the temperature dependent void evolution in Ni SP-CSA is one of the main objectives of this dissertation, the effect of temperature on the irradiation response of other non-equiatomic HEAs will be presented here as reference. For instance, Kumar *et al.* [40] studied the microstructural stability and mechanical behavior of $Fe_{0.28}Ni_{0.27}Mn_{0.18}Cr$ to 10dpa at 400-700℃ using 3.0/5.8 MeV Ni ions. Yang *et al.* [41] studied the defect evolution in $Al_{0.1}CoCrFeNi$ irradiated to 31 dpa at 250-650℃ using 3MeV Au ions. In both cases, the density of dislocation loops decreased while the size increased with increasing irradiation temperature. However, no voids were observed in both cases at all tested temperatures. In Kumar's study, the irradiation dose of up to 10 dpa may be too low to form voids to be detected by their TEM analysis, given the good swelling resistance reported in HEAs. Additionally, the observation of stacking fault tetrahedra (SFTs) by Yang [41] when irradiated at 500 and 650 ℃ to 31 dpa indicates that SFTs may be the minimum energy form for vacancy clusters in $Al_{0.1}CoCrFeNi$, suggesting that void

formation is unlikely in their testing conditions.

Temperature Effect on Dislocation Microstructures

The evolution of interstitial loop can be described by its response to temperature and dose, as shown in Figure 2.16 and Figure 2.17, respectively. The dominating dislocation microstructure at relatively low temperature region includes "black dots" (which usually refer to defect clusters smaller than 2 nm) and dislocation network. The density of Frank loops increases with increasing irradiation temperature, while the density for black-dots decreases. Please note that the temperature effect demonstrated here use austenitic stainless steel as an example, a temperature shift is expected when applying similar concepts on CSAs. Furthermore, higher dose of irradiation damage will result in lower dislocation loop density but larger average loop size.

Zinkle *et al.* [42] studied the stacking fault tetrahedra and dislocation loops on nickel irradiated with fission neutrons from 0.01-0.25 dpa at about 230℃. Figure 2.18 summarized the dose dependence of defect cluster density for irradiation conducted between room temperature and 300 ℃. The dislocation density in nickel increased considerably as dose increased from 0.098 to 0.25 dpa. Based on the result, the authors noted that the defect cluster density accumulation in nickel is independent of irradiation temperature up to at least 200℃ (0.27 T_m). Furthermore, the defect cluster density (SFTs and dislocation loops) saturates around 0.1 dpa at temperature < $0.3T_m$. The evolution of the defect cluster morphology irradiated at 200 ℃ is shown in Figure 2.19. Based on the limited data available, the authors suggested a gradual transition from a SFT-dominant microstructure at low doses to an interstitial dislocation loop-dominant microstructure beyond 0.1 dpa.

Ryan [39] studied the dislocation loops in Ni irradiated with $^{58}Ni^{+}$ at a dose rate of $4 \times 10^{-3}\ dpa/sec$ to various elevated temperatures. It is found that the dislocation number density saturates at around 50 dpa when irradiated at 525℃, while dislocation loops grow into dislocation lines as temperature keeps increasing, as shown in Figure 2.20.

Yang *et al.* [41] analyzed the microstructure of $Al_{0.1}CoCrFeNi$ irradiated to 31 dpa at 250-650℃ using 3MeV Au ions. The authors observed a shift of dominating defect features and

defect migration as temperature increased, as presented in Figure 2.21. No phase decomposition or incoherent precipitation was observed based on the selected area electron diffraction (SAED) pattern. The main defect structure shifted from dislocation loops to long dislocation line segments as temperature increased from 500 ℃ to 650 ℃, which corresponds to 0.46 T_m and 0.55 $T_{m,}$ respectively.

2.4.2 Effect of Pre-Existing Defect Sinks

In general, any microstructure features that can affect the concentration of irradiation-induced defects can be addressed as defect sinks. However, the term pre-existing defect sinks here specifically refers to grain boundaries, pre-existing dislocation lines, and precipitates. The effect of pre-existing defect sinks can be best captured in the equation of defect concentration, described in chapter 2.3. In the equation, the third term on the right summarizes the vacancies/interstitials lost due to interactions such as absorption, annihilation or escape through sinks. Nano-crystalline metals [30-31], oxide-dispersion-strengthened (ODS) steels [32-33] and HT9/T91 ferritic martensitic steels [43] are examples of materials designed with increasing defect-sink interactions in mind. However, the complex microstructure of these materials made studying the direct interaction between defects much more challenging. The design of SP-CSAs took a different approach, instead of focusing on increasing the defect-sink interactions, it minimized the effect of pre-existing defect sinks by growing single crystals or polycrystals with hundreds of μm grain size. Without the interference from extra pre-existing sinks, one can assume that the final microstructure of irradiated SP-CSAs is primarily the result of direct defect interactions, which is also the main objective of this thesis study. However, since majority of materials applied in the nuclear industry do not have the single crystal form, the role of pre-existing sink to defect evolution is equally important. The effect of pre-existing sinks on defect evolution in Ni SP-CSAs is an ongoing work, but it has not been included in the scope of this dissertation study.

2.4.3 Solute Atomic Effect

Nickel and various single-phase nickel alloys are commonly used as model fcc metals in studying the alloying effects in irradiation induced defect evolution. Neutrons, heavy-ions and electrons are generally used as the irradiation source. The review of the most relevant reference

will be focused on the study of defect evolution in Ni-based alloys when alloying with various alloying elements and different concentrations.

Neutron Irradiation on Ni and Ni Based Solid Solutions

Brimhall et al. [44] studied void formation using neutron irradiations in copper, nickel and copper-nickel alloys. The studied copper-nickel alloys consisted of 98Cu-2Ni, 80Cu-20Ni, 50 Cu-50Ni, 20Cu-80 Ni and 2Cu-98 Ni in weight percent. The main purpose of the investigation was to observe void nucleation behavior. Samples were prepared in TEM disc shape with a thickness of about 0.1 mm. Most of the irradiation was conducted at 285℃, except one copper sample was irradiated at 260℃. The study found that void formation is more difficult in alloys than pure metals, and the size of dislocation loops varied slightly with alloy compositions. The suppression of void formation in alloys was attributed to preferential trapping or binding of point defects. However, the study failed to consider the changes of melting temperature as alloy composition varies, and its effect on void swelling. Furthermore, since the testing temperature was on the edge of the lower temperature threshold for void formation in nickel, the possibility of having too low of an irradiation temperature to form voids cannot be completely excluded.

Yoshida et al. [45] studied the effects of impurities on defect cluster evolution in Ni at 290℃. The authors found that the density and size of defect clusters are depending on both neutron fluence, and the impurity level of tested alloys. Ni specimens with higher impurity content tended to have higher defect cluster densities.

Mitchell and Garner [46] studied the neutron-induced swelling behavior in binary Ni-Al alloys. Five alloys with aluminum levels of 1.1, 2.6, 4.2, 7.1 and 13.3 wt % were irradiated at eight temperatures in the EBR-II fast reactors. The irradiation temperatures ranged from 400 to 650℃. The swelling in this study was defined as the percentage decrease in density, which accounted for both void swelling and lattice parameter changes arising from solute redistribution and precipitate formation. Figure 2.22 shows the swelling of Ni-Al alloys as a function of aluminum content at 400-650 ℃ to various neutron fluences. As can be seen, the swelling rate was especially sensitive to irradiation temperature when aluminum concentration is low.

Furthermore, the observed decrease of swelling rate as aluminum content increases suggested a modification on the irradiation process.

Yoshiie and Kiritani [47] reviewed and categorized mechanisms that determine the destination of point defects in collision cascade damage. These factors included the initial distribution of point defects, the type and distribution of annihilation sites, and the style of migration of point defects and their mobility. Each factor was evaluated and supported by different experimental designs using fission and fusion neutron irradiation under a variety of conditions. The mechanisms proposed by Yohiie are summarized below.

- The compactness or diluteness of cascades is determined by materials parameters.
- A strong void growth is expected when the differences in point defect distribution are large.
- The mutual annihilation with the opposite types of point defects is high for a compact cascade.
- Interstitial clusters and vacancy clusters can both grow into a larger size if they nucleate at the same time.
- If the nucleation rate is different for interstitial and vacancy type of clusters, the defect with slower nucleation rate will prevent further growth of the other defect clusters.
- Permanent sinks such as dislocations, grain boundaries, surfaces etc. will affect the microstructural evolution of irradiation-induced defects.
- Different mode of point defect migration will also affect the microstructural evolution. For instance, the one dimensional (1-D) motion of interstitial clusters tends to have a longer jumping length and a relatively weaker reactivity than the usual random walk of interstitials diffusing in the same direction. This leads to a low mutual annihilation rate of moving clusters and a preferential growth of dislocation loops.
- The addition of alloying elements will block the replacement sequence collision, which reduces the differences in the distributions of interstitials and vacancies, and increases the mutual annihilation. Alloying elements will also alter the mobility of point defects, as over-sized and under-sized elements tend to react with interstitials and vacancies, respectively.

The mechanisms proposed above suggested that the microstructural evolution strongly depends on the geometrical relationship, meaning the mobility and migration direction of point defects will change based on irradiation temperature and the strain fields from various sources. However, a more systematic study is desired to further consolidate the mechanisms.

Hamada *et al.* [10] studied pure Ni and Ni binary alloys with 2 at% Si, Cu, Ge and Sn as solutes using neutron irradiation at several elevated temperatures. Their result showed that, in the alloys with Si or Sn (with -5.8% and 74.08% volume size factor compared to Ni, respectively), solutes played an important role in preventing the unfaulting of faulted interstitial-type dislocation loops. Contrarily, the Cu and Ge solute atoms (with 7.18% and 14.76% volume size factor) were regarded not to have significant influence on the evolution of defect structure.

Yoshiie *et al.* [11-12] further suggested that the 1-D movement of interstitial clusters in Ni-Si and Ni-Sn alloys is strongly suppressed by solute atoms of Si and Sn. It was concluded that the reduction on defect clusters mobility leads to the reduction in void growth in Ni-2 at% Si and Ni-2 at% Sn.

Sato *et al.* [13] studied the effect of solute atom concentration in Ni alloys using positron annihilation lifetime measurements. The research indicated that the size of vacancy clusters in Ni-Si and Ni-Sn alloys decreases with an increase in the solute atom concentration. The authors concluded that the frequency and mean free path of the 1-D motion depends on the solute concentration and amount of segregation from solute atoms.

Heavy-Ion Irradiation on Ni and Ni Based Solid Solutions

Compared to neutron irradiation, ion irradiation not only is more accessible, it also has the advantage of faster dose rate, flexible incident ions energy, low to none residual activity. Consequently, ion irradiation has been widely proposed and successfully demonstrated to emulate the reactor irradiation damage on materials [5].

Zinkle *et al.* [48] studied the helium bubble formation in Cu, Ni and Cu-Ni alloys irradiated using 200-400 keV ^{3}He ions to less than 10^{-3} dpa at 0.65 T_m. A low density of He

bubbles was observed in all tested samples, but no dependence was found between the bubble sizes, density to alloy composition. The relatively low implanted helium concentration, high homologous temperature and low damage dose may contribute to the small difference observed in vacancy migration energy for Cu-Ni alloys.

Wang *et al.* [49] studied the microstructural evolution in irradiated Ni-Cu alloys using cross-sectional TEM samples. Ni-10at%Cu, Ni-50at%Cu and pure Ni were irradiated using 14 MeV Ni ions at $0.45T_m$ homologous temperature to 100 dpa at the peak damage. Most samples were pre-injected with 5 MeV oxygen ions at room temperature prior to irradiation. It was found that concentrated Ni-Cu alloys have higher resistance to void formation than pure Ni. Furthermore, the average dislocation loop size was much smaller and their density was 5-7 times higher in Ni-50Cu than in Ni-10Cu.

On a similar study, Wang *et al.* [50] studied the effect of pre-injected helium in nickel ion irradiated Ni-Cu alloys. The pure Ni, Ni-10at%Cu, Ni-50at%Cu were irradiated with 14 MeV Ni ions at $0.45T_m$ homologous temperature to 3-5 dpa at a depth of 1 um from the surface. It was found that the defect structures in the three tested materials are distinctly different, as shown in Figure 2.23. The amount of swelling was highest in pure Ni while the dislocation loops constituted the major type of defect clusters observed in Ni-Cu alloys. The loop density increased with increasing copper concentration, whereas the loop size decreased. The trapping of vacancies and gas atoms by fine-scaled clusters of like atoms was suggested to be responsible for the higher resistance on void formation in Ni-Cu alloys.

Wakai *et al.* [14] investigated the effect of solute atoms on swelling in Ni alloys and pure Ni using 25 keV He^+ irradiation at 500℃. The studied materials included Ni, Ni-Si, Ni-Co, Ni-Mn and Ni-Pd binary alloys with different volume size factors. All binary alloys had 5at% solute concentration. Table 2.6 lists the volume size factors of solute atoms in Ni, the number density and mean size of dislocation loops. Figure 2.24 shows the dislocation loops formed in pure Ni and binary Ni alloys irradiated to $1.0 \times 10^{19}\ m^{-2}$ at 500℃. It was suggested that the mean size of loops and swelling tend to increase with the volume size factor of solute atoms, while the number densities of bubbles tend to increase with the absolute values of the volume size factor,

see Table 2.7.

As stated in one of the publications from this dissertation [18], the credibility of the result from Wakai [14] is hindered due to the use of helium ions as the irradiation ion. In the conclusion section, the authors suggested themselves that helium irradiation may promote the nucleation of dislocation loops by forming He-point defect complexes rather than di-interstitial and interstitial-solute complexes. Furthermore, the swelling calculations included a high density of bubbles, which can be easily formed with high dose helium irradiation and have different interaction mechanisms with interstitials than with voids. The effect of grain size was also not discussed in this study. This missing information is important as the grain boundary can act as a strong sink to irradiation induced defects. The conclusions not only have contradicted the result obtained from neutron radiation, but also the observed correlation on dislocation loop size and swelling has a minimal influence from solute atoms in their study.

These listed studies present a clear picture showing that the addition of minor elements in Ni alters the defect accumulation in both neutron and heavy ion irradiation. However, most of the studies only investigate the defect evolution in dilute binary alloys. The defect evolution and interaction mechanisms in concentrated solid solution alloys, at various doses, temperatures and increased chemical complexities have not been systematically studied. It is known that the dominating migration mode of interstitial clusters will transition from long-ranged 1-D to relatively short-ranged 3-D as the solute concentration increases, which results in different material properties in terms of void swelling, irradiation hardening etc. To attempt to understand and fill in the gap between dilute and concentrated alloys, it is critical to determine how the solute atomic size, binding energy with irradiation defects, temperature and chemical complexity will affect defect evolution.

In one of the early research on irradiation performance of Ni SP-CSAs, Zhang *et al.* [51] reported that Ni-based CSAs exhibit superior radiation resistance compared to pure Ni through changes in its chemical complexities. The resistance was measured by Rutherford backscattering technique (RBS) and using ion channeling to characterize the relative irradiation damage. The complexity can be easily modified through increasing the number of principal elements, as

shown in Figure 2.25. The superior resistivity for more complex CSAs was attributed to a substantial reduction in electron mean free path and orders of magnitude decrease in electrical and thermal conductivity.

2.4.4 Special Considerations for Ion Irradiation

Ion irradiation has numerous advantages when apply to emulate neutron irradiation. However, to understand, preserve and compare physical quantities generated between these two types of irradiations, the concept of variable shifts and special features induced by ion irradiation should be considered. Since the comparison between neutron and ion irradiations are not the focus of this thesis work, the variable shifts will be briefly addressed for the completeness of the discussion.

The irradiation variable shifts are defined as the shift in other variables caused by the changes from one irradiation variable to preserve a physical quantity describing the behavior of defects during irradiation [28]. The most common variables are temperature, dose and dose rate or the ions used for irradiation. Figure 2.26 presents the general relationship between these variables in the context of radiation-induced segregation.

Unlike neutrons, charged particles used in ion irradiations lose energy through electronic excitation in addition to vie elastic collisions. Therefore, the displacement rate of ion irradiation is depth and energy dependent. To provide a complete picture of irradiation-induced defect evolution, the depth dependent complexities from ion irradiation, such as surface effects, self-interstitial injection effect and diffusional spreading should be considered.

Surface Effects

The primary effects arise from the sample surface include sputtering, loss of defects and dislocations, with the latter two being the most relevant ones to our study on defect evolution. The free surface can serve as a competing sink for point defects and dislocations. Yoo and Mansur [52-53] calculated the effect of free surface on defect distributions and concluded that denuded zones of voids and dislocation loops should exist near the surface. According to their estimation, the affected depth from surface effect is about 10% or less of the depth of peak dose.

Self-interstitial Injection Effects

During ion irradiation, the bombarding ions use to displace atoms will eventually have energy below the threshold energy to further displace atoms, and reside in the material structure as self-interstitials. These injected ions can play a significant role in suppressing void swelling and even shift the swelling peak. Mansur and Yoo [53] calculated the reduction of void swelling caused by injected interstitials and predicted that the effect of injected interstitials is expected to be small on void growth when most irradiation-induced point defects are absorbed at sinks, while the effect is expected to be important when most defects are lost to recombination. Shao *et al.* [54] and Short *et al.* [55] showed that injected interstitials not only resulted in the formation of double peaks on swelling, it also shifted the peak saturation level and void nucleation rate location towards the free surface by ~200 nm.

Diffusional Spreading

Ion irradiations result in a depth-dependent displacement rate profile. The concept of diffusional spreading arises from the fact that steady-state point defect concentration at a given depth does not consider the thermodynamic diffusion of defects. Point defects generate at damage peak may diffuse out, even beyond the calculated end of range, due to its high concentration gradient. Comparing with the calculated damage profile, this diffusion process leads to a broadened swelling profile and a lower swelling rate/displacement rate ratio for heavy ion irradiation.

2.5 Other Irradiation Effects

In addition to the depth dependent complexities arise from ion irradiations, other irradiation effects that may affect the mechanical properties of materials are presented here. The first part will focus on radiation induced segregation while the second part will address the hardening behavior induced by irradiations.

2.5.1 Radiation-Induced Segregation

Radiation-induced segregation (RIS) of alloying elements is the result of a preferential coupling between defects and alloying elements to defect sinks, such as grain boundaries,

dislocations and voids. The segregation or depletion of alloying elements can result in the formation, dissolution of precipitates, and lead to detrimental degradation on the mechanical properties of materials. In general, RIS closely resembles the bell curve behavior as void swelling at 0.3-0.5T_m, and can be explained by two mechanisms: inverse Kirkendall effect [56] and solute size effect [57]. The inverse Kirkendall effect considers the preferential migration of vacancies and interstitials via A-B atoms in a binary A-B alloy. The segregation of a certain type of atoms can be decided by:

$$\frac{d_{Av}}{d_{Bv}} - \frac{d_{Ai}}{d_{Bi}}$$

where d_{xy} is the partial diffusion coefficient of x (x=A,B) atoms through y (y=v,i) migration; v and i represents vacancies and interstitials, respectively. The segregation behavior at sinks depends on the differences between vacancy and interstitial diffusion coefficients of the alloying elements. The mechanism predicts that slow-diffusing atoms will be enriched at sinks, while faster-diffusing atoms will be depleted at sinks. If $d_{Av}/d_{Bv} > d_{Ai}/d_{Bi}$, the concentration gradient of A atoms follows that of vacancies, and A atoms will be depletion at the sink.

The solute size effect also plays a major role in determining the segregation direction of alloying elements. It has been well recognized that the undersized atoms tend to interact with interstitials, while the oversized atoms tend to interact with vacancies to achieve a minimum energy state in the lattice. This migration preference due to atom size results in the undersize atoms migrating as interstitials while the oversize atoms migrating against the vacancy flux. In a simple binary alloy system, oversized solute atoms will be depletion at sinks while undersized solute atoms will be enriched.

Rehn *et al.* [58] studied the RIS on binary alloys of 1 at% Al, Ti, Mo and Si in Ni irradiated with 3.5 MeV Ni^+ ions at temperature ranged from 385-660℃. The authors found that oversized solutes, Al, Ti and Mo were all depleted near the irradiated surface, while the undersized solute Si was enriched. It was also found that the magnitude of segregation diminished at both end of the tested temperatures.

Kumar *et al.*[40] analyzed the RIS on high angle grain boundaries of $Fe_{0.28}Ni_{0.27}Mn_{0.18}Cr$ irradiated to 10 dpa at 400-700 ℃ using 3.0/5.8 MeV Ni ions. Their result showed that Ni was enriched at grain boundaries, while Fe, Cr and Mn were depleted. The temperature dependence of RIS was recorded to be the most significant at 600℃, with no notable segregation being observed at 400℃. The decrease of RIS magnitude at 700℃ was attributed to the increase in defect mobility and back-diffusion with increasing temperature. The RIS result was compared to $FeCr_{0.20}Ni_{0.24}$ irradiated with 3.2 MeV using protons to a damage level of 0.1-3 dpa. The authors suggested the higher temperature regime of RIS in $Fe_{0.28}Ni_{0.27}Mn_{0.18}Cr$ can be attributed to the sluggish diffusion kinetics reported in HEAs. However, the suggestion is questionable when only compared in direct temperature. Some latest researches [23-27] have shown that the sluggish behavior of CSAs does not always apply when comparing different alloys in the absolute temperature setting. The comparison should be made in homologous temperature to normalize the difference in melting temperatures between alloys.

Yang et al. [41] applied atom probe tomography (APT) to study clusters of alloying elements in $Al_{0.1}CoCrFeNi$ irradiated to 31 dpa at 250-650 ℃ using 3MeV Au ions. The observation of Ni, Co- enriched clusters in APT tips suggested a preferential segregation of Ni and Co at defects, such as dislocation loops and dislocation line segments. The segregation behavior was investigated with changing temperatures. It has been found that at the lower temperature regime (250-350℃), most of the enriched dislocation loops were disk-shaped and accompanied with few ring-shaped dislocation loops. As temperature increased to 500-650℃, only disk-shaped dislocation loops were observed. Disk-shaped dislocation loops indicates the segregation occurs on the whole habit plane of dislocation loops. In the ring-shaped dislocation loops, the solute segregation only occurs at the edge of loops.

2.5.2 Hardening

The microstructural changes induced by irradiations can have profound effect on mechanical properties of materials. Radiation hardening refers to the increase in yield stress and ultimate tensile strength of the studied material after irradiation. The hardening effect also decreases the total and uniform elongation of the material in a stress-strain test. Addition to the hardening induced by irradiation, alloying elements in solid solution alloys have been known to

have strengthening effect on materials, making the movement of screw dislocations becomes more difficult. The theories for dilute solutions are relatively well-developed than the theories for CSAs. Fleisher [59] studied the binary interaction of solute strengthening in copper alloys. It was found that the critical shear stress to overcome obstacles is loosely proportional to the atomic size misfit. Labusch [60] investigated the movement of a dislocation through an array of obstacles using statistical methods, and obtained a critical shear stress that is proportional to the two-thirds power of solute concentration. The illustration of these two proposed models is shown in Figure 2.27.

Contrarily, little is known about the solute strengthening mechanism on CSAs where the concept of solute or solvent may no longer apply. In the equiatomic alloy, all alloying elements have the same atomic concentration, and the interaction of a dislocation will not be restrained to two elements. Wu *et al.* [3] investigated a family of single-phase fcc equiatomic alloys ranging from binary, ternary and quaternary alloys with Fe, Ni, Co, Cr and Mn as principal elements. These alloys underwent similar process treatments to achieve equiaxed microstructures with comparable grain sizes. The tensile test was performed using an engineering strain rate of 10^{-3} s^{-1} at temperature ranging from 77-673 K. The alloy properties and testing results are shown in Table 2.8 and Figure 2.28, respectively. The work hardening from increased chemical complexity was defined as the difference between the ultimate and yield strengths, and the result is shown in Figure 2.29. Of all the tested CSAs, NiCoCr has the highest yield strength, ultimate strength, work hardening and great uniform elongation capability. Since the solution strengthening model proposed by Labusch taken the atoms all around the space into consideration, it has been proposed by Wu *et al.* [61] to explain the solution strengthening mechanism in concentrated solid solutions. For the derivation of the model applied in equiatomic solid solution alloys, please refer to reference [61].

The combination of work hardening and radiation hardening has been studied by Jin *et al.* [62] using nanoindentation on pristine and irradiated area of SP-CSAs. The result of hardness before, after irradiation and the difference is shown in Figure 2.30. The irradiation was performed using 3 MeV Ni^{2+} ions to fluences of up to $5 \times 10^{16} cm^{-2}$at 500℃. The hardness measurement of pristine samples can be arranged from low to high as: Ni, NiCo, NiCoFe, NiFe,

NiCoFeCr, NiCoFeCrMn and NiCoCr. Their result was similar to the yield strength measured by Wu *et al.* [61] in tensile tests. The irradiation-induced relative hardening was also presented here, but little explanation was yielded in this comparison due to the difference in pristine hardness amoung SP-CSAs. Therefore, a more detailed microstructure characterization on TEM samples is desirable to reveal the cause of solution hardening.

Table 2.1 Configurational entropies of equimolar alloys with constituent elements up to 13 [63].

n	1	2	3	4	5	6	7	8	9	10	11	12	13
ΔS_{conf}	0	$0.69R$	$1.1R$	$1.39R$	$1.61R$	$1.79R$	$1.95R$	$2.08R$	$2.2R$	$2.3R$	$2.4R$	$2.49R$	$2.57R$

Table 2.2 Configurational entropies calculated for typical traditional alloys [63].

Systems	**Alloys**	**ΔS_{conf} at liquid state**
Low-alloy steel	4340	$0.22R$ low
Stainless steel	304	$0.96R$ low
	316	$1.15R$ medium
High-speed steel	M2	$0.73R$ low
Mg alloy	AZ91D	$0.35R$ low
Al alloy	2024	$0.29R$ low
	7075	$0.43R$ low
Cu alloy	7-3 brass	$0.61R$ low
Ni-base superalloy	Inconel 718	$1.31R$ medium
	Hastelloy X	$1.37R$ medium
Co-base superalloy	Stellite 6	$1.13R$ medium
BMG	$Cu_{47}Zr_{11}Ti_{34}Ni_8$	$1.17R$ medium
	$Zr_{53}Ti_5Cu_{16}Ni_{10}Al_{16}$	$1.30R$ medium

Table 2.3 The atomic radius of principal elements used in this study respective to Ni.

Alloying Element	Solute atomic volume size factor [a] (%)
Ni	0
Co	1.76
Fe	10.57
Cr	10.34
Mn	23.20
Pd	41.33

[a] The atomic volume size factors of solute atoms in Ni is calculated by King *et al.* [9].

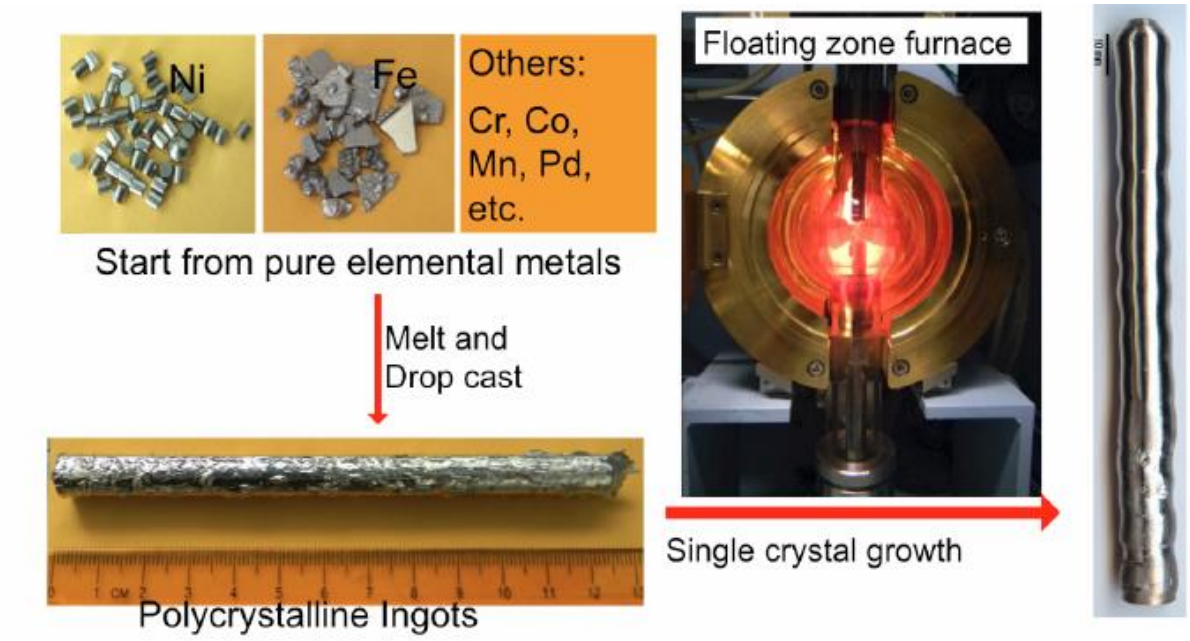

Figure 2.1 The procedure of growing single crystal Ni-containing SP-CSAs [64].

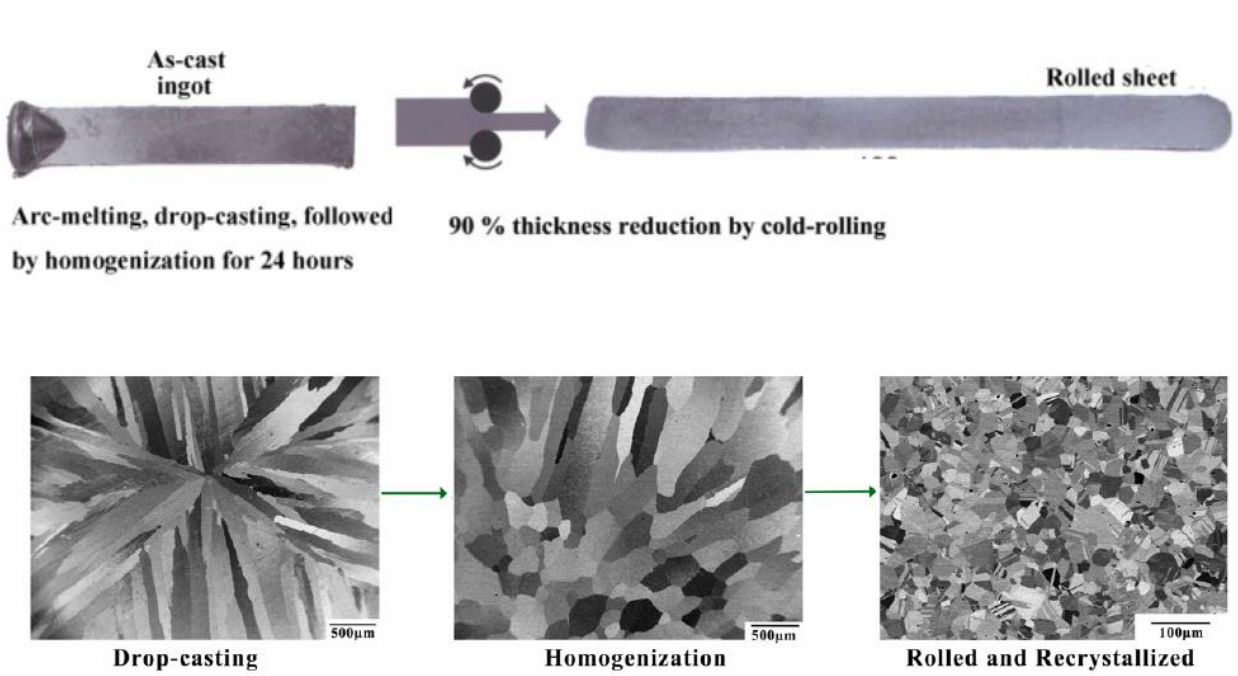

Figure 2.2 General process of growing Ni-containing SP-CSAs and its corresponding grain structure [64].

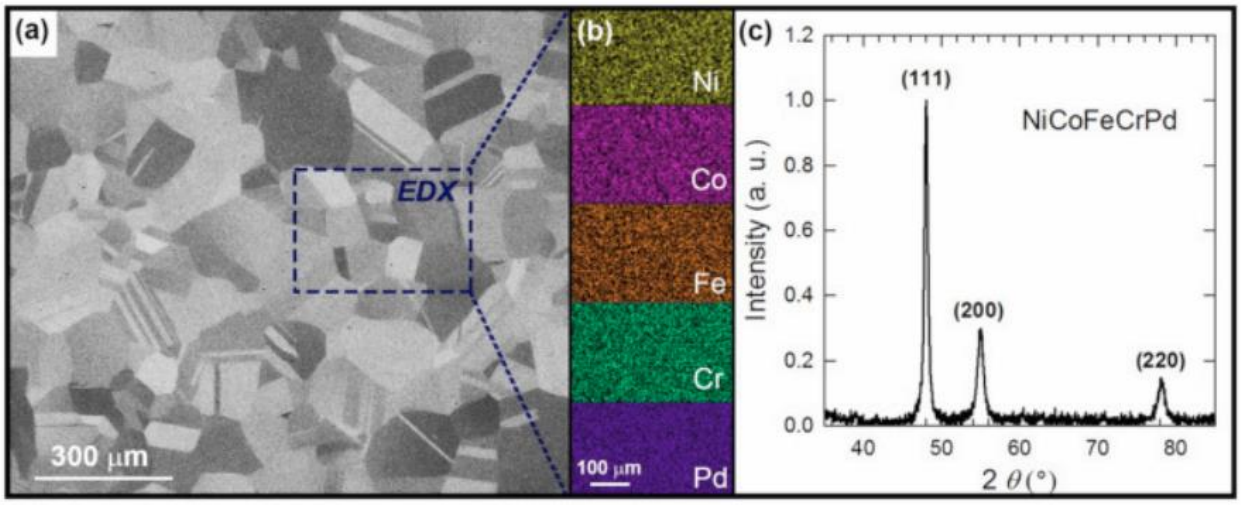

Figure 2.3 The microstructure and composition of NiCoFeCrPd under SEM, EDX, XRD [64].

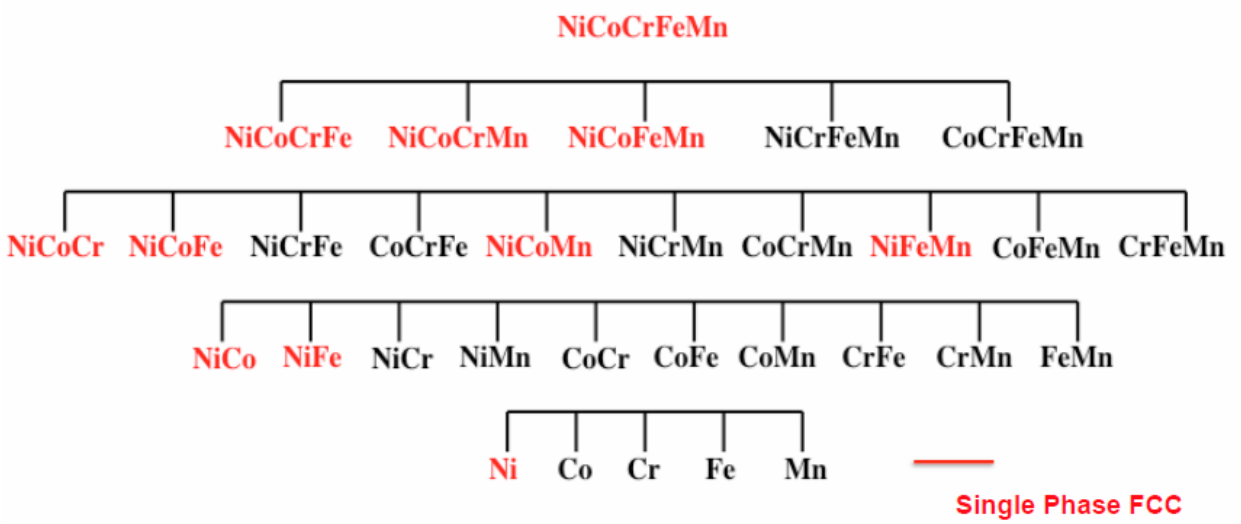

Figure 2.4 All possible fcc single phase solid solutions among the equiatomic subsets of NiCoFeCrMn [65].

Table 2.4 The concentration limits of principal elements in Ni SP-CSAs to maintain fcc single phase structure [64].

Alloys	Tunable elements	Ranges
NiCr	Cr	0-22%
NiFe	Fe	0-70%
NiCo	Co	0-60%
NiPd	Pd	0-100%
NiFeCr	Cr	0-20%
NiCoCr	Cr	0-33%
NiCoFe	Fe	0-33%
NiCoCrFe	Cr, Fe	0-25%
NiCoCrFeMn	All ele.	15-25%
NiCoCrFePd	All ele	15-25%

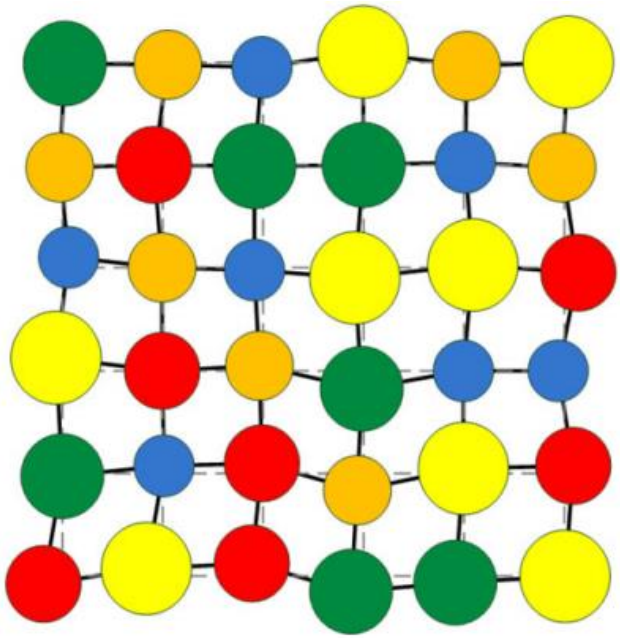

Figure 2.5 Illustration of severely distorted lattice in a multielement crystal structure [63].

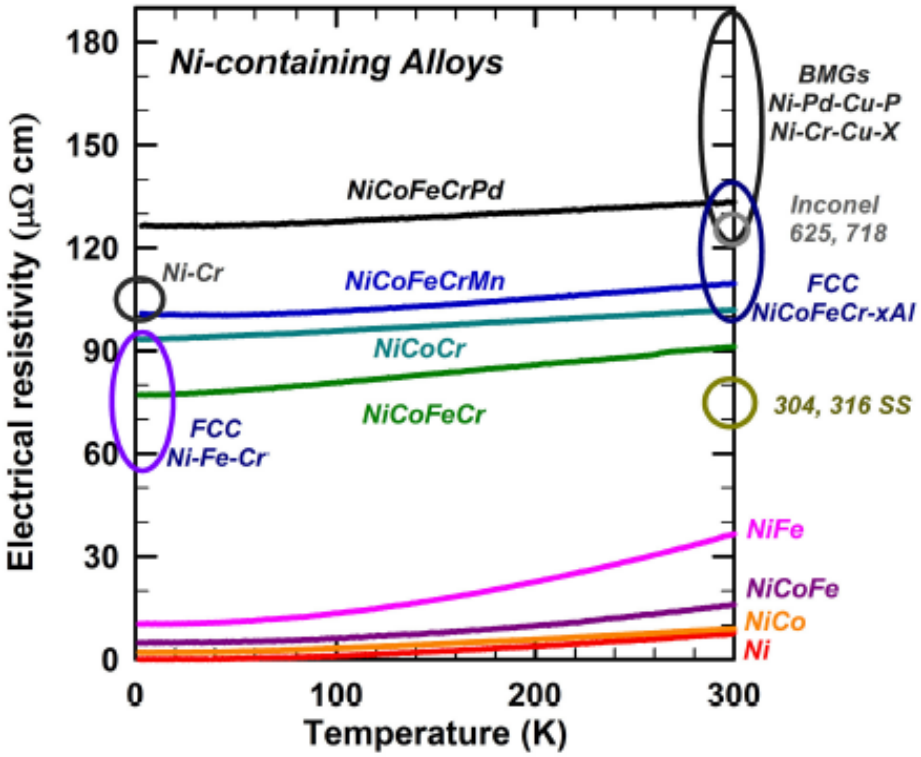

Figure 2.6 Comparison of electrical resistivity of Ni-containing FCC SP-CSAs, several conventional alloy systems and BMGs [66-72].

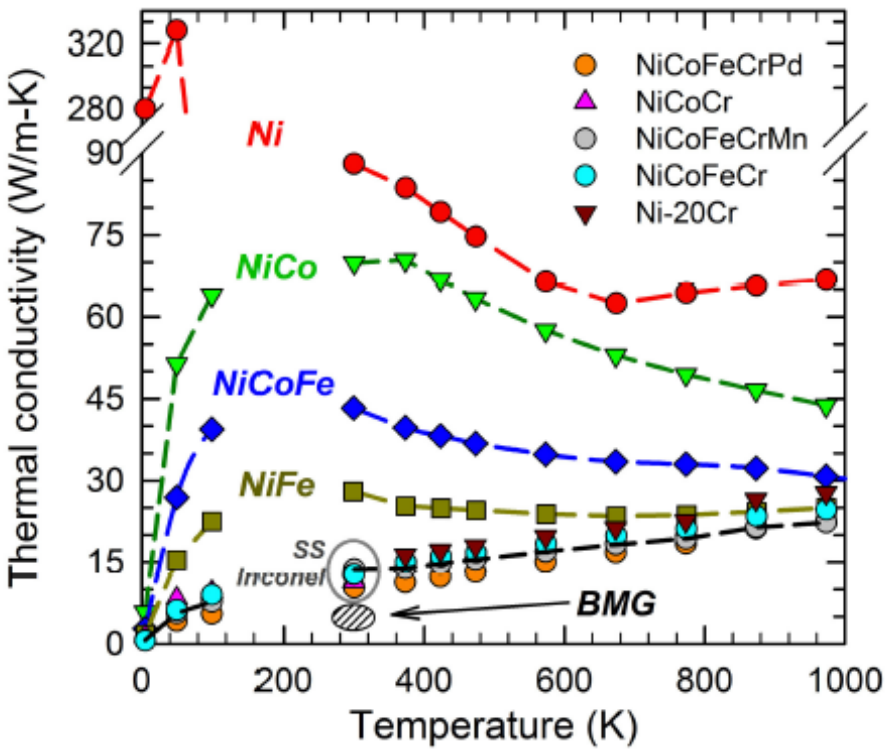

Figure 2.7 Comparison of thermal conductivity of Ni-containing FCC SP-CSAs, several conventional alloy systems and BMGs [68, 70, 72-73].

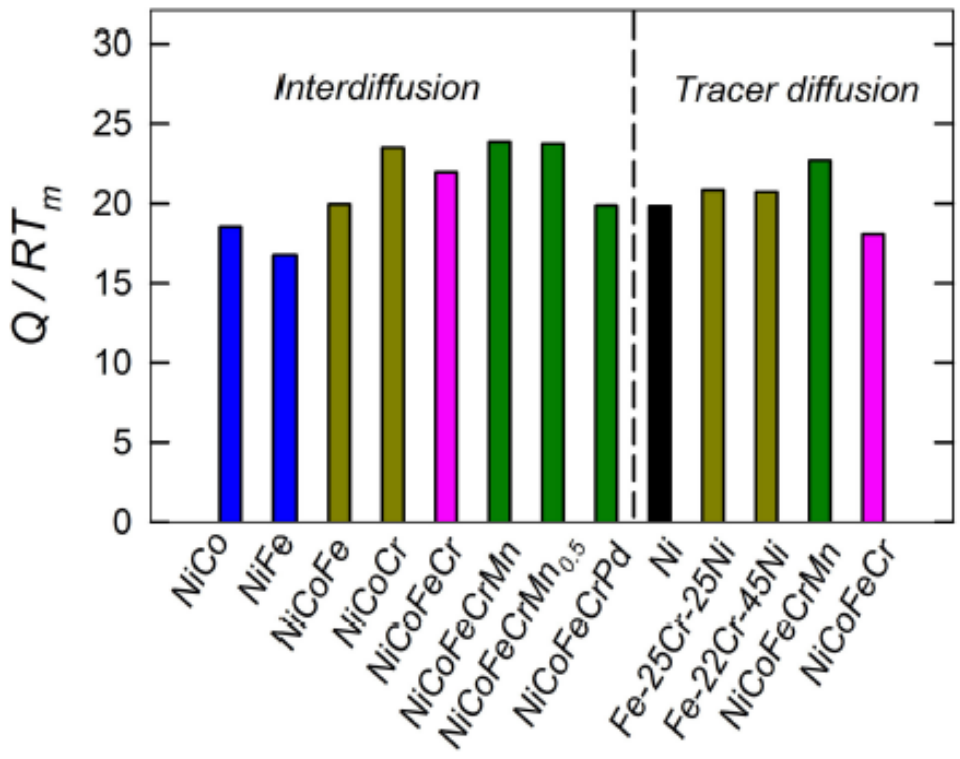

Figure 2.8 Comparison of normalized diffusion activation energy in Ni-containing CSAs [24-25,74].

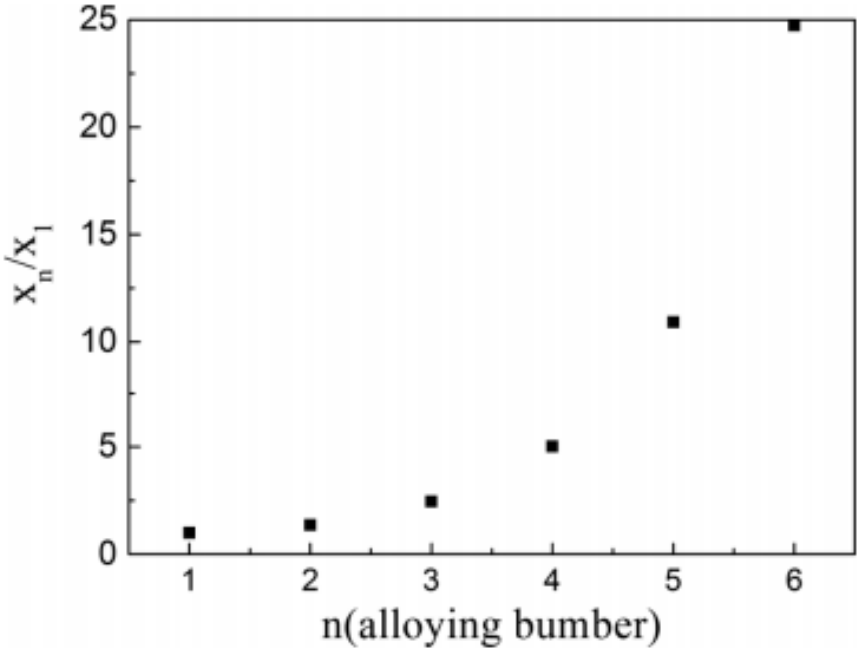

Figure 2.9 The increased vacancy concentration from the contribution of configurational entropy compared with the pure metal in equiatomic HEAs with n components [29].

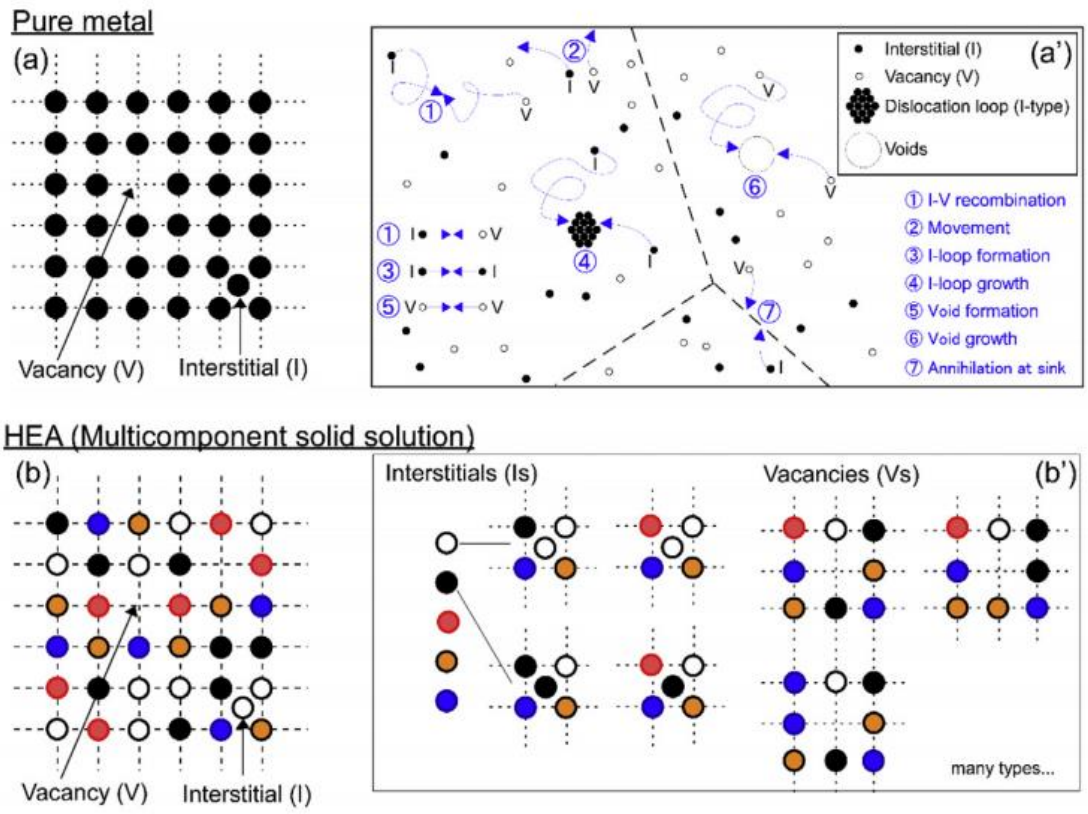

Figure 2.10 The schematic illustration of the simplest type of defects introduced by the electron knock-on effect in pure metal and HEA [75].

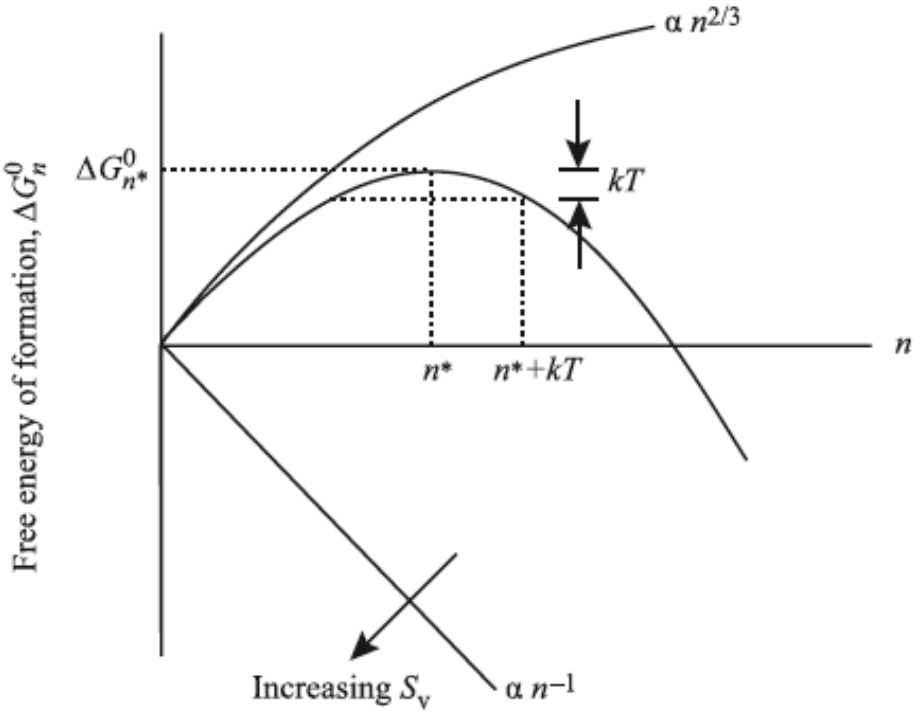

Figure 2.11 Schematic illustration of free energy of formation of a spherical void consisting of *n* vacancies, and the effect of thermal fluctuation on critical embryo size [28].

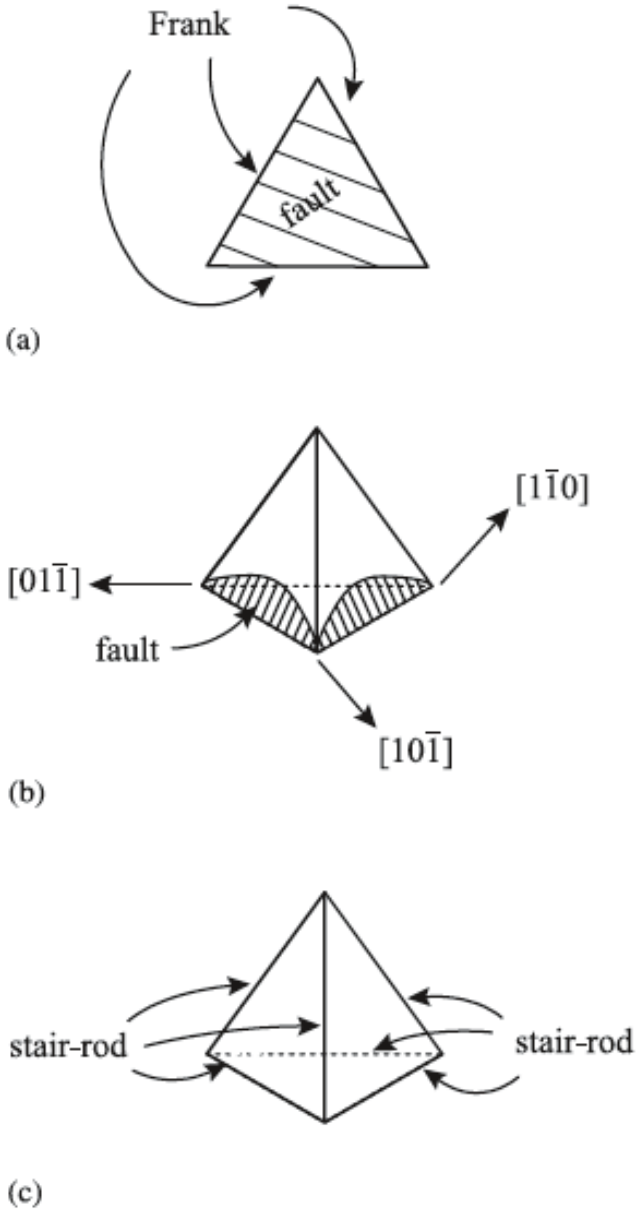

Figure 2.12 Illustration of a stacking fault tetrahedron (SFT) formed by faults on each of the faces on the tetrahedron [76].

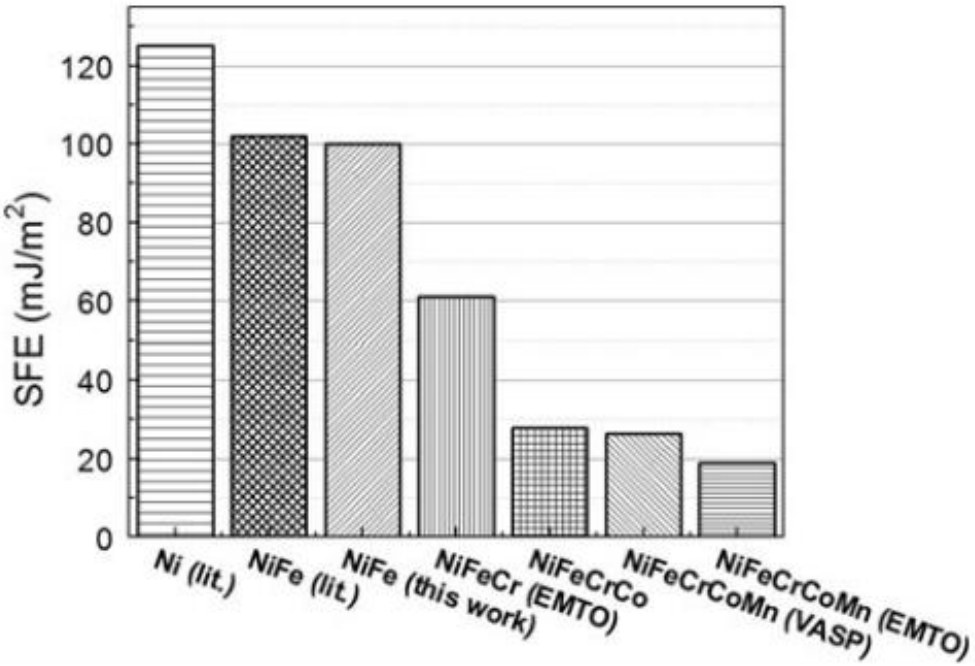

Figure 2.13 SFEs of equiatomic fcc metals from pure Ni to NiFeCrCoMn [36].

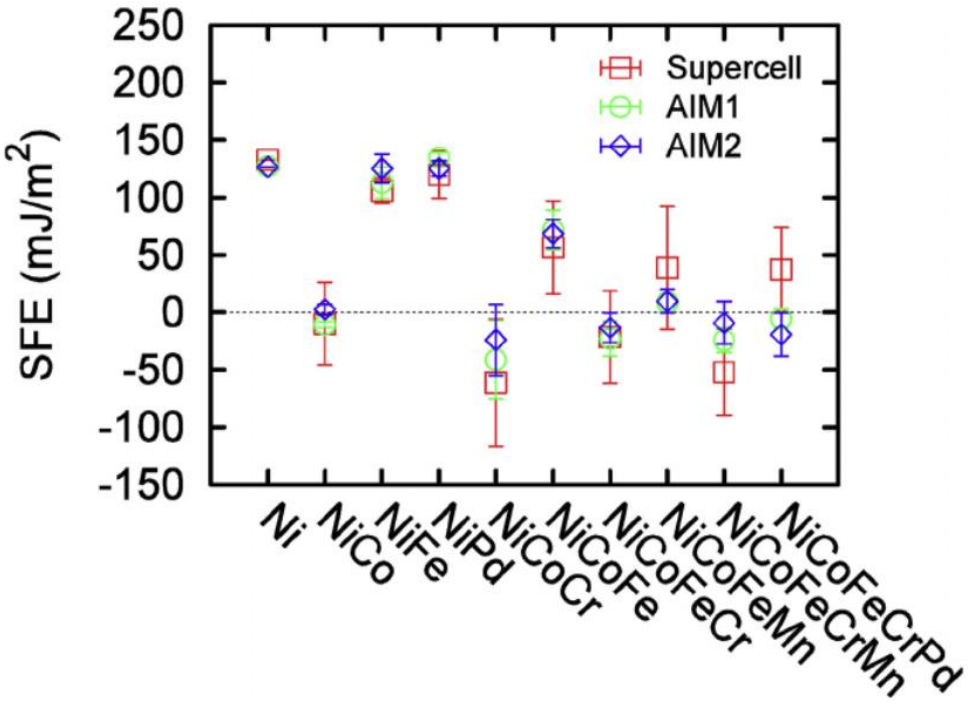

Figure 2.14 Stacking fault energies of CSAs calculated by the supercell method as well as the AIM model [37].

Table 2.5 Effect of irradiation temperature on voids and dislocations in nickel [38].

Irrad. temp. (°C)	Void density (cm^{-3})	Mean void diameter (Å)	Std. dev. of diameter (Å)	Swelling (%)	Dislocation density (cm^{-2})
375	–	–	–	–	7.8×10^{10}
425	–	–	–	–	4.5×10^{10}
475	–	–	–	–	4.5×10^{10}
525	7.6×10^{15}	100	20	0.48	2.9×10^{10}
575	6.9×10^{15}	130	20	0.90	2.0×10^{10}
625	1.8×10^{15}	225	45	1.2	5.6×10^{9}
675	3.0×10^{13}	725	145	0.62	2.8×10^{9}
725	1.4×10^{13}	800	120	0.40	1.6×10^{9}

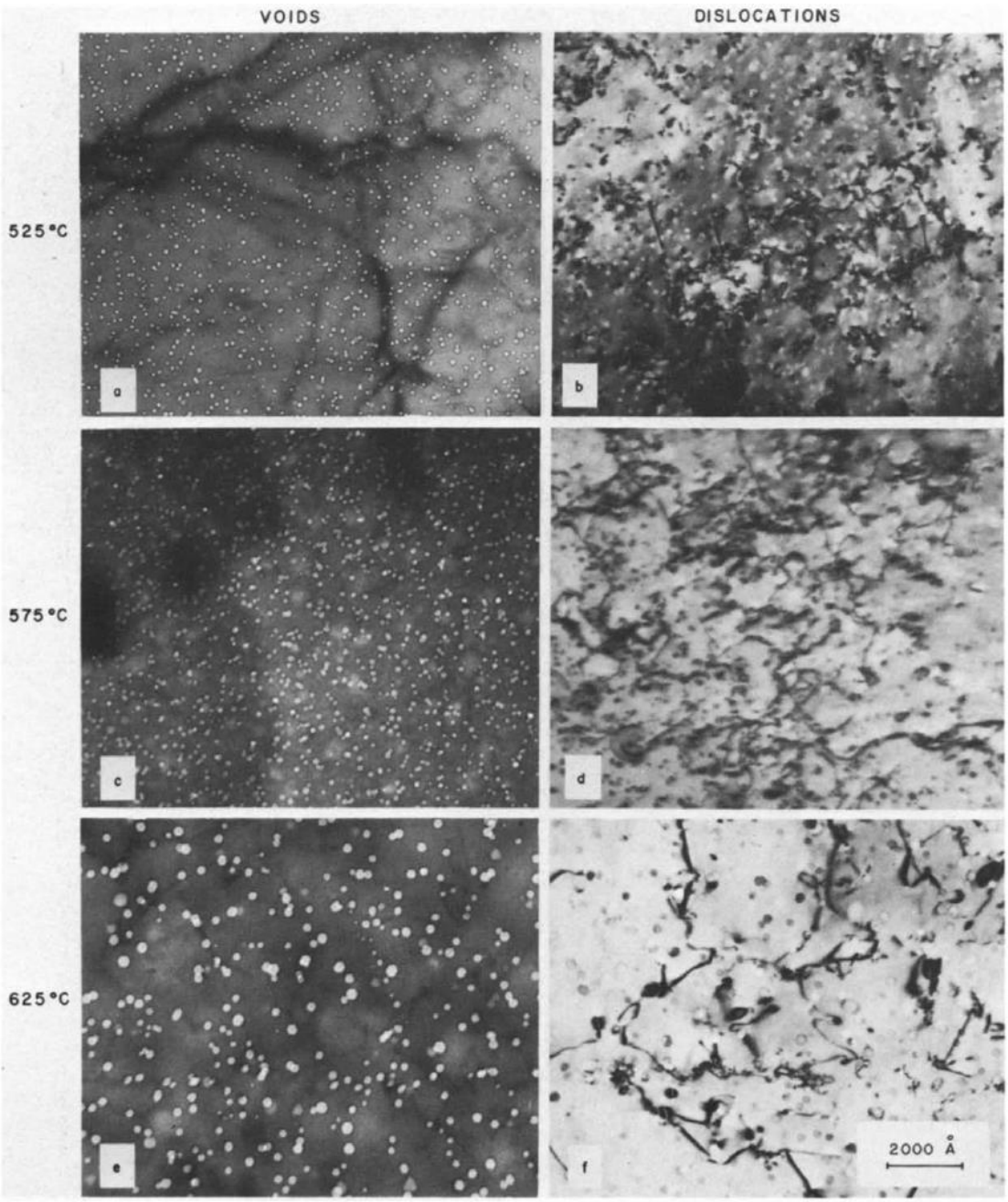

Figure 2.15 Plain view TEM images on voids and dislocations observed in high-purity nickel irradiated with 2.8 MeV $^{58}Ni^{+}$ ions to a damage level of 13 dpa [38].

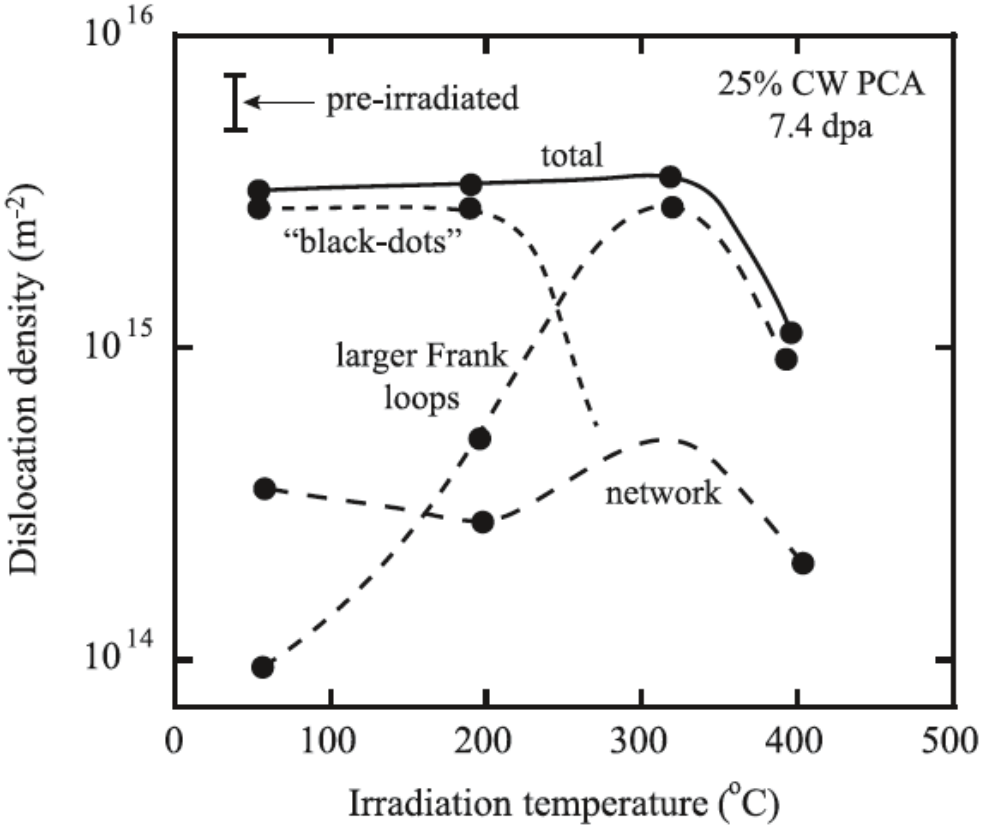

Figure 2.16 Effect of irradiation temperature in the range 50-400℃ on the components of the dislocation density in neutron-irradiated austenitic stainless steel [77].

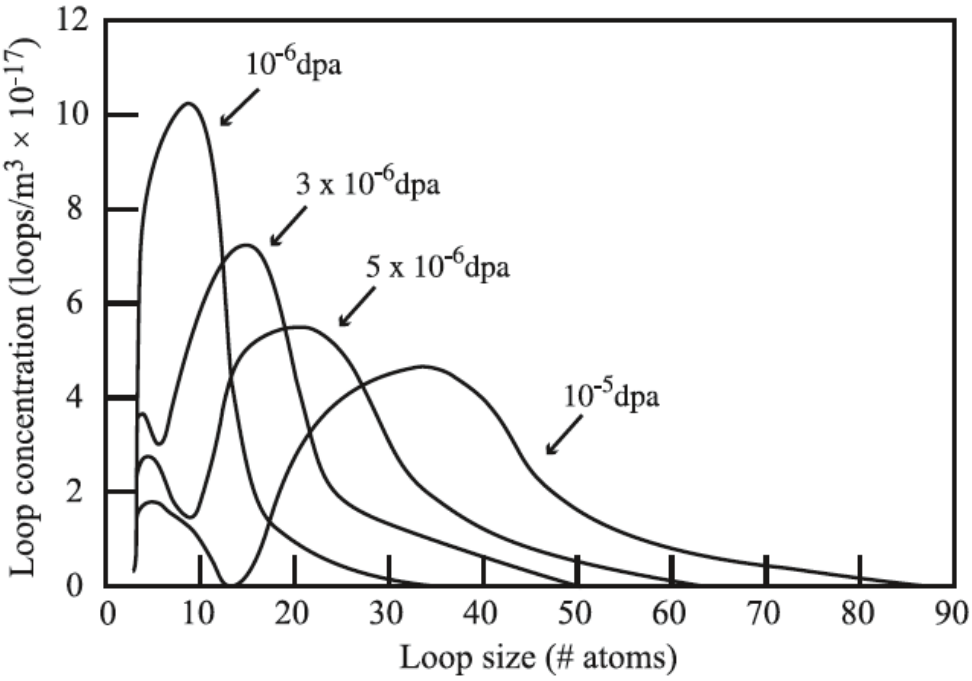

Figure 2.17 Development of the interstitial loop size distribution with dose in 316 stainless steel irradiated at a dose rate of 10^{-6} dpa/sec and a temperature of 550 ℃ with initial dislocation density of 10^{13} m^{-2}[78].

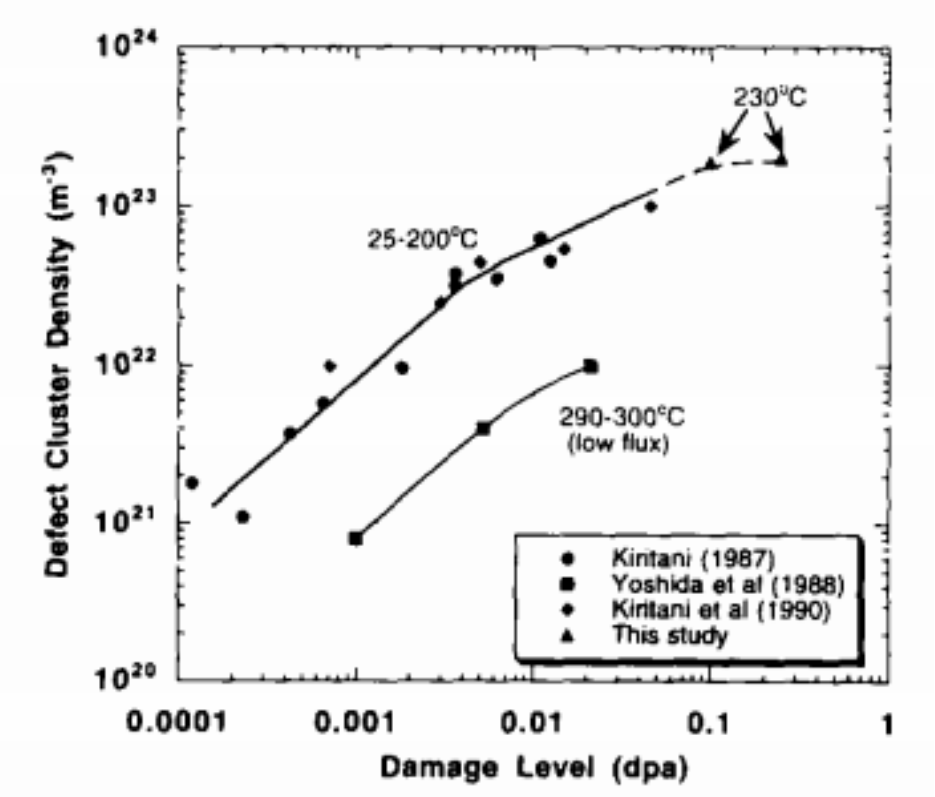

Figure 2.18 Dose dependence of defect cluster density in nickel irradiated at temperatures between room temperature and 300℃ [42].

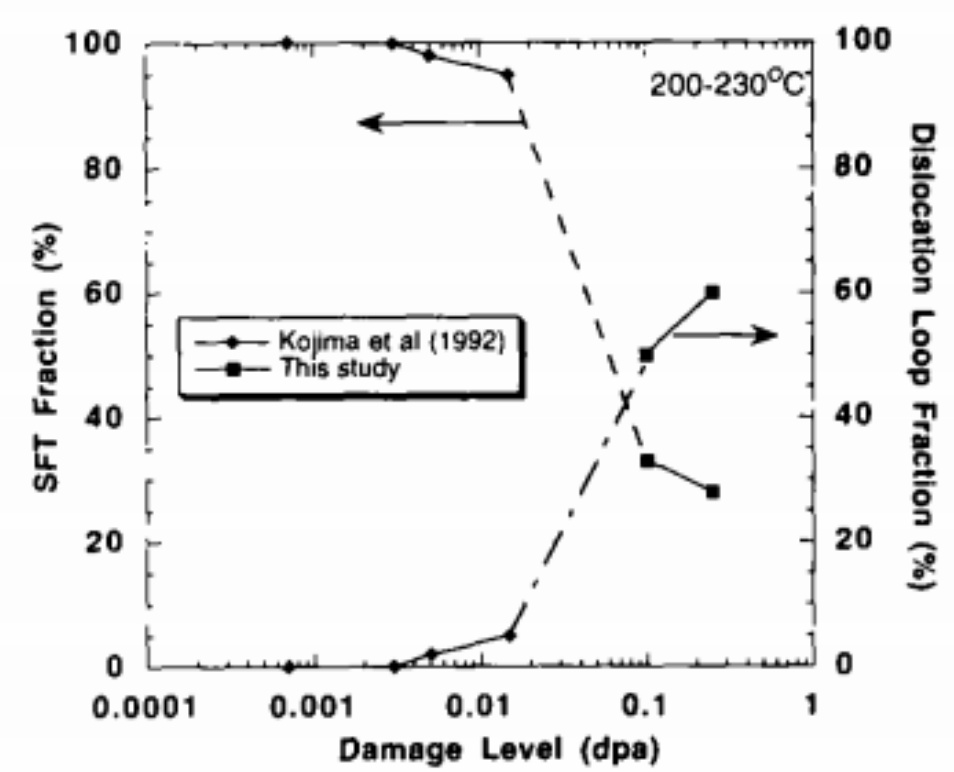

Figure 2.19 Evolution of the defect cluster in nickel irradiated between 200-230℃ [42].

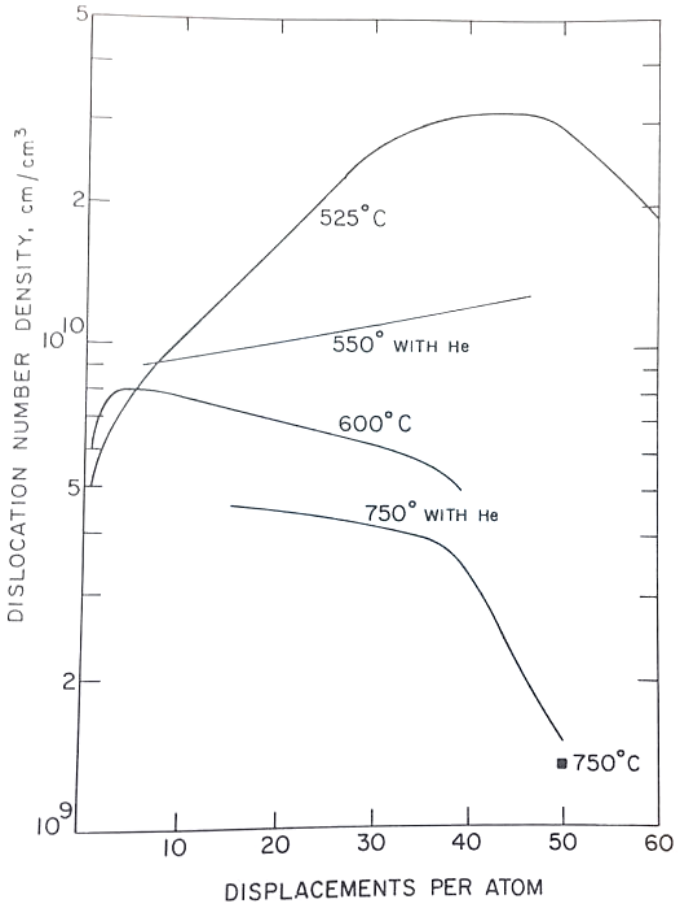

Figure 2.20 The dislocation density developed during $^{58}Ni^{+}$ ion irradiation [39].

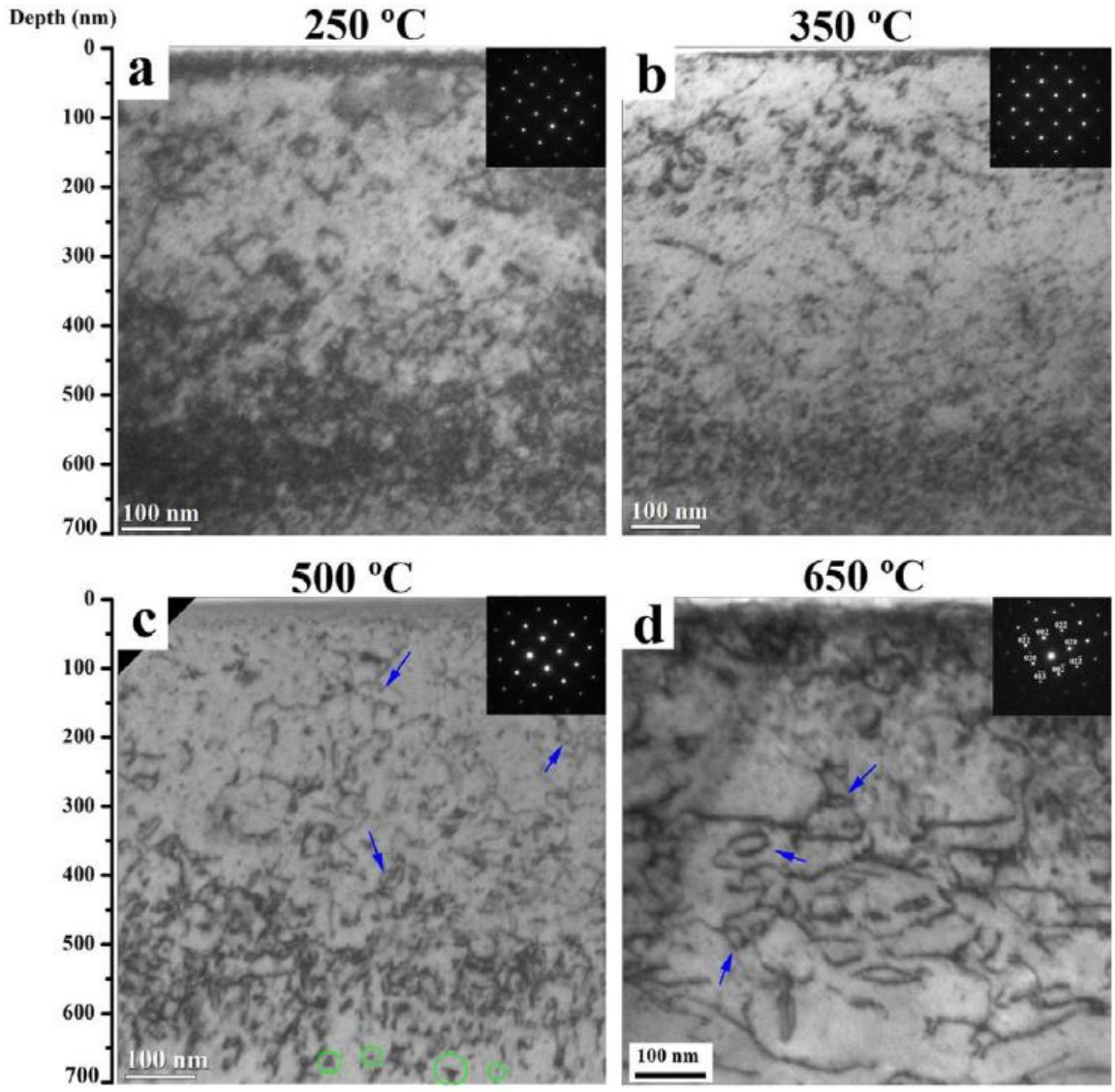

Figure 2.21 Bright field images and selected area electron diffraction patters of $Al_{0.1}CoCrFeNi$ irradiated by 3 MeV Au ions to ~31 dpa. Perfect loops and SFTs are marked by blue arrows and green circles, respectively [41].

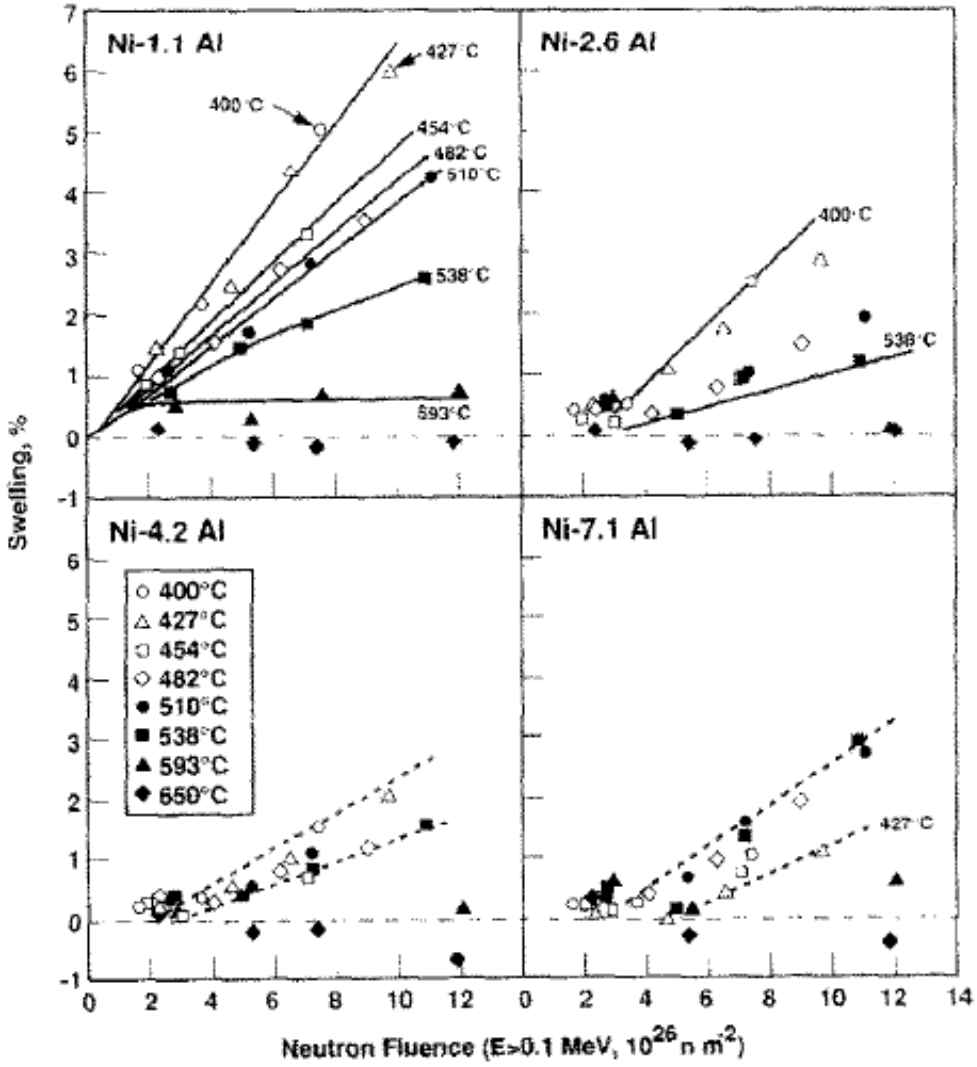

Figure 2.22 Swelling of Ni-Al alloys at 400-650 ℃ as a function of aluminum content and various neutron fluences [46].

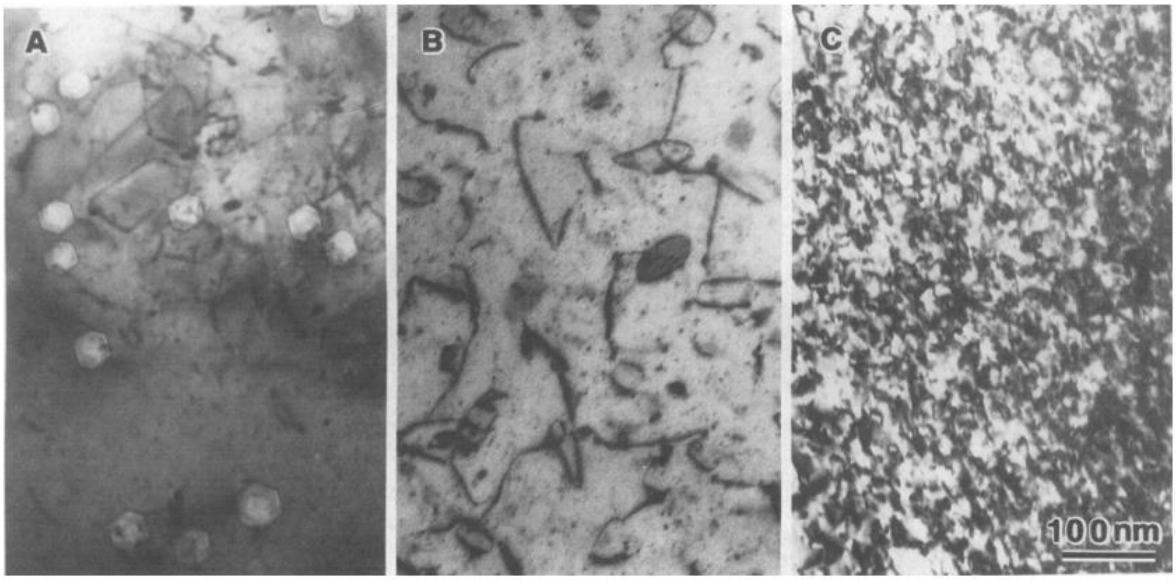

Figure 2.23 Comparison of major defect clusters in 14 MeV Ni ion irradiated (a) pure Ni, (b) Ni-10at%Cu and (c) Ni-50at%Cu, all with 50 appm He preinjection. The images were taken from 0.6-1.0 um below the irradiated surface [50].

Table 2.6 The number density and mean size of dislocation loops in pure Ni and binary Ni alloys irradiated by 25 keV He^+ ions to 1.0×10^{19} m^{-2} at 500℃ [14].

Specimen	V_{sf} (%)	Number density (m^{-3})	Mean size (nm)
Ni	0	1.5×10^{22}	19.5
Ni–Si	−5.7	2.3×10^{22}	13.2
Ni–Co	1.8	1.6×10^{22}	13.5
Ni–Cu	7.2	1.5×10^{22}	17.3
Ni–Mn	23.2	1.2×10^{22}	18.2
Ni–Pd	43.3	1.4×10^{22}	18.9
Ni–Nb	51.2	1.3×10^{22}	16.8

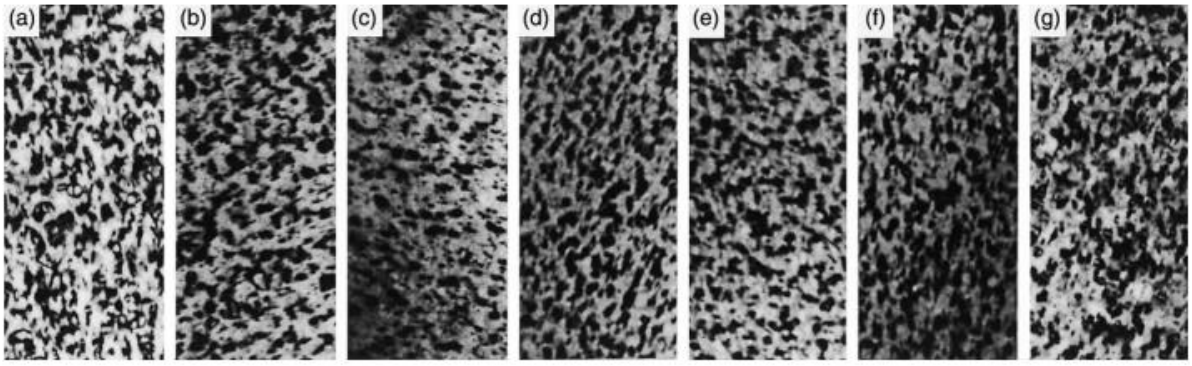

Figure 2.24 Dislocation loops formed in (a) pure Ni, (b) Ni-5%Si, (c) Ni-5%Co, (d) Ni-5%Cu, (e) Ni-5%Mn, (d) Ni-5%Pd, (e) Ni-2%Nb irradiated by 25 keV He^{+} ions to 1.0×10^{19} m^{-2} at 500℃ [14].

Table 2.7 The number density, mean size of bubbles and swelling in pure Ni and binary Ni alloys irradiated by 25 keV He^+ ions to 4.1×10^{20} m^{-2} at 500℃ [14].

Specimen	V_{sf} (%)	Flux (He^+/m^2 s)	Number density (m^{-3})	Mean size (nm)	Swelling (%)
Ni–Si	−5.8	5.6×10^{18}	4.9×10^{23}	2.0	0.2
Ni–Co	1.8	5.6×10^{18}	3.8×10^{23}	5.0	2.5
Ni–Cu	7.2	5.6×10^{18}	6.2×10^{23}	5.0	4.2
Ni	0	3.2×10^{18}	1.5×10^{23}	4.2	0.6
Ni–Si	−5.8	3.2×10^{18}	3.1×10^{23}	3.3	0.6
Ni–Mn	23.2	3.2×10^{18}	4.2×10^{23}	4.0	1.0
Ni–Nb	51.2	3.2×10^{18}	3.0×10^{23}	6.5	4.5

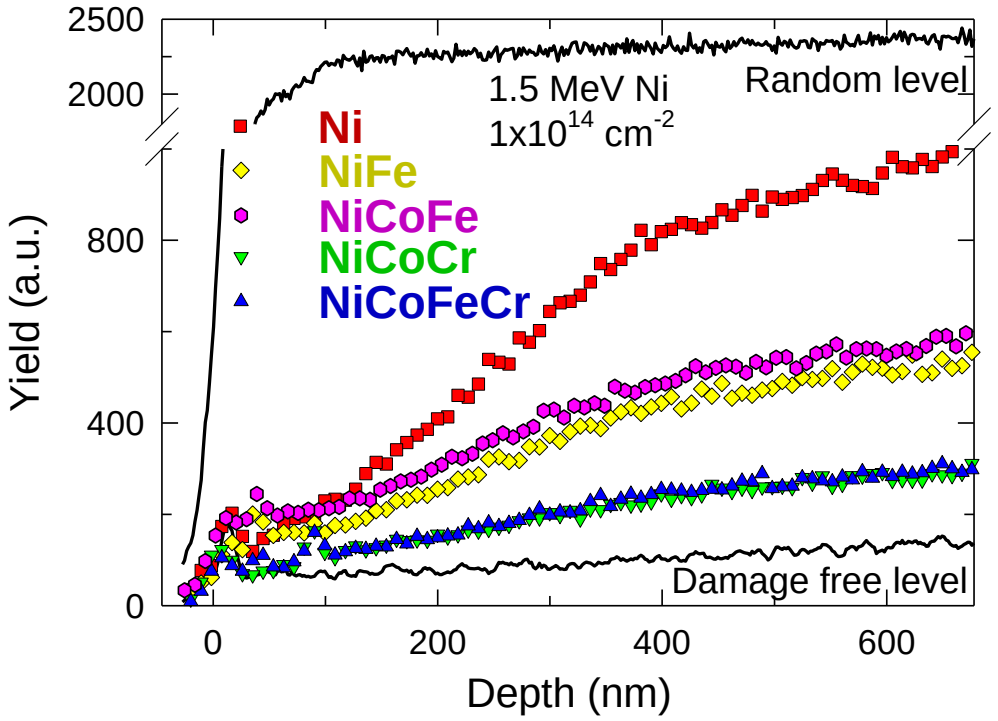

Figure 2.25 The deformation yield in Ni and Ni-SPCSAs irradiated using 1.5 MeV Ni ions to 1.0×10^{14} cm^{-2} at room temperature and measured by Rutherford backscattering and channeling technique [51].

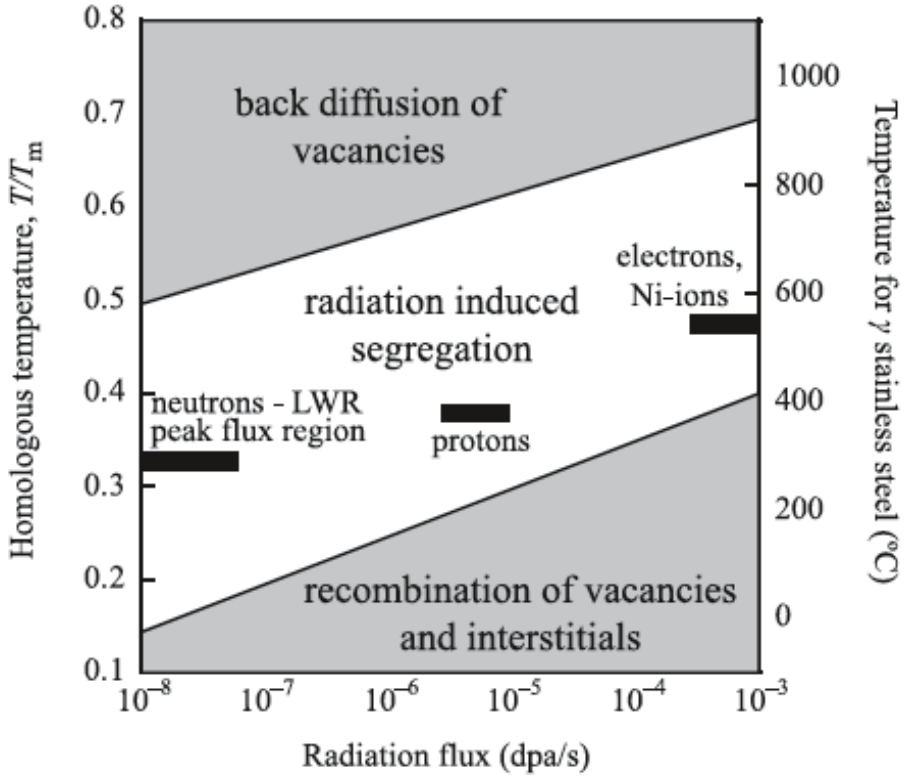

Figure 2.26 Relation between temperature and dose rate in the context of radiation-induced segregation, and the locations of neutron, proton and nickel ion irradiations [28].

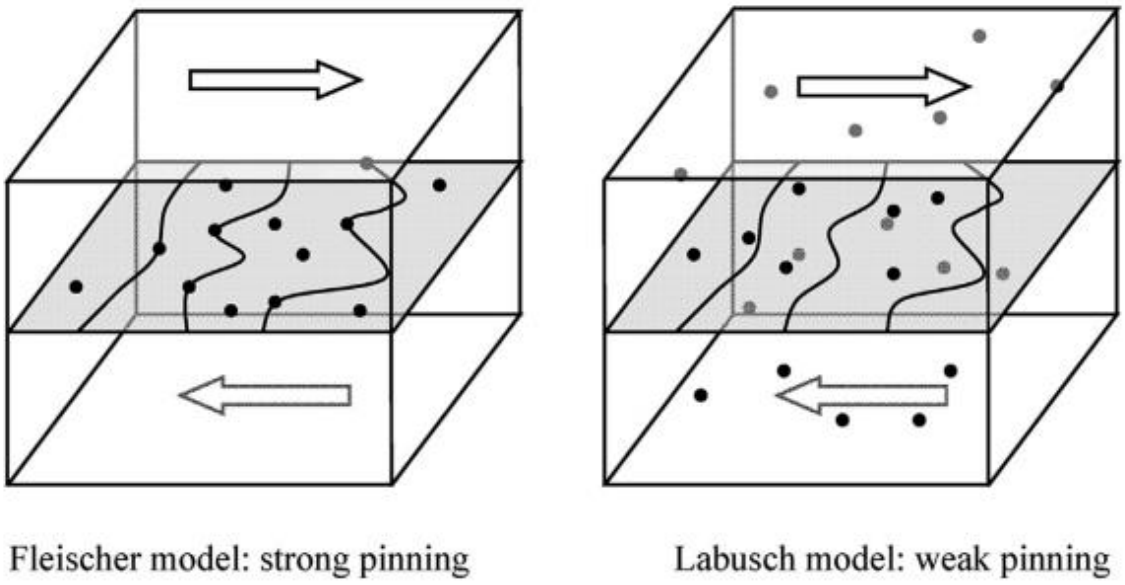

Figure 2.27 Illustration of two classic solution strengthening mechanisms: Fleischer model involves strong pinning of dislocations by solute atoms on the gliding plane, while Labusch model is based on weak pinning by solute atoms around the space [61].

Table 2.8 Processing conditions and grain sizes of the equiatomic alloys tested by Wu *et al.* [3].

Alloy	Homogenization temperature (K)	Reduction in thickness (%)	Annealing temperature (K), time (h)	Grain size (μm)
FeNiCoCr	1473	92	1173, 1	24
FeNiCoMn	1373	90	1273, 1	48
NiCoCrMn	1373	90	1273, 1	36
FeNiCo	1473	92	1173, 1	28
NiCoCr	1473	92	1273, 1	41
FeNiMn	1373	90	1173, 1	30
NiCoMn	1373	90	1173, 1	32
FeNi	1473	92	1173, 1	35
NiCo	1473	92	1073, 1	35
Ni	1473	92	1073, 0.5	85

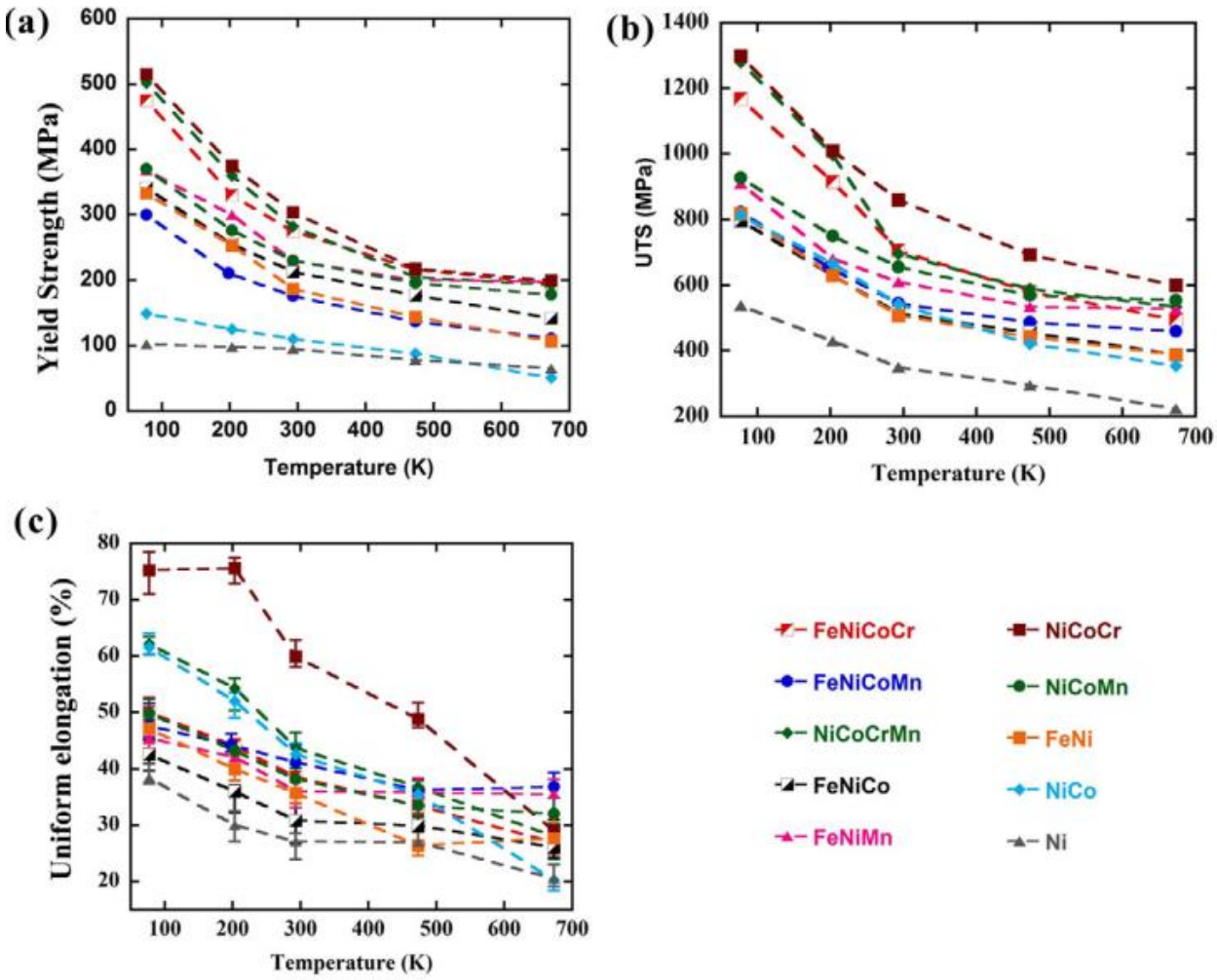

Figure 2.28 Temperature dependence of: (a) the 0.2% offset yield stress (σ_y); (b) the UTS; and (c) the uniform elongation to fracture for the equiatomic alloys and Ni tested by Wu *et al.* [3].

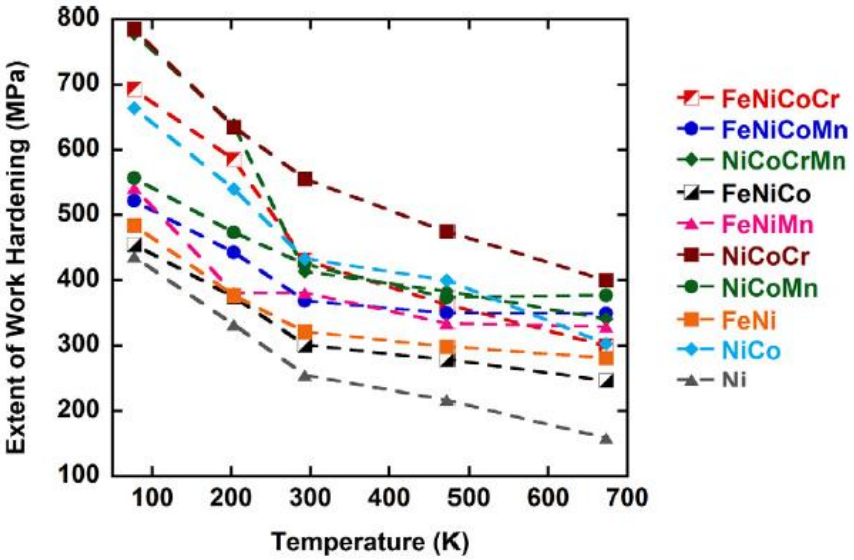

Figure 2.29 Temperature dependent work hardening (difference between the ultimate and yield strengths) for the equiatomic alloys and Ni [2-3].

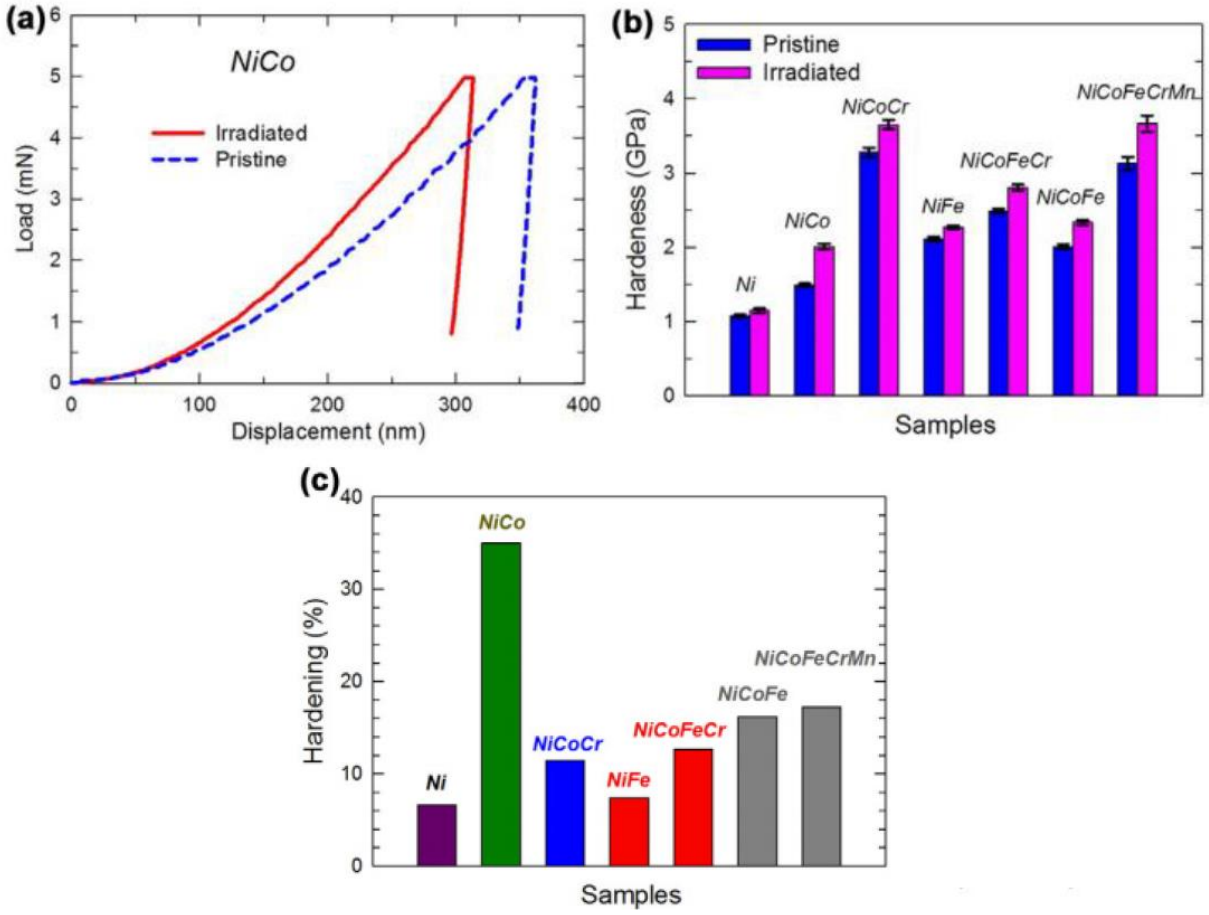

Figure 2.30 (a)Load-unload curves of a pristine and an irradiated NiCo; (b) Hardness before and after irradiation; (c) irradiation-induced relative hardening [62].

Chapter 3-Experimental Procedure

This chapter presents the experimental procedure describing the sample preparation, ion irradiation, post-irradiation sample preparation and microstructure characterization.

3.1 Alloy and Sample Preparation

The alloys used for this work were Ni-based single-phase concentrated solid solution alloys (SP-CSAs) with simple fcc crystal structure. The alloys can be fabricated in the form of single crystals or large grain polycrystals, and the principal elements used in the alloys included Ni, Co, Fe, Cr, Mn and Pd. Pure Ni was included in this work as well to serve as a reference. As mentioned previously in Chapter 2, the elemental metals with more than 99.9% purity were weighted and mixed by arc melting. The melting process was repeated five times before the drop casting process. To prepare single crystals, a high temperature optical floating-zone directional solidification method was applied on the polycrystalline ingots. For polycrystals, the polycrystalline ingots were homogenized at 1200 °C for about 24 hours and rolled at room temperature to a final thickness of ~1.8 mm. The rolled specimens were then annealed at ~1170 °C for several days to remove the effect of cold work, and to achieve an average grain size of a few hundreds of μm to minimize the effect of grain boundaries. The list of alloys studied in this work and their crystal structures are listed in Table 3.1. Most of the studied materials were equiatomic alloys unless the concentration of a specific element was specifically specified in atomic percent.

Prior to irradiation, circular shaped plate samples (with a diameter of 1-1.3 cm) were cut into smaller size using electrical discharge machining (EDM) before mechanical polishing. Smaller samples allowed one to efficiently utilize the irradiation area, and minimize the potential fluctuations between different irradiation batches. EDM is a manufacturing process which applies rapid current discharge through two electrodes to remove and form a desired shape on

materials. The process can result in a geometric precision of about 1 μm.

All samples were then mechanically polished using silicon carbide grinding papers. First, the samples were mounted on a metallic puck using Crystalbond™ adhesive glue, which will melt and create consistent bond between samples and the puck once heated. The puck and samples were then placed on a hot plate. Grits of 240, 320, 400, 600, 800 and 1200 were used to polish the sample, with a 90-degree consecutive rotation on polishing directions to ensure the removal of previous damage. In between the grinding steps, samples were rinsed with deionized water to remove residues from grinding. After the 1200 grit grinding step, the to-be-irradiated surface was further polished using a cloth with a colloidal silica solution. The goal is to achieve a mirror-like surface with roughness below 3 nm. To remove the polished samples, the puck was placed back to the heating plate to soften the adhesive glue. And to remove the residual adhesive, samples were cleaned in a beaker of acetone followed by methanol and ethanol, successively.

3.2 Ni^{2+} Irradiations

3.2.1 Irradiation Set-up

The summary of irradiation experiments and characterization performed for this thesis were listed in Table 3.2. The irradiation conditions included using 3.0 MeV Ni^{2+} ions for experiments conducted at elevated temperatures (420, 500, 580 and 675℃). The samples were irradiated using a 3 MV Pelletron (model 9SDH-2) tandem electrostatic accelerator at the Ion Beam Materials Laboratory located at the University of Tennessee, Knoxville.

Heavy ions used for irradiations were produced from a solid cathode by Cs^+ sputtering. To generate Ni^{2+} ions, pure Ni cathodes were used to avoid difficulties of mass separation from Cu. The negative ion beam, produced from the Source of Negative Ions by Cesium Sputtering (SNICS) II with pre-acceleration energies of a few tens of keV, was bent at a 30° angle by the injection magnet into the central beamline of the accelerator. The negative charges from the generated ions were then stripped in the accelerator by stripper gas (nitrogen) and became positive ions. These positive ions were then focused using a magnetic quadrupole and a Y-axis electrostatic steerer into the analyzing magnet and bent into one of the three research beamlines.

For more details about the facility, please refer to [79].

To-be-irradiated samples were mounted on a 17 mm diameter circular molybdenum plate, with a thickness of 0.5 mm, and secured by molybdenum spring-loaded clips. The irradiation temperature was measured by a chromel-alumel thermocouple clamped to the sample surface or the molybdenum plate. Figure 3.1 shows an image of a fully constructed irradiation stage, with the thermocouple and irradiated area marked by an arrow and a square, separately. During the irradiation, the temperature was carefully monitored by the combination of two thermocouples, one from the backside of the holder and the other one clamped to the sample surface, and an additional infrared pyrometer.

The determination of ion fluence was measured using a Faraday cup located below the sample holder. During the experiment, the beam current was monitored using a current monitor and digital counter (CMDC). The ion fluence can be calculated from the beam spot size, which was regulated by the double slits on the beamline. The uncertainty of irradiation fluence for the IBML facility is within $\pm$10% [79]. A wobbled-defocused beam was used in the irradiation, with scanning frequencies of 517 and 64 Hz for the horizontal and vertical direction, respectively, to irradiate a homogeneous region. The ion flux was controlled at $2.8 \times 10^{12}\ cm^2/s^{-1}$and was equivalent to about 0.003 dpa/s^{-1} at the peak damage dose. The irradiation time was about 5 hours to achieve a peak dose of 60 dpa.

3.2.2 SRIM Damage Calculations

The irradiation-induced damage profile and injected ion concentration were calculated using SRIM-2013 in Quick Kinchin-Pease Mode [80-81] with a displacement threshold energy of 40 eV for all elements. The damage induced by irradiation is typically measured in displacements per atom (dpa). As mentioned previously in Chapter 2.4.4, the result of ion irradiation is depth dependent and varies with incident ion energy, material composition, and the depth of examination. A representative case calculated by SRIM is shown in Figure 3.2. The calculation showed here did not consider the potential modifications on material density due to severe void-induced swelling, the modifications will be discussed in the discussion session. In general, the results from SRIM calculation show no significant differences in penetration depth

or displacements among most of tested materials. However, due to the relatively high atomic density from element Pd, the resulting damage dose was higher for alloys containing Pd than the rest of tested materials at a slightly shallower depth. The calculated peak damage dose was about 53 dpa for the tested ion fluences in Ni-SPCSAs without element Pd, while the peak damage dose was about 60 dpa for Ni-20Pd and NiCoFeCrPd.

The conversation between the measured ion fluence, damage dose and irradiation time can be calculated by the equation below:

$$Irr.Time = \frac{(Desired\ dpa)(Number\ Density)(Ion\ charge)(Irradiated\ Specimen\ Area)}{(Average\ Current\ on\ Specimens)(SRIM\ damage\ rate)}$$

$$= \frac{(\frac{displacement}{atom})(atom/cm^3)(C/ion)(10^6 \mu C/C)(cm^2)}{(\mu A)(\frac{displacement}{atom \cdot Å})(10^8 Å/cm)}$$

3.3 Post Irradiation Characterization Methods

Following ion irradiation, samples irradiated at IBML were removed from the stage and shipped to University of Michigan for post irradiation characterizations. This section details the preparation and analysis used to study the microstructure of Ni-based SP-CSAs after irradiation.

3.3.1 TEM Specimen Preparation

The cross-sectional TEM samples used in this study were all prepared by the focused ion beam (FIB) lift-out technique on an FEI Helios Nanolab workstation at the Michigan Center for Material Characterization at the University of Michigan (MC^2). This technique allowed users to characterize the depth dependent defect evolution up to several microns into the surface while maintaining the thickness of the sample to be electron microscopy transparent. Due to its high efficiency and the requirement of small amount of samples, FIB technique has been widely used in the TEM sample preparation.

The steps of preparing TEM samples are summarized as follows, with slight variations on the operating conditions based on different needs. Some of the key steps of FIB lift-out process

are highlighted in Figure 3.3. By utilizing the dual beams equipped in Helios workstation; an electron beam and a gallium ion bean set 52° apart, it allowed users to do milling and monitoring sample preparation through different angles.

1. Load sample on a small metal holder with copper tape/carbide glue then vent the chamber of Helios workstation.
2. Place the holder in and secure it with screw before pumping down the chamber.
3. Open the column valves once the vacuum is better than 1×10^{-5}Torr.
4. Adjust the stage to an appropriate working distance and align the electron gun and ion gun.
5. To minimize ion damage induced by sample preparation, deposit a thin Pt layer (0.2-0.4 nm) to protect the surface of the sample.
6. Set the desired voltage and current to cut two trenches on both sides of area of interest. The final goal is to prepare a thin lamella.
7. Deposit Pt to attach the thin lamella with the omniprobe tip before detach the lamella from the bulk sample.
8. Lift out the lamella and mound it on the TEM lift out grid.
9. Perform the thinning process to desired thickness.

The undesirable ion damage induced by FIB preparation can increase the difficulty in analyzing irradiation-induced defects, since both defects were generated by interactions with energetic ions. Two approaches were applied in this study to address the issue, the low energy cleaning method and flash polishing technique.

Low energy cleaning method was simply performed at the last step of TEM lamella preparation. This was done through the application of relatively low voltage and current conditions (5 kV and then 2 kV) on a larger tiling angle ($\pm$ 5°from edge on mode) for an extended period of time (5-10 minutes on each side). The ion damage induced by previous higher energy ions was removed while minimizing the newly created FIB damage.

Flash polishing technique applied a similar concept as electropolishing, but in a relatively

short time frame. The total polish time typically lasted for less than 0.1 second compared to 15-30 seconds or longer in the traditional electropolishing method. An electrolytic solution of 4% perchloric acid in 96% ethanol was used in this study. The solution was constantly stirred by a stirrer with stirrer bar during polishing. The electric potential was set to 12 volts with a polishing temperature below -40 ℃. The negative output of the power supply was connected to a platinum mesh to serve as cathode, while the positive output of the power supply was connected to sample to serve as anode. A polishing loop was formed once both electrodes were put into the electrolyte solution, and the power of power supply was turned on. On the anode (sample), oxidation reaction will occur and generate anions, which resulting in the reduction of thickness on sample. The polishing time was controlled by an accurate timer with accuracy down to 0.01 second. Polished samples were cleaned with regent alcohol in four separate beakers at temperature below -20 ℃ to ensure the removal of residual polishing solution. Infrared light was applied to dry the samples after the cleaning step. The image of experimental setup is shown in Figure 3.4. The TEM images of before and after flash polishing are presented in Figure 3.5. As can be seen from the images, the main damage band from irradiation was significantly more obvious than the non-polished sample.

In a comparison between these two polishing techniques, flash polishing can achieve better results in terms of removing undesirable FIB induced defects, provided the polishing condition has been developed. On the other hand, low energy cleaning method is relatively time consuming but can be applied to any materials easily.

3.3.2 Voids Imaging and Characterization

To study the irradiation effect on a macroscopic scale, it is necessary to understand the microstructure evolution at an atomic scale. Depending on the irradiation conditions, irradiation-induced defects may include dislocation loops, voids or bubbles, and precipitates. These defects are all in the scale range of several to hundreds of nanometers. Transmission Electron Microscope (TEM) has the imaging capability of less than 1 nm and has been widely applied in studying small defect clusters from irradiation.

In this study, the characterization of irradiation-induced defects was conducted using a

JEOL 3011TEM with under-focused conditions in bright field (BF), a JEOL 2100 STEM and a JEOL 3100 STEM in high angle annular dark field (HAADF). To fully utilize the capability of a microscope, a proper alignment procedure must be performed. This includes illumination centering, apertures centering, sample focusing and astigmatism correction. Traditionally, convention TEM images have been applied to image voids/bubbles using through-focus imaging techniques. Rühle and Wilkens [82] reported that by measuring the first Fresnel fringe appeared in a 800-1000 nm under-focused mode, the measured size of voids will correspond to within 10% of the actual size. In this work, all images taken by TEM for void analysis were recorded in a slightly under-focused condition at a magnification of 8000 and an exposure time of 2 seconds. A small degree of tilting away from the zone axis was applied to TEM samples to enhance the contrast for voids. Images of different magnifications were taken as well, but the magnification of 8000 was chosen to present the representative features of Ni SP-CSAs for comparison.

In some cases, the representative feature of voids is harder to capture in TEM images as the void becomes larger and the number density drops with increasing temperature. The appearance of larger voids not only increases the difficulty in adjusting to the appropriate under focused condition, but it can also easily lead to image overexposure or fewer counting statistics due to the overlapping of voids at a different depth. In this case, HAADF STEM imaging was applied to better capture the representative features. Contrary to the BF TEM images, voids appeared as black circles in HAADF images due to the lack of mass in the voids area when imaged using atomic mass contrast. Consecutive images were taken across the length of the sample with some extent of overlap to help to map out the entire specimen. An example of HAADF image is shown in Figure 3.6.

Sample thickness was measured using the electron energy loss spectroscopy (EELS) method in a JEOL 2100F aberration-corrected STEM. The EELS method estimated sample thickness by measuring the amount of energy lost on electrons when passing through the sample. A calibrated zero-loss spectrum was measured at a spot away from the sample using 1 nm probe size and 2 cm camera length. The corresponding collection angle was about 38 mrad. By applying the equipped DigitalMicrograph ® software to compare the spectra of energy lost and zero-loss, the thickness of the sample can be calculated. In average, six areas of the sample in the

depth range of ~500 nm were chosen to calculate the EELS measurement. The final sample thickness was the average of these six measurements, which typically ranged between 100-150 nm. The estimated error in EELS measurement is about 10% [83].

The calculation method for void swelling is described as follows. A software named ImageJ was used as the image processing software for counting voids. Manual void counting and sizing were applied in this work. The counted voids were marked off on the image to avoid double counting. The voids were generally profiled in 100 nm increments in depth starting from the surface. In some cases, where the average void diameter exceeded 100 nm, a bin size of 200 nm was applied instead. In this work, it is challenging to select a certain depth region for swelling analysis due to the wide ranged void distribution across various temperatures and diverse Ni SP-CSAs. Therefore, two types of data presentation can be seen in this study when discussing swelling behavior. One is the depth-dependent swelling, which divided the void swelling using the incremental counting bin size; another is the total swelling, where all voids observed at a depth up to 1800 nm were taken into consideration when discussing swelling behavior. The total depth was selected to be consistent with previously published studies [15, 62, 84]. The choice of data presentation depends on the main focuses of discussion.

The percentage of swelling in each bin was calculated using the equation listed below.

$$S(\%) = \frac{\frac{\pi}{6}\sum_{i=1}^{N} d_i^3}{A \times \delta - \frac{\pi}{6}\sum_{i=1}^{N} d_i^3} \times 100$$

the parameter A represents the imaged area; δ represents the sample thickness; d_i represents the void diameter and N represents the number of voids counted in each size group. The overall swelling was calculated using the same equation as above but has the bin size set as 1800 nm [84]. An example of the counted TEM images and depth dependent voids profiling are shown in Figure 3.7 and Figure 3.8, separately.

In the case of Ni irradiated to 1.5×10^{16} and $5.0 \times 10^{16} cm^{-2}$ (~17 and 60 dpa at peak dose), the void swelling profiles were recalculated as a function of mass depth to include the density correction due to the large amount of swelling induced by ion irradiation. Mass depth is

calculated by multiplying the effective density ($\rho_{effective}$) by the thickness of each depth region, defined as:

$$\rho_{effective} = (1 - \frac{\Delta V}{V}) \times \rho \qquad [85]$$

where $\Delta V/V$ is the swelling and ρ is the density of the material. With the large amount of swelling, the distribution of injected ion concentration will inevitably be affected as well. Hence, after voids were profiled in depth, the resulting swelling profile was used to recalculate the injected ion concentration. By adopting the swelling profile, the SRIM calculation with modified material densities as a result of void swelling was calculated, assuming that the effect of voids is homogenous throughout each layer. The updated densities were input into SRIM as discrete layers of 100 nm and 200 nm each for the case of nickel irradiated to 1.5×10^{16} and $5.0 \times 10^{16} cm^{-2}$, respectively. The resulting nickel ion distributions will then represent the case with modified material densities. By adjusting the bulk atomic density in each layer, the nickel ion concentration is calculated. The distribution depth is converted to mass depth by multiplying with the original nickel density.

3.3.3 Dislocation Loops Imaging and Characterization

As previously mentioned, the dislocation loops in Ni SP-CSAs usually consist of a mixture of perfect 1/2<110> and faulted 1/3<111> loops. The TEM samples for dislocation loops imaging were also prepared on an FEI Helios Nanolab workstation using FIB lift-out method. But the thickness of the sample was left to be around 250 nm for further flash polishing. Since the defects induced by FIB preparation mainly appear as interstitial clusters or small dislocation loops under TEM, it is critical to remove the undesirable FIB damages before imaging dislocation loops. The majority of Ni SP-CSAs investigated in this study can be successfully polished using the set up described in Chapter 3.3.1. However, the successful rate for polishing NiPd and NiCoFeCrPd has been relatively low after many attempts due to their fast oxidation rates. For these two SP-CSA samples, the low energy cleaning method was applied instead to remove the FIB induced damage. Sample thickness was measured using the EELS method in a JEOL 2100F aberration-corrected TEM. The final sample thickness typically ranged between 100-150 nm after flash polishing or low energy cleaning method was applied.

The dislocation loops were imaged near [110] zone axis using a two beam condition of g=[200] after flash polishing. This is because the polishing process may inevitably affect the size of voids but not dislocation loops. The dislocation loops were characterized in a similar method as profiling voids, with the loop sizes determined by measuring the longest axis. The counted loops included edge-on and tilted dislocation loops. Typically, hundreds of dislocation loops were counted in each testing condition to increase statistical accuracy. For equiatomic SP-CSAs, the region of 500 ± 100 nm with a dose about 38 ± 5 dpa was chosen for the statistic of loop distribution. This region was selected to avoid the artificial effects associated with the surface sinks and to minimize the injected interstitial effects. The loop feature was not measured in Ni, NiCo and NiCoCr due to the extensive overlapping of dislocation loops and voids in this region. For Ni-20X binary alloys, the damage region of 200-1000 nm was profiled. For Ni-xFe binary alloys, only qualitative images were presented due to the large variation of dislocation loop distribution.

In this work, all images taken by TEM for dislocation loops analysis were recorded at a magnification of 8000 and an exposure time of 2 seconds. A small degree of tilting away from the exact two beam condition was applied on TEM samples to reduce the contrast for dislocation loops. Depending on the size of dislocation loop features, some higher magnification images were taken to present a more detailed view of dislocation loop evolution. An example image of different types of dislocation loops in NiFe is shown in Figure 3.9.

3.3.4 Estimation of Errors

In the laboratory testing, some extent of experimental error is unavoidable despite given the best effort to operate the measuring instrument or follow the measuring procedures. However, error calculations can be applied to ensure the accuracy of experimental measurements. In this thesis study, systematic errors that arise due to the calibration and limitation of instruments were accounted for, but not the random errors arise from false judgment. To ensure good statistics from data collection, at least two TEM samples for each condition were extracted and studied. This is equivalent to at least 2 μm^2 of examined area. The variation between different grains was not a major concern in this study since most of the SP-CSAs analyzed in this study were single crystal, or polycrystals with an averaged grain size of a

few hundreds of μm. However, more samples were examined if the density of irradiation-induced defects was low.

For defect characterizations conducted in this study, two main factors were considered to contribute the most to measurement errors. They are error due to TEM resolution and error due to EELS thickness measurements. The following discussion is organized based on the error in measuring defect size, defect density and void swelling.

The resolution for the images taken was 0.47 and 0.7 nm/pixel for TEM and STEM, respectively. To simplify the calculation, it was assumed that the resolution error is less than 1 nm, regardless of defect size. The measurement error of defect size was calculated using the equation below:

$$\mu_{res} = \frac{1nm}{D}$$

where *D* is the length of the defect measurement. This measurement error can be applied to both voids and dislocation loops. Since the calculation of void swelling was derived from void diameter, this measurement error also contributed to its error calculation.

The measurement error of defect density can be regarded as only depends on the error of EELS thickness measurement. As mentioned previously, error in EELS measurement is 10%; hence, error in number density is estimated to be 10%.

The measurement error of void swelling depends on both TEM resolution and EELS thickness measurement, as void size and sample thickness were both included in the derivation. In the derivation, void swelling is proportional to the number density and proportional to the cube of void diameter, as shown below:

$$\frac{\Delta V}{V} \propto N_D \propto \left(\frac{D}{2}\right)^3$$

Where $\Delta V/V$ represents void swelling, N_D represents number density of vacancies, D represents the void diameter. According to the above relation, the propagation of error for void swelling can

be calculated as:

$$\mu_{swelling} = \sqrt{\left(\frac{\sigma_{N_D}}{N_D}\right)^2 + \left(n * \frac{\sigma_D}{D}\right)^2} = \sqrt{\left(\mu_{N_D}\right)^2 + (3 * \mu_D)^2}$$

where μ_{N_D} and μ_D represent the fractional errors in number density and diameter, respectively. The calculated error in defect size, number density and void swelling is plotted in Figure 3.10 as a function of defect size [86].

Table 3.1 The material properties of Ni and Ni-SPCSAs studied in this work.

Materials (at %)	Melting temperature (K)	Lattice parameter (Å)	Density (g/cm^3)	Crystal structure*
Ni	1728	3.524	8.908	SC
NiCo	1735	3.535	8.848	SC
NiFe	1703	3.583	8.233	SC
NiPd	1513	3.714	---	SC
NiCoFe	1724	3.569	8.390	SC
NiCoCr	1690	3.559	8.273	SC
NiCoFeCr	1695	3.572	8.144	SC
NiCoFeCrMn	1553	3.599	7.979	PC
NiCoFeCrPd	1560	3.673	8.915	PC
Ni-20Cr	1693	3.546	8.543	SC
Ni-20Mn	1480	3.572	---	PC
Ni-20Pd	1555	3.616	---	PC
Ni-20Fe	1713	3.548	---	SC
Ni-10Fe	1714	---	---	SC
Ni-35Fe	1713	---	---	SC

*SC represents single crystal, while PC represents polycrystal.

Table 3.2 The experimental details and microstructural characterization for the irradiated Ni and Ni-SPCSAs.

Irradiation Completion Date	Materials	Beam Energy (MeV)	Peak Damage (Kinchin-Pease dpa)	Irradiation Temperature (℃)	Voids Characterization	Dislocation Loops
11/20/15	Ni	3	17	500	✓	✓
	NiCo				✓	✓
	NiFe				✓	✓
	NiCoFeCr				✓	✓
08/27/15	Ni	3	60	500	✓	×
11/20/15	NiCo				✓	✓
	NiFe				✓	✓
	NiCoFe				✓	✓
	NiCoFeCr				✓	✓
06/20/16	Ni-10Fe	3	60	500	✓	✓
	Ni-15Fe				✓	✓
	Ni-20Fe				✓	✓
	Ni-35Fe				✓	✓
11/22/16	Ni	3	60	500	✓	✓
	Ni-20Fe				✓	✓
	Ni-20Cr				✓	✓
	Ni-20Mn				✓	✓
	Ni-20Pd				✓	✓
	NiPd				No voids	✓
12/06/16	Ni-20Mn	3	60	420	✓	✓
	Ni-20Pd				✓	✓
	NiPd				No voids	✓
	NiCoFeCrMn				✓	✓
	NiCoFeCrPd				✓	✓
05/19/17	NiCoFeCrMn	3	60	675	No voids	×
	NiFe				No voids	×
09/20/17	NiCoCr	3	60	420	✓	✓
	NiCoFeCr				✓	✓
	NiCoFeCrMn				✓	✓
	NiCoFeCrPd				✓	✓
09/20/17	NiCoCr	3	60	500	✓	✓
	NiCoFeCr				✓	✓
	NiCoFeCrMn				✓	✓
	NiCoFeCrPd				✓	✓
09/20/17	NiCoCr	3	60	580	✓	×
	NiCoFeCr				✓	×
	NiCoFeCrMn				✓	✓
	NiCoFeCrPd				✓	✓

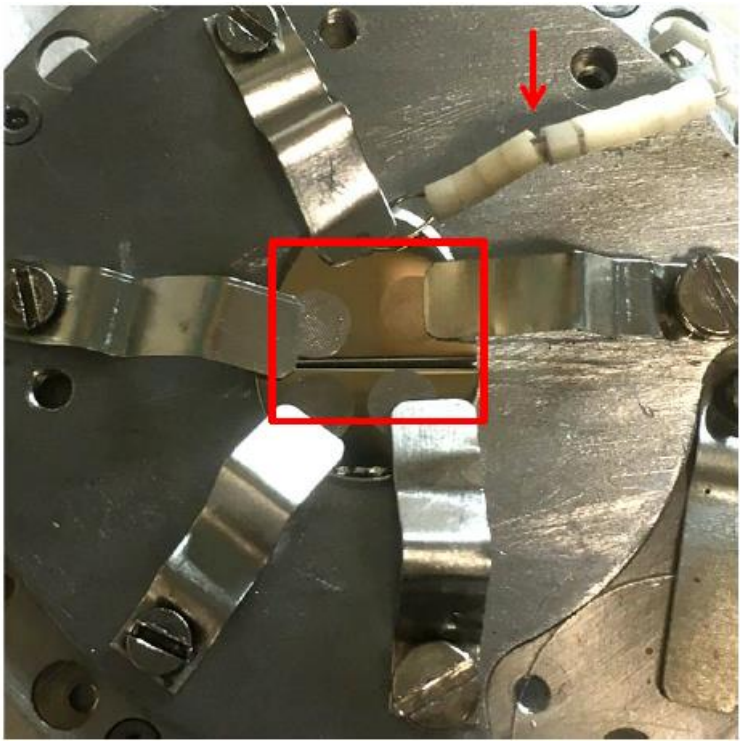

Figure 3.1 An image of a fully constructed irradiation stage. The arrow indicates the thermocouple attached on the sample surface, and the square area indicates the irradiation region.

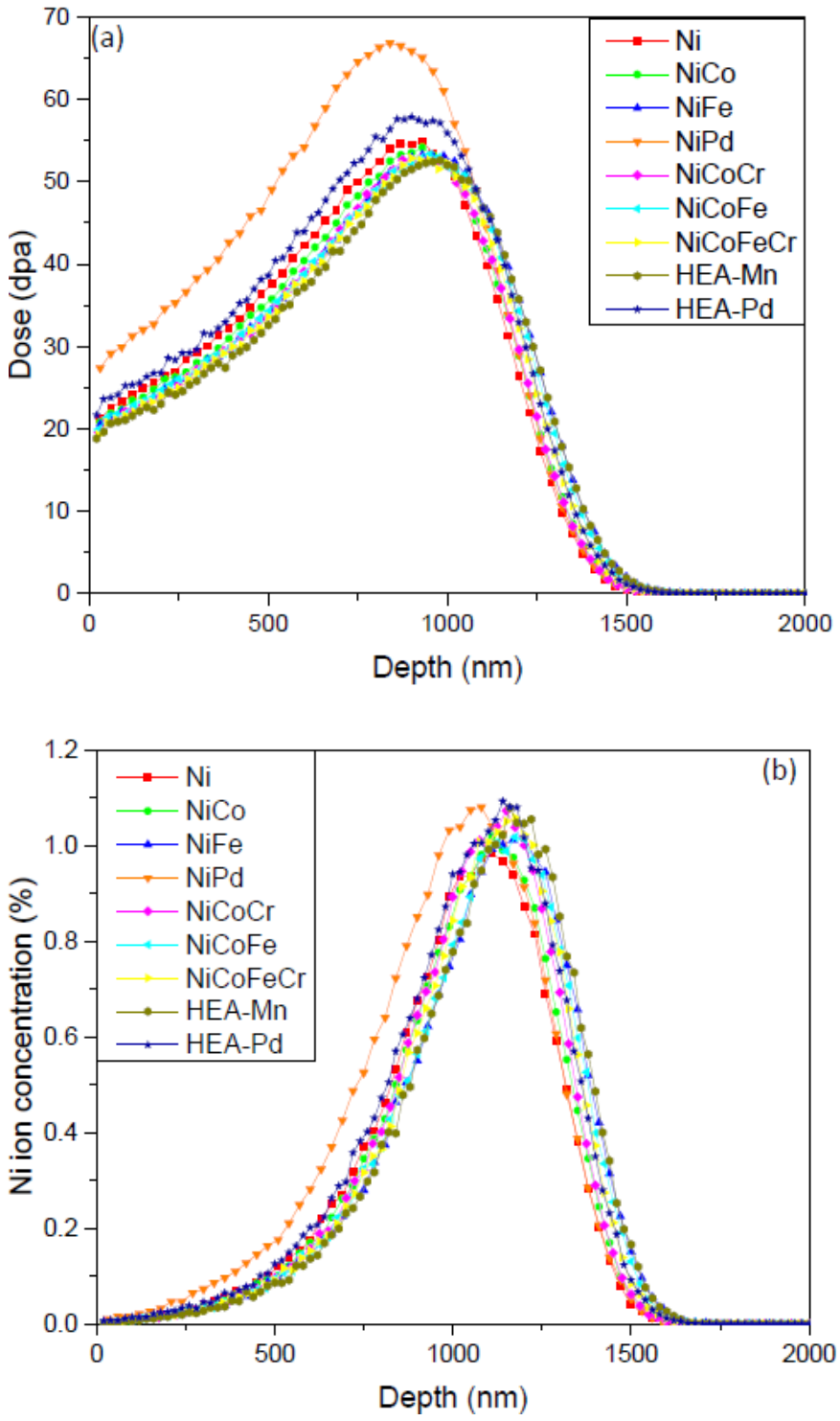

Figure 3.2 SRIM prediction profile of (a) displacement damage and (b) implanted ions using 3.0 MeV Ni^{2+} ions irradiated to 5.0×10^{16} ions/cm^2 in Ni SP-CSAs.

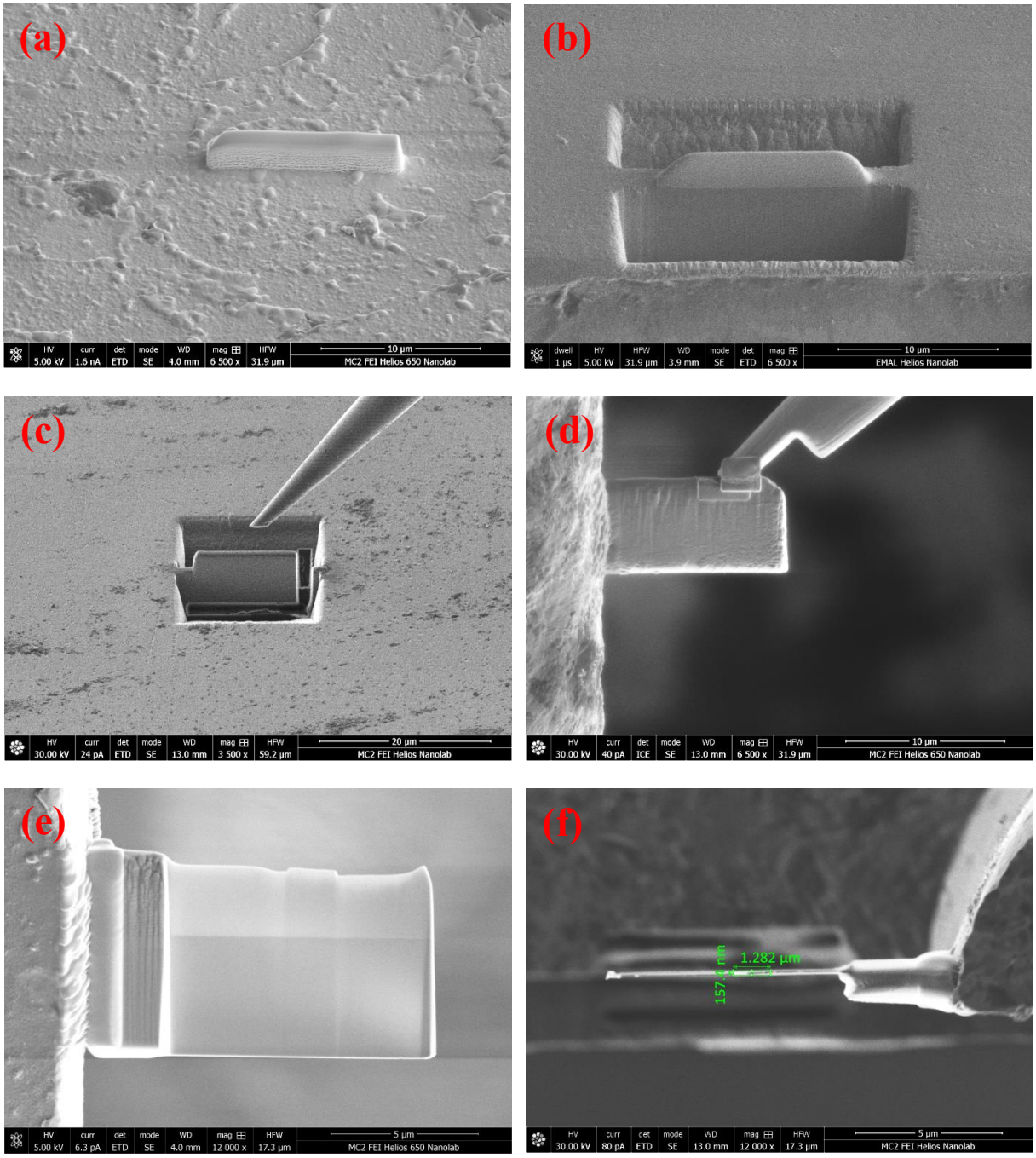

Figure 3.3 Demonstration of the FIB process, showing (a) platinum deposition on the surface, (b) trenching around the previous platinum deposition, (c) undercut of the sample and attaching the Omniprobe to the surface, (d) attaching the sample to the sample grid, (e) a thinned FIB specimen, and (f) estimation of sample thickness under ion beam.

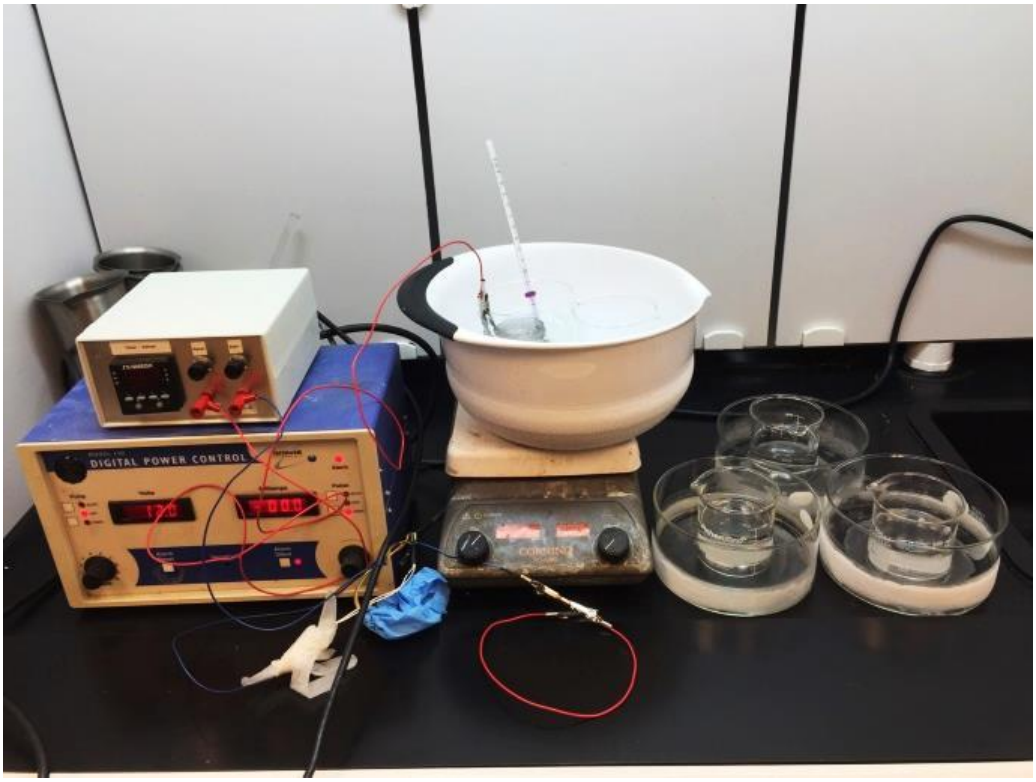

Figure 3.4 An image of experimental set up for flash polishing.

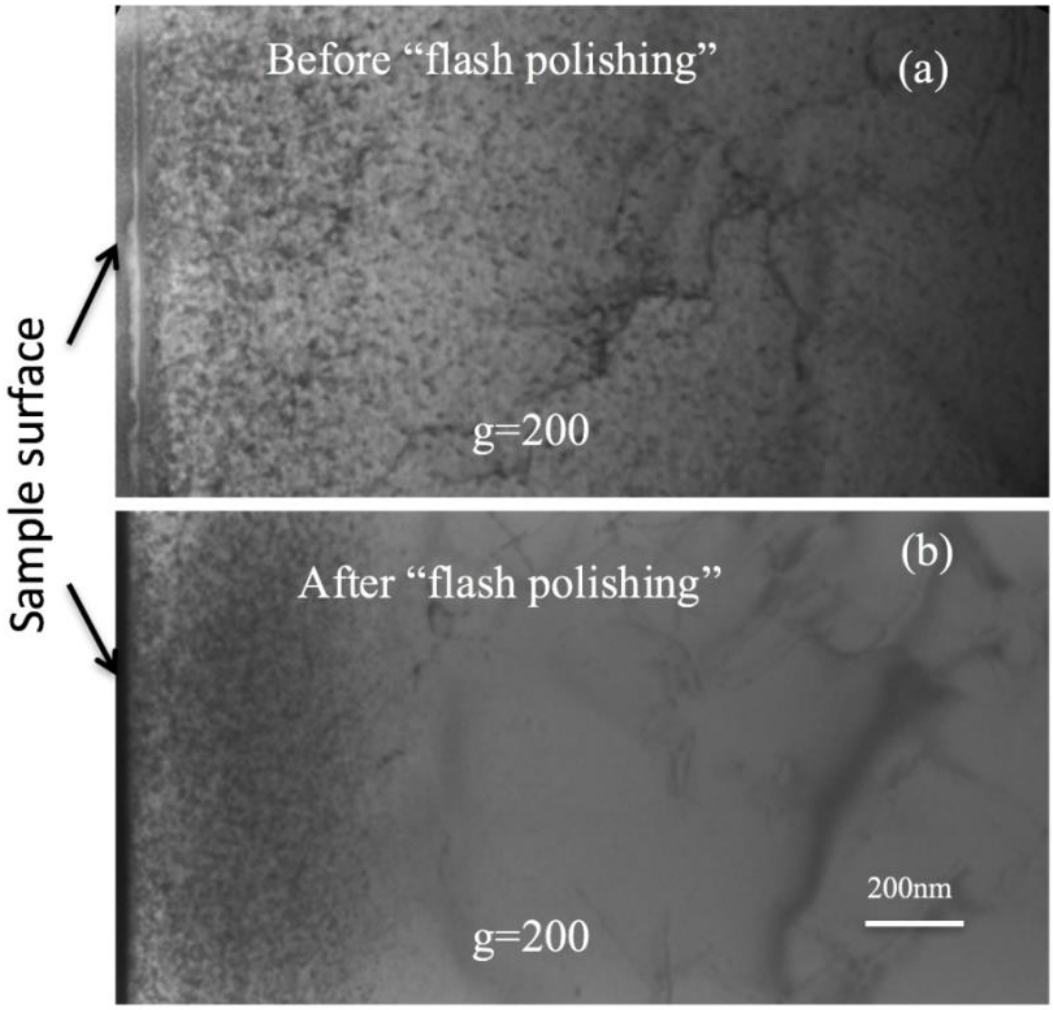

Figure 3.5 Bright field TEM cross-sectional images of NiCo (a) before and (b) after applying flash polishing [87].

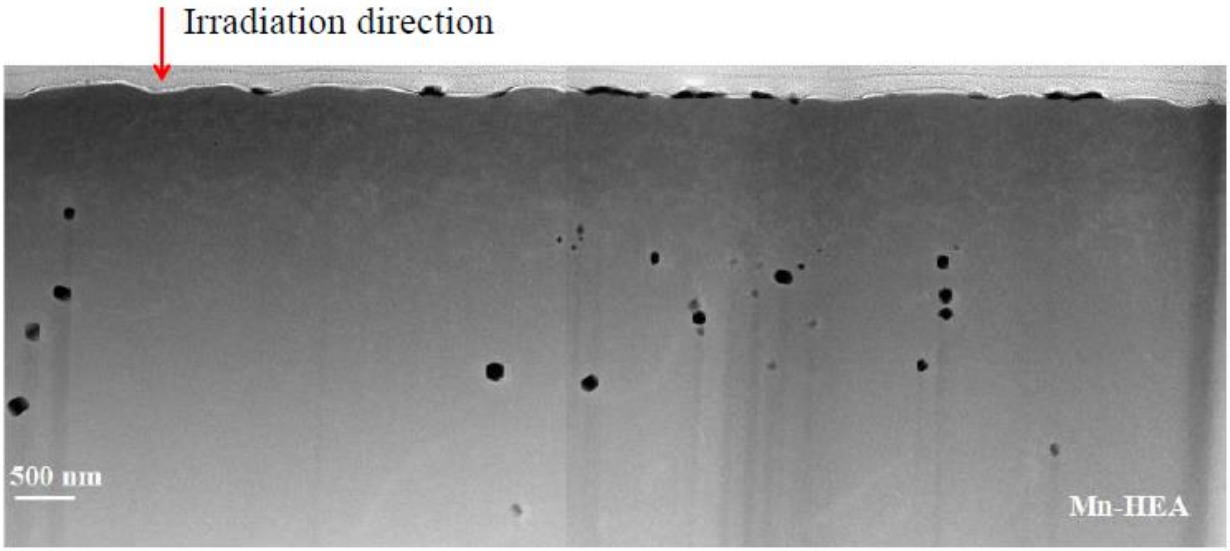

Figure 3.6 Cross-sectional HAADF STEM images of NiCoFeCrMn (Mn-HEA) irradiated by 3.0 MeV Ni^{2+} ions to 5.0×10^{16} ions/cm^2 at 580℃ [17].

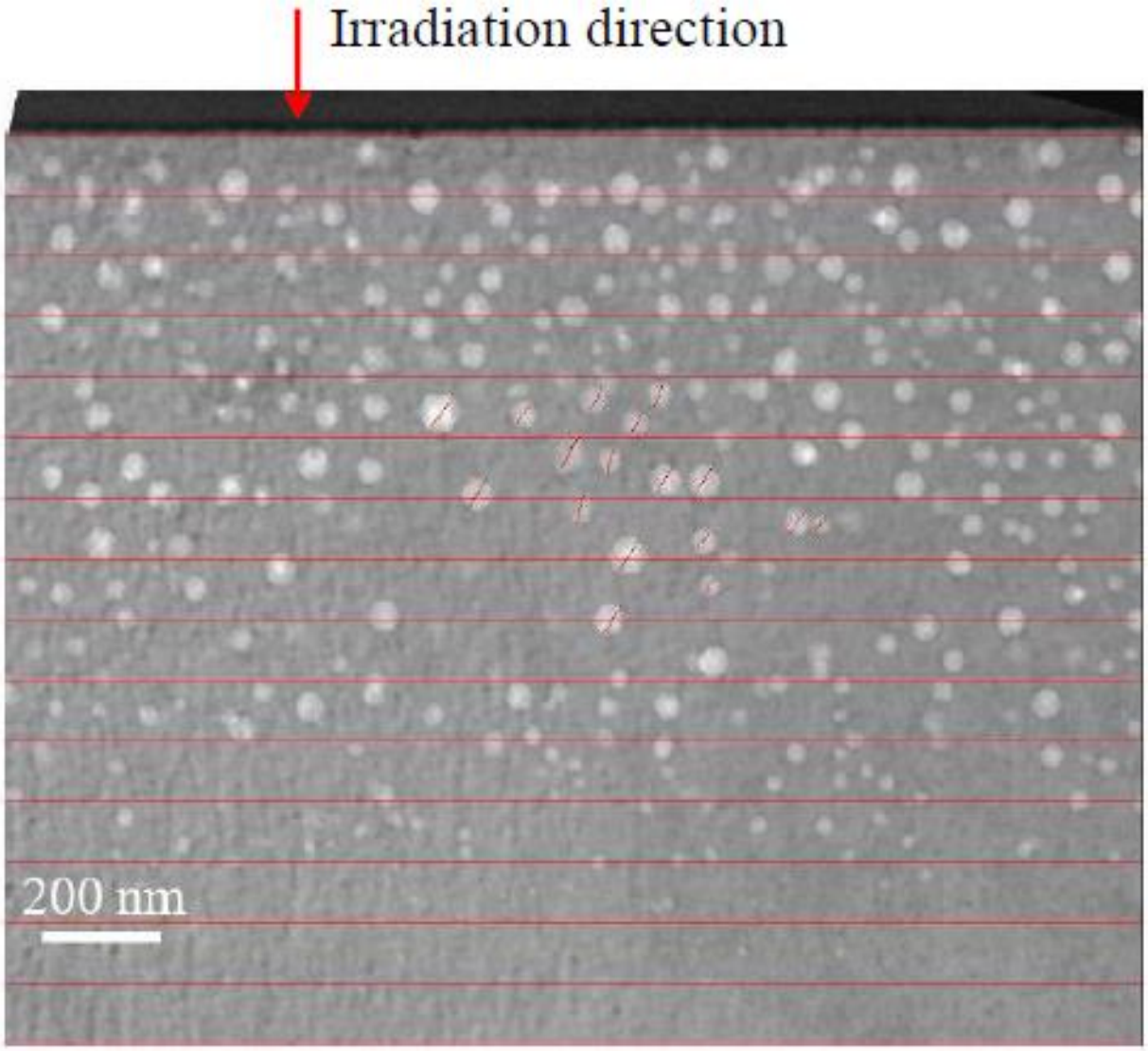

Figure 3.7 An example of a partially counted cross-sectional TEM image.

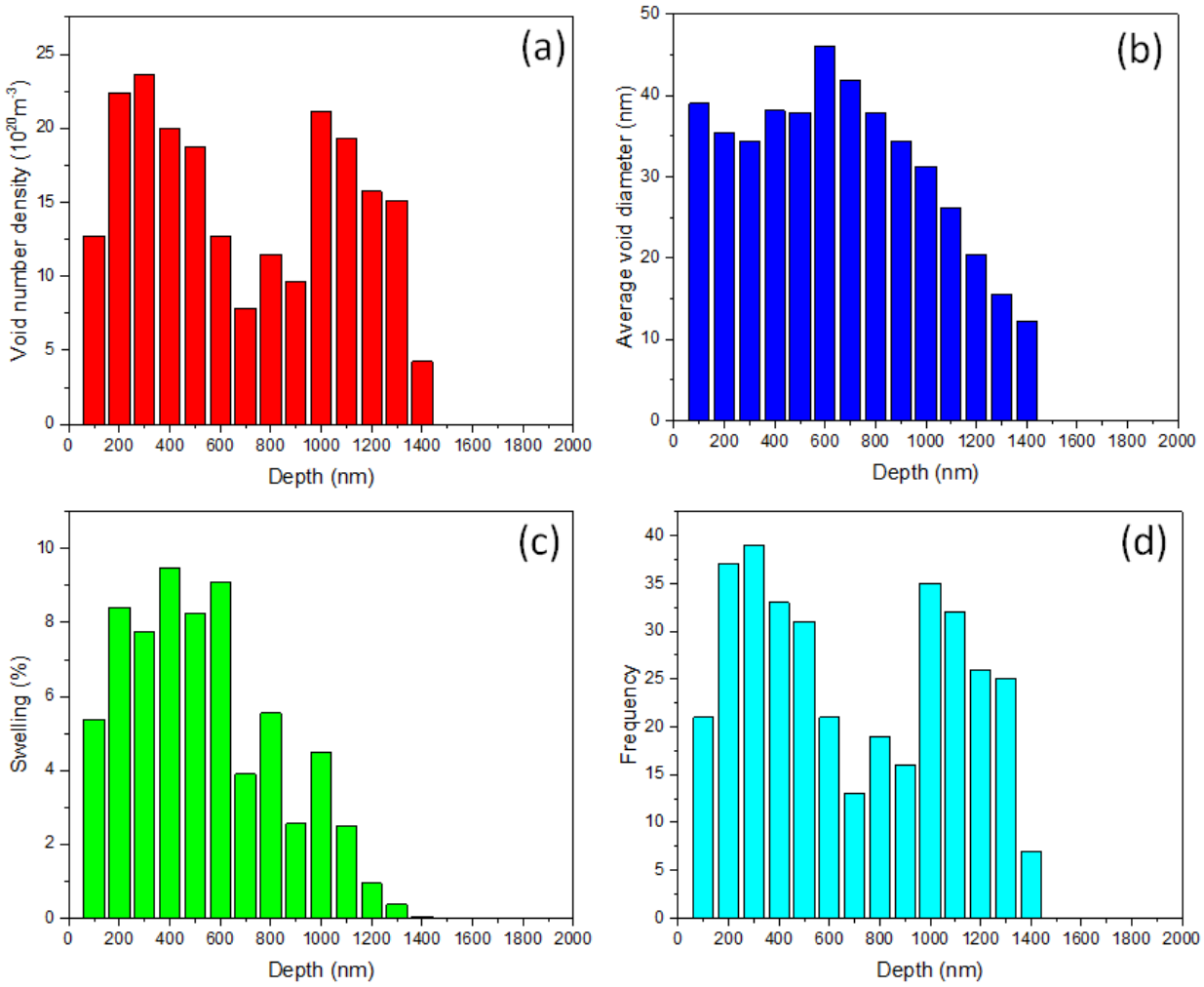

Figure 3.8 An example of depth dependent void profiling in NiCo irradiated to 60 dpa peak dose at 500℃ (a) void number density, (b) average void diameter, (c) swelling and (d) number of voids counted.

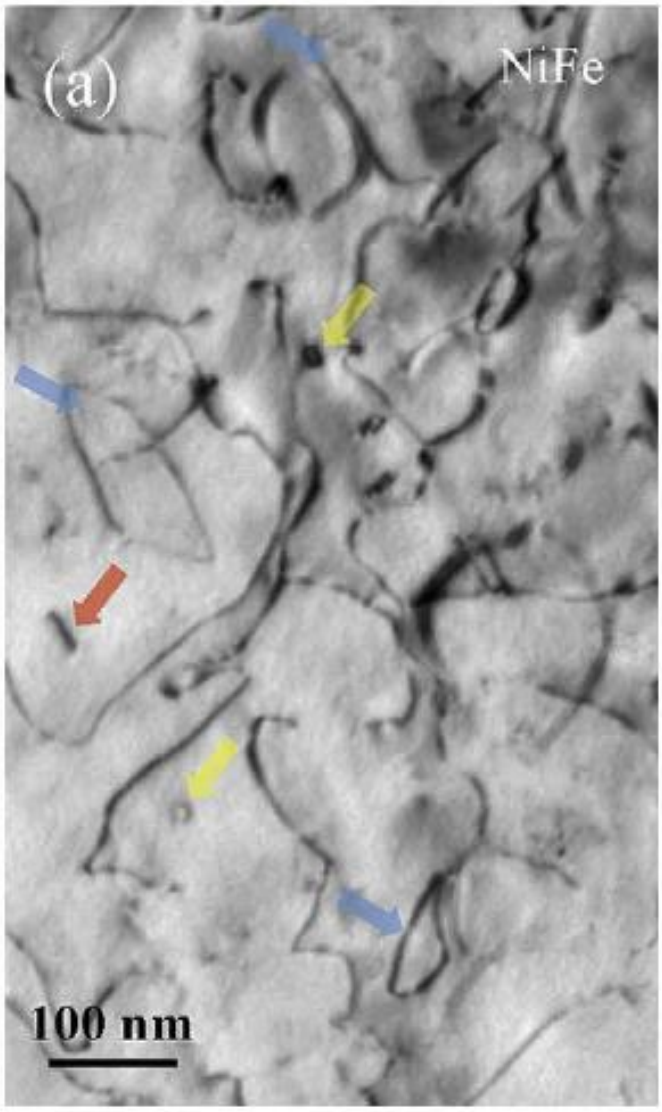

Figure 3.9 An example image of dislocation loops imaged at near two beam condition g=[200] on NiFe irradiated to 38±5 dpa at 500℃. Perfect loops are marked by blue arrows, faulted loops are marked by yellow arrows, edge-on faulted loops are marked by red arrows [35].

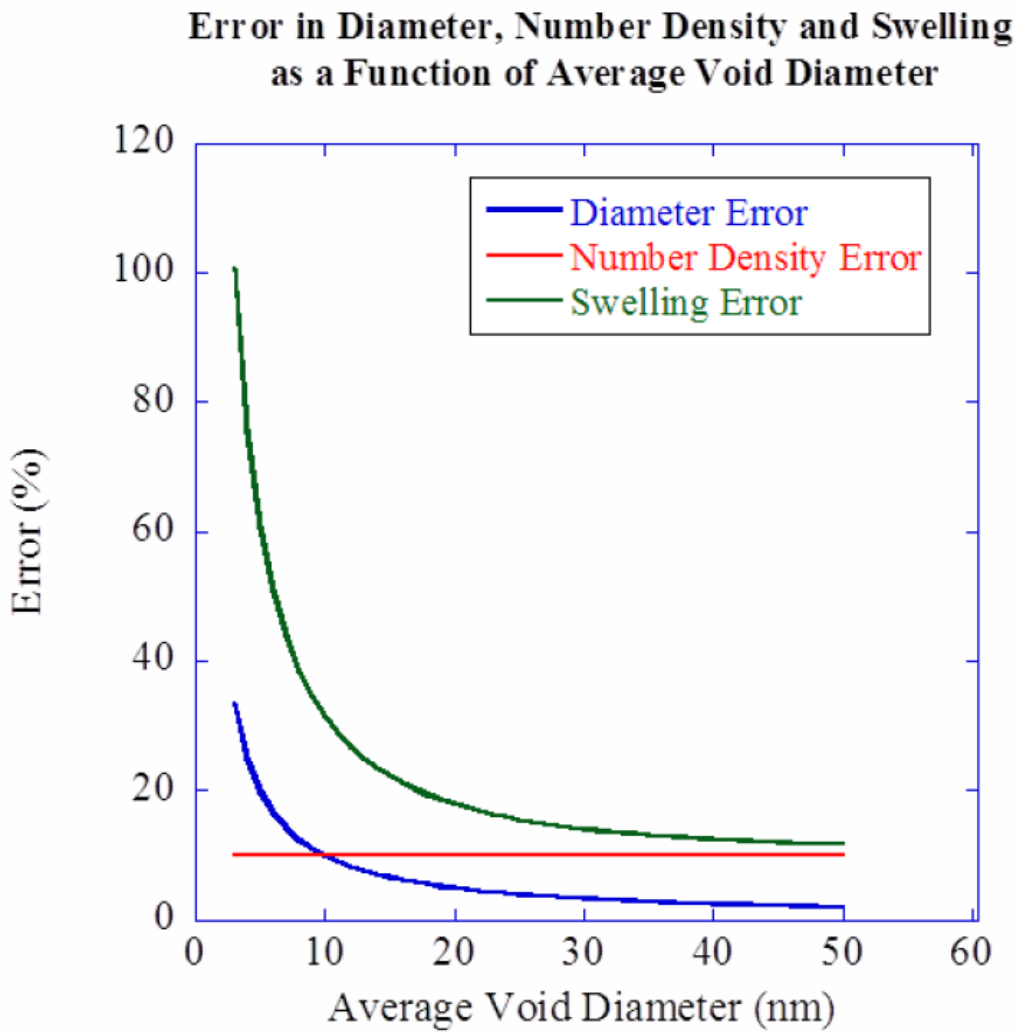

Figure 3.10 The calculated error in defect size, number density and void swelling is plotted as a function of defect size [86].

Chapter 4-Experimental Results

The chapter presents the characterization results of ion irradiation experiments described in Chapter 3. This result section is divided into three parts based on the materials studied, and each part presents the void swelling result prior to the dislocation loop result. The materials analyzed in this thesis study can be roughly categorized into: equiatomic Ni-containing SP-CSAs, nickel-iron binary alloys with changing iron concentration, and Ni concentrated binary alloys with changing alloying elements.

4.1 Void Swelling and Dislocation Loop Results in Equiatomic Ni SP-CSAs

4.1.1 Defect Evolution at Single Elevated Temperature

As mentioned previously in Chapter 2.3 Radiation damages on materials, voids are the result of vacancy agglomeration while dislocation loops are the result of interstitial clusters. Both can result in significant changes in material properties and mechanical behaviors, and hence are the main interest of this study. In this subchapter, the result of SP-CSAs irradiated at 500℃ is presented.

The irradiation-induced damage profile and injected ion concentration were calculated using SRIM-2013 in Quick Kinchin-Pease Mode with a displacement threshold energy of 40 eV for all elements. The results of the calculations are plotted in Figure 4.1. No significant differences in penetration depth or displacements were observed between most of Ni SP-CSAs. However, due to the relatively high atomic density in NiPd, the resulting damage dose was higher than the rest of the tested materials at a slightly shallower depth. The implanted Ni ion concentration was similar for all tested materials, with the concentration peak for NiPd being about 100 nm closer to the surface.

Figure 4.2 shows the cross-sectional TEM bright field images of all the equiatomic Ni-containing SP-CSAs irradiated using 3 MeV Ni^{2+} ions at 500℃ to a peak dose of about 60 dpa. Various sizes of voids were observed at all studied materials, except NiPd. The image of dislocation loops is included here to demonstrate the lacking of voids. Table 4.1 summarizes the results of the void characterization, including the average void size, densities, overall swelling and examined area. These parameters were plotted in Figure 4.3 (a) to (c) respectively. Note that the swelling data of Ni, NiCo and NiCoCr was plotted separately and inserted in the same plot with the rest of SP-CSAs for better data presentation. Comparing to the swelling result of Ni presented in [38], the dose rate was one order lower in this study and therefore shifted the temperature region for void formation to lower temperature.

Cross-sectional images of dislocation loops of all the equiatomic Ni-containing SP-CSAs are shown in Figure 4.4. These samples were irradiated using 3 MeV Ni^{2+} ions at 500℃ to a peak dose of about 60 dpa. As mentioned in 3.3.3, the dislocation loops were imaged near [110] zone axis using a two beam condition of g=[200] after flash polishing, except NiPd and NiCoFeCrPd, where low energy cleaning method was applied. The edge-on and tilted dislocation loops were all accounted for. To minimize the surface effect and potential influence from injected Ni concentration, the region of 500 ± 100 nm with a dose about 38 ± 5 dpa was chosen for the statistic of loop distribution. The dislocation loop features in Ni, NiCo and NiCoCr were not measured in this study due to the largely overlapping of voids and dislocation loops in this selected region. NiCoFeCrPd was not measured in this study due to its high density of dislocation loops. For those samples that were not measured quantitatively, a qualitative comparison based on TEM images was provided instead. The result of dislocation loop characterization is summarized in Table 4.1 as well. Figure 4.5 (a) and (b) respectively plot the average dislocation loop size and number density of equiatomic SP-CSAs.

The void swelling result shows that the suppression of swelling does not necessarily become more significant with increasing number of alloying element, but depends on certain specific constituents instead. The result of binary alloys suggests that alloying with Pd has a stronger suppression effect on void swelling than alloying with Fe, follows by Cr. The result of ternary alloys indicates that Fe is more effective in reducing swelling than Cr, when alloyed with

Ni and Co. Furthermore, alloying with Mn or Pd did not necessarily result in the smallest average void size or lowest swelling when irradiated at 500 ℃. Of all the equiatomic SP-CSAs irradiated at 500 ℃, NiCoFeCr has the smallest average void size and lowest swelling. This result is contrary to the proposed four "core effects" of HEAs, and indicates that when comparing the void swelling result, the melting temperature of alloys should be taken into consideration.

Based on the relative depth distribution of voids and dislocation loops, this group of samples can be roughly separated into three groups. The first group contains Ni, where the average void size was drastically larger and located in the irradiated region closer to the sample surface, while the dislocation loops were separated from voids and existed in a deeper region [84]. The second group contains NiFe, NiCoFe, NiCoFeCr, NiCoFeCrMn and NiCoFeCrPd, where much smaller voids distributed beyond the end of the predicted ion range, while dislocation loops dominated the main irradiated region. The third group contains NiCo and NiCoCr with a mixed defect distribution between the previous two groups. The contributing defect migration mechanisms are discussed in Chapter 5. In general, with the increasing number of principal elements alloyed in SP-CSAs, the dislocation loop size decreases while the number density increases.

4.1.2 Damage Dependence of Defect Evolution

The primary motivation of studying damage dependence in SP-CSAs was twofold: to confirm the relative irradiation performance between materials, and to study the defect evolution as a function of damage dose. Two irradiation damages were studied for these purposes, including 17 dpa and 60 dpa at peak dose. The studied SP-CSAs included Ni, NiCo, NiFe and NiCoFeCr. The data of 60 dpa has been reported previously in 4.1.1, but it is also included here for direct comparison. Figure 4.6 and Figure 4.7 show the representative cross-sectional TEM images of voids and dislocation loops in tested SP-CSAs, respectively. Table 4.2 summarizes the dose-dependent defect evolution irradiated using 3 MeV Ni^{2+} ions at 500℃. The characterization result of voids and dislocation loops are plotted in Figure 4.8 and Figure 4.9, respectively. The results of higher damage dose are marked with asterisk signs.

In general, the distribution of voids is inhomogeneous and depth-dependent for all tested irradiation damages. Among the characterized materials, the swelling behavior can be separated into two groups based on the distribution of voids: one group has larger voids and a relatively even distribution, i.e. Ni and NiCo; the other group has much smaller voids, and these voids are mainly distributed in a deeper region from the surface with few scattered voids closer to the surface, i.e. NiFe and NiCoFeCr. NiCoFeCr exhibits the highest swelling resistivity follow by NiFe, NiCo and then Ni. At lower damage dose (17 dpa at peak damage), NiFe exhibits a similar amount of swelling as NiCoFeCr. However, at higher damage dose (60 dpa at peak damage), the average void size in NiFe has significantly increased while the one in NiCoFeCr has remained similar with slightly higher number density. This indicates that NiCoFeCr has a stronger tendency in suppressing the void growth than NiFe. The trend of swelling resistance in tested SP-CSAs is consistent at two different damage doses. Furthermore, the average dislocation loop size increases with increasing damage dose, as shown in Figure 4.7 and Table 4.2. The average dislocation loop size in NiFe increases ~2 times with increasing damage dose, while the average dislocation loop size remains relatively constant in NiCoFeCr with a slight increase in number density.

Additionally, the depth-dependent profiling on defects was applied to provide a more quantitative microstructure characterization. Some passages in this subchapter have been quoted from the published article [84] of this thesis work. The depth-dependent swelling behavior for the two ion fluences of 1.5×10^{16} and $5.0 \times 10^{16} cm^{-2}$ (~17 and 60 dpa as peak dose) are shown in Figure 4.10 to Figure 4.12. Figure 4.10 shows the void number density distribution as a function of depth in pure nickel, NiCo, NiFe and NiCoFeCr. The profile of irradiation-induced damage and implanted nickel ion concentration was overlaid on the plot to emphasize the effects on the void distribution. An obvious separation of two bands of voids was observed in NiCo and NiCoFeCr for both ion fluences, and swelling is suppressed by the injected interstitials. The calculated damage peak coincides with the valley of the void number density for both fluences, while the peak for injected ion concentration shifted deeper from the valley.

Figure 4.11 shows the depth distribution of the average diameter of voids. For nickel, the void size gradually increased with depth and peaked at around 800 nm from the surface for both

fluences before gradually decreasing. The size distribution for NiCo at lower fluence showed two peaks; one peak is closer to the surface at around 300 nm, while the second peak is much deeper, appearing at around 1000 nm. For NiCo at higher fluence, there is only one peak at around 600 nm with a relatively larger void size around 100 nm. Additionally, for NiFe at higher fluence, the void size increased with depth and showed a peak at around 1800 nm before dropping abruptly to zero.

Figure 4.12 presents the depth distribution of swelling. Data are presented in two groups due to a scale difference of two orders. For the pure nickel, the correction method can yield different statistical results [85] since swelling higher than 10% was observed. The swelling vs. depth and nickel ion concentration is replotted in Figure 4.13 using the effective thickness method as described in Chapter 3.3.2. The swelling distribution of Ni in Figure 4.12 shows the original depth vs. swelling without density correction for better comparison with data that has swelling values much lower than 10%. NiCo at lower fluence barely shows any degree of swelling at the same depth of the swelling peak for pure nickel. In NiCoFeCr, there is no swelling in the depth range between 600-1000 nm for both fluences. At lower fluence, the two swelling peaks are separated just as observed in NiCo, but only wider. The swelling for NiFe is entirely located at the deeper region compared with the other samples.

4.1.3 Temperature Dependence of Defect Evolution

Void induced swelling has an optimum formation temperature ranges between 0.3 to 0.6 melting temperature of the material. At the beginning of the study, a single elevated temperature was chosen to study the general irradiation performance of Ni-based SP-CSAs. However, since the melting temperature of tested equiatomic SP-CSAs can range from 1553 to 1728 K, see Table 3.1, it is critical to perform a systematic study on the temperature dependence of void swelling in equiatomic SP-CSAs. To this end, the homologous temperature was chosen to normalize the difference inherited in the melting temperature. The selected SP-CSA samples included Ni, NiCoCr, NiCoFeCr, NiCoFeCrMn and NiCoFeCrPd. Most of the samples were irradiated with 3 MeV Ni^{2+} ions to three temperatures, i.e. 420, 500 and 580°C, to a peak dose ~ 60 dpa. Ni and NiCoFeCrMn were also irradiated at 675°C to study the limit of void formation temperature. The corresponding homologous temperature and testing conditions are recorded in Table 4.3.

Since the focus of this sub-objective is using homologous temperature to provide a fair comparing ground between different equiatomic SP-CSAs, the characterization result is divided based on their homologous temperature. Figure 4.14 to Figure 4.17 present the cross-sectional images of voids in tested materials from 0.41, 0.45, 0.50 to 0.55 T_m, respectively. The temperature deviation between calculated homologous temperatures and actual irradiation temperatures was controlled to vary within ±15℃. The characterization result of voids is summarized in Table 4.4. No voids were observed in Ni and NiCoFeCrMn when irradiated at 675°C, indicating the irradiation temperature is beyond the optimum void formation temperature range.

Figure 4.18 to Figure 4.21 present the TEM cross-sectional images of dislocation loops and dislocation lines in tested materials from 0.41, 0.45, 0.50 to 0.55 T_m, respectively. As mentioned in Chapter 3.3.3, the region of 500 ± 100 nm with a dose about 38 ± 5 dpa was chosen for the statistic of loop distribution in equiatomic SP-CSAs. Samples with voids overlapping in this specific region were not quantitatively measured but discussed qualitatively. The characterization result of dislocation loops and dislocation lines is summarized in Table 4.4. The size of the dislocation loops was consistently smaller and with higher loop density in HEAs than non-HEAs. Despite adapting two different cleaning methods, the main irradiation damage region can still be clearly distinguished.

The normalized distribution of void size is plotted in Figure 4.22 (a) and Figure 4.22 (b) based on the homologous temperatures tested. Void size increases for Ni and all Ni SP-CSAs with the increase of irradiation temperatures. The total swelling of Ni and Ni SP-CSAs is plotted in Figure 4.23 as a function of irradiation temperature. According to the results shown in Figure 4.22 and Figure 4.23, NiCoFeCrPd and NiCoFeCrMn (both are HEAs) exhibit smaller swelling throughout the whole irradiation temperature range than non-HEAs.

4.2 Void Swelling and Dislocation Loop Results in Ni-xFe

To study the effect of alloying element concentration on defect evolution, Ni-xFe binary alloys with x= 10, 15, 20, 35 at% were chosen for this objective. Samples were irradiated with 3 MeV Ni^{2+} ions to 500 °C, to a peak dose ~ 60 dpa. Only a single irradiation temperature was

tested in this objective due to a similar melting temperature between studied alloys. The melting temperature of studied binary alloys can be referred to Table 3.1.

The irradiation-induced damage profile and injected ion concentration were calculated using SRIM-2013 in Quick Kinchin-Pease Mode with a displacement threshold energy of 40 eV for all elements. The results of the calculations are plotted in Figure 4.24. No significant difference in displacements or injected Ni ion concentration was observed between Ni-xFe alloys. The cross-sectional STEM BF and HAADF images are shown in Figure 4.25 to present the void distribution as a function of depth. As described in Chapter 3.3.2 Voids Imaging, voids appear in white features in STEM BF but appear in black features in HAADF images. The overall void distribution can be best presented in STEM images when void number density is low. However, to be consistent with the previous method, Figure 4.26 still shows the distribution of voids at cross-sectional BF TEM images. The characterization results of void diameter, number density and swelling are presented in Figure 4.27 as a function of depth. As can be seen, the distribution of voids in Ni-xFe binary alloys is heterogeneous: from the large voids observed closer to the surface in Ni to mainly small voids distributed beyond the main calculated damage peak calculated (~900 nm) as iron concentration increases. Furthermore, the void growth between different Ni-xFe is closely related to the concentration of Fe. The void size decreases significantly with increasing iron concentration in Ni-Fe binary alloys. Despite the increase in void number density, the result in depth dependent swelling shows that swelling is better suppressed in Ni-Fe binary alloys with higher Fe concentration.

The representative cross-sectional images of dislocation loops in Ni-xFe binary alloys are shown in Figure 4.28. The higher magnification images of dislocation loops taken at a diffraction vector of g=[200] are shown in Figure 4.29. Different types of dislocation loops are also identified using the guidelines provided in Jenkins and Kirk [88] and marked in different colors in Figure 4.29. The dislocation loop number density and ratio of faulted to all dislocation loops were deduced from more than 10 higher magnification of TEM images at 400-600 nm depth from the surface. The perfect loops 1/2 <110> are marked by blue circles, the faulted loops 1/3 <111> are marked by yellow circles. The edge-on faulted loops are marked by red arrows while the non-edge-on faulted loops are marked by yellow arrows.

The characterization results of dislocation loop size, number density and fraction of faulted loops to perfect loops are shown in Figure 4.30. Similar to the trend observed in void distributions, the size of interstitials has a negative correlation with the Fe concentration in Ni-Fe alloys. Contrarily, the number density of dislocation loops and the ratio of faulted to perfect loops both increase with the Fe concentration.

4.3 Void Swelling and Dislocation Loop Results in Ni-20X

The irradiation-induced damage profile and injected ion concentration were calculated using SRIM-2013 in Quick Kinchin-Pease Mode with a displacement threshold energy of 40 eV for all elements. The results of the calculations are plotted in Figure 4.31. The representative cross-sectional TEM images of voids in Ni-20X (X= Fe, Cr, Mn and Pd, all in at%) binary alloys and pure Ni are presented in Figure 4.32. Samples were irradiated with 3 MeV Ni^{2+} ions to $0.45T_m$, to a peak dose ~ 60 dpa. The melting temperature of studied binary alloys can be referred to Table 3.1. The depth profiling of swelling and average diameter of the voids are shown in Figure 4.33. The number of voids and dislocation loops counted, along with the area probed is provided in Table 4.5. In general, an imaged area of at least 2.2 um^2 was counted to achieve better statistics.

Some passages in this subchapter have been quoted from the published article [18] of this thesis work. In general, the distribution of voids is inhomogeneous and depth dependent. In the region closer to the irradiated surface, some voids were observed only in Ni-20Fe, Ni-20Cr and Ni-20Mn samples. In the region deeper than damage peak (>1000 nm), some isolated voids were observed in all tested alloys, with varying void size. In addition, a clear decrease in the size of voids is observed from the transition of pure Ni to binary alloys, the size of voids further decreases with increasing atomic volume factor in solutes, which has been presented in Table 2.3. Among the binary alloys, Ni-20Fe has the highest amount of swelling compared with other materials and was plotted on a different y scale to equitably present the difference between other alloys. Due to the heterogeneous distribution of swelling, a direct comparison is difficult to make between Ni-20Cr, Ni-20Mn and Ni-20Pd. Most of the depth- dependent swelling is smaller than 0.2%. Pure Ni was presented here mainly as a reference to Ni binary alloys.

The representative cross-sectional images of dislocation loops in Ni-20X binary alloys are shown in Figure 4.34. The higher magnification images of dislocation loops taken at a diffraction vector of g=[200] are shown in Figure 4.35, with the g vector direction marked by an arrow. Figure 4.35 also presents the diffraction patterns of each sample after irradiation to confirm that the fcc crystal structure remained unchanged. The dislocation loop features and size are highlighted in these images showing the 500-1000 nm depth region. The type of dislocation loops is not distinguished in this study due to its high density and relatively small loop size for most alloys. However, the majority of the dislocation loops are believed to be unfaulted loops.

Figure 4.36 (a) presents the average size of dislocation loops in Ni-20 binary alloys as a function of depth. As mentioned previously in Chapter 3.3.3, the dislocation loop sizes were determined by measuring the longest axis. Similar to the average void size, the general trend shows that the average size of dislocation loops decreases as the atomic volume factor of solute increases. The relatively large fluctuation of dislocation loop size in Ni-20Fe and Ni-20Cr can be attributed to the artificial counting error from the chosen counted bin size (100 nm). As the dislocation loop size becomes larger, the loop density decreases and the larger loop features are more likely to lie between two continuous bins. The counting error arose because the loop will only be counted in the depth region where the majority of loop resides, with a lower loop density, a fluctuation can be created between two adjacent depth/bins. This fluctuation is not accounted for in the presented measurement error.

Figure 4.36 (b) presents the number density of dislocation loops, where the loop density increases with the atomic volume factor of the solutes. An exception lies in the case of Fe and Cr. Cr atoms have a slightly smaller atomic size factor than Fe atoms, yet the defect clusters are significantly smaller in Ni-20Cr for both voids and interstitial loops. Ni-20Cr also has higher dislocation loop density than Ni-20Fe throughout the entire damage range. This case is analyzed in detail in the discussion session. Furthermore, the density of dislocation loops in Ni-20Pd is an order higher than in Ni-20Fe. In the analysis, the dislocation loops within 100 nm depth were excluded due to a potential strong surface effect.

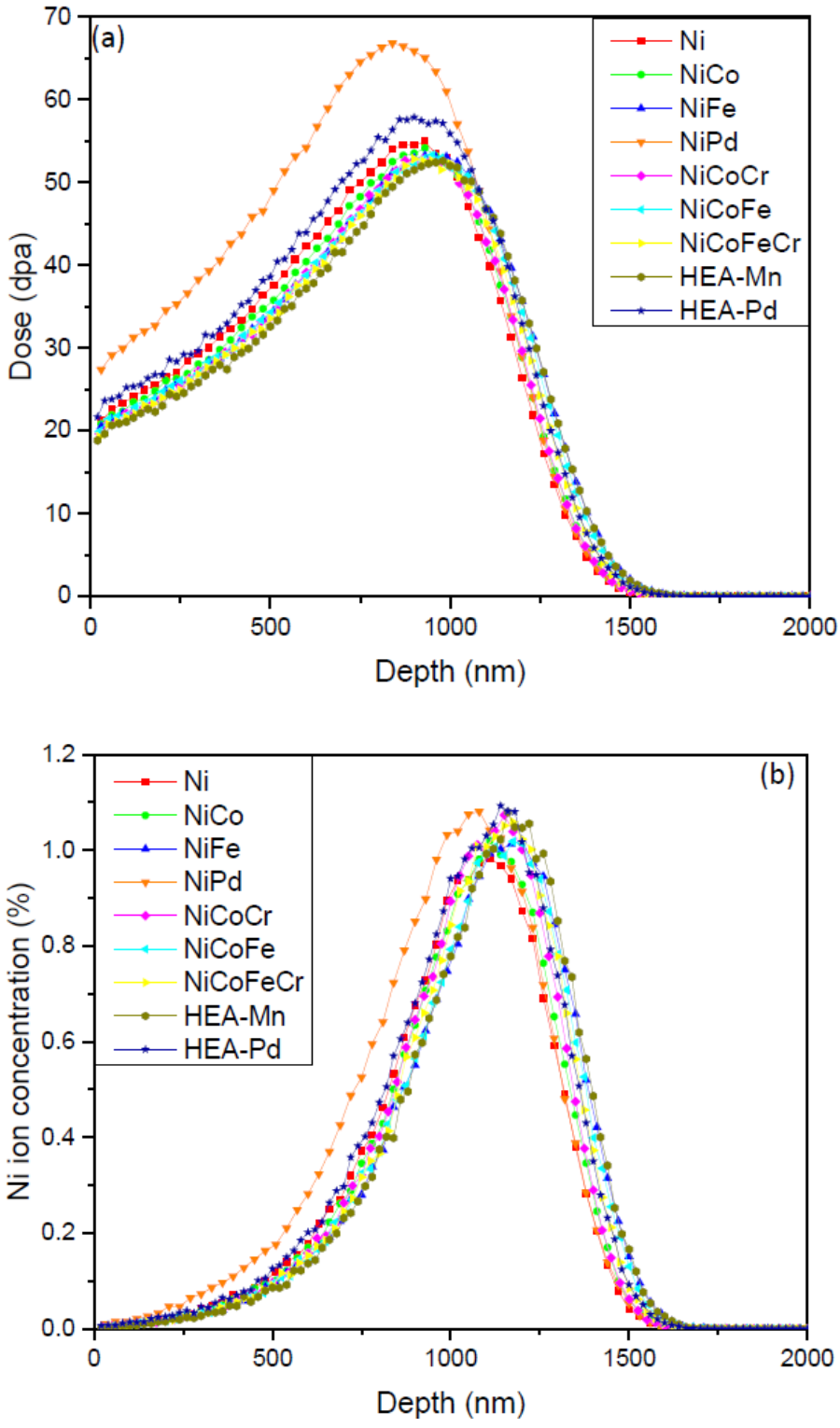

Figure 4.1 SRIM prediction profile of depth distribution of (a) displacement damage and (b) implanted ions for Ni SP-CSAs using 3.0 MeV Ni^{2+} ions irradiated to 5.0×10^{16} ions/cm^2.

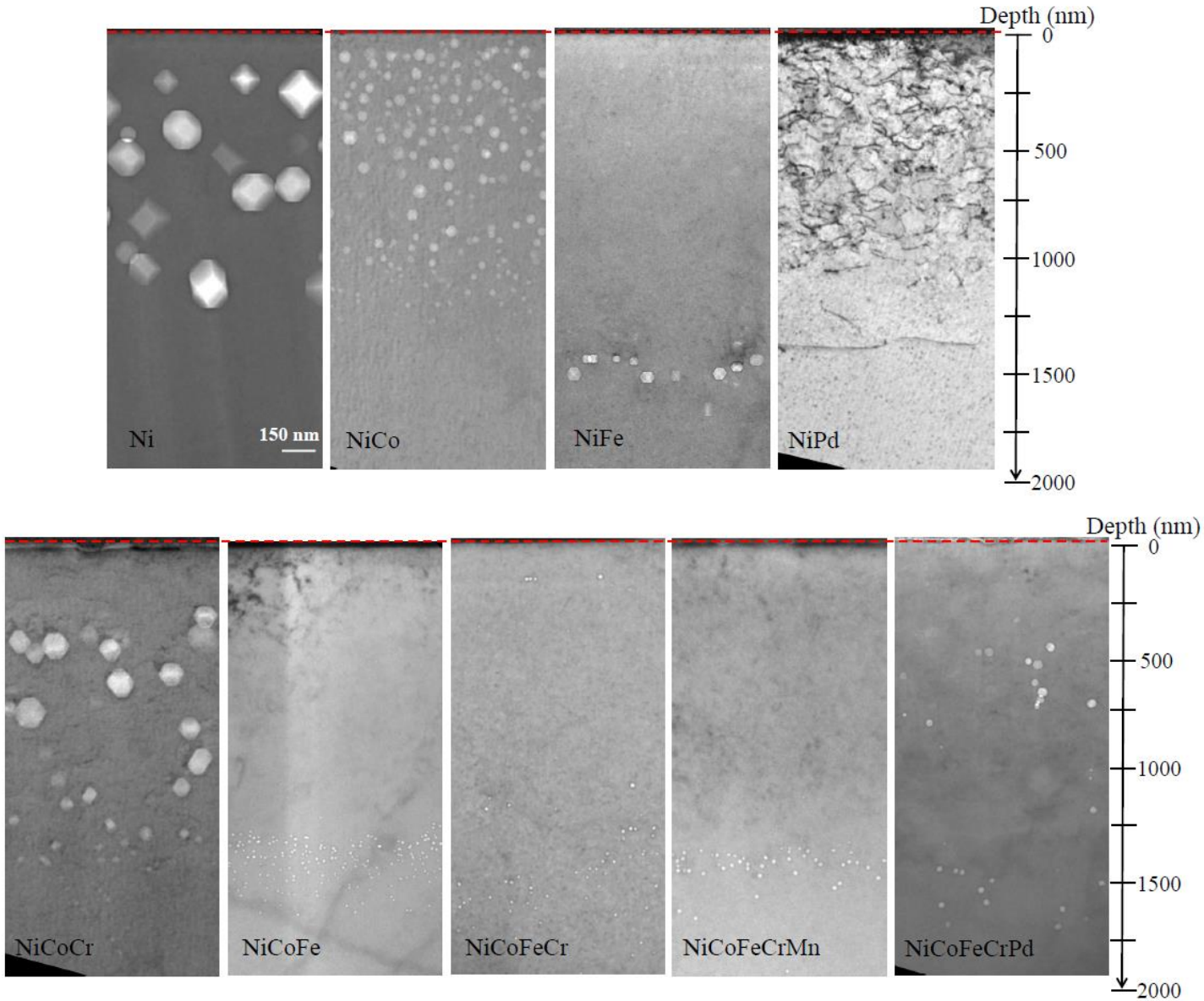

Figure 4.2 Summary of void swelling in Ni SP-CSAs irradiated using 3 MeV Ni^{2+} ions at 500℃ to a peak dose of ~60 dpa.

Table 4.1 Summary of defect results in equiatomic Ni SP-CSAs irradiated using 3 MeV Ni^{2+} at 500℃ to a peak dose of ~60 dpa.

Materials (at %)	Average void diameter (nm)	Void number density (10^{20} m^{-3})	Total Swelling (%)	Area examined (μm^2)	Average dislocation loop size (nm)	Dislocation loop number density (10^{20} m^{-3})	Area examined (μm^2)
Ni	131.6±4.0	0.60±0.06	12.59±2.26	6.8	N.M.	N.M.	N.M.
NiCo	32.7±1.3	11.93±1.2	3.60±0.67	3.5	N.M.	N.M.	N.M.
NiFe	44.9±1.4	0.54±0.05	0.38±0.07	3.6	53.0±2.1	7.9±0.8	0.60
NiPd	---	---	---	3.0	34.0±1.3	14.69±1.5	0.61
NiCoFe	9.0±0.9	9.70±0.97	0.041±0.015	3.3	25.9±1.0	24.5±2.5	0.61
NiCoCr	67.2±2.0	2.03±0.2	7.01±1.19	13.7	N.M.	N.M.	N.M.
NiCoFeCr	9.0±0.9	3.29±0.3	0.016±0.005	2.9	30.4±1.2	17.6±1.8	0.60
NiCoFeCrMn	14.4±1.1	3.84±0.4	0.072±0.02	4.0	18.9±1.1	28.2±2.8	0.52
NiCoFeCrPd	24.2±1.5	0.98±0.1	0.10±0.017	12.9	N.M.	N.M.	N.M.

*Dislocation loops were counted at 400-600 nm depth from the surface.
*N.M. represents the data was not mea

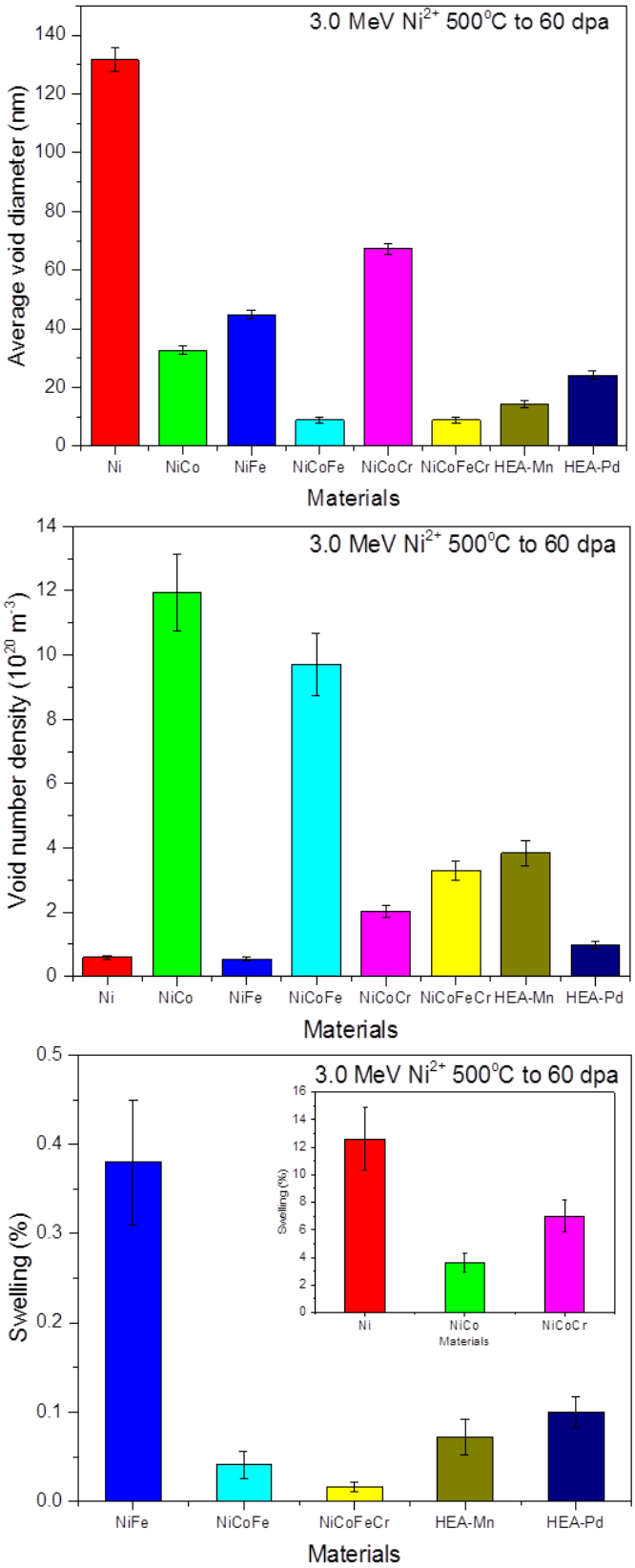

Figure 4.3 (a) Average void diameter, (b) number density, (c) swelling in Ni containing, equiatomic SP-CSAs.

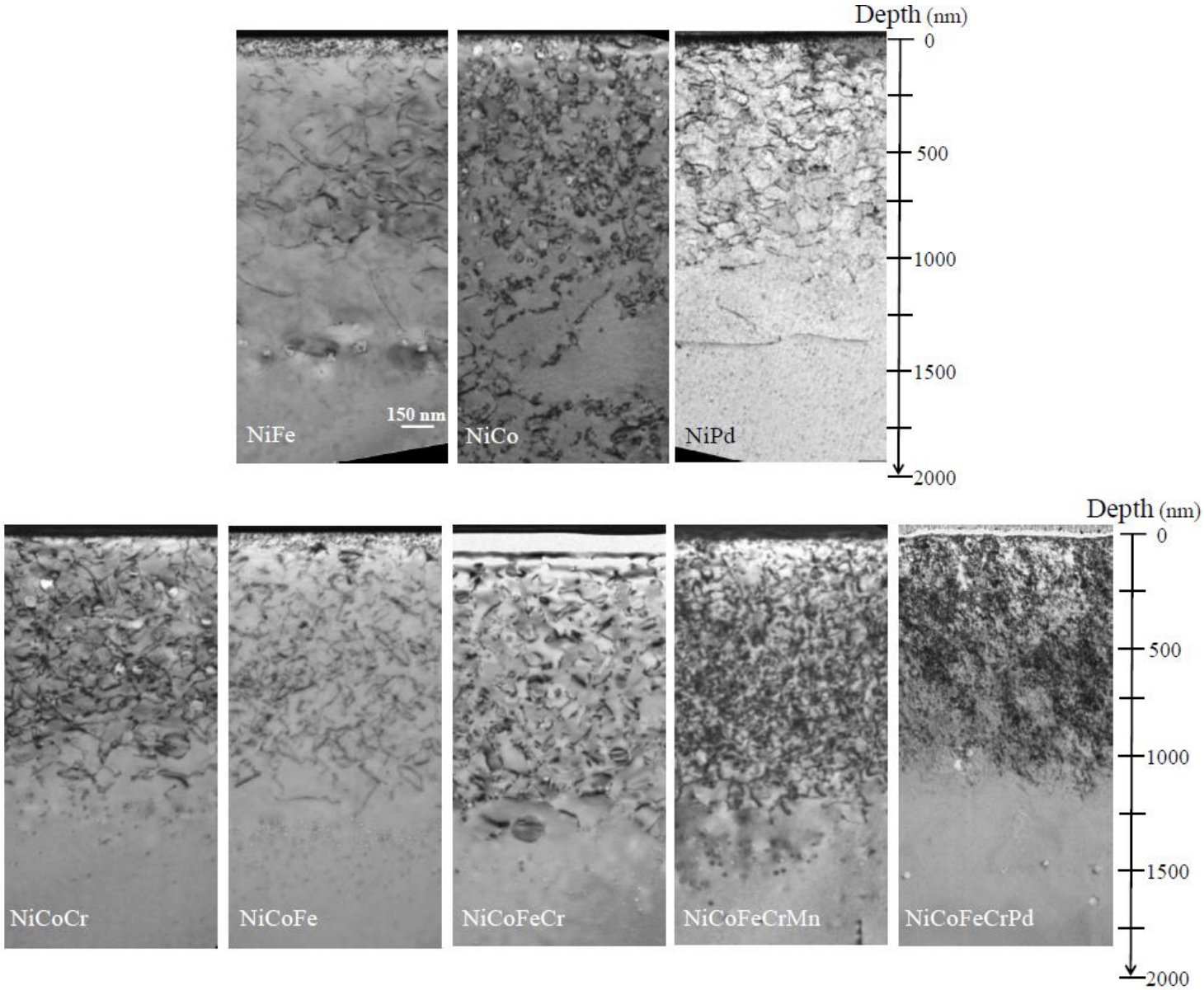

Figure 4.4 Summary of dislocation loops in Ni containing SP-CSAs irradiated using 3 MeV Ni^{2+} ions at 500℃ to ~60 dpa.

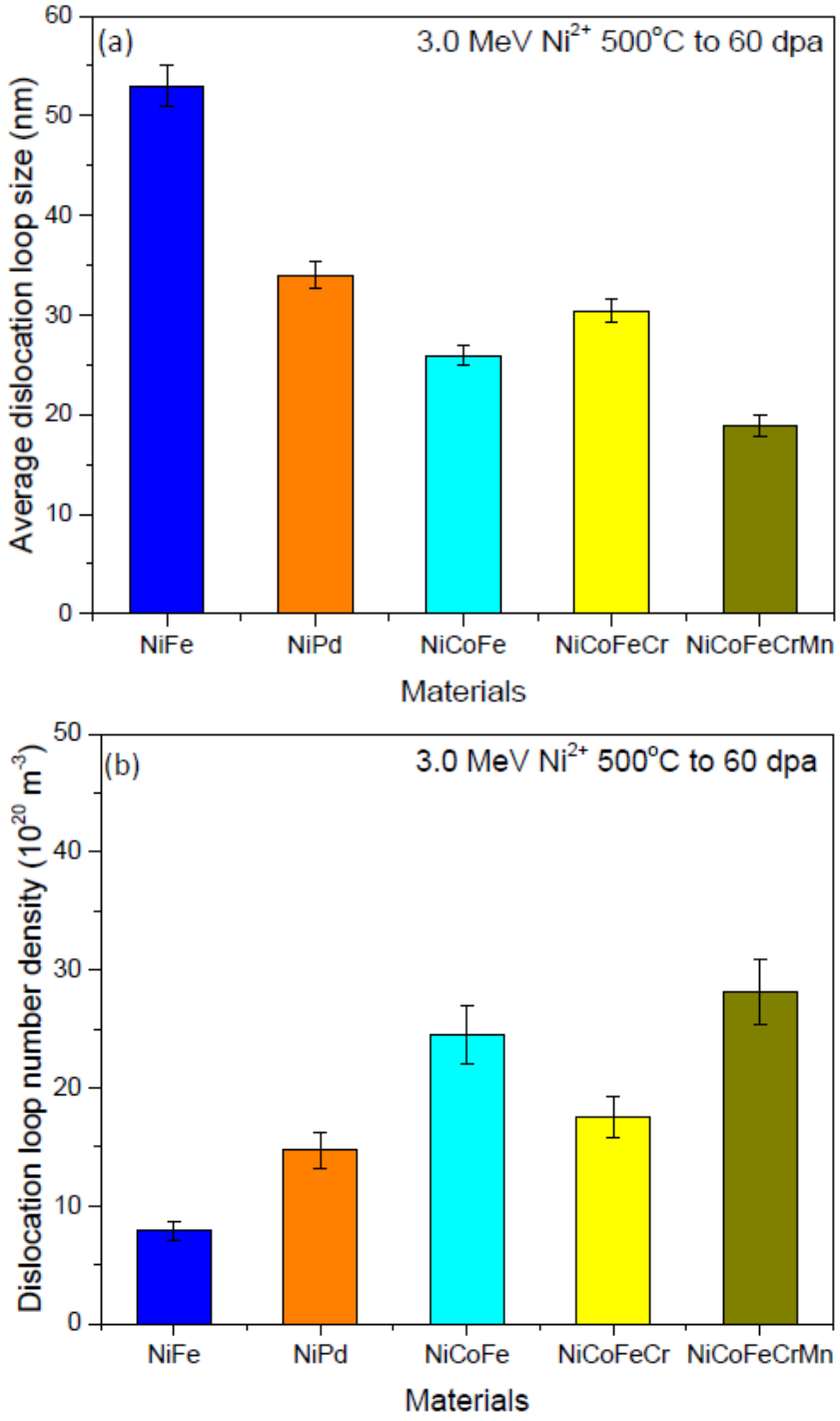

Figure 4.5 (a) Average dislocation loop size, (b) number density in Ni containing, equiatomic SP-CSAs.

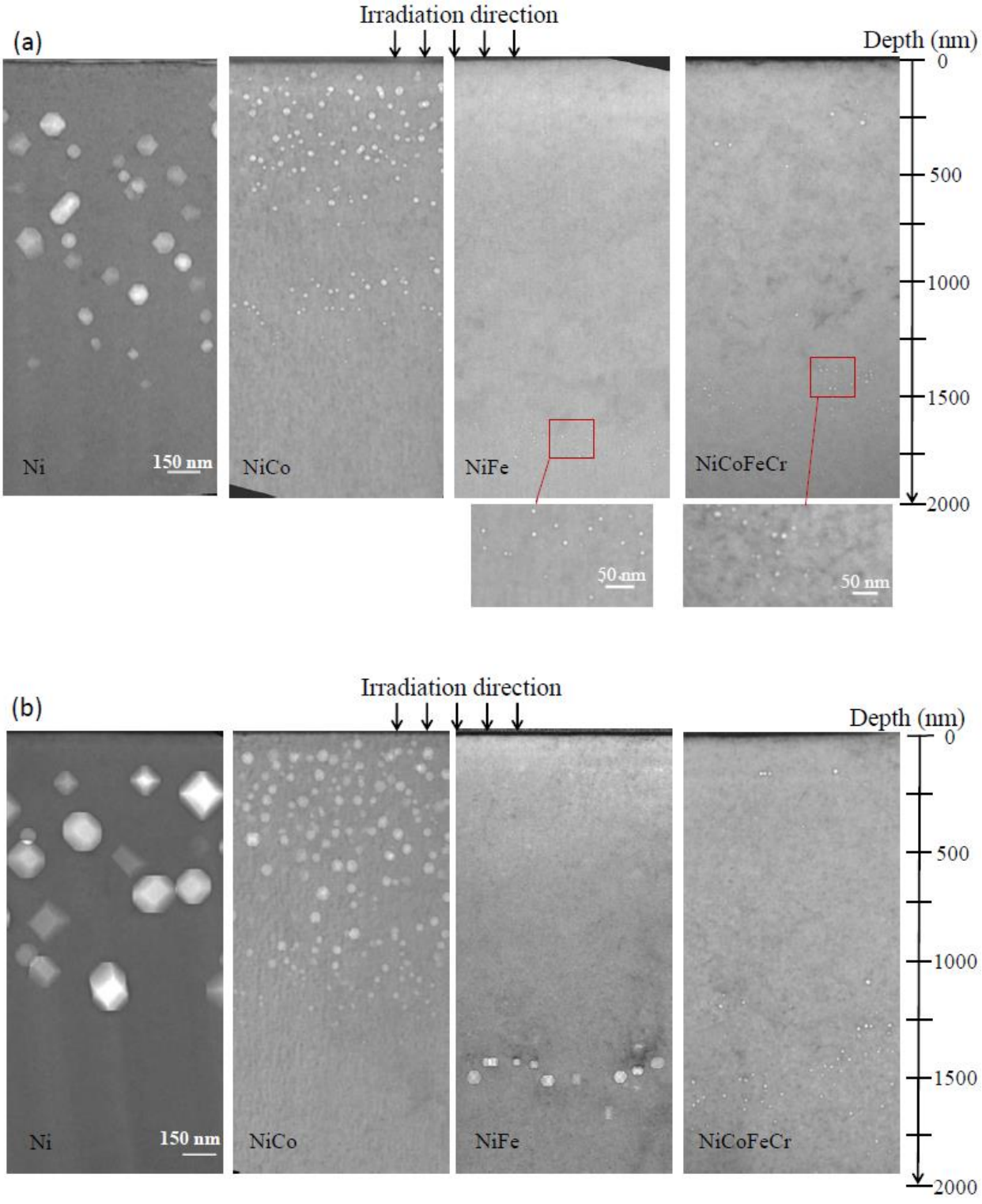

Figure 4.6 Void swelling in Ni containing SP-CSAs irradiated using 3 MeV Ni^{2+} ions at 500℃ to a peak dose of (a) 17 and (b) 60 dpa [84].

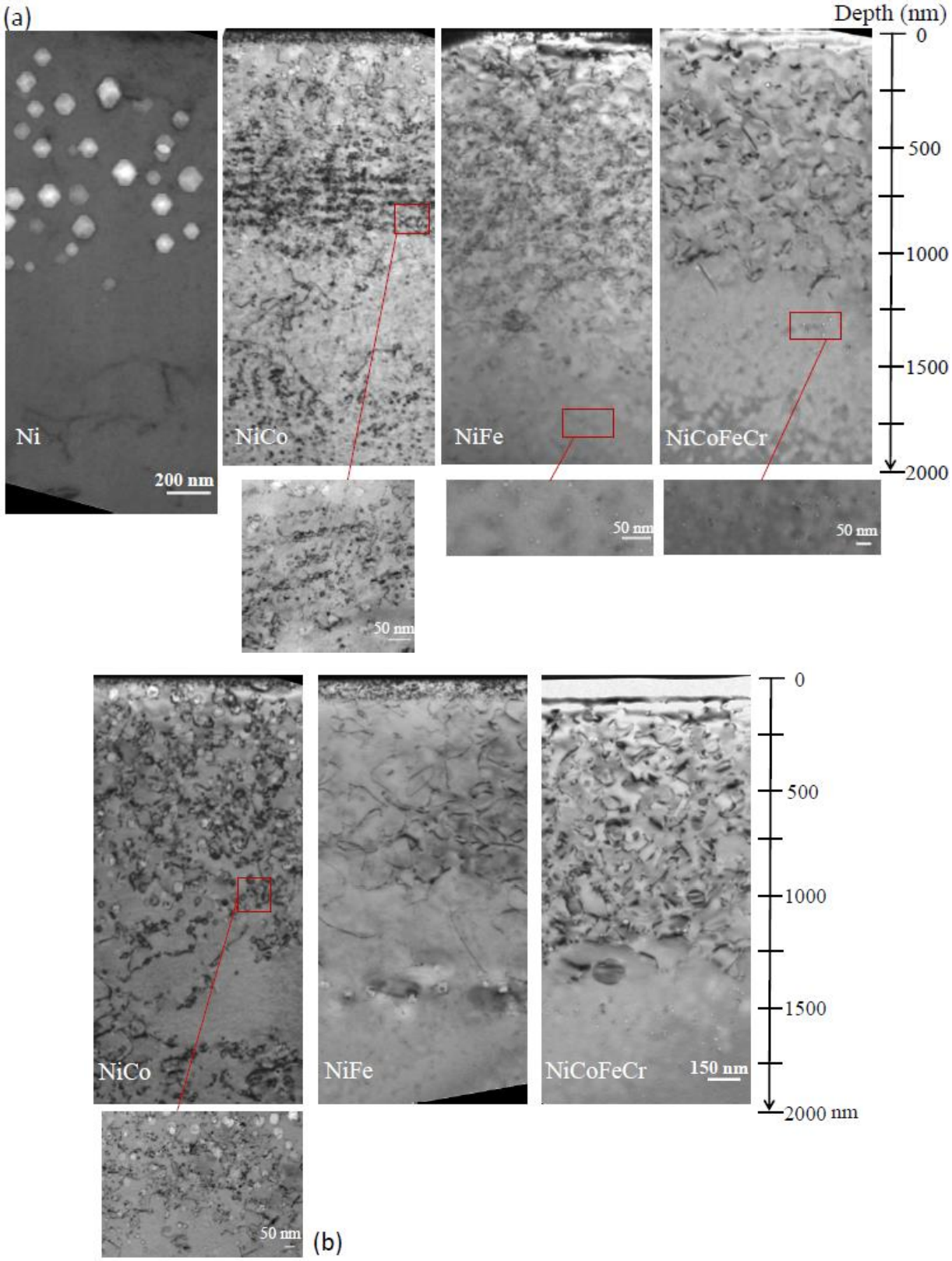

Figure 4.7 Dislocation loop features in Ni containing SP-CSAs irradiated using 3 MeV Ni^{2+} ions at 500℃ to a peak dose of (a) 17 and (b) 60 dpa [84].

Table 4.2 Summary of dose dependent defect results in equiatomic SP-CSAs irradiated using 3 MeV Ni^{2+} at 500℃.

Material	Peak dose (dpa)	Average void diameter (nm)	Void density ($10^{20}m^{-3}$)	Swelling (%)	Area examined (μm^2)	Average dislocation loop size (nm)	Number density ($10^{20}m^{-3}$)	Area examined (μm^2)
Ni	17	76.1±2.3	1.28±0.13	4.64±0.84	3.3	N.M.	N.M.	---
NiCo	17	21.9±1.0	7.21±0.72	0.55±0.11	3.3	N.M.	N.M.	---
NiFe	17	6.7±1.0	4.03±0.40	0.0084±0.0046	3.6	20.5±1.0	19.4±2.0	0.54
NiCoFeCr	17	8.2±1.0	3.37±0.34	0.0138±0.0047	2.1	26.8±1.2	13.9±1.4	0.57
Ni	60	131.6±4.0	0.60 ± 0.06	12.59±2.26	6.8	N.M.	N.M.	---
NiCo	60	32.7±1.3	11.93±1.2	3.60±0.67	3.5	N.M.	N.M.	---
NiFe	60	44.9±1.4	0.54±0.05	0.38±0.07	3.6	53.0±2.1	7.9±0.8	0.60
NiCoFeCr	60	9.0±1.0	3.29±0.3	0.016±0.005	2.9	30.4±1.2	17.6±1.8	0.60

*Dislocation loops were counted at 400-600 nm depth from the surface.
*N.M. represents the data was not measured.

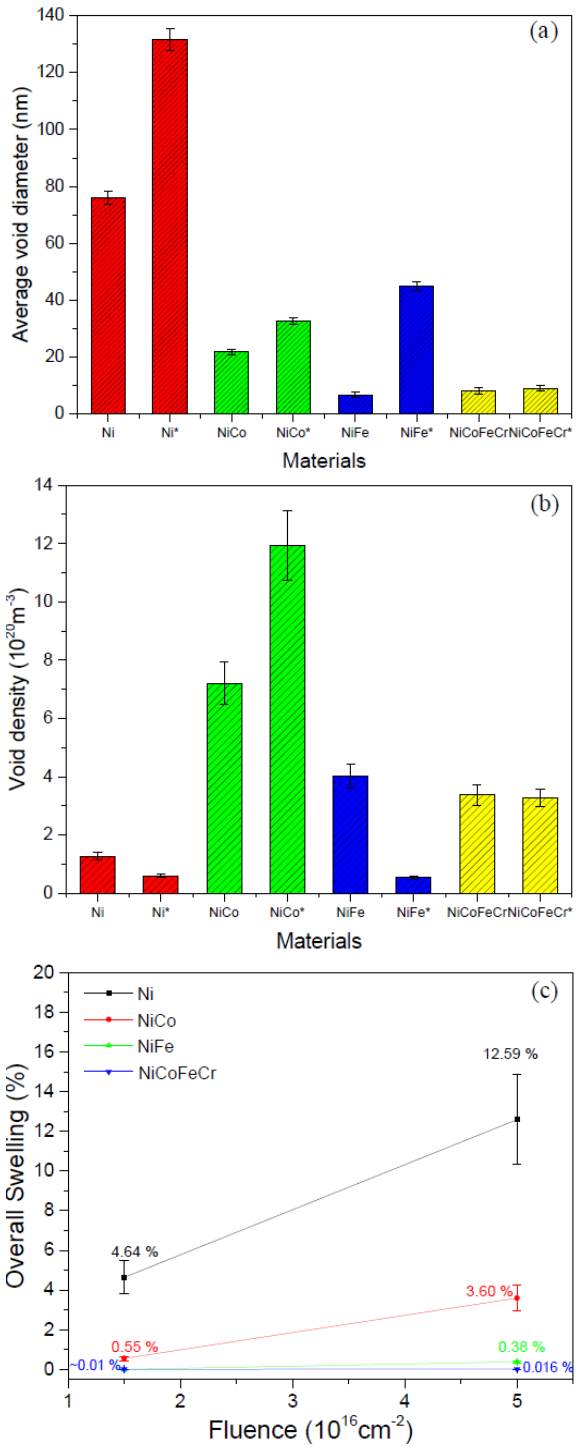

Figure 4.8 Dose dependent result of (a) Average void diameter, (b) number density, (c) swelling in Ni containing equiatomic SP-CSAs [84]. The alloy with asterisk mark was irradiated to a peak dose of 60 dpa while the one without was irradiated to a peak dose of 17 dpa.

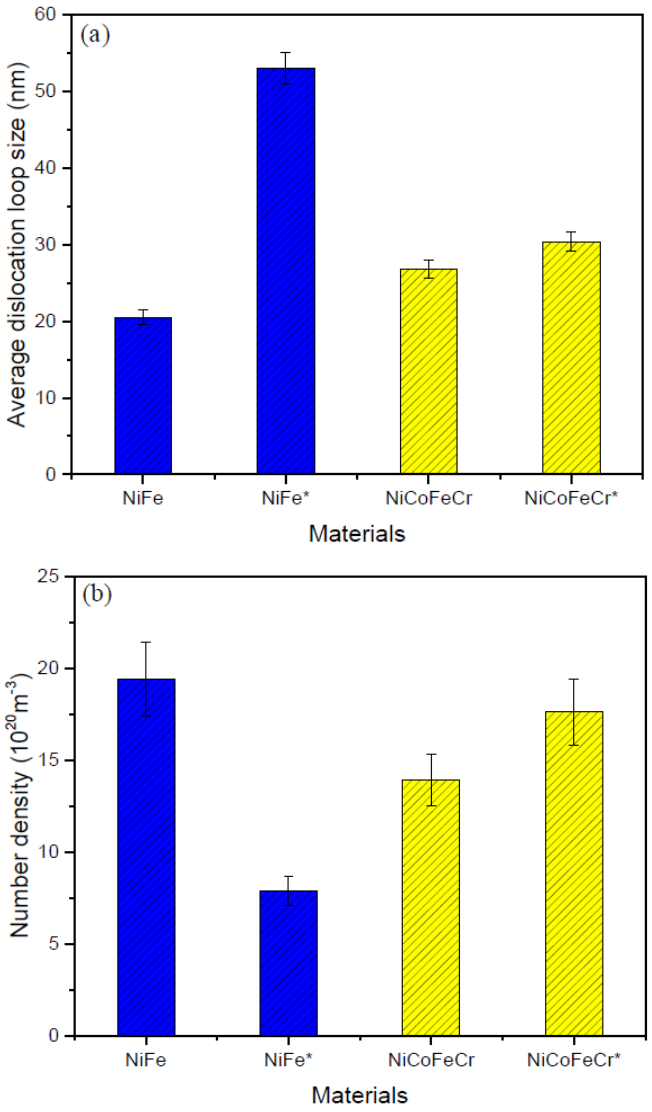

Figure 4.9 Dose dependent result of (a) Average dislocation loop size, (b) number density in Ni containing equiatomic SP-CSAs. The alloy with asterisk mark was irradiated to a peak dose of 60 dpa while the one without was irradiated to a peak dose of 17 dpa.

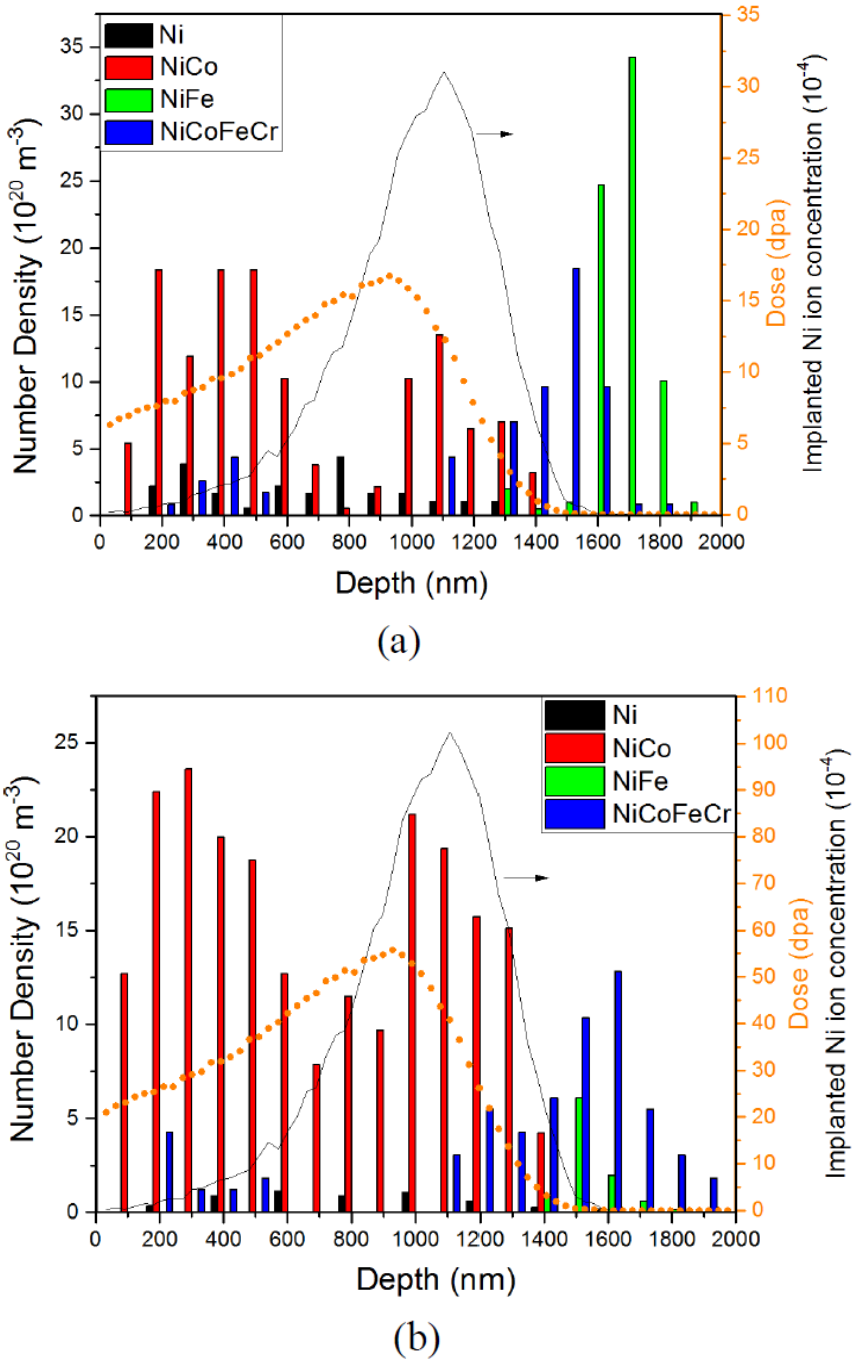

Figure 4.10 Depth distribution for void number density is overlaid on the damage dose (orange dotted line) and implanted ion concentration (black smooth line) for 3 MeV Ni^{2+} irradiation in Ni and Ni-containing equiatomic alloys to (a) 17 dpa and (b) 60 dpa [84].

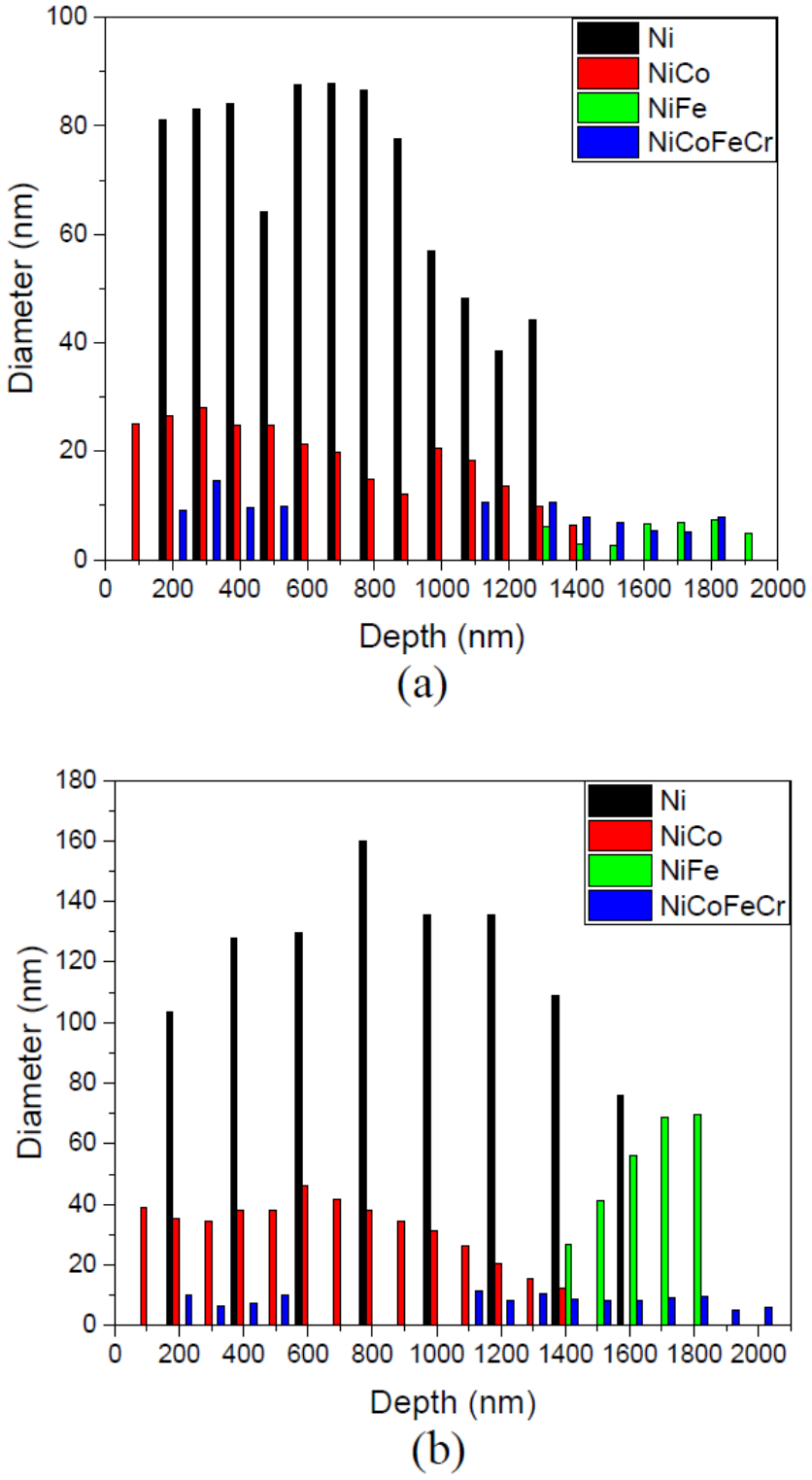

Figure 4.11 Depth distribution for average void diameter using 3 MeV Ni^{2+} irradiation in Ni and Ni-containing equiatomic alloys to (a) 17 dpa and (b) 60 dpa [84].

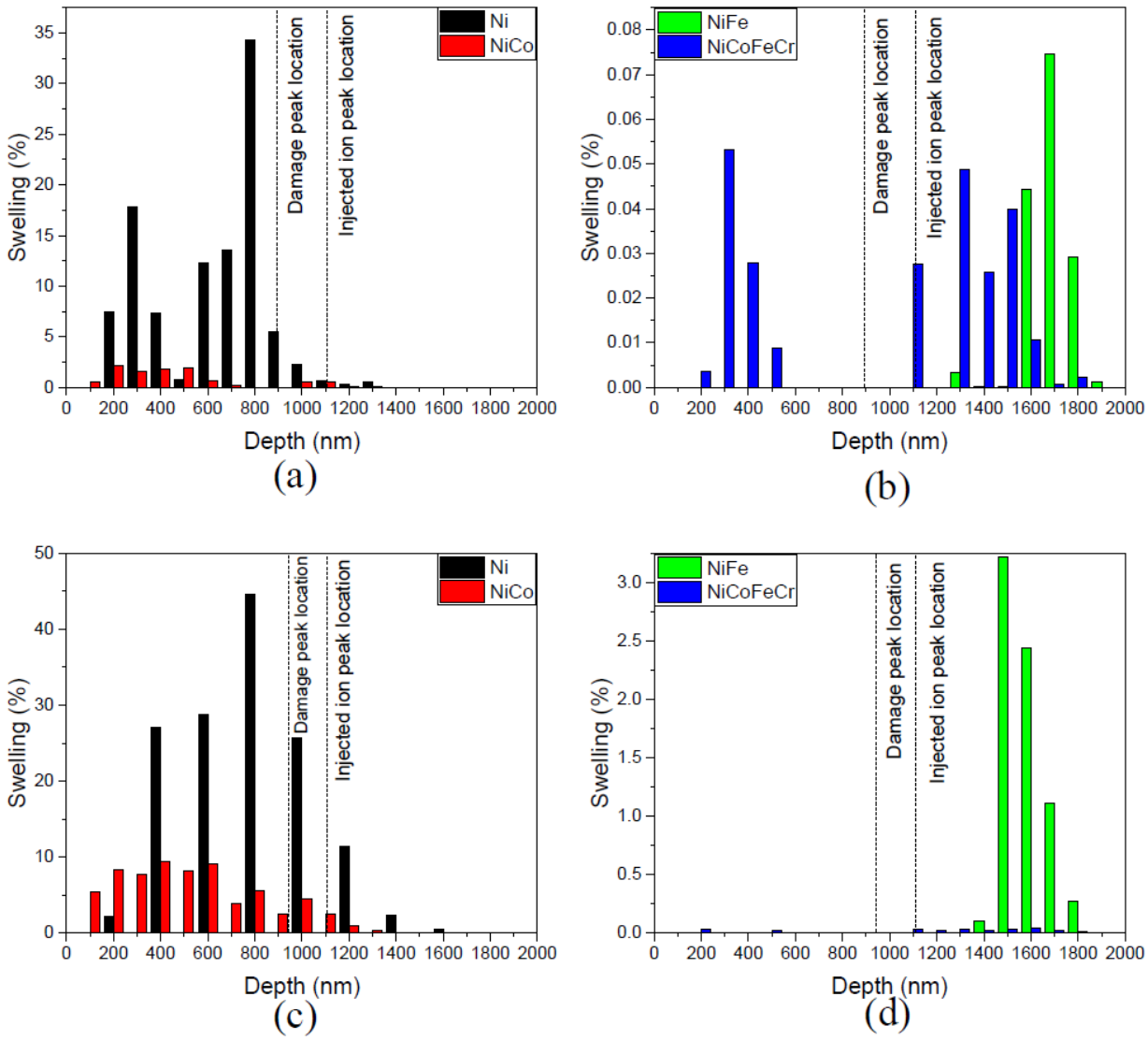

Figure 4.12 Depth distribution for swelling on 17 dpa (a) Ni and NiCo (b) NiFe and NiFeCoCr; and 60 dpa (c) Ni and NiCo (d) NiFe and NiFeCoCr [84].

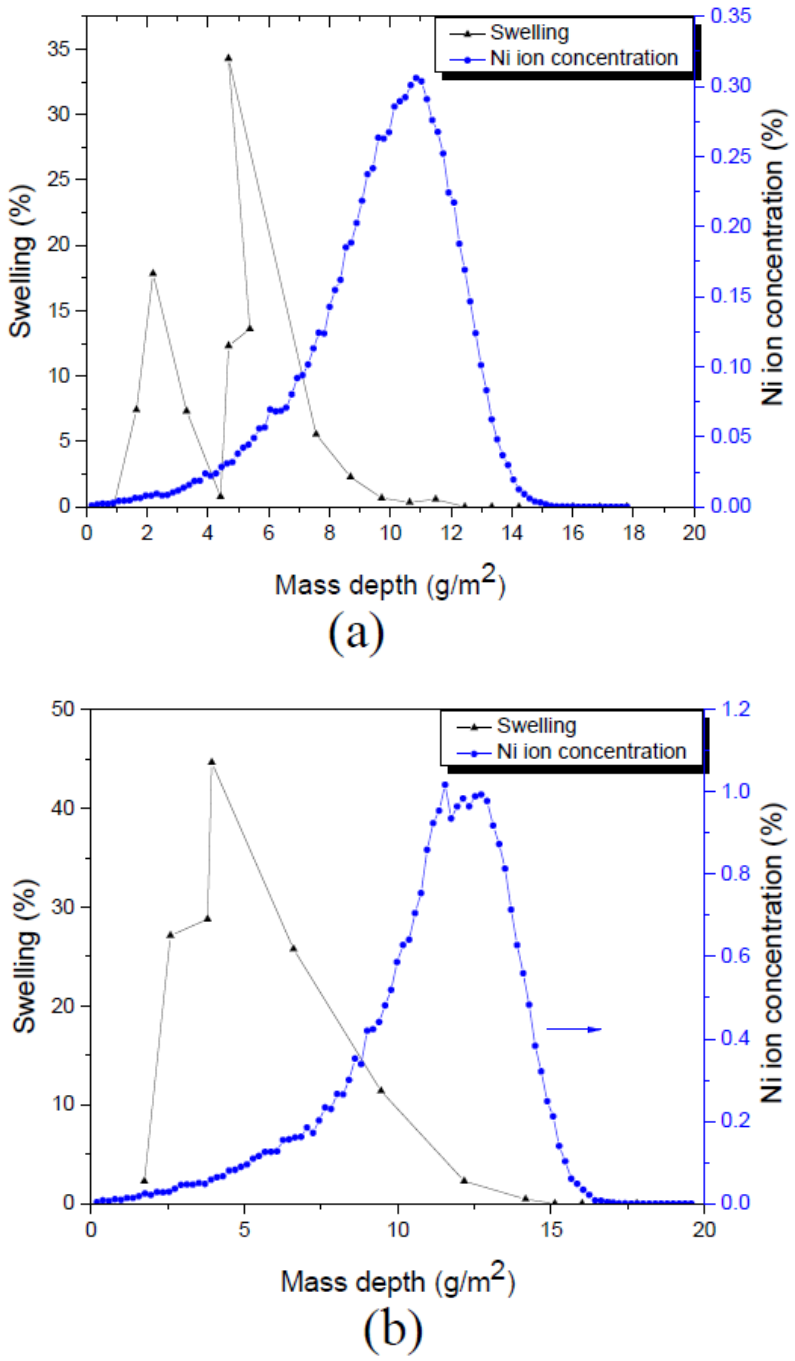

Figure 4.13 Swelling profile and modified Ni ion concentration for Ni as a function of mass depth irradiated to (a) 17 dpa and (b) 60 dpa [84].

Table 4.3 Summary of melting temperature of Ni-based SP-CSAs and its corresponding homologous temperatures.

Materials (at %)	Melting temperature (K)	$0.41T_m$ (℃)	$0.45T_m$ (℃)	$0.5T_m$ (℃)	$0.55T_m$ (℃)	$0.61T_m$ (℃)
Ni	1728	435.5	504.6		677.4	
NiCoCr	1690	419.9	487.5	572.0		
NiCoFeCr	1695	422.0	489.8	574.5		
NiCoFeCrMn	1553		425.9	503.5	581.2	674.3
NiCoFeCrPd	1560		429.0	507.0	585.0	

[a] The irradiation temperatures of 420, 500 and 675 ℃ has been tested on Ni.
[b] The irradiation temperatures of 420, 500 and 580 ℃ has been tested on NiCoCr, NiCoFeCr, NiCoFeCrMn and NiCoFeCrPd.

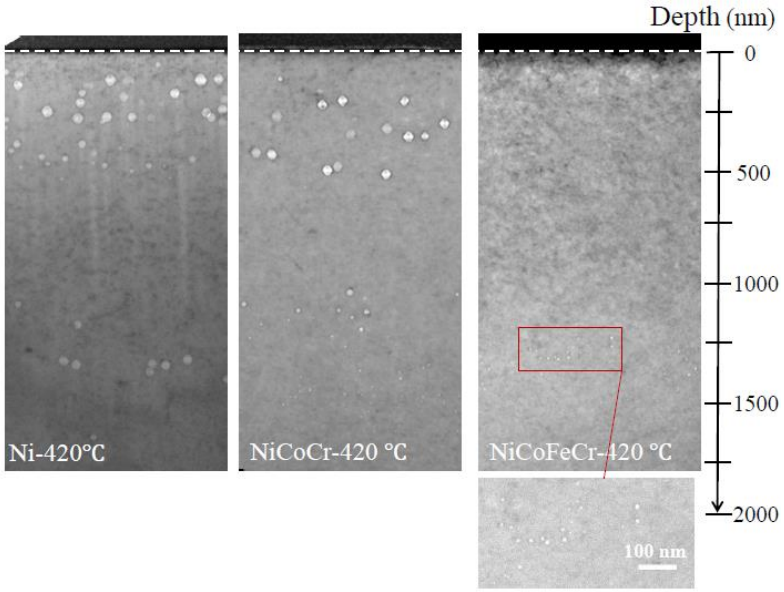

Figure 4.14 Void swelling in Ni, NiCoCr and NiCoFeCr irradiated using 3 MeV Ni^{2+} ions at $0.41T_m$ (420°C) to a peak dose of 60 dpa.

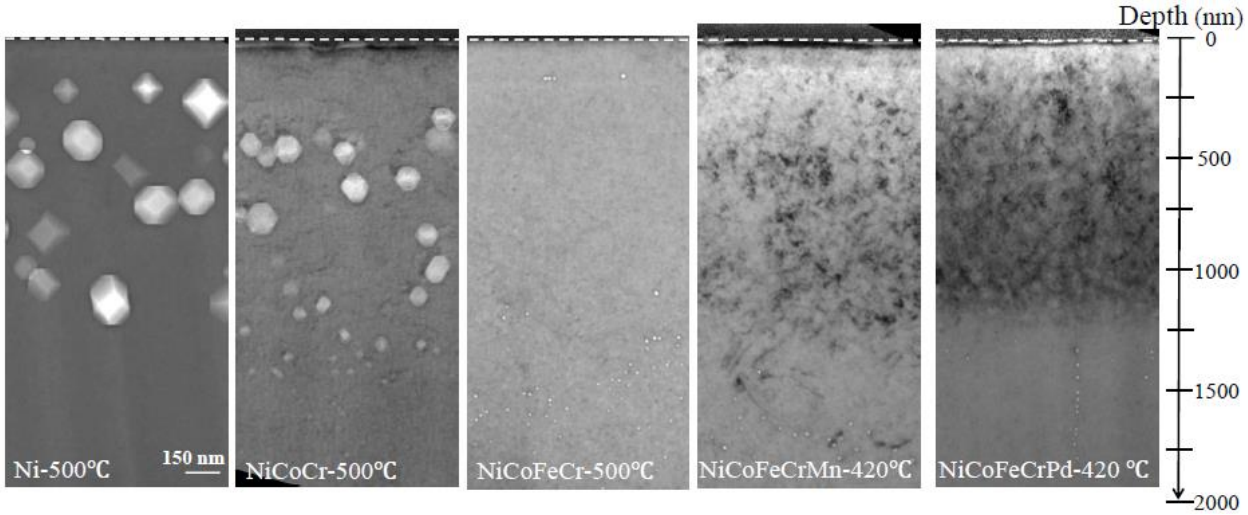

Figure 4.15 Void swelling in Ni, NiCoCr, NiCoFeCr, NiCoFeCrMn and NiCoFeCrPd irradiated using 3 MeV Ni^{2+} ions at $0.45T_m$ to a peak dose of 60 dpa.

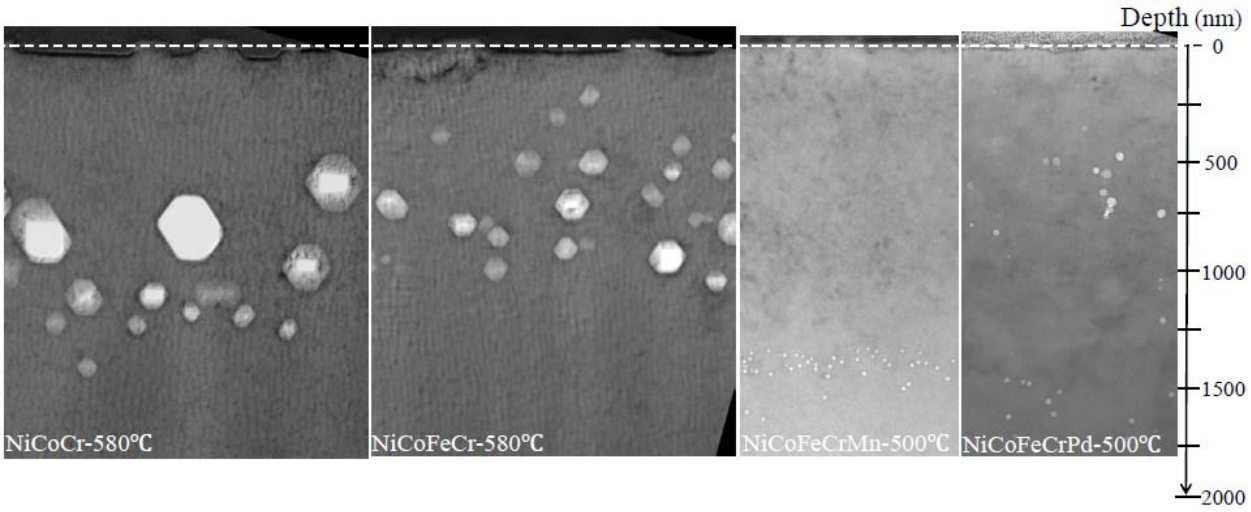

Figure 4.16 Void swelling in NiCoCr, NiCoFeCr, NiCoFeCrMn and NiCoFeCrPd irradiated using 3 MeV Ni^{2+} ions at $0.5T_m$ to a peak dose of 60 dpa.

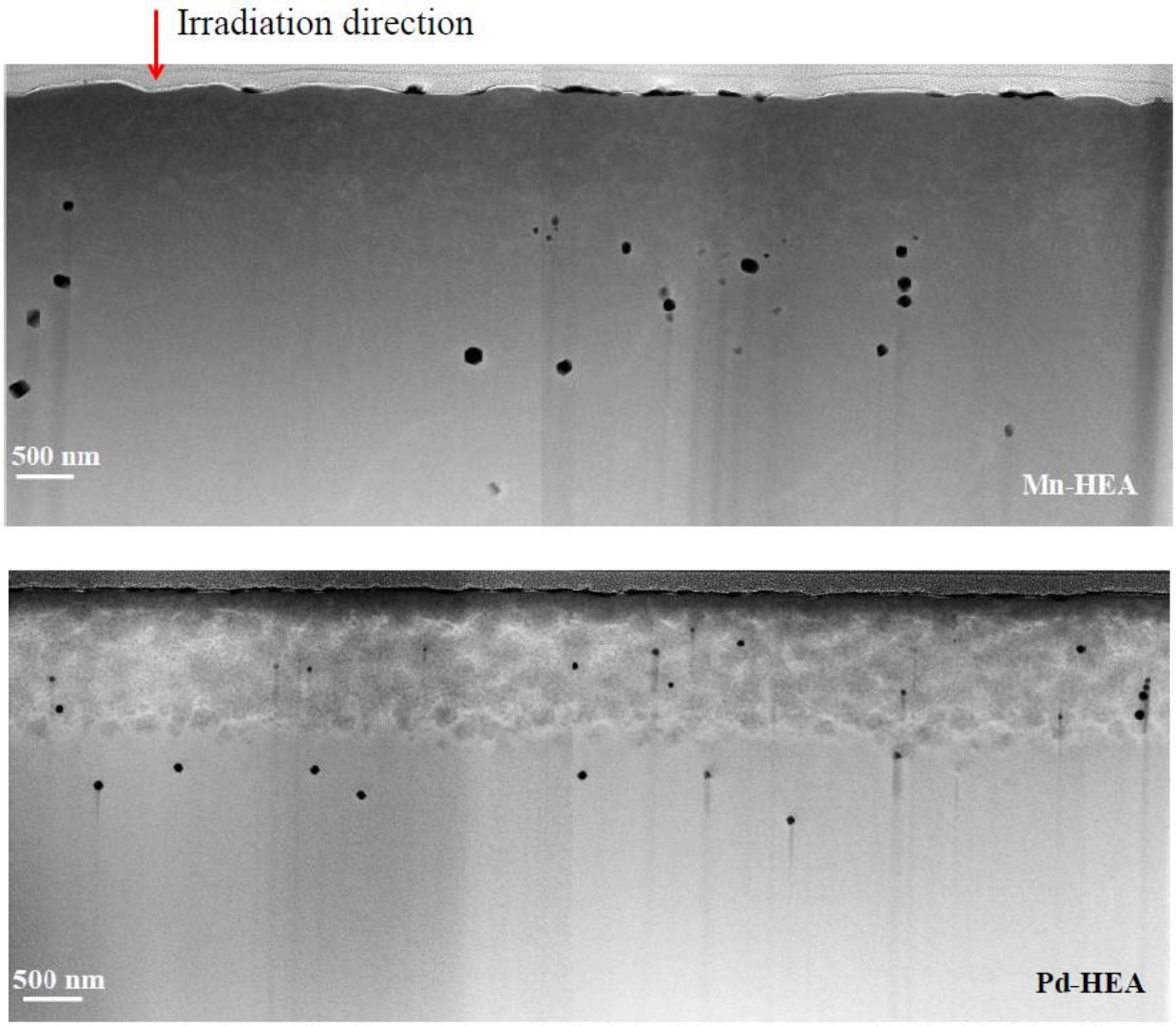

Figure 4.17 Void swelling in NiCoFeCrMn (Mn-HEA) and NiCoFeCrPd (Pd-HEA) irradiated using 3 MeV Ni^{2+} ions at 0.55Tm (580℃) to a peak dose of 60 dpa [17].

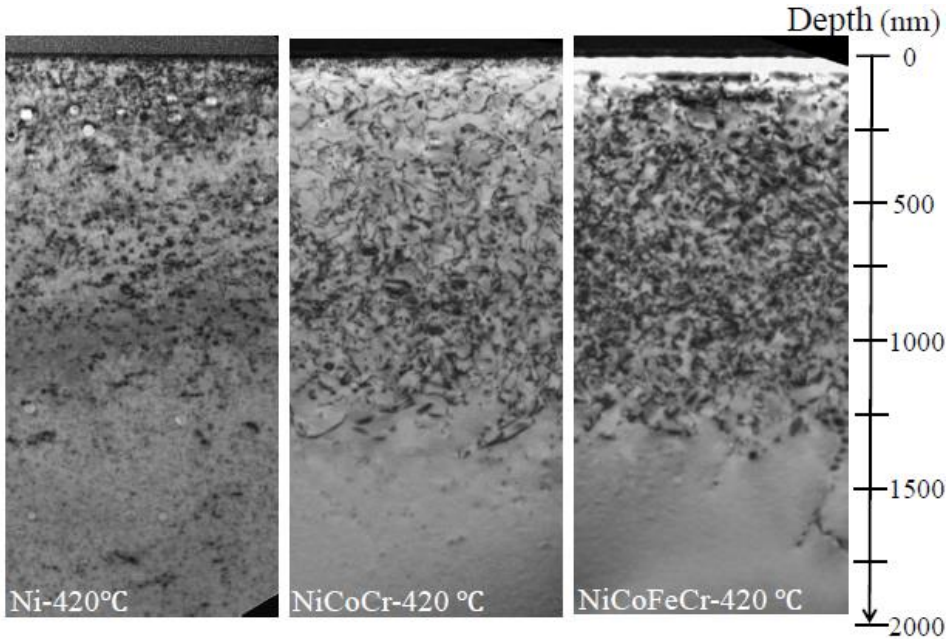

Figure 4.18 Distribution of dislocation loops in Ni, NiCoCr and NiCoFeCr irradiated using 3 MeV Ni^{2+} ions at $0.41T_m$ (420℃) to a peak dose of 60 dpa.

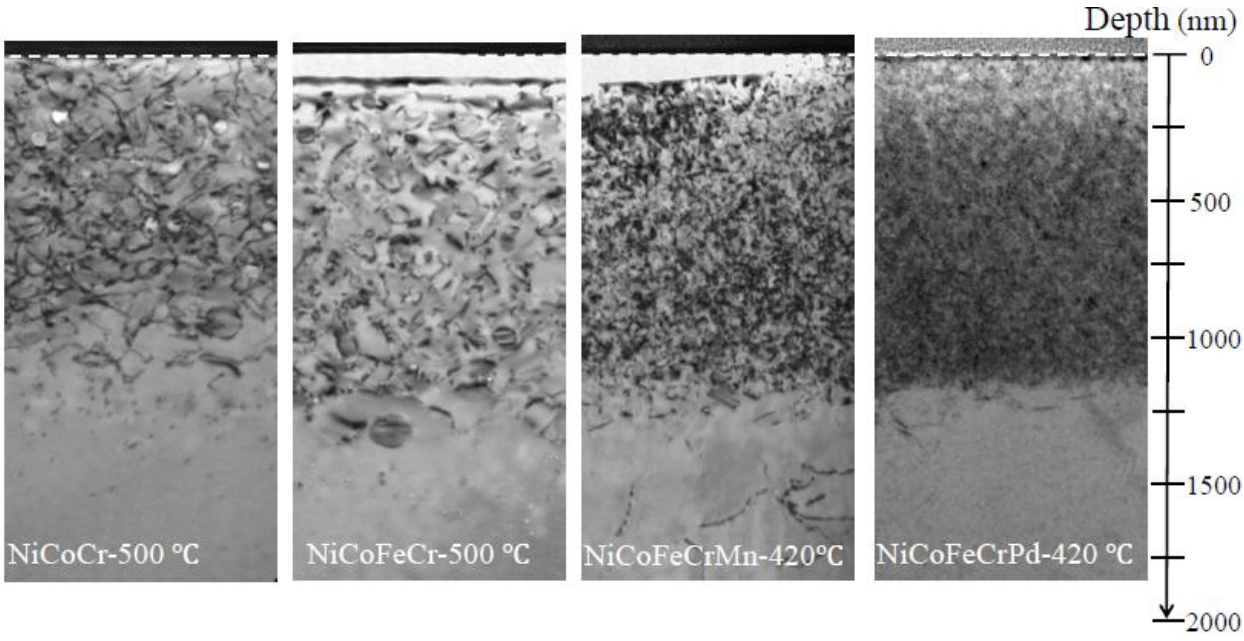

Figure 4.19 Distribution of dislocation loops in NiCoCr, NiCoFeCr, NiCoFeCrMn and NiCoFeCrPd irradiated using 3 MeV Ni^{2+} ions at $0.45T_m$ to a peak dose of 60 dpa.

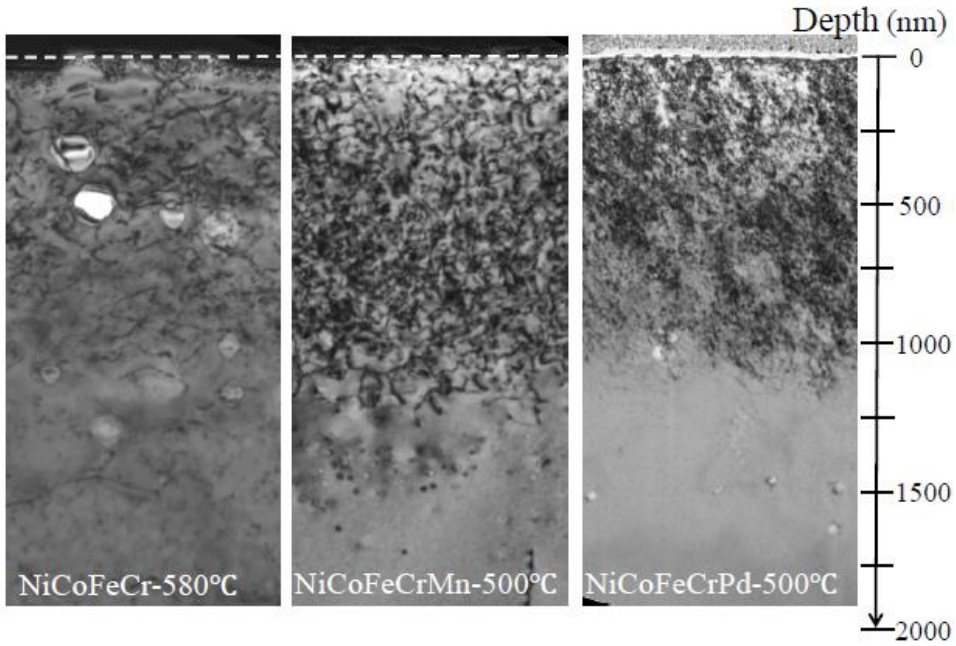

Figure 4.20 Distribution of dislocation loops in NiCoFeCr, NiCoFeCrMn and NiCoFeCrPd irradiated using 3 MeV Ni^{2+} ions at $0.5T_m$ to a peak dose of 60 dpa.

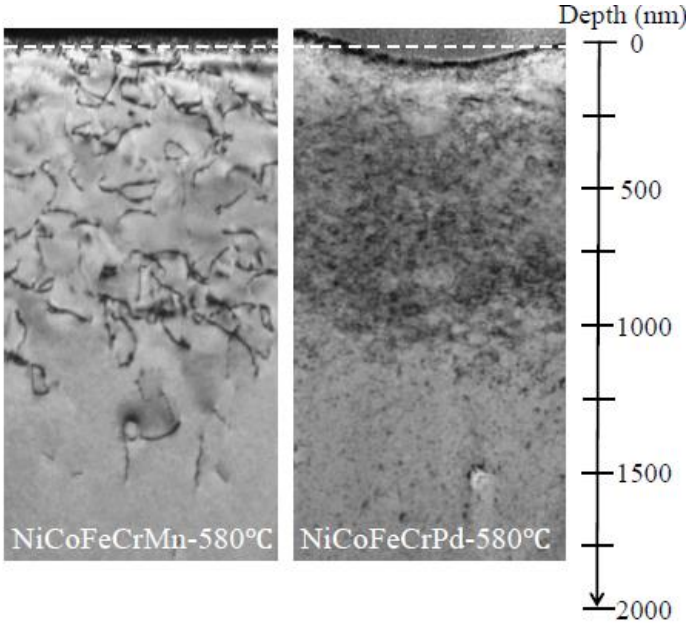

Figure 4.21 Distribution of dislocation loops in NiCoFeCrMn and NiCoFeCrPd irradiated using 3 MeV Ni^{2+} ions at $0.55T_m$ (580℃) to a peak dose of 60 dpa.

Table 4.4 Summary of void characterization results in equiatomic Ni SP-CSAs using homologous temperature, and irradiated using 3 MeV Ni^{2+} to a peak dose of ~60 dpa.

Homologous Temperature	Materials (at%)	Average void diameter (nm)	Void density ($10^{20}m^{-3}$)	Swelling (%)	Average dislocation loop size (nm)	Number density ($10^{20}m^{-3}$)
0.41 T_m	Ni	32.7±1.6	2.4±0.24	0.58±0.08	N.M.	N.M.
	NiCoCr	15.0±1.5	3.3±0.33	0.24±0.053	N.M.	N.M.
	NiCoFeCr	7.6±1.3	2.7±0.27	0.0075±0.003	17.1±1.0	61.5±6.2
0.45 T_m	Ni	131.6±4.0	0.60 ± 0.06	12.59±2.26	N.M.	N.M.
	NiCoCr	67.2±2.0	2.0±0.2	7.0±1.19	N.M.	N.M.
	NiCoFeCr	9.0±1.0	3.3±0.33	0.017±0.005	30.4±1.2	17.6±1.8
	NiCoFeCrMn	13.2±1.1	1.09±0.11	0.015±0.004	14.8±0.9	49.2±4.9
	NiCoFeCrPd	8.8±0.9	0.60±0.06	0.0026±0.001	N.M.	N.M.
0.50 T_m	NiCoCr	142.8±4.3	0.32±0.03	9.34±1.49	N.M.	N.M.
	NiCoFeCr	105.7±3.2	0.42±0.04	3.64±0.58	N.M.	N.M.
	NiCoFeCrMn	14.4±1.1	3.8±0.38	0.072±0.022	18.9±1.1	28.2±2.8
	NiCoFeCrPd	24.2±1.5	0.98±0.10	0.10±0.017	N.M.	N.M.
0.55 T_m	Ni	---	---	---	N.M.	N.M.
	NiCoFeCrMn	92.1±3.7	0.05±0.005	0.37±0.044	N.M.	N.M.
	NiCoFeCrPd	67.0±2.6	1.60±0.16	0.29±0.046	11.5±1.2	3.5±0.4
0.61 T_m	NiCoFeCrMn	---	---	---	N.M.	N.M.

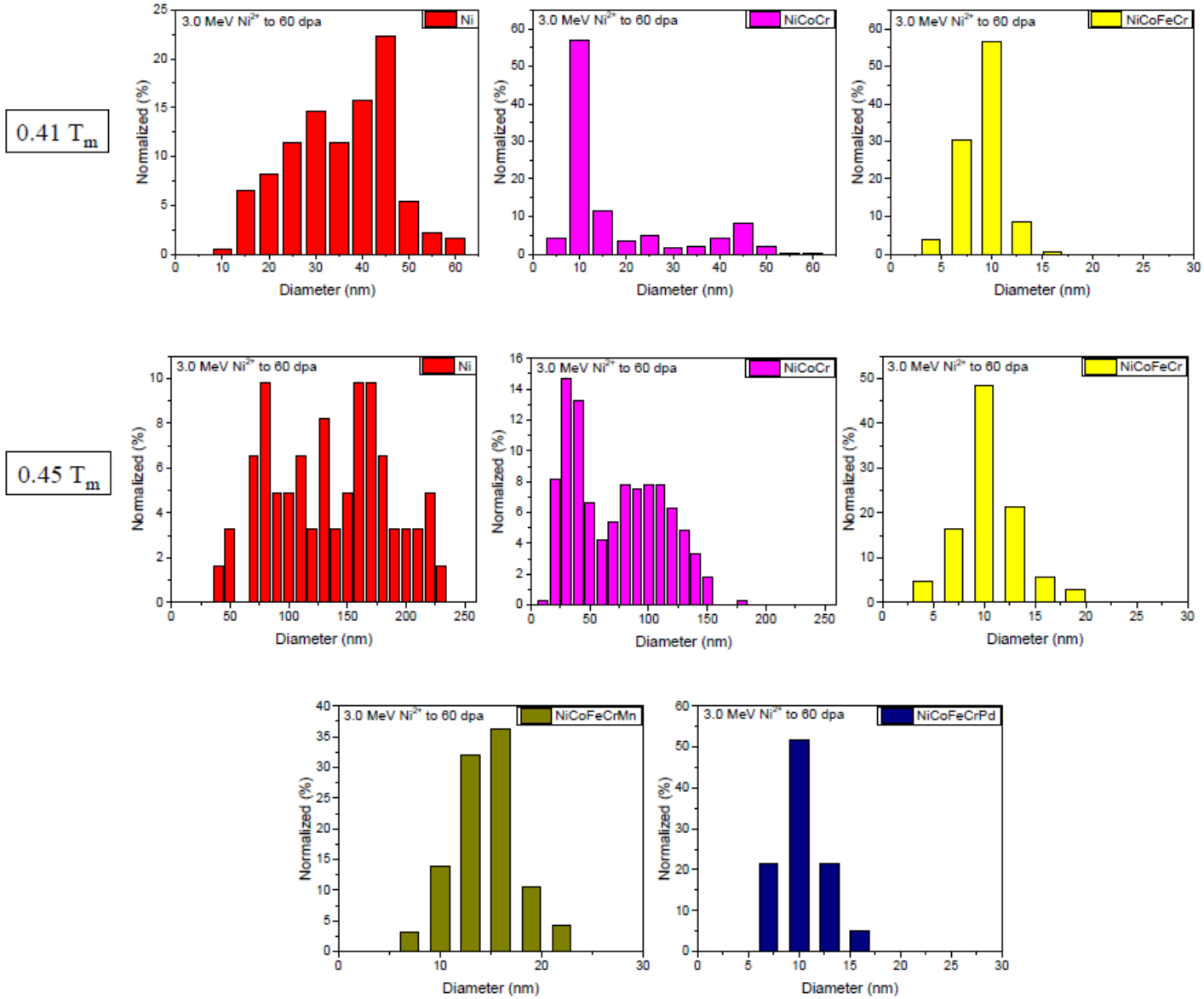

Figure 4.22 (a) Void distribution in Ni and Ni SP-CSAs irradiated to 60 dpa peak dose at 0.41 and 0.45 T_m of studied materials.

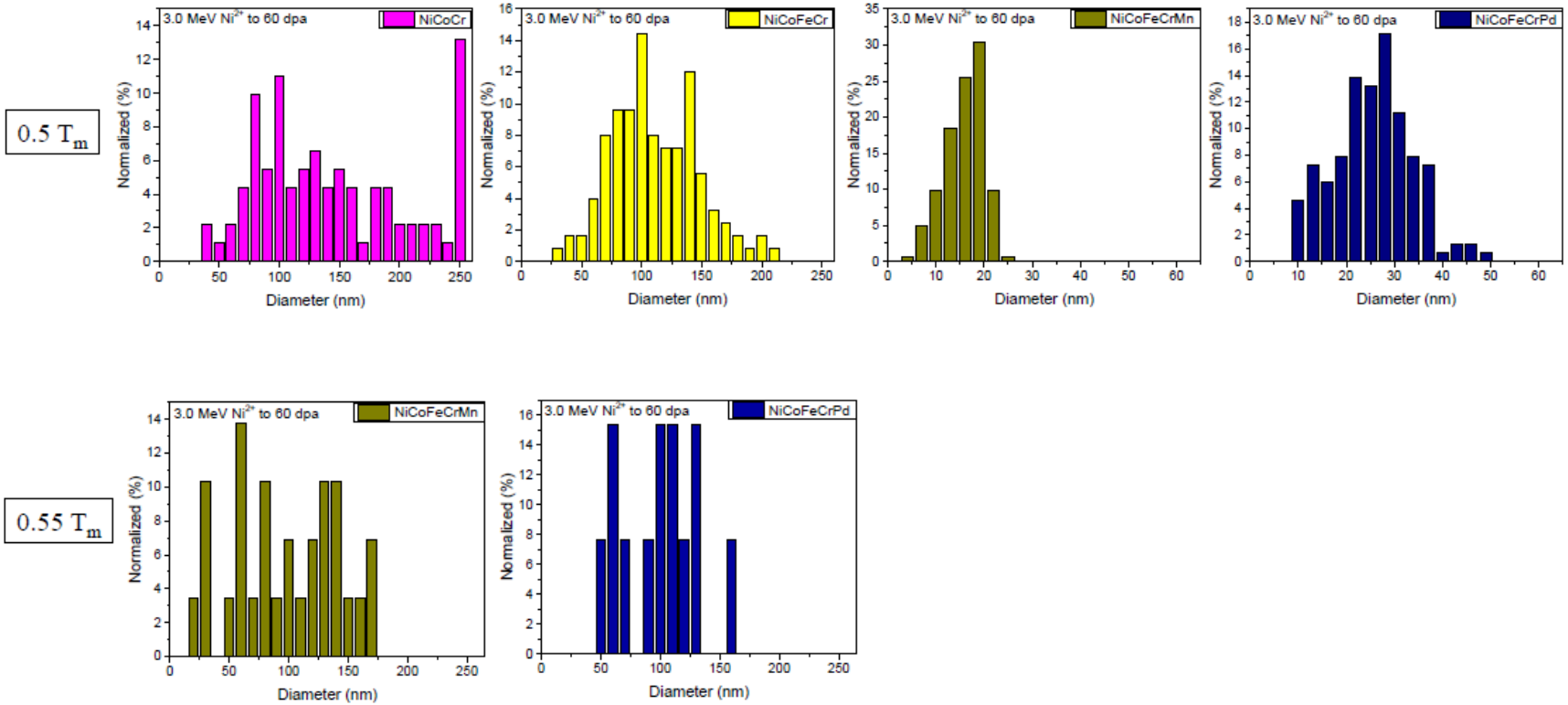

Figure 4.22 (b) Void distribution in Ni SP-CSAs irradiated to 60 dpa peak dose at 0.5 and 0.55 T_m of studied materials.

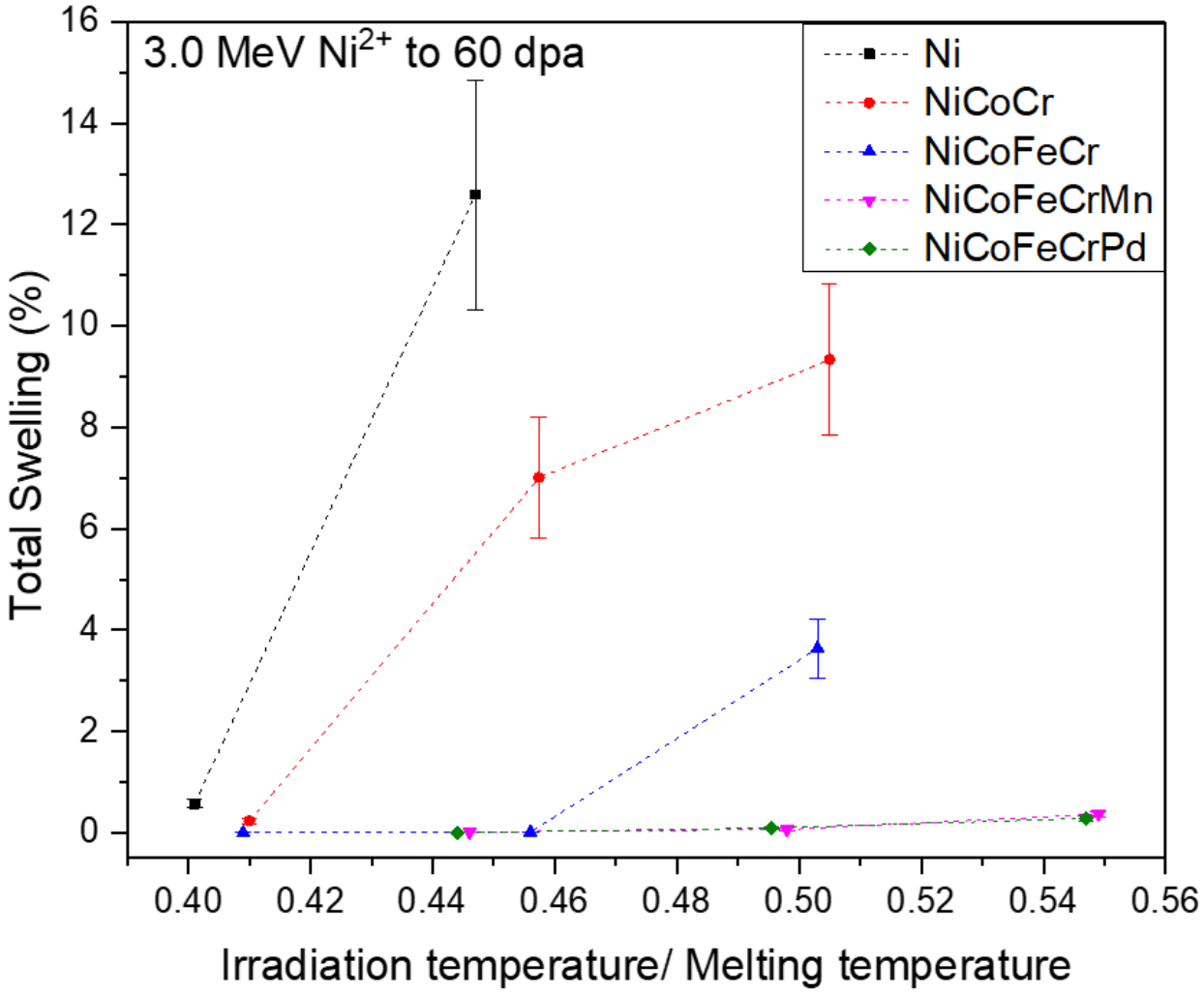

Figure 4.23 Temperature dependent total swelling of Ni, NiCoCr, NiCoFeCr, NiCoFeCrMn and NiCoFeCrPd irradiated to ~peak dose of 60 dpa.

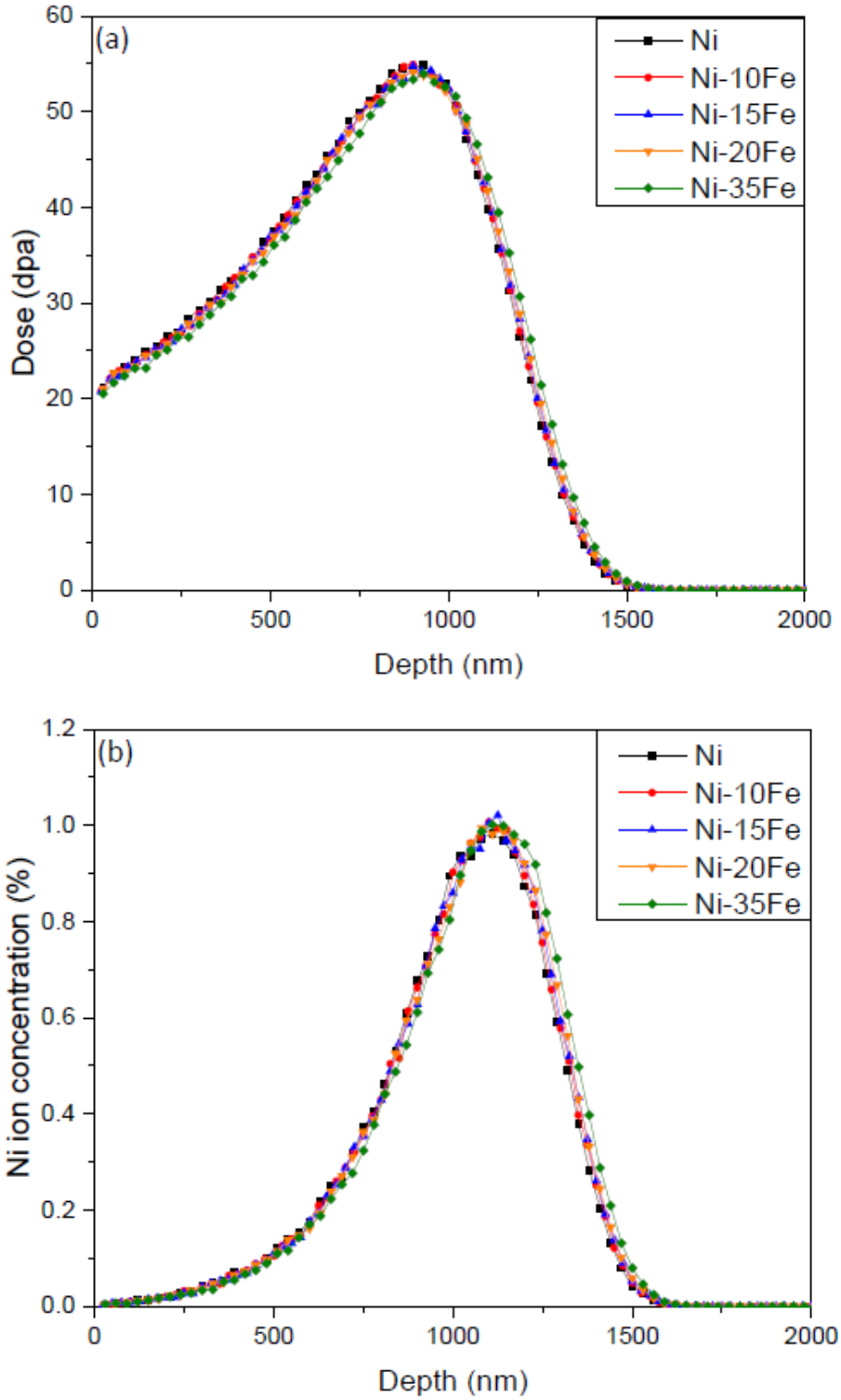

Figure 4.24 SRIM prediction profile of depth distribution of (a) displacement damage and (b) implanted ions for Ni-xFe using 3.0 MeV Ni^{2+} ions irradiated to 60 dpa.

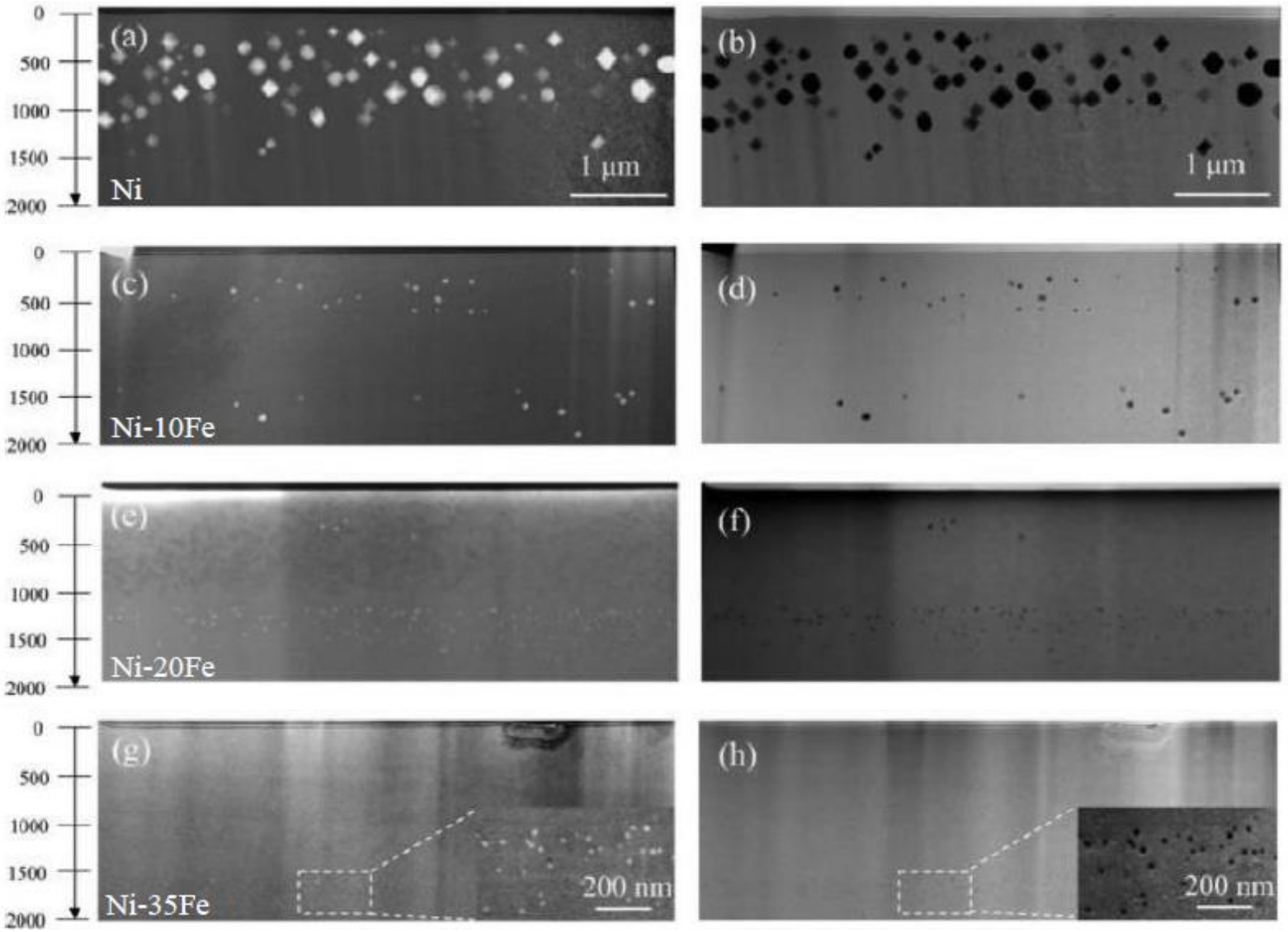

Figure 4.25 Cross-sectional STEM-BF (left) and HAADF (right) images showing void distributions in (a)(b) nickel, (c)(d) Ni-10Fe, (e)(f) Ni-20Fe and (g)(h) Ni-35Fe irradiated with 3.0 MeV Ni^{2+} ions to 60 dpa [89].

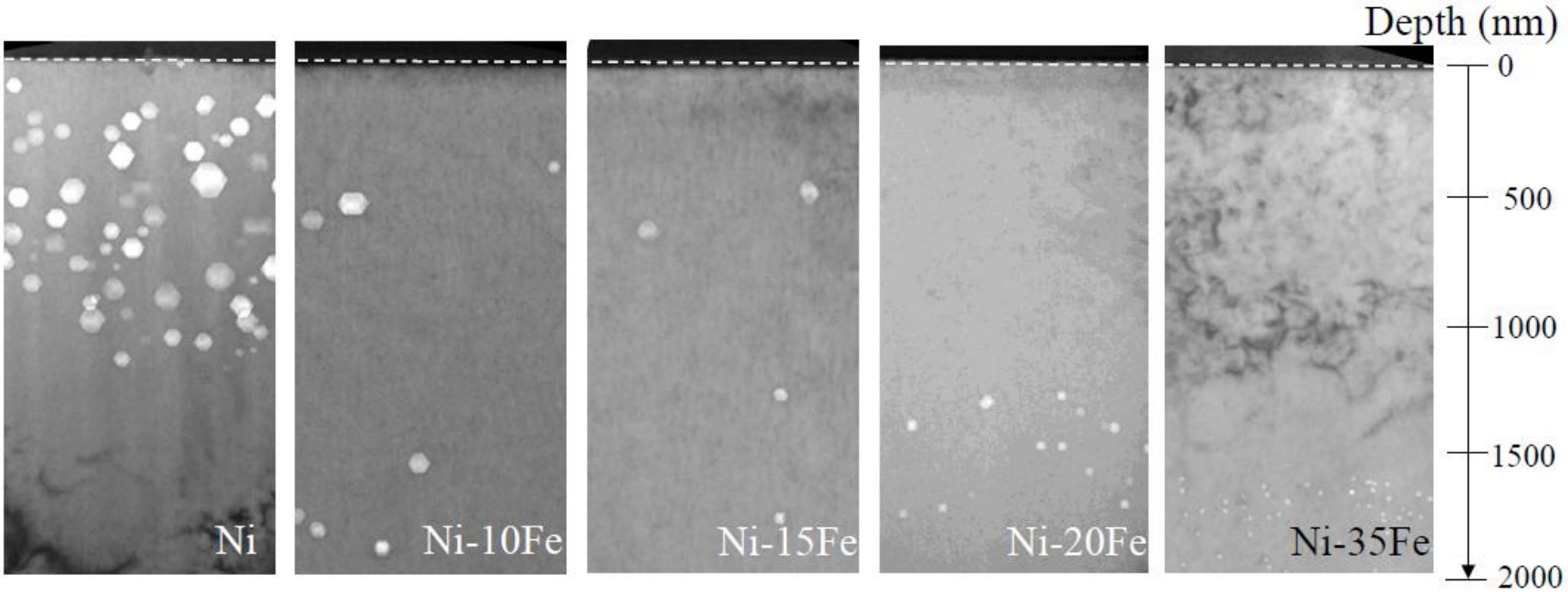

Figure 4.26 Distribution of voids at cross-sectional BF TEM images of Ni and Ni-xFe (x=10, 15, 20, 35 at%) irradiated by 3.0 MeV Ni^{2+} ions to 60 dpa at 500℃.

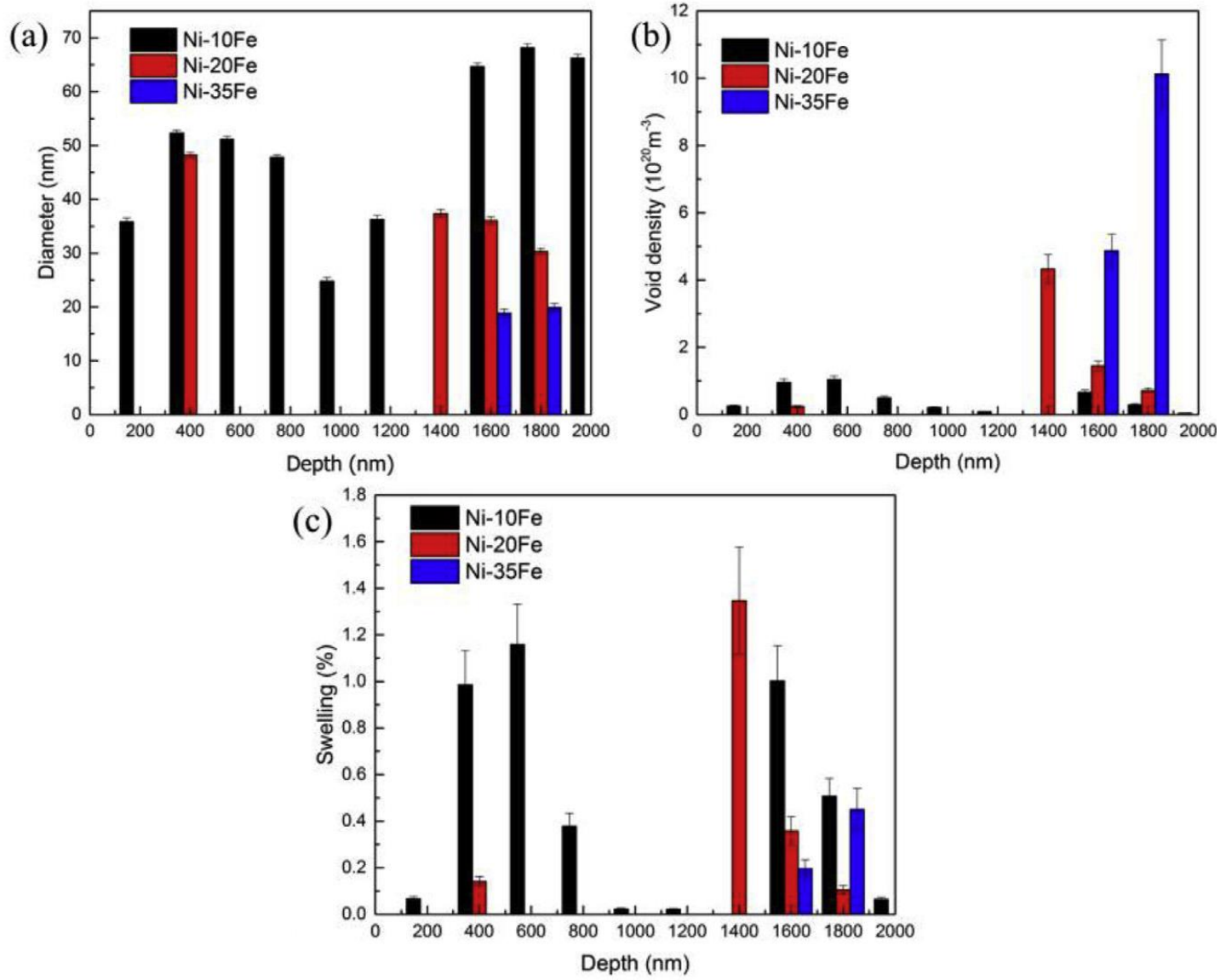

Figure 4.27 Depth distribution of (a) void diameter, (b) void number density and (c) swelling in Ni-xFe (x=10, 20 and 30 at%) irradiated with 3.0 MeV Ni^{2+} ions to 60 dpa at 500℃ [89].

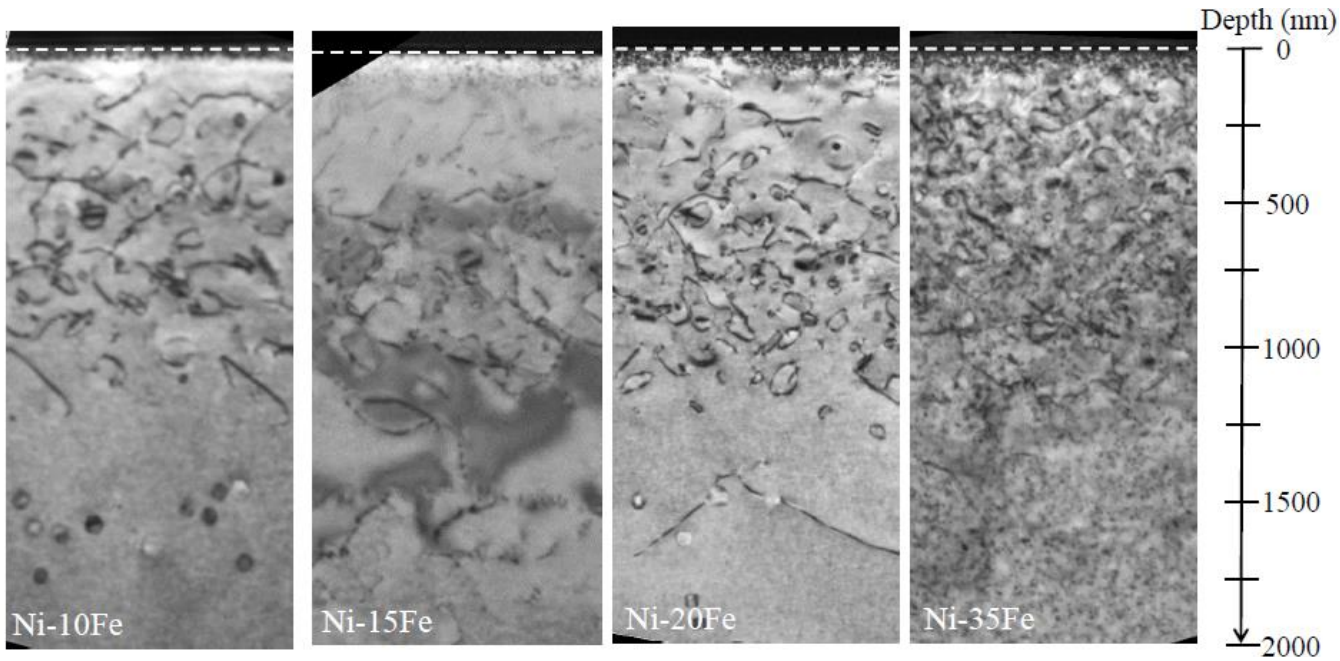

Figure 4.28 Distribution of dislocation loops at under-focus cross-sectional BF TEM images of Ni-xFe (x=10, 15, 20, 35 at%) irradiated by 3.0 MeV Ni^{2+} ions to 60 dpa at 500℃.

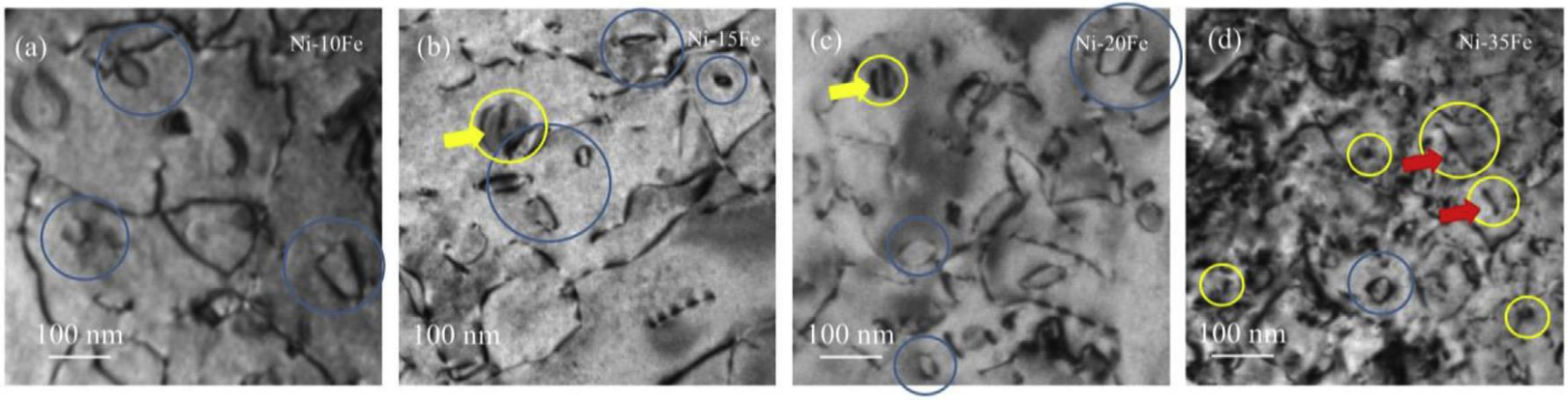

Figure 4.29 BF images of dislocation loops in Ni-xFe alloys imaged using kinetic two beam condition g=[200]. Perfect loops are marked by blue circles, faulted loops are marked by yellow circles, edge-on faulted loops are marked by red arrows, non-edge-on loops are marked by yellow circles. (a) Ni-10Fe; (b) Ni-15Fe; (c) Ni-20Fe; (d) Ni-35Fe [89].

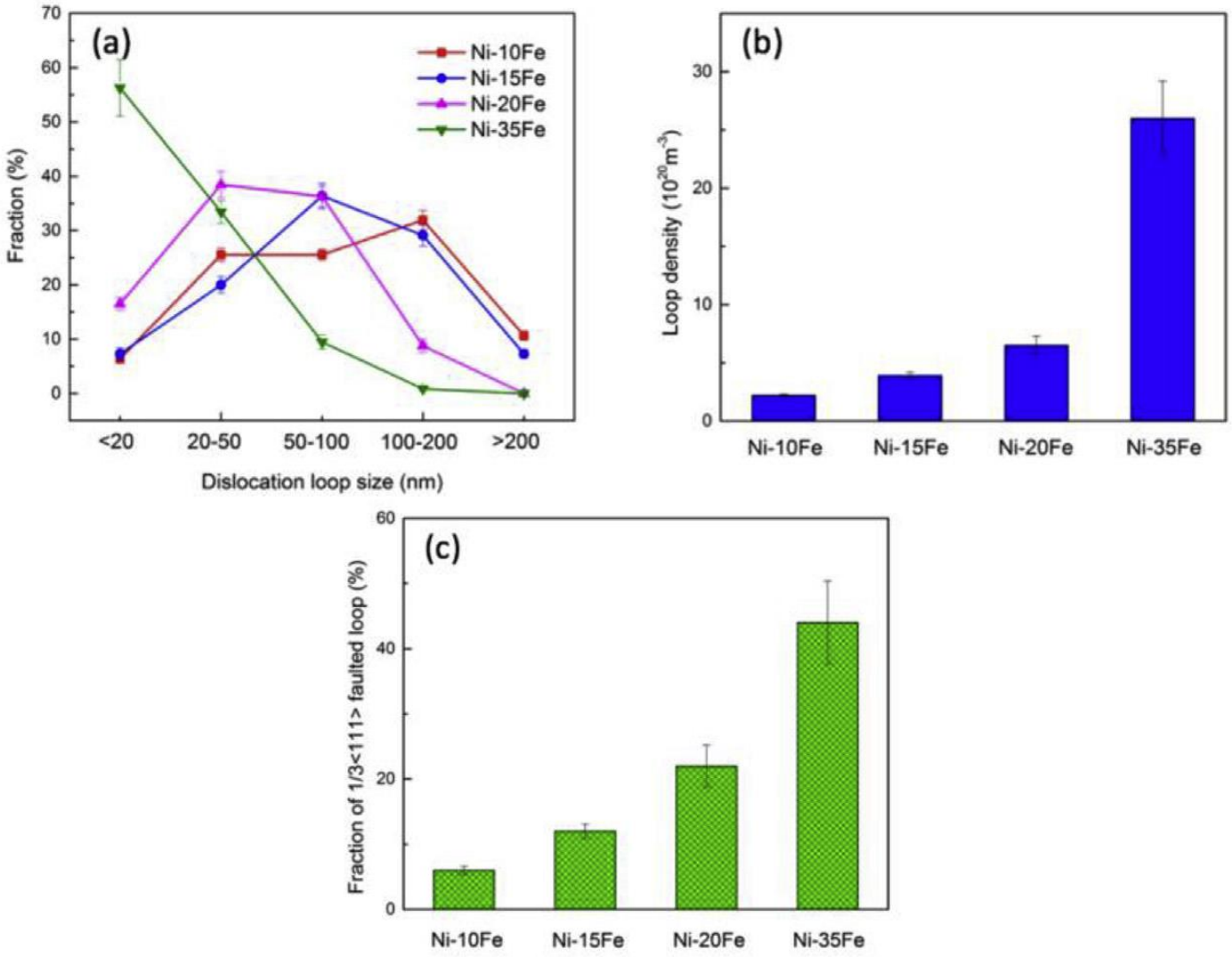

Figure 4.30 Characterization result of dislocation loops in Ni-xFe (x=10, 15, 20 and 35 at%) irradiated by 3.0 MeV Ni^{2+} ions to 60 dpa at 500℃ [89], (a) fraction of dislocation loop size; (b) dislocation loop density and (c) fraction of faulted loop density to the overall loop density.

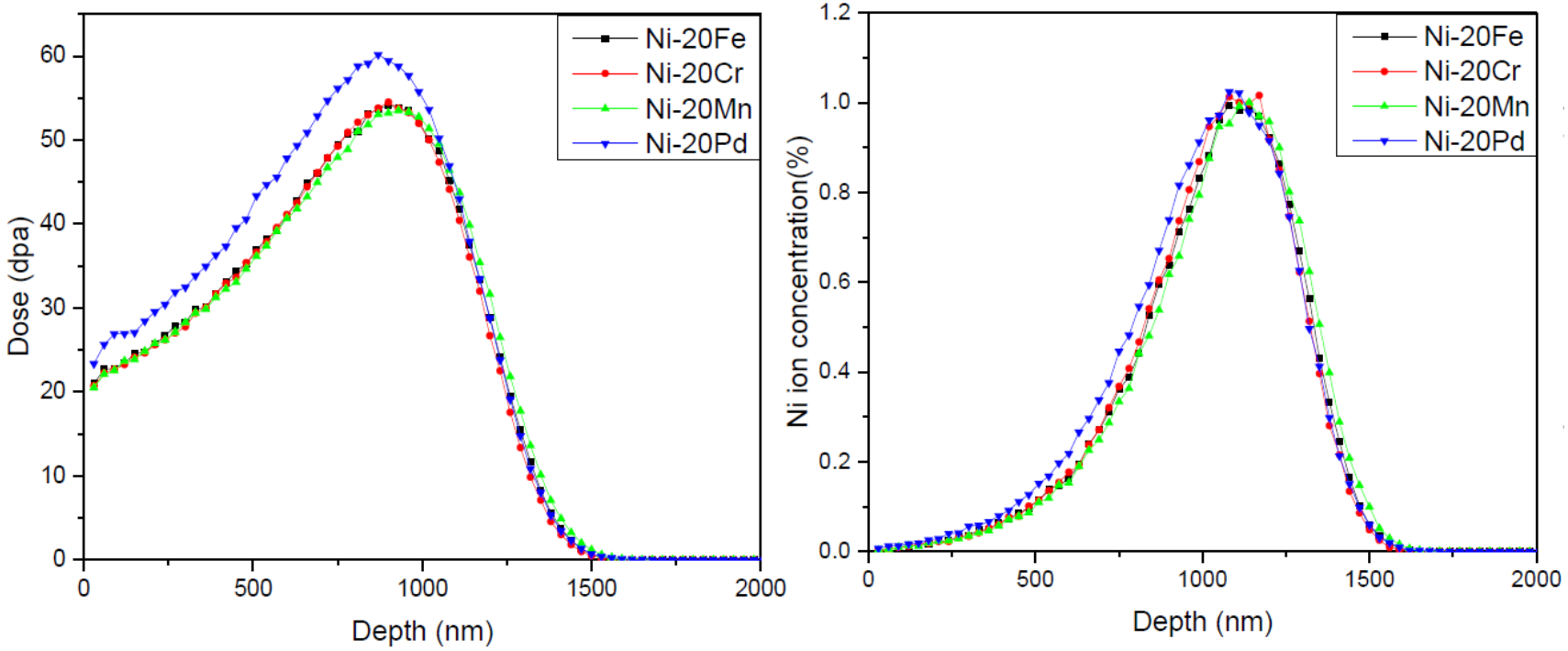

Figure 4.31 SRIM prediction profile of depth distribution of (a) displacement damage and (b) implanted ions for 3.0 MeV Ni^{2+} ions irradiated to ~60 dpa [18].

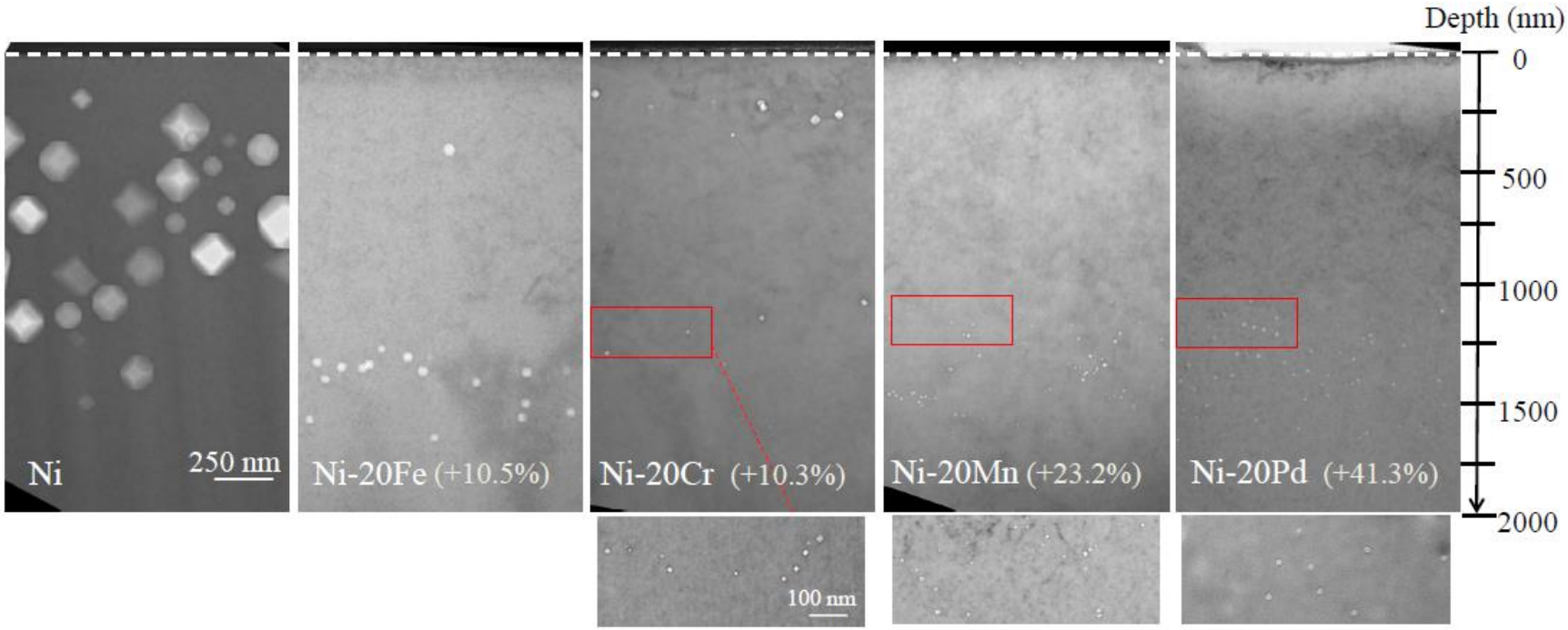

Figure 4.32 Under-focus cross-sectional BF TEM images of Ni and Ni binary alloys irradiated by 3.0 MeV Ni^{2+} ions to ~60 dpa [18].

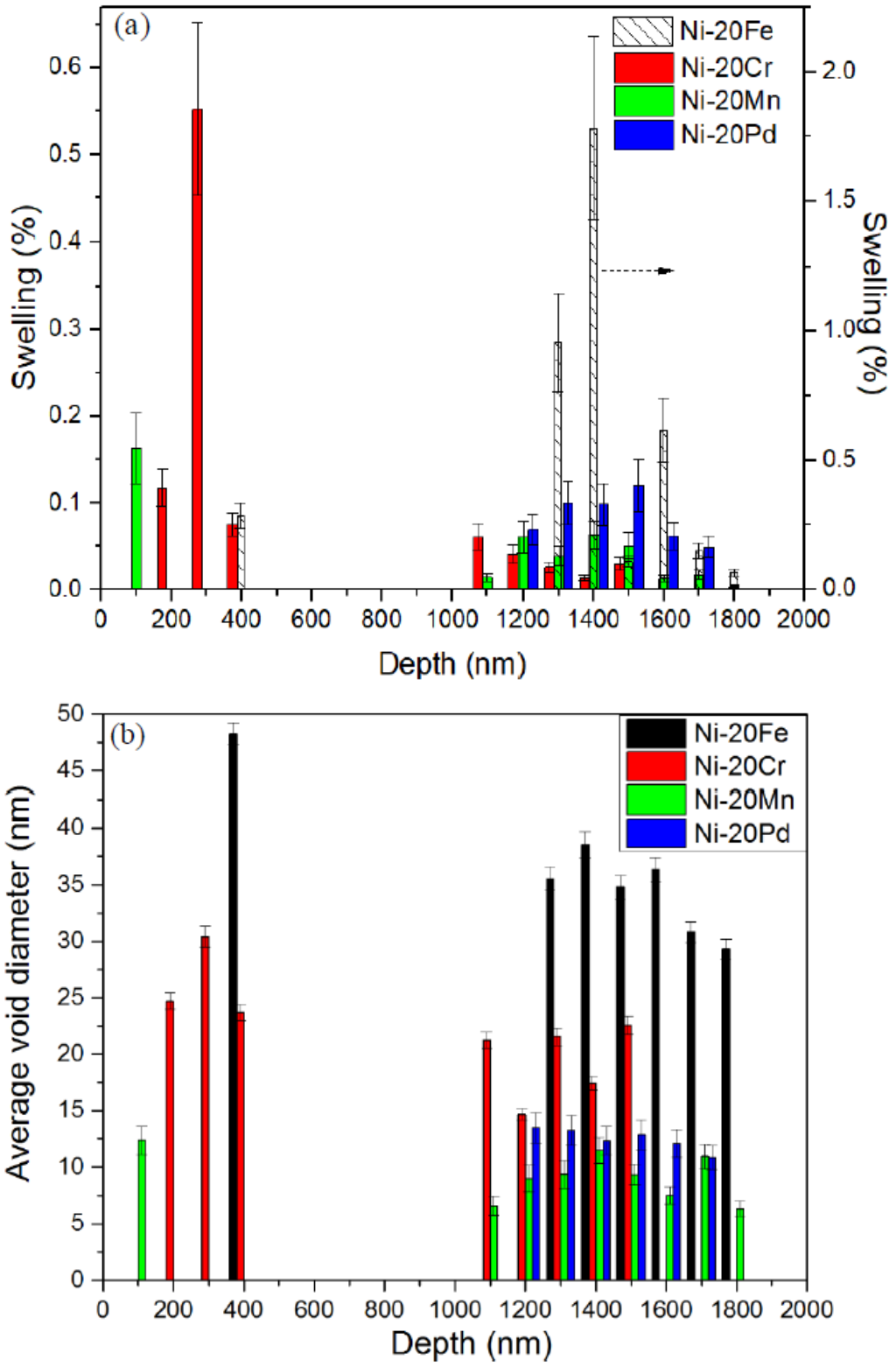

Figure 4.33 Depth distribution for (a) void swelling and (b) average void diameter using 3.0 MeV Ni^{2+} ions in Ni binary alloys irradiated to 60 dpa [18].

Table 4.5 Summary of voids and dislocation loops in 3 MeV Ni^{2+} irradiated Ni binary alloys in the region of 0-1800 nm [18].

Material	Number of voids/dislocation loops* counted	Area examined (um^2)
Ni-20Fe	27	3.65
Ni-20Cr	18	3.65
Ni-20Mn	97	3.36
Ni-20Pd	66	3.64
Ni-20Fe*	226	3.56
Ni-20Cr*	346	2.80
Ni-20Mn*	691	2.21
Ni-20Pd*	972	2.19

The dislocation loop data is marked with *.

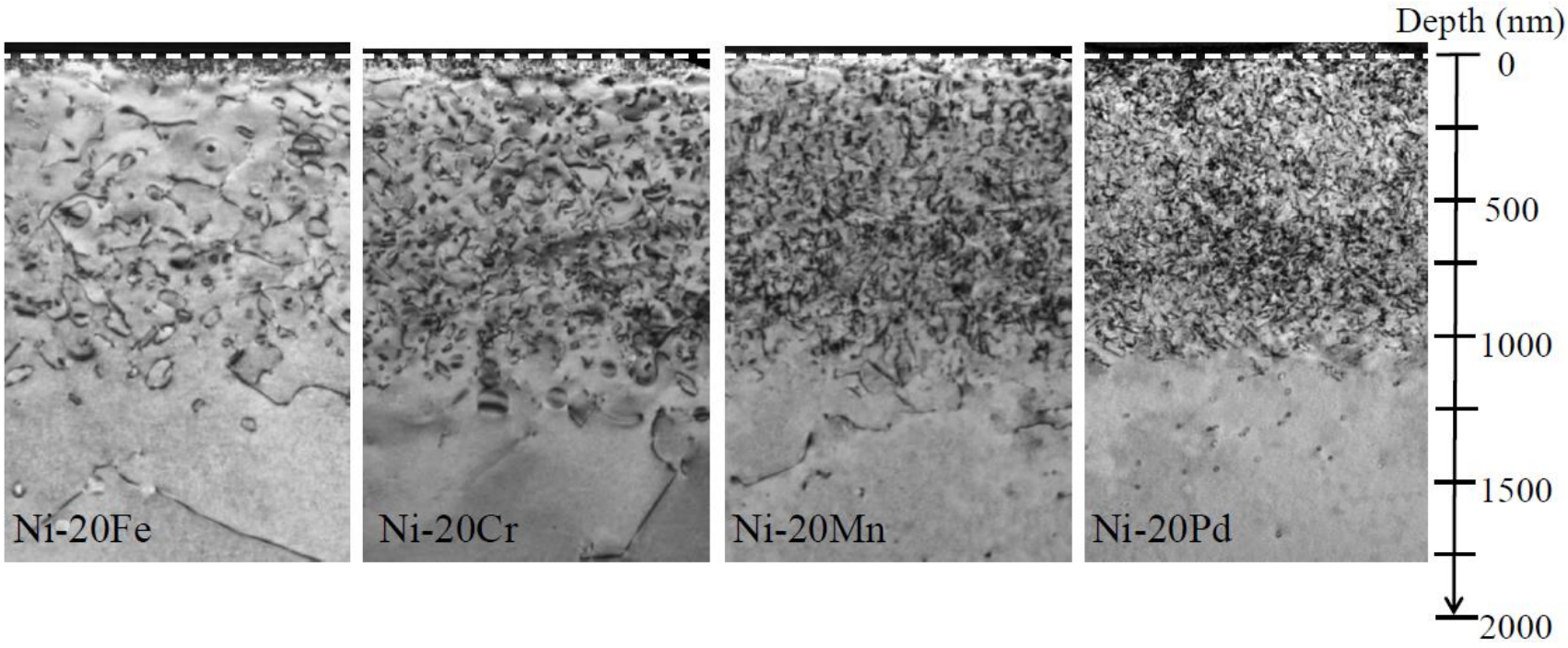

Figure 4.34 Distribution of dislocation loops at under-focus cross-sectional BF TEM images of Ni-binary alloys irradiated by 3.0 MeV Ni^{2+} ions to 60 dpa [18].

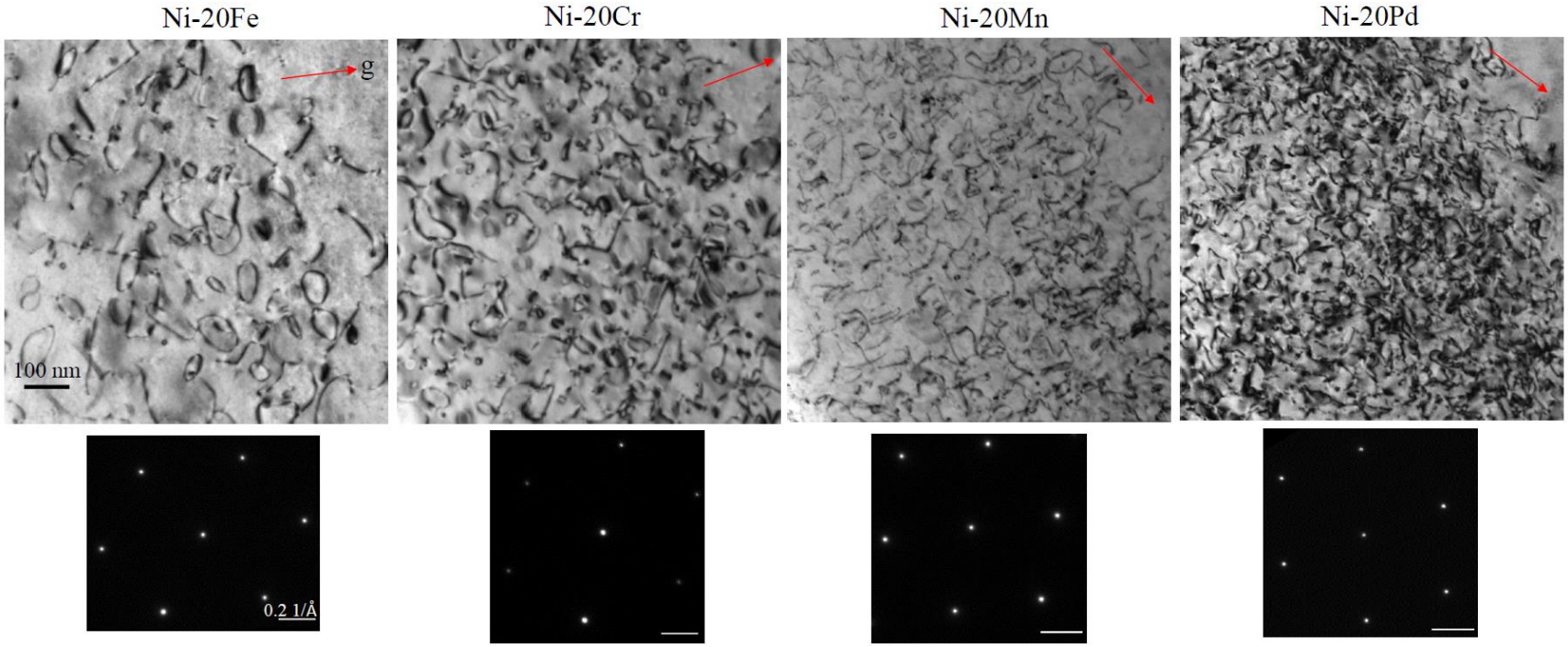

Figure 4.35 Dislocation loops in kinetic two-beam condition BF images of Ni-binary alloys at irradiation depth of 500-1000 nm from the surface. The two-beam condition g = [200] is marked by the red arrow. All the scale bars for diffraction patterns are 0.2 $Å^{-1}$[18].

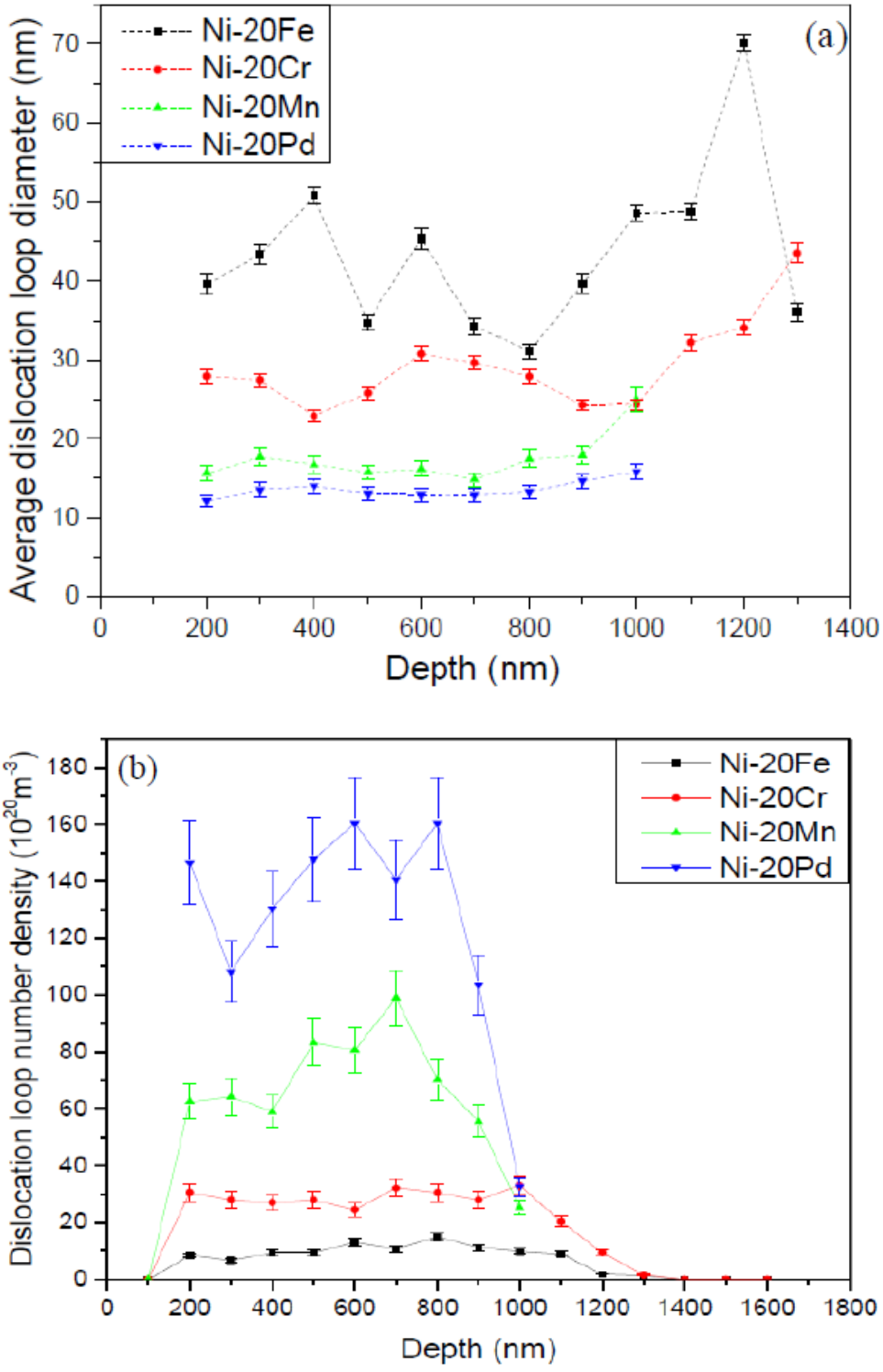

Figure 4.36 Depth distribution for (a) average dislocation loop size and (b) number density of dislocation loops using 3.0 MeV Ni^{2+} ions in Ni binary alloys irradiated to ~60 dpa [18].

Chapter 5-Discussion

The discussion of the results showed in Chapter 4 is presented here and separated into three subchapters: the one-dimensional to three-dimensional defect migration mechanisms, the influence of irradiation temperature on defect evolution in Ni-based SP-CSAs, and the effect of specific elements on defect evolution in Ni-20X binary alloys.

5.1 1-D to 3-D Defect Migration Mechanisms

To determine the defect migration mechanisms and their influence on defect evolution, the result of equiatomic Ni SP-CSAs irradiated at 500℃ were first presented. To demonstrate the transition of 1-D to 3-D defect migration mechanisms, Ni-Fe binary alloys with changing Fe concentration were considered. The effect of injected interstitial on Ni SP-CSAs were discussed using dose-dependent defect distributions in Ni, NiCo, NiFe and NiCoFeCr.

5.1.1 Transition of Migration Mechanisms in Equiatomic Ni SP-CSAs

In this work, the determination of defect migration mechanisms in equiatomic Ni SP-CSAs first depended on the qualitative comparison of defect distributions. The observation of defect movements from in-situ TEM [90], and results from simulations [15,89] were included to assist with the explanation.

One unique feature of using ion irradiation is the depth dependent information related to the irradiation direction. The depth-dependent defect distribution can provide insights into understanding defect mobility and interactions with increasing chemical complexities. Based on the qualitative distribution of voids and dislocation loops shown in Figure 4.2 and Figure 4.4, the equiatomic Ni SP-CSAs can be roughly categorized into three groups. As mentioned in Chapter 4.1.1, the first group contains Ni, where the average void size was drastically larger and had voids located in the irradiated region closer to the sample surface, while the dislocation loops

were separated from voids and existed in a deeper region. The second group contains NiFe, NiCoFe, NiCoFeCr, NiCoFeCrMn, and NiCoFeCrPd, where much smaller voids mainly distributed beyond the end of the predicted ion range, while dislocation loops dominated the main irradiated region. The third group contains NiCo and NiCoCr with mixed defect distributions between the previous two groups. The feature of the third group included relatively larger void size and coexistence of voids and loops in the irradiated region.

To explain the observed defect distributions after irradiation, two different modes of interstitial cluster migration mechanisms were proposed and illustrated in Figure 5.1: long-distanced one-dimensional (1-D) mode and a relatively short-ranged, localized three-dimensional (3-D) mode. In the 1D mode, interstitial clusters have relatively low migration barriers and can quickly migrate along the direction of their Burgers vector, <110> for Ni [15]. The high mobility of interstitial clusters allowed them to migrate to regions beyond the depth calculated by SRIM, or to escape from the surface more easily, leaving high supersaturation of vacancies behind and resulted in severe swelling. In the 3D mode, interstitial clusters not only migrated along the <110> direction but have been observed to randomly change directions and create numerous short <110> segments [15, 90]. The relatively localized movement of interstitial clusters was attributed to the complex atomic environments in SP-CSAs, which enhanced the recombination between interstitials and vacancies, and naturally resulting in less swelling on materials.

To further assist the interpretation of the experimental observations, molecular dynamics (MD) simulations data for selected Ni and NiFe are cited in Table 5.1. The comparison of migration energy (E_m) of interstitial clusters showed that interstitial clusters in Ni have higher mobility than NiFe, and the difference of E_m between two materials only increased as cluster size increased. Furthermore, direct observations from in-situ irradiations at elevated temperature showed that the jumping distance and frequency of loops were both higher in Ni than in NiCo, NiFe and NiCoFeCr, as shown in Figure 5.2 [90]. The observed diminishing jumping distance and frequency of loops in Ni SP-CSAs strengthen the proposed hypothesis: higher migration barriers for interstitial clusters as chemical complexity is increased. The overall lower migration mobility in SP-CSAs has also been observed at irradiations conducted at room temperature, where the total damage depth was shorter and exhibited smaller defect size in Ni SP-CSAs than

Ni [87, 91-92]. All these observations indirectly confirmed that the proposed 3D migration mechanism dominates in more chemically complexed materials.

To be noted, the concept of 1D and 3D interstitial migration motion is determined here by the relative mobility of interstitial clusters and its resulting defect distributions. Applying this principle, the relatively mobile, long-range 1D mode was proposed to be the dominating interstitial migration mode in Ni, which showed large voids in the irradiated region and tangled dislocation lines beyond the irradiated region. Contrarily, the relatively sessile, short-range 3D mode was proposed to be dominating in more complex Ni SP-CSAs, where a high density of dislocation loops was observed in the irradiation damaged region and small, isolated voids in a deeper region. The defect distribution results of NiCo and NiCoCr were proposed to be equally influenced by both migration modes, which resulted in mixed features.

The diffusion distance of voids is estimated here for selected Ni SP-CSAs to provide an explanation for the voids observed beyond 1500 nm. Since the information of migration energy for a single vacancy is only available for NiCo, NiFe, NiCoCr and NiCoFeCr, these four alloys were selected as demonstration. The migration energy of single vacancy was calculated using the simulation result [93, 108], with the migration energy of NiCo = 1.16 eV; NiFe = 1.43 eV; NiCoCr =0.90 eV and NiCoFeCr =0.79 eV. The vacancy diffusion coefficient D_v can be expressed as follows:

$$D_v = \alpha a^2 \nu \exp(\frac{S_m^v}{k}) \exp(\frac{E_m^v}{kT})$$

To simply the calculation, the term $\exp(\frac{S_m^v}{k})$ is assumed to equal to 1. α is equal to 1 for vacancy diffusion mechanism in fcc lattices; a is the lattice parameter; ν is the Debye frequency (~$10^{13}s^{-1}$); E_m^v represents the migration energy for a single vacancy; k is the Boltzmann constant; and T is the temperature.

The diffusion distance x can be calculated as:

$$x = \sqrt{2D_v t}$$

where t represents the total irradiation time. The calculated vacancy diffusion coefficient D_v equals to $3.7 \times 10^{-10}, 4.5 \times 10^{-10}, 1.8 \times 10^{-8}, 9.0 \times 10^{-8}\, cm^2/s^{-1}$ for NiCo, NiFe, NiCoCr and NiCoFeCr, respectively. Using the irradiation condition of 60 dpa at peak dose and a dose rate of ~ 0.003 dpa/s at 500 ℃ as an example, the diffusion distance of single vacancy was derived. The calculated diffusion distance of single vacancy is 36412, 40383, 257091 and 568007 nm for for NiCo, NiFe, NiCoCr and NiCoFeCr, respectively during the duration of irradiation. Despite vacancy typically migrates as vacancy clusters and their migration energy are slightly different than the single vacancy, the calculation here still demonstrated that vacancies can easily migrate to the region beyond 1500 nm from the irradiated surface.

The difference between calculated diffusion distance and migrated distance observed on TEM samples can be attributed to several reasons. Besides the migration energy difference between monovacancy and vacancy clusters, the recombination effect between vacancy and interstitials were not considered in the calculation. Since Ni SP-CSAs are known for their enhanced recombination capability in chemically complex alloys, this factor alone can potentially greatly reduce the migration distance of vacancies and resulting in the much shorter migration depth observed in this study.

The effect of alloying with different principal elements is addressed here along with the discussion of void swelling behavior and dislocation loop characterization result. As shown in Table 4.1 and Figure 4.3, NiCoFe and NiCoFeCr had the smallest average void size among tested SP-CSAs. But with a higher void number density observed in NiCoFe, NiCoFeCr exhibited the lowest amount of total swelling followed by NiCoFe, NiCoFeCrMn, NiCoFeCrPd, NiCo, NiCoCr then Ni. In addition, when Ni only alloyed with Co, or a combination of Co and Cr tended to result in a larger void size and exhibited higher swelling. Contrarily, when Ni alloyed with Fe, Mn or Pd, the combination of alloying elements effectively reduced void swelling. Through simulation, Zhao *et al.*[93] have studied the distribution of defect formation and migration energies in CSAs, and concluded that the specific atoms in the crystal structure determine the elemental diffusion properties. Osetsky [94] and Zhao [95] have further

determined the preferential diffusion in CSAs, where vacancy and interstitial defects migrate via different paths and form preferential dumbbells in different alloys systems. This result resonates with the observation concluded by other researches [23, 25, 72, 96]:

The irradiation resistance on Ni-SPCSAs does not purely depend on numbers of high concentration alloy elements involved, but also depends on the type and the combination of alloy elements to form the alloy.

Despite the fact that no voids were observed in NiPd, NiCoFeCrPd did not exhibit the lowest swelling but had swelling higher than NiCoFeCrMn. The result is contrary to the original prediction that materials with the highest amount of lattice distortion (i.e NiCoFeCrPd [97]) will result in the exhibition of smallest swelling. Furthermore, no direct correlation was found between void and dislocation loop size in SP-CSAs irradiated at 500℃, as shown in Figure 4.3(a) and Figure 4.5(a). NiCoFeCrPd exhibited the smallest dislocation loop size followed by NiCoFeCrMn. When comparing the total swelling result between NiCoFeCr, NiCoFeCrMn and NiCoFeCrPd irradiated at 500 ℃, several factors can contribute to the contradicting discovery. These factors included variations between different batches of irradiation experiments, different swelling behaviors arise from 150 K of melting temperature difference. The batch to batch difference was harder to compare and more expensive to investigate; therefore, the effort was focusing on addressing the second factor. As mentioned in Chapter 2.4.1, voids are formed when materials undergo volumetric swelling, with an optimum formation temperature ranges between 0.3 to 0.6 T_m. Furthermore, the swelling curve has a bell-curve temperature dependence on void swelling, which makes further studies on the temperature dependence of radiation tolerance of Ni SP-CSAs more desirable.

5.1.2 Transition of Migration Mechanisms in Ni-xFe

From the discussion presented in Chapter 5.1.1, it has been concluded that the intrinsic disorder or chemical complexity of Ni SP-CSAs has a profound influence on irradiation-induced defect evolution and defect migration mechanisms. However, the loss of translational invariance associated with the intrinsic chemical disorder poses a great challenge in providing direct, quantitative measures in SP-CSAs [98]. To systematically study the transition of defect migration

mechanisms, the number of principal elements alloy in SP-CSA has to be reduced. To this end, Ni-xFe binary alloys with changing iron concentration were chosen. The distribution result of voids and dislocation loops show in Figure 4.25 and Figure 4.28 presented a consistent shifting trend towards smaller defect size as the iron concentration increases. Furthermore, the increase of faulted loops fraction with increasing iron concentration, along with smaller dislocation loop size show in Figure 4.30 indicate the extension of the incubation period for faulted-to-perfect loop transformation [89]. These results suggest the delay of loop evolution and growth in Ni-Fe alloys with higher Fe concentration.

The collaborated simulation work [89] adapted the concept of mean free path (MFP) to trace and define the average length of each <110> segment of an interstitial cluster movement, as shown in Figure 5.3. The result showed a sharp decrease in MFP when iron concentration increases from 0 to 10 at%, suggesting a strong correlation of interstitial cluster mobility to iron concentration. Based on the experimental observation and simulation result, an updated illustration of 1D to 3D migration mechanism is presented in Figure 5.4. The defect evolution for 1D and 3D dominated mechanisms has been discussed in Chapter 5.1.1; therefore, the focus here is on the transition region. During the intermediate stage, interstitial clusters have mobility lower than the ones in pure Ni, but higher than the ones in Ni-50Fe, meaning the average movement of interstitial clusters will be shorter than those in pure Ni and may have some changes of directions like those presented in 3D mode [89]. These interstitial clusters can agglomerate and form large dislocation structures both in and out of the cascade region. Additionally, vacancy clusters at this stage have higher mobility than those in pure Ni and can migrate beyond the cascade region to form large voids. The observed distribution of defect clusters in Ni-10Fe and Ni-15Fe matches well with the intermediate stage.

As the iron concentration further increased to 20% and beyond, the dominance of 3D migration mode became apparent, as shown in Figure 4.25 to Figure 4.28. The much shorter MFP (~10 nm in Ni-20Fe, compared to 50 nm in Ni) indicates a higher interaction probability between interstitials and vacancies, and an enhancement of defect recombination. The study of defect and mass transport in Ni-xFe alloys by Osetsky *et al.* [94] also found that at ~below 20 at% iron, the continuous transport path through Fe should be broken and thus inhibiting the

diffusion of vacancies while promoting the diffusion of interstitials. Despite the quantitative method demonstrated here uses a simplified Ni binary system as an example, the concept and characterization methods should be transferable to more complex Ni SP-CSAs with further pursuit of modeling developments.

5.1.3 Damage Dose and Injected Interstitial Effect on Defect Evolution

As mentioned in Chapter 4.1.2, the primary goal of studying damage dependence in SP-CSAs was to confirm the relative irradiation performance between materials, and to study the defect evolution as a function of damage dose. The result found a consistent trend of swelling in tested SP-CSAs at two damage doses, as shown in Figure 4.8(c). NiCoFeCr exhibited the lowest amount of swelling in tested materials due to insignificant growth on voids and dislocation loops as damage dose increases. The calculated overall swelling using TEM characterization method is then compared with the swelling measured using optical profilometer [62]. Table 5.2 shows the comparison of swelling. Under the same irradiation condition, the overall swelling measured by different methods presents a similar trend between Ni containing SP-CSAs. The variations between the two methods can arise from a variety of measurement errors such as TEM resolution, EELS thickness measurement, void diameter measurement or the inherent errors from the step-height measurement. More importantly, due to the different defect cluster motion behavior in different materials, the swelling may appear at different depths in different SP-CSAs, thus making the selection on the overall material volume counted for swelling challenging.

Addition to the total swelling that considers whole imaged FIB samples, cross-sectional TEM samples have the advantage of providing depth-dependent information. This is critical in ion irradiation characterizations, as the damage dose and injected ion concentrations are both depth-dependent as well. Another important depth-dependent effect from ion irradiation is the influence of injected interstitials on defect evolution. It has long been recognized that injected interstitials can suppress the swelling by recombining with vacancies. The source of extra interstitials varies but is mainly due to the injected ions during heavy ion irradiation [53-54, 99-100]. The effect of injected interstitials can be seen clearly in the depth distribution of void number density and swelling, in Figure 4.10 and Figure 4.12, respectively. In this sub-section, the influence of injected interstitials on dose-dependent SP-CSAs was addressed along with the

previously discussed interstitial migration mechanisms and discussed separately for different SP-CSAs (Ni, NiCo, NiFe and NiCoFeCr to be specific).

Effects of injected interstitials in different SP-CSAs

Some passages in this subchapter have been quoted from the published article [84] of this thesis work. As can be seen in the cross-sectional TEM images (Figure 4.6(a) and (b)) along with the depth dependent distribution of void number density and swelling, the void separation is the most apparent in NiCo and NiCoFeCr, but the dominating mechanism seems to differ in these two cases. The separation band where no voids are present is narrower in NiCo but much wider in NiCoFrCr. The defect migration energy E_m is considered in an attempt to explain the observed difference. In Table 5.1, the defect migration energy ($E_m^{i,v}, i$ represents interstitials while v represents vacancies) calculated by MD simulations [15] shows that nickel has much lower E_m^i for interstitial clusters than NiFe (0.002 eV versus 0.974 eV for 4 interstitial clusters); while NiFe has lower E_m^v for vacancies and their clusters than nickel (0.515 eV versus 0.9 eV for 2 vacancy cluster). Mansur and Yoo [53] have suggested that the influence of injected interstitials toward void growth rate is more pronounced in systems with high vacancy migration energy. The calculated E_m^v for a single vacancy is 1.32 eV and 0.756 eV for pure nickel and NiFe [15], respectively. According to Mansur and Yoo, this E_m^v is relatively low and a significant injected interstitial effect is not expected. However, Plumton and Wolfer [101] have investigated the injected interstitial effect on void nucleation and have concluded its effect is most pronounced where defect recombination dominates. Garner [100] also has proposed that the injected interstitial effect would be enhanced as long as the chance of an extra interstitial finding a void prior to finding other sinks was increased.

Ni

In the case of Ni, it has the lowest E_m^i due to the least amount of lattice distortion in all tested material. At first sight, the suppression effect on void formation and growth from injected interstitials may not seem significant from the direct observation of TEM images. However, the swelling and modified Ni ion concentration versus mass depth in Figure 4.13 shows an obvious suppression on void swelling in the region of injected interstitials. The same trend was observed in both high and low doses for Ni. The influence of sputtering yield from 3 MeV Ni^{2+} ions is less

than 10 nm for the tested fluences and is therefore negligible in this case. The irradiation response in Ni and NiCo will be compared later.

The overall swelling quoted in Figure 4.8 is a comparison among different alloys and serves as a reference for detailed investigation of depth dependent swelling. It should be pointed out that the swelling in nickel has the tendency to saturate with increasing dose, as has been observed in several neutron irradiation studies [44, 102-104]. However, the results of nickel in this study are limited to two fluences and therefore it remains uncertain as to when the saturation may occur. An accurate swelling rate also could not be determined due to the limited damage doses studied.

NiCo

In the previous result published by Lu and Yang *et al.* [15], NiCo was categorized with the same group of defect migration mechanism as nickel for their similar void and dislocation loop distributions. However, as the peak dose increased from 4 dpa in their case [15] to 17 and 60 dpa in this study, it was found that in NiCo, there are significant amount of dislocation loops closer to the surface and existing in the same region as voids. This observation contradicted the previous result of NiCo irradiated to 4 dpa from [15], that only voids appeared closer to the surface. Based on the defect distribution from the TEM images, it is proposed that the defect migration mechanism for NiCo actually acted as a transition in between the 1-D and 3-D motion. This can be supported by observing the region closer to the surface, with the amount of dislocation loops increasing as the peak dose increased from 17 to 60 dpa. Furthermore, the observation of relatively ordered dislocation loops in the region of void denuded zone at lower dose provides interesting insight into how the injected interstitials can suppress voids formation. However, with the current data, it is hard to distinguish if the ordered dislocation loops were formed solely due to injected interstitials. The voids appearing after the denuded zone might be due to the fact that it takes longer for the injected interstitials to reach a concentration that is sufficient to have an effect on nucleation; while the highly mobile interstitials induced by irradiation already form a vacancy supersaturated zone in the cascade collision region.

Another interesting result is that the difference between the injected interstitial effect on

Ni and NiCo. In Ni, the suppression on void swelling was dominant at the peak of Ni ion concentration and no void denuded zone was observed; while in NiCo, the injected interstitial resulted in a void denuded zone between two regions with a large amount of swelling. This is likely because of the difference in E_m^i, which is lower for Ni but may be relatively higher in NiCo due to the increased chemical complexity. In Ni, the injected interstitials have the same mobility as the interstitials generated from irradiation displacement and would quickly migrate away. They would either escape toward the surface or toward a much deeper region through 1-D motion. Furthermore, the concentration of injected interstitials accumulated throughout the irradiation would have a minimal effect toward swelling suppressing if a material has a higher void nucleation rate. Hence, the recombination effect would not be significant enough to form a void denuded zone in Ni. This matches well with the research of Mansur and Yoo [53], where they concluded that the injected interstitial effect is more pronounced in systems with low bias, low sink strength and high vacancy migration energy. In NiCo, it is suspected that with increasing chemical complexity, there will be a transition in the migration mechanism of defect clusters. In Figure 4.7(a) and (b), it is observed that the defect distribution still possesses some of the features of 1-D motion, with the majority of voids closer to the surface and dislocation loops in the much deeper region. However, there is also an increased amount of dislocation loops distributed in the region closer to the surface, which is the main feature for 3-D motion. The trend is enhanced with increased dose in NiCo and contradicted with the model proposed in [15] where they suggested Ni and NiCo have the same defect migration mechanism. With the new data from this study, it is proposed that NiCo has the defect clusters migration mechanism in a transition between 1-D and 3-D motion resulting from increasing locally irradiation-induced disorder.

NiFe and NiCoFeCr

NiFe and NiCoFeCr have relatively low interstitial migration mobility compared to nickel. Based on the interpretation of 3-D interstitial motion, these sessile interstitials tend to form dislocation networks in the cascade region. The amount of injected interstitials is relatively low compared with the amount of interstitials created from irradiation displacement, hence, the injected interstitial effect should be relatively minor compared with the case of nickel and NiCo.

It is proposed in this study that the defect migration mechanism in NiFe and NiCoFeCr is dominated by the 3-D motion with a minor effect from injected interstitials. The isolated voids found in NiCoFeCr but not NiFe can be explained from the different degree of lattice distortion. As the lattice distortion is relatively higher in NiCoFeCr than NiFe, this makes it harder for the vacancies in NiCoFeCr to escape from the surface and they tend to form isolated voids in the region close to the irradiated surface instead.

While the injected interstitial effect behaves differently based on material composition in testing SP-CSAs, the influence of other irradiation parameters should not be ignored. This includes temperature, displacement rates, ion energies and raster frequencies, etc. The void separation band was not observed in another set of SP-CSAs irradiated to 4×10^{14} and 3×10^{15} cm^{-2} (with peak damage equal to about 0.53 and 4 dpa, respectively) using 1.5 MeV Ni ions at 500 ℃. In this case, the suppression on void swelling was not observed in the region where injected interstitials come to rest. A potential explanation would be that the low concentration of injected interstitials was not enough to affect the voids nucleation process. Further study would be required to determine the effects of different irradiation parameters on injected interstitials.

5.2 The Influence of Irradiation Temperature on Defect Evolution in MEAs and HEAs

Even though from the application point of view, the materials are typically exposed to a set temperature environment, the overall temperature dependent void swelling should be thoroughly studied to provide a better understanding on material performance. Figure 4.23 shows total swelling as a function of homologous temperature, demonstrating the superior swelling resistance of HEAs over medium entropy Ni SP-CSAs. Compared to non-HEAs, minimal swelling is observed on HEAs at temperatures ranging from 0.41 to 0.55 Tm, despite the variations of melting temperatures between SP-CSAs. Furthermore, the normalized void distributions presents in Figure 4.22 clearly indicates the delay of void growth in HEAs than MEAs. The average void size in MEAs irradiated at 0.5 T_m are one order higher than HEAs, and are even larger than the ones of HEAs irradiated at 0.55 T_m. However, based on the available irradiation temperatures, the peak swelling temperature cannot be determined for NiCoCr and NiCoFeCr from this study. It is likely that the swelling peaks for NiCoCr and NiCoFeCr are

located beyond $0.5T_m$. For these two materials, the increase of swelling from 420 °C to 580 °C ($\sim 0.5T_m$) was mainly contributed by the drastic increase of average void size, as shown in Figure 4.22 and Figure 5.5 for normalized void size distribution and average void size, respectively.

In addition, the distribution of voids in NiCoCr and NiCoFeCr shifted toward the damage peak region as irradiation temperature increased. Several factors can contribute to this shift of defect distribution: firstly, as irradiation temperature increases, the recombination or annihilation effect between vacancies and interstitials is expected to drop. Secondly, at higher irradiation temperature, vacancies have higher mobility and tend to agglomerate to form large voids instead of small isolated voids. While for interstitials, the prefered form is tangled dislocation lines instead of small dislocation loops, as seen in Figure 4.18 to Figure 4.20. Thirdly, higher mobility vacancies can much easily escape from the surface and resulting in a final void distribution that is relatively concentrated at the damage peak region.

Figure 5.6 shows the comparison of the highest swelling observed at 60 dpa from MEAs and HEAs to austenitic 316 stainless steels and ferritic steels. It is found that NiCoCr exhibits comparable swelling with 316SS, which also have fcc crystal structure. While NiCoFeCrMn and NiCoFeCrPd exhibit similar swelling as ferritic steels, which have bcc crystal structure and have been known to have better swelling suppression than materials with fcc structure. To be noted, this is a rough comparison and did not consider other parameters that can affect the material swelling, such as the dose rate, or the choice of irradiation source and its energy, or characterization methods. However, it does provide further evidence that NiCoFeCrMn and NiCoFeCrPd exhibit great swelling resistance.

In general, two HEAs constantly exhibit the lowest swelling among tested medium to higher entropy solid solution alloys. Therefore, the temperature dependent swelling behavior of two HEAs is the primary focus of discussion as follows. In general, Mn-HEA exhibited higher total swelling than Pd-HEA. At 420℃, the higher swelling observed in Mn-HEA than Pd-HEA is primarily due to higher void number density, and a slightly larger void size. At 500℃, Mn-HEA and Pd-HEA have similar total swelling, when taking the swelling uncertainties into consideration. However, the main contributor toward swelling is different. In this case, the void

number density of Mn-HEA is ~ 4 times higher than Pd-HEA, despite the average void size of Pd-HEA being ~ 2 times larger than Mn-HEA. At 580℃, the swelling of Mn-HEA is higher than Pd-HEA due to the significantly increased void size (92.1 v.s. 67.0 nm) as temperature increased. The contribution from changes in void size in Mn-HEA outweighed the contribution from an order higher of void number density observed in Pd-HEA. The total swelling of the two HEAs is plotted separately in Figure 5.7 to highlight the details. The swelling trend indicates that at 420 ℃(~0.45T_m), the void growth is restricted due to low vacancy mobility as predicted by theory. It is also reasonable to derive that for irradiation temperatures lower than 420℃, voids are unlikely to form for both tested HEAs up to 60 dpa at peak damage, given the small, isolated voids observed in the current condition.

Despite showing comparable swelling resistance as ferritic steels, it is found that at least an order higher of swelling increase is observed in both HEAs when increasing irradiation temperature from 0.45 to 0.55T_m. Furthermore, the average void size increased in both HEAs with increasing temperature. However, Pd-HEA seemed to have a stronger effect in suppressing void growth than Mn-HEA. The increment of void growth with changing temperatures is not as pronounced as the case in Mn-HEA, as shown in Figure 4.22 and Figure 5.5. This stronger suppression is attributed to higher lattice distortion in Pd-HEA and stronger binding energy between vacancies and atoms with larger atomic size. The former has been demonstrated by Tong [97] using X-ray total scattering, while the latter has been observed by Yang [18] in Ni-20Pd and Ni-20Mn. Both interactions can effectively restrict the vacancy mobility, promote a higher recombination rate between vacancies and interstitials, leaving less free point defects and eventually lead to smaller void swelling, as shown in [105]. The dose dependence of swelling is not performed in this study. However, if a higher dose experiment is conducted in the future, the swelling trend is predicted as follows: the larger the atomic size of alloying elements involved in solid solution alloys, the further the incubation period for void nucleation can be prolonged, and the void growth will be further suppressed, similar to the result observed by Kato *et al.* [106].

Based on the HAADF images shown in Figure 4.17, one can observe distinguished void distributions between two HEAs. In Mn-HEA, voids are constantly distributed beyond the 1000 nm depth from the surface across three irradiation temperatures. Furthermore, the overall

distribution region widens as vacancy mobility is increased with increasing temperature. While in Pd-HEA, at 420℃, only isolated voids were observed beyond 1000 nm. As irradiation temperature increased to 500℃, voids were observed not only in the region beyond 1000 nm, but in the main irradiation damage region (<1000 nm) as well. The distribution trend holds true when temperature increased to 580℃, with no significant extension of the distribution region. This indicates that the increase of vacancy mobility is not as pronounced in Pd-HEA than Mn-HEA. For Pd-HEA, the coexistence of large voids and high density dislocation loops in the main irradiation damage region is contrary to the solute trapping effect on defects. Previous theory [105] suggests added solute atoms (or increase lattice distortion) can effectively increase the recombination rate between vacancies and interstitials by trapping point defects. In that sense, Pd-HEA should exhibit better swelling resistance than Mn-HEA in this region, but that was not the case. One potential explanation for the co-existence of voids and high density dislocation loops may be a smaller nucleation rate difference between vacancies and interstitials [47] in Pd-HEA. Combining with a stronger binding energy between alloying elements and defects, both defects were allowed to grow simultaneously. Further simulation work is desired to thoroughly investigate the interaction between irradiation-induced defects.

The evolution of dislocation loops in HEAs with increasing temperature is discussed here. Figure 5.8 shows the cross-sectional TEM images of dislocation loops in two HEAs for all tested conditions. The size of the dislocation loops was consistently smaller and with higher loop density in Pd-HEA than Mn-HEA. Despite adapting two different cleaning methods, the main irradiation damage region can still be clearly distinguished. For Mn-HEA, as temperature increases to 580℃, the dominating feature shifts from small dislocation loops to tangled dislocation line segments. While in Pd-HEA, small dislocation loops remain to be the main defect feature. The pronounced delay in dislocation loop growth can be attributed and viewed as direct proof to the limited interstitial mobility arising from higher lattice distortion in Pd-HEA than Mn-HEA. The mobility of interstitials can be more effectively retarded when alloying with elements with larger atomic size differences, i.e. Pd [18, 106-107]. Studying Ni SP-CSAs using homologous temperature instead of absolute temperature provided a fair comparison ground and demonstrated that HEAs exhibit better swelling resistance than non-HEAs.

5.2.1 Contribution from Intrinsic Properties of High Entropy Alloys

It has been demonstrated experimentally in Chapter 5.2 that HEAs can better suppress void swelling and further delay the growth of dislocation loops through enhanced defect recombination arises from higher chemical complexity. In this section, the effect of entropy on thermodynamic equilibrium vacancy concentration is discussed to provide a more theoretical understanding.

As shown in Chapter 2.2, the concentration of intrinsic point defects can be expressed as:

$$C_x = \frac{n_{eq}}{N} = \exp\left(\frac{\Delta S_v^x}{k}\right)\exp\left(\frac{-\Delta h_f^x}{kT}\right) = \exp(\frac{-\Delta G_f^x}{kT})$$

For actual applications, $\Delta S_v^x = S_f^x$, the formation entropy of the defect; and $\Delta h_f^x = E_f^x$, the formation energy of the defect. The derivation of equilibrium concentration of vacancies is used for the demonstration here as the vacancy concentration is higher than the one for interstitials at all temperature range. By assuming the term $\exp(S_f^x/k)$ is equal to 1, Wang *et al.* [29] derived the equilibrium concentration of vacancy in an equiatomic multicomponent solid solution alloys as:

$$C_{v,m} = \frac{\exp(m - 1 - E_f^v/kT)}{m + \exp(m - 1 - E_f^v/kT)}$$

with *m* represents the component number in the solid solution alloys.

To evaluate the effect of temperature on equilibrium C_v, two assumptions were proposed by Wang *et al.* [29] and listed as follows:

(1) The vacancy formation energy of pure fcc Ni (1.4 eV) was used as E_f^v.
(2) The formation energy of a vacancy does not change as the number of components increases.

The first assumption was made due to challenges of finding real vacancy formation

energies in an ever-changing atomic environment in CSAs. Furthermore, the stable crystal structure of individual elements is not always fcc structure. For instance, Fe and Cr have bcc structure while Co has hcp structure. Therefore, the vacancy formation energy of fcc Ni was chosen by Wang and the calculated result was shown in Figure 5.9 (a) as a function of temperature and number of components in CSAs. To be noted, the number of components directly affects the configuration entropy of solid solution alloys. And the higher equilibrium vacancy concentration indicates that they may accommodate more interstitials generated from irradiation [29]. In addition, the versatile atomic environment can hinder the mobility of vacancies in more complex CSAs and result in a stronger recombination tendency between defects.

In reality, the vacancy formation energy is a distributed function instead of a fixed number. The effect of choosing different E_f^v was shown in Figure 5.9 (b). The results showed that the lower the formation energy for a vacancy, the higher the equilibrium vacancy concentration, as would be expected. Furthermore, the alloy with more component numbers always has a higher equilibrium vacancy concentration. An example of vacancy clusters in HEAs has been calculated by Wang *et al.* [29] using heliem irradiation, but that will not be addressed here.

The main criticisms of the model proposed by Wang [29] include: firstly, assuming the formation energy of a vacancy does not change as more components are alloyed in CSAs. In reality, the formation energy of vacancy depends on the vacant site and its surrounding atomic configurations. Secondly, the information of different alloy element choices is lost in the calculation. More precisely, the current equation cannot be used to distinguish the C_v between CSAs with the same number of components, ex. NiCoFeCrMn and NiCoFeCrPd, or NiCo and NiFe.

The current simulation method cannot yet predict the C_v in quinary. But the drawbacks mentioned above can be solved by adopting the average E_f^v calculated by Zhao *et al.*[93, 108], which considered the surrounding atomic composition of each alloying elements and the local short-range order. The C_v for NiCo, NiFe, NiCoCr and NiCoFeCr was then calculated using the equation of equilibrium concentration of vacancy derived by Wang *et al.* [29], and the results are

shown in Figure 5.10. Contrary to the ideal model proposed by Wang, the average vacancy formation energy for CSAs is found to be higher than the one for pure Ni [108]. In addition, the calculated result did not show a drastic increase in equilibrium vacancy concentration as the number of alloying elements increased. This can be attributed to the first drawback of the model, where Wang assumed that the vacancy formation energy remained constant in more complex CSAs. Furthermore, the illustration showed in Figure 5.9 (b) is misleading in the sense that it only presented the vacancy concentration calculated using lower C_v. The result shows in Figure 5.10 (a) indicates that the contribution of higher vacancy formation energy to C_v can sometimes outweigh the contribution from the number of components in CSAs.

In consideration of the new discovery, the theory proposed by Wang should be modified. The results present in Figure 5.10 (a) and (b) indicate that the main contribution to enhanced defect recombination and superior swelling resistivity in HEAs comes from the interstitial migration mechanism and defect mobility. The result may have a relatively weak correlation to the equilibrium vacancy concentration due to the calculated difference is ~2×10^{-11} at 800 K, and even smaller difference at lower temperatures. In the irradiated temperature range tested in this study (693-853 K), there is no significant difference between the C_v for NiCo, NiFe, NiCoCr or NiCoFeCr. Therefore, the dominating factor in deciding the swelling behavior and defect distribution should still be the defect mobility and diffusion mechanism.

5.3 The Effect of Specific Elements on Defect Evolution in Ni-20X

Some passages in this subchapter have been quoted from the published article [18] of this thesis work. Contrary to the concentrated binary Ni alloys, the effect of solute atoms in dilute (less than 10at% of solutes) Ni binary alloys has been investigated intensively. The research from Hamada [10], Yoshiie [11-12] and Sato [13] systematically indicated that the size of vacancy clusters in Ni-Si and Ni-Sn alloys (with -5.8% and 74.08% volume size factor compared to Ni, respectively) decreases with an increase in the solute atom concentration. While the Cu and Ge (with 7.18% and 14.76% volume size factor) are regarded not to have significant influence on the evolution of defect structure in Ni binary alloys. The effect of element concentration on interstitial migration mechanism has been previously demonstrated in Ni-xFe, which showed a

drastic decrease of mean free path as iron concentration increased from 0-20 at% [89]. The result from [89] and [13] have concluded that the frequency and mean free path of the 1-D motion depends on the element concentration and amount of segregation from element atoms. The void swelling result from Ni SP-CSAs further indicates that the final defect distributions are closely related to the type of elements alloyed in the material.

Wakai *et al.*[14] have investigated the effect of solute atoms on swelling in Ni and its binary alloys with 5 at% of solute atoms as Si, Co, Cu, Mn and Pd using He^+ ions. Their research suggests that the mean size of loops and void swelling tend to increase with the volume size factor of the solute atoms. However, the credibility of the result is hindered due to the use of helium ions as the irradiation ion. As suggested in their paper, helium irradiation may promote the nucleation of dislocation loops by forming He-point defect complexes rather than di-interstitial and interstitial-solute complexes. Furthermore, the swelling calculations have included a high density of bubbles, which can be easily formed with high dose helium irradiation and have different interaction mechanisms with interstitials than with voids. The conclusions not only have contradicted the result obtained from neutron radiation, but also the observed correlation on dislocation loop size and swelling has a minimal influence from solute atoms in their study. To clarify the effect of elements on defect evolution in Ni binary alloys, a comprehensive study with higher solute concentration is needed and discussed as follows.

5.3.1 Influence of alloying elements on void swelling

The void swelling peak for pure Ni is around 0.45 T_m, and the Ni binary alloys with various melting temperatures were irradiated at the same homologous temperature in an attempt to achieve a similar equilibrium vacancy concentration. From the cross-sectional TEM images shown in Figure 4.32, and the depth dependent average void size in Figure 4.33 (b), it is apparent that the swelling dropped dramatically as other alloying elements were added. The main mechanism for this suppression on swelling can be attributed to the change in defect migration behavior. Similar to the sluggish interstitial mobility observed in Ni SP-CSAs, the increased intrinsic chemical complexity from the addition of a high concentration of alloying elements can reduce the effective interstitial mobility and enhance the defect recombination under irradiation [15, 51, 62, 84, 90, 96, 109-110].

There are several factors that can affect the void evolution in Ni binary alloys, these include: the concentration of alloying elements in the solution, the atomic volume size relative to the Ni atoms and the mobility of vacancy clusters. By adding solute atoms or high concentration alloying elements into the solution, it is reasonable to derive that the atomic misfit between Ni and introduced alloying elements will create stress inside the crystal structure. And defects will have different preferential sites inside the lattice depending on the stress type. Due to the nature of the defect size, vacancies tend to be attracted to the tensile stress environment while interstitials prefer the compressive stress environment.

The increase of concentration of alloying elements will enhance the influence from these elements on void swelling, as the probability of the added atoms encountering the irradiation-induced defects increases as well. The diffusion trajectory of vacancies or atoms can be greatly altered as a large variety of atomic configuration becomes possible with increasing solute concentration. Wang *et al.* [49-50] have observed an increasing resistance to void formation in Ni-Cu alloys as the copper concentration increased from 0 to 50at%. Briggs *et al.* [111] also reported a decrease in swelling as the chromium concentration increased in Ni-Cr binary alloys. Lu and Yang *et al.* [89] systematically studied the depth dependent defect distributions with increasing iron concentration in Ni-Fe binary CSAs. Their research has shown that, for interstitial clusters, not only the migration distance decreases continuously, but changes in migration direction also gradually increase as the iron concentration increases. Contrary to the long distance 1-D motion observed in pure Ni and dilute binary alloys, this relatively localized interstitial motion (3-D motion) is found to be dominant in Ni-20Fe and can greatly increase the recombination probability between interstitials and vacancies. The increase in alloying element concentration not only alters the average migration distance of interstitial clusters, it also transforms the dominating defects upon irradiation. A high density of dislocation loops with interstitial nature are found predominantly in the defect production region; while isolated, small voids are mainly observed in a much deeper region from the irradiated surface. Based on the qualitative defect distribution showed in Figure 4.32 and Figure 4.34, defect migration in all the Ni-20X concentrated alloys is mainly controlled by the 3-D motion.

In addition to the concentration, the size of alloying atoms also plays a significant role in

altering the defect migration motion and influences the final defect size. It has been well recognized that during irradiation, the undersized atoms tend to interact with interstitials while the oversized atoms tend to interact with vacancies to achieve a minimum energy state [96]. Therefore, in the environment where solute-vacancy binding is not the dominant mechanism, it is hypothesized that in concentrated Ni binary CSAs, the greater the atomic volume misfit between alloying elements and Ni, the easier it is for vacancies to exchange sites with larger alloying atoms. This can lead to higher vacancy mobility and a smaller void size due to less vacancies being available for void growth. As can be seen in the average void size presented in Figure 4.33 (b), Ni-20Fe exhibited the largest void size, followed by Ni-20Cr, Ni-20Pd and Ni-20Mn. The difference between Ni-20Pd and Ni-20Mn can be considered within the measurement error. A general trend has shown that the average void size indeed decreases as the atomic volume misfit increases. The relatively minor correlation between void size and solute atomic size may arise from the dominating dislocation loop features and higher recombination rate in the concentrated Ni binary alloys. The correlation is likely to be enhanced with increasing damage dose.

Defect migration is more complicated than just exchanging sites with solute atoms based on the solute size or concentration. And the difference in void size between Ni-20Fe and Ni-20Cr, (atomic volume factors 10.6% and 10.3% respectively, see Table 2.3) cannot be explained solely by the solute atomic size theory. Therefore, an experimentally derived trend on vacancy migration energy is applied here to account for other factors that could potentially affect the defect migration in concentrated binary alloys. The derivation is based on a unique feature of cross-sectional TEM samples irradiated using heavy ions, where the damage dose and injected ion concentration are depth dependent. The depth of where voids are located reflects the mobility of vacancy clusters. The following discussion will be separated into two parts according to the relative defect depth where voids reside: the region closer to the surface (< 500 nm from the irradiated surface) and the region deeper than SRIM calculated damage peak (> 1000 nm).

5.3.1.1 The region closer to the surface

In the region of < 500 nm from the irradiated surface, voids were presented in varying depth, see Figure 4.33. Based on the residing depth, studied alloys can be arranged in the order of Ni-20Fe, Ni-20Cr and Ni-20Mn, with Ni-20Mn has voids closest to the surface. Two

mechanisms are vying for vacancies in this region: the recombination from high density interstitial-type dislocation loops and the escape from irradiated surface. Vacancies are more likely to escape from the surface than to recombine with interstitials as getting closer to the surface. The recombination effect gradually becomes the dominating mechanism as the irradiation depth increases. It is true that oversized solute atoms can potentially trap the vacancies, but in this region, it is believed that the surface effect is stronger than the solute-vacancy binding effect, as the voids are located very close to the irradiated surface. Assuming the surface effect is the dominating mechanism for voids observed in this region, and there is no major difference on defect production between the studied Ni binary alloys, the shorter depths of voids in these representative TEM images can serve as an indication of a higher mobility for vacancy clusters in the order of Ni-20Fe< Ni-20Cr <Ni-20Mn< Ni-20Pd.

The higher vacancy mobility in Ni-Cr than Ni-Fe has been reported in simulations before [93, 112-113]. Furthermore, the discrepancy of solute atomic size effect toward defect size can be explained through the induced stress environment. Egami *et al.* [114] studied the atomic-level pressure of HEAs against local volume, and found that in CoCrFeNi, the Cr atoms are under stronger tension than Fe atoms. This correlates with our previous theory that vacancies prefer to reside in a tension environment. But instead of purely relying on the atomic volume factor, the induced stress in the lattice environment seems to play a bigger role in deciding the vacancy mobility when solute atomic sizes are similar, as in the case of Ni-Cr and Ni-Fe. The smaller void size in Ni-20Cr than Ni-20Fe serves as another demonstration that the faster vacancy mobility in Ni-Cr leaves less vacancies to form larger voids. For the case of Ni-Mn and Ni-Pd, the larger atomic size leads to higher tension in the lattice environment and faster vacancy mobility prevails. No voids were observed on the surface of Ni-20Pd, which suggests that the vacancy mobility was very high and led to a void denuded zone in this region. It is likely that the solute-vacancy binding resulted in a smaller void size in alloys with larger atomic volume factor, but without further investigation through simulation, it is difficult to further determine the effect of solute-vacancy binding in this region.

5.3.1.2 The region deeper than SRIM calculated damage peak

In the region of > 1000 nm from the irradiated surface, the void microstructure can be

separated into two groups: (1) Ni-20Fe, which exhibited large voids and high swelling and (2) Ni-20Mn and Ni-20Pd, where a high density of small voids was observed. Two mechanisms can potentially lead to this void evolution. One is the alloying binding effect where solutes enhance the void formation by trapping excess vacancies and form solute-vacancy complex, the other one is the injected interstitial effect. Kato *et al.* [115] observed that the addition of oversized transition metal solutes effectively suppressed void growth. But at higher irradiation dose, an abrupt increase in the number of small voids was observed. Hepburn *et al.* [116] proposed that the oversized solutes may help nucleate voids in this case, and for a given number of vacancies, the alloy microstructure with oversized solutes will have many small rather than few large voids. The different void features observed between Ni-20Fe and Ni-20Mn/Ni-20Pd can be explained using the same theory. The largely oversized Mn and Pd atoms may have stronger binding energy with excess vacancies than Fe. Comparing to the case closer to the surface, there is no free surface as predominant sink for vacancies in this region. And the vacancies escaped from the recombination with high density dislocation loops can be easily trapped by the largely oversized solute atoms and form isolated small voids, as observed in our case. As the injected ion peak calculated by SRIM falls around 1000 nm, the effect of the injected interstitials may also influence the void behavior in this region. However, it is believed that the recombination from injected interstitials should be relatively minor, as the peak injected ion concentration is only ~1%.

In the case of Ni-20Cr, since the solute atomic size of added Cr atoms was not as large as Mn/Pd, it is likely that the Cr atoms have a weaker binding energy toward vacancies, as suggested by Tucker *et al.* [113]. The excess vacancies are more likely to move freely and annihilate with the interstitials, leading to fewer voids in the deeper region, as presented in Figure 4.32.

In the region of 500-1000 nm from the irradiated surface, very few voids were observed. This is mainly attributed to the dominating recombination effect between interstitial type dislocation loops and vacancies, leaving a large void-denuded zone in this region.

5.3.2 Influence of alloying elements on dislocation loops

The influence of alloying elements on dislocation loops can be separated into two categories based on the solute concentration. For dilute binary alloys, since solute atoms only account for a very small portion of the material composition, the dominating interstitial migration mechanism is still the long range 1-D motion with a vacancy-dominant environment. The solute atoms need to have a much larger atomic volume factor and compete with the strong sink strength from vacancies to have a significant influence on dislocation loop evolution. For instance, Hamada *et al.* [10] observed no strong influence on the dislocation loops for the case of Ni-2at%Cu and Ni-2at%Ge, where the atomic size factor was 7.18% and 14.76%, respectively. Another path for small atomic volume solutes to affect the defect evolution is by forming irradiation-induced clusters [50] or precipitates [13], which can create repulsive forces toward interstitial clusters and limit their migration range to form smaller dislocation loops. For concentrated binary alloys, a high concentration of alloying elements not only alters the dominating interstitial migration mode to a relatively localized 3-D motion, it also transforms the main defect type in the irradiated region to interstitial-dominant dislocation loops. Therefore, the alloying elements with similar atomic size factors have a higher impact on dislocation loop evolution than in dilute binary alloys, as the dominating defect shifted with increased solute concentrations.

Normally, self-interstitial defects with larger size tend to create a compressive environment in the local lattice and lead to repulsion to oversized solutes placed in these sites. However, Hepburn *et al.* [116] have demonstrated using first principles calculations that magnetic oversized transition metal solutes (Cr, Mn, Co and Ni) can act as strong trapping sites for self-interstitial defects. The study stated the larger the solute atomic size factor, the stronger the trapping force for interstitials. But this theory has never been tested in concentrated binary solid solutions. Figures 4.34-4.36 present the systematic study of solute atomic size factor toward interstitial evolution in concentrated Ni binary alloys. The result has shown a general trend that the dislocation loop size decreases as the solute atomic volume factor increases, with the largest dislocation loop size in Ni-20Fe and the smallest in Ni-20Pd. The difference in average dislocation loop size is about 4 times smaller in Ni-20Pd than in Ni-20Fe. This result can be interpreted as a higher migration barrier for interstitials and its clusters with increasing atomic

size factor. The reduced interstitial movement is similar to the sluggish core effect observed in HEAs [15, 36, 40, 117-118]. And the higher the migration barrier for interstitial clusters, the harder it is for interstitials to move, resulting in a smaller cluster size, which leads to a smaller dislocation loop size.

A further step in the interpretation of the interstitial migration energy can be conducted based on the depth dependent information obtained from cross-sectional TEM characterization. The shorter total migrated depth of dislocation loops in Ni-20Mn and Ni-20Pd indicates that they have a higher interstitial migration barrier than Ni-20Fe and Ni-20Cr. The interstitial mobility between Ni-Fe and Ni-Cr is hard to differentiate based on our solute atomic size theory. Tucker *et al.* [113] demonstrated that Cr is the faster diffusing species in dilute Ni binary alloys than Fe, but Cr solutes binds strongly to the interstitial defects. This strong binding to interstitials may help explain why the atomic volume factor cannot be used to interpret the dislocation loop size between Ni-20Fe and Ni-20Cr. Hepburn *et al.* [116] contributed this favorable interaction with the interstitials to magnetism in Cr. The effect of solute atomic size to defect evolution has also been simulated by Ullah [119-120]. All the simulation result on defect cluster size showed similar trend with this study, with Ni-20Fe has the largest interstitial clusters follow by Ni-20Cr then Ni-20Pd.

The dramatically increased dislocation loop density found in alloys with larger solute atoms is consistent with the increase of lattice distortion and the higher interstitial migration barrier. This further indicates that a larger fraction of the produced interstitials is trapped in the lattice as the lattice distortion increased. And the high concentration of alloying elements can be viewed as pinning sites for interstitials. This can be seen clearly from the more than an order of magnitude higher dislocation loop density in Ni-20Pd than that in Ni-20Fe, as presented in Figures 4.35 and 4.36 (b). The increased density of both dislocation loops and dislocation lines should provide higher resistance to void swelling, as the recombination of vacancies and interstitials increases.

The loop features observed using g=[200] includes both faulted loops and unfaulted/ perfect loops. Due to increased difficulties induced from the relatively high dislocation loop

density and small size for most binary alloys, no special effort was made in this study to qualitatively distinguish the type or ratio of faulted to unfaulted loops. However, by using the Rel-rod technique on flash-polished samples (results not shown here), it is believed the majority of the loops are unfaulted loops. This relatively low faulted loop ratio has been demonstrated by Lu and Yang *et al.* [35] that the degree of chemical complexity will influence the ratio of faulted loop versus perfect loop. Where the alloy with lower chemical complexity (such as NiFe) has a relatively low percentage of faulted loops compared with alloys with higher chemical complexity (such as NiCoFeCr and NiCoFeCrMn). The radiation-induced segregation (RIS) was not measured in this study, but has been analyzed in other studies [34-35] showing that the smaller Ni atoms were favored at the interstitial-type loops for Ni binary alloys.

5.3.3 Other mechanisms that affect defect evolution

In addition to the factors discussed above, there are other mechanisms that can affect defect evolution. For example, the temperature deviation from $0.45T_m$ may result in different defect behavior. From Table 3.1, Ni-20Cr and Ni-20Mn are the two samples that deviate larger than 10 ℃ between their $0.45T_m$ homologous temperatures and the actual irradiated temperature. Samples irradiated at higher temperature tend to induce a slight increase in the defect size, due to increased thermal emission and higher defect mobility. However, this should not affect the previous argument that larger solute atoms create a higher degree of distortion in the crystal structure and increase the interstitial migration barriers that lead to a smaller size of defects. As the actual irradiated temperatures are both higher than the homologous $0.45T_m$ temperature, assuming the measured defects are affected by this increased temperature, the "ideal" average defect size for Ni-20Cr and Ni-20Mn would only be smaller than the one currently measured. Based on the calculated defect migration energy, the smaller "ideal" defect size would only further complement the proposed hypothesis.

Another factor that hasn't been considered is the higher dose in Ni-20Pd due to higher atomic density, see Figure 4.31. This can lead to higher defect density and larger defect size. However, the difference on dislocation loop density is an order higher in Ni-20Pd while the peak dose differ at ~7 dpa, less than 15%, so the influence from higher damage dose should be negligible as well.

Overall, there is a noticeable decrease in defect size and a significant increase in dislocation loop density in the Ni-20X concentrated alloys over the increased solute atomic volume at all depths, regardless of the other effects discussed here.

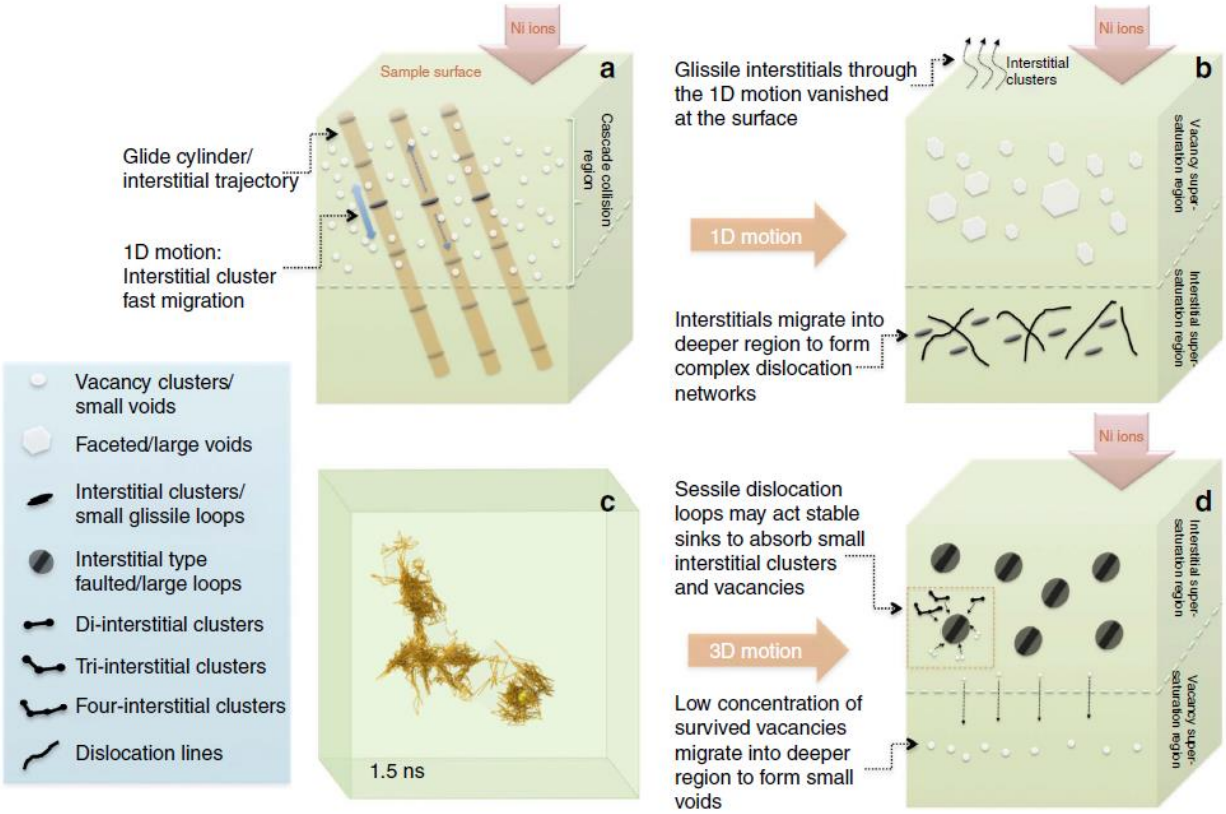

Figure 5.1 1D and 3D interstitial clusters migration modes under ion irradiation. (a) Schematic illustration of 1D motion in Ni, where interstitial clusters migrated relatively fast along the glide cylinder. (b) Schematic sketch of defect evolution and distribution in Ni as a result of **a**. (c) MD simulation result of the trajectory of a four-interstitial cluster in NiFe showing a relatively localized 3D migration mode. (d) Schematic sketch of defect evolution and distribution in more complexed Ni SP-CSAs as a result of **c** [15].

Table 5.1 Migration energy barriers, E_m of point defects (vacancy and interstitial) and their clusters in NiFe as compared with that in pure nickel [15].

Cluster	Em(eV)	
	NiFe	Nickel
I_1	0.516	0.16,0.1
I_2	0.617	0.12
I_3	0.728	0.04
I_4	0.974	0.002
V1	0.756	1.32
V2	0.515	0.9
V3	0.624	-
V4	0.747	-

Note: I represents interstitial and V represents vacancy.

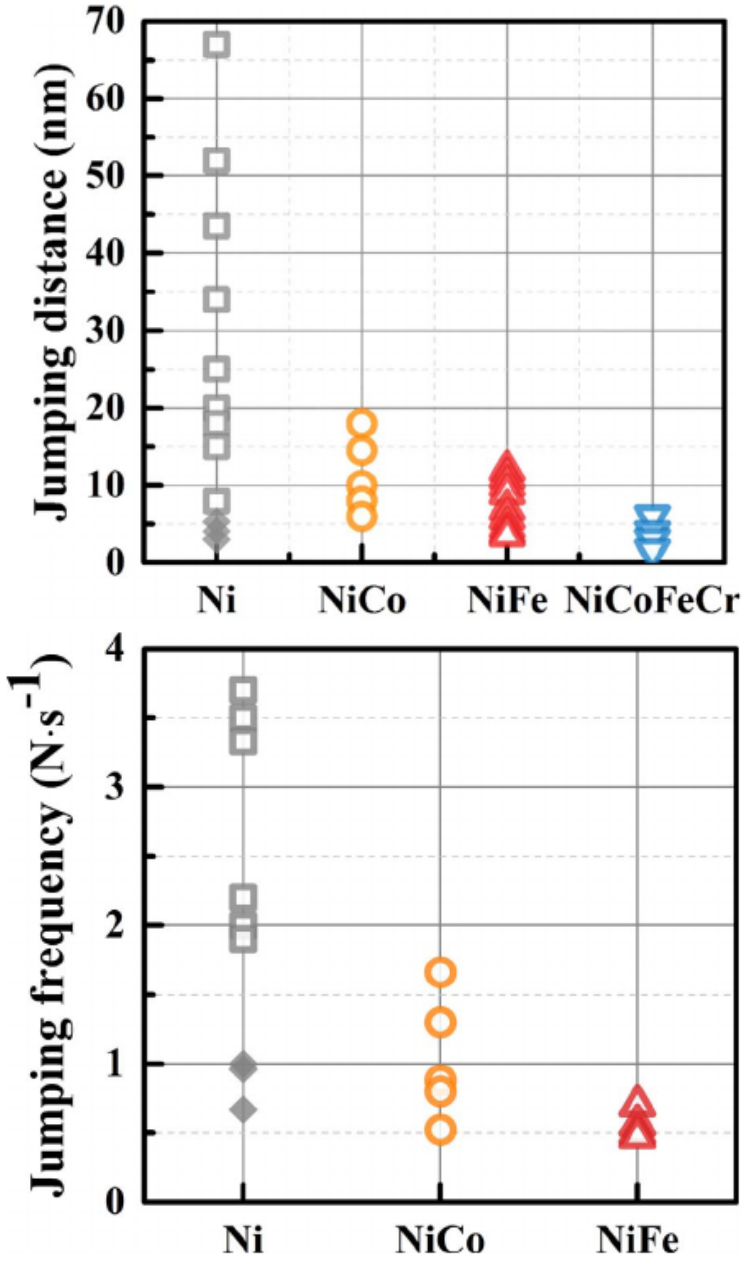

Figure 5.2 Projected (top) glide distance and (bottom) frequency of loops as a function of alloy composition. Loops with diameter less than 10 nm are shown by open markers, while ones larger than 20 nm in Ni are indicated by solid diamond symbols [90].

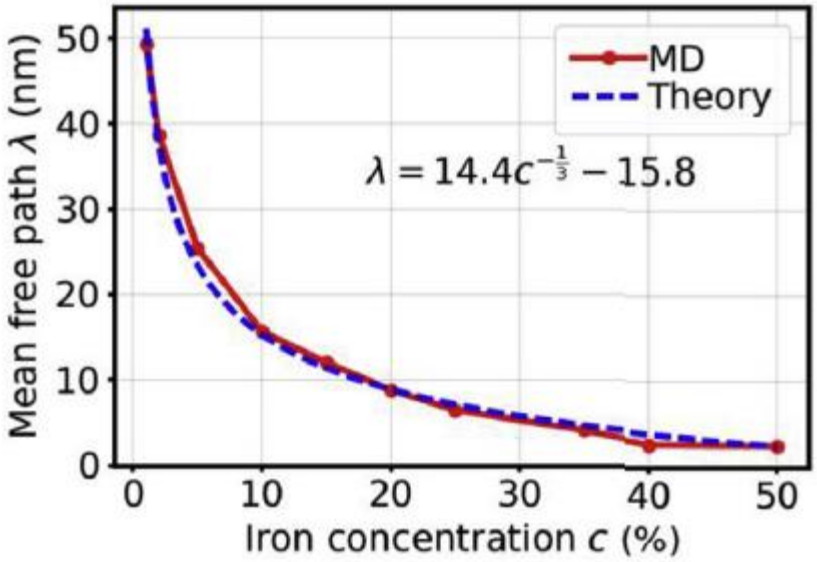

Figure 5.3 Dependence of mean free path of interstitial clusters on iron concentration. The red line indicates the plot of the calculated mean free path of a nine-interstitial cluster in nickel and Ni-Fe alloy systems with different iron concentration at 1200 K in a period of 20 ns; the dashed blue line indicates the fitting profile to mean free path curve based on the cage model [89].

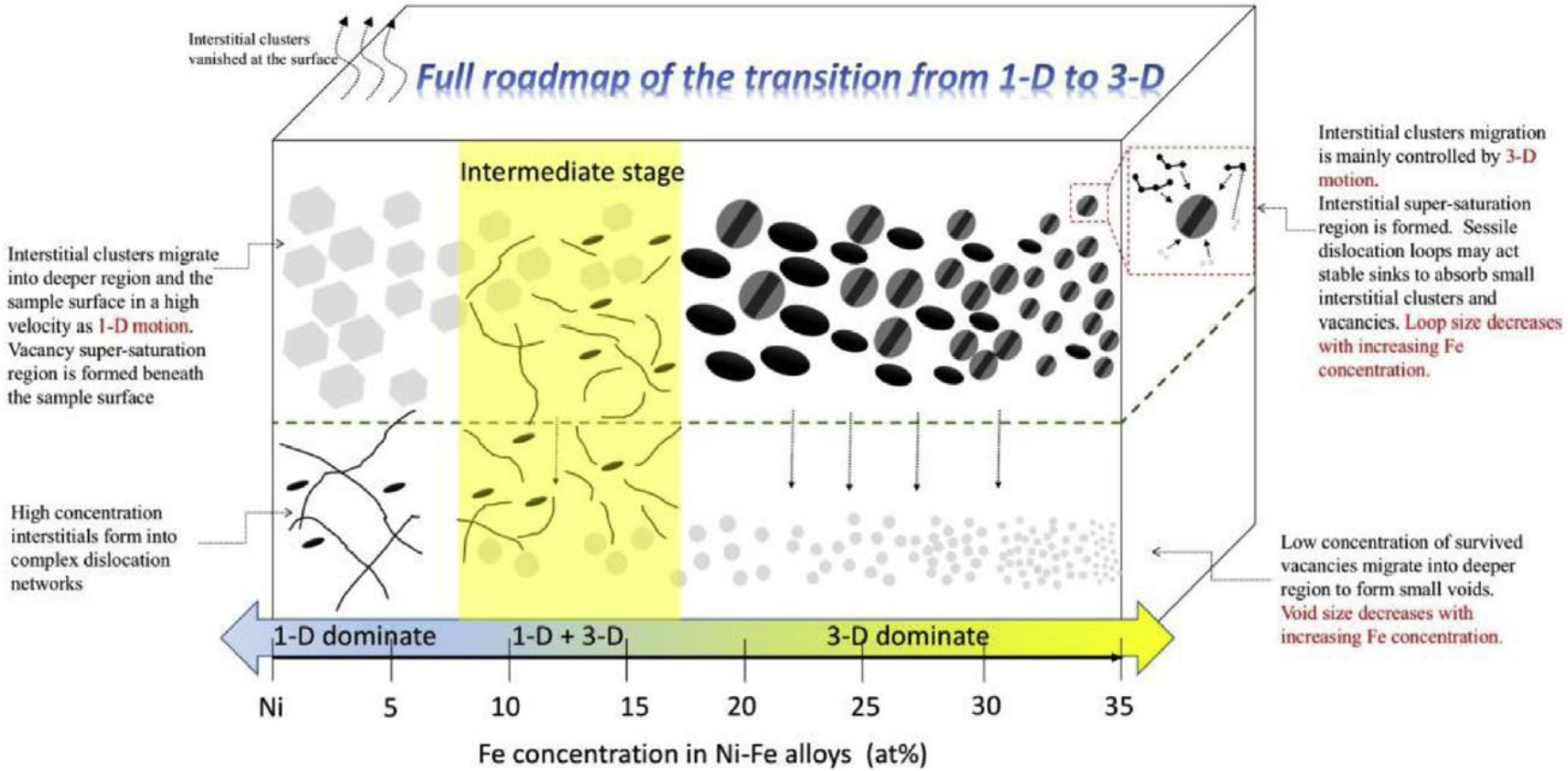

Figure 5.4 Schematic sketch showing defect evolution and distribution in Ni and Ni-xFe alloys as the interstitial migration behavior tailored from 1D to 3D with increasing iron concentration [89].

Table 5.2 The comparison of SP-CSAs swelling measured by cross-sectional TEM images and optical profilometer. All materials were irradiated to 60 dpa using 3MeV Ni^{2+} ions at 500 ℃ [84].

Material	Swelling (%)*	Swelling (%)**
Ni	12.59±2.26	6.7
NiCo	3.60±0.67	3.5
NiFe	0.38±0.07	0.33
NiCoFeCr	0.016±0.005	<0.2

*The swelling calculated in this study using cross-sectional TEM images.
**The swelling calculated by Jin [21] using optical profilometer.

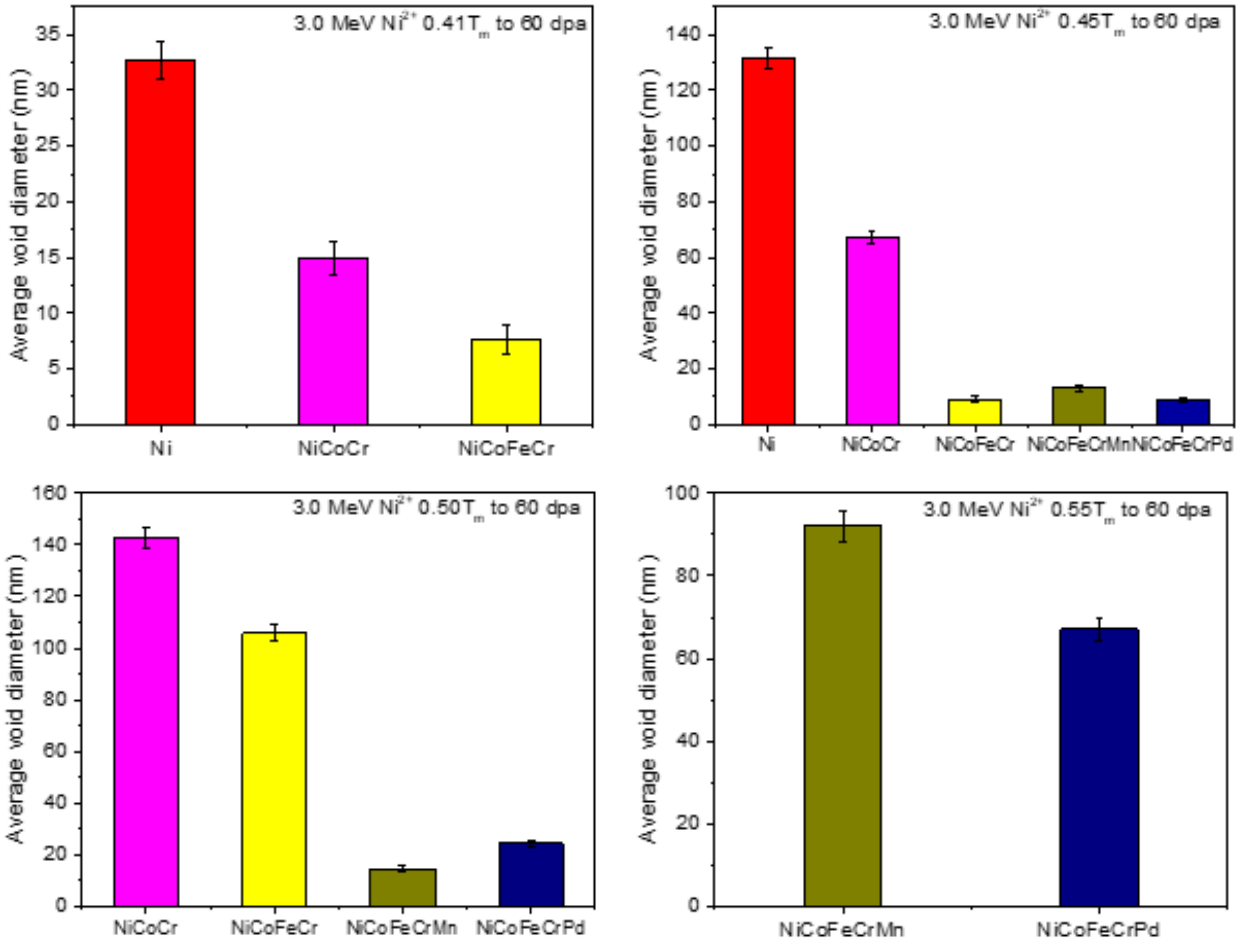

Figure 5.5 Average void diameter for medium to high entropy Ni SP-CSAs as a function of homologous temperature.

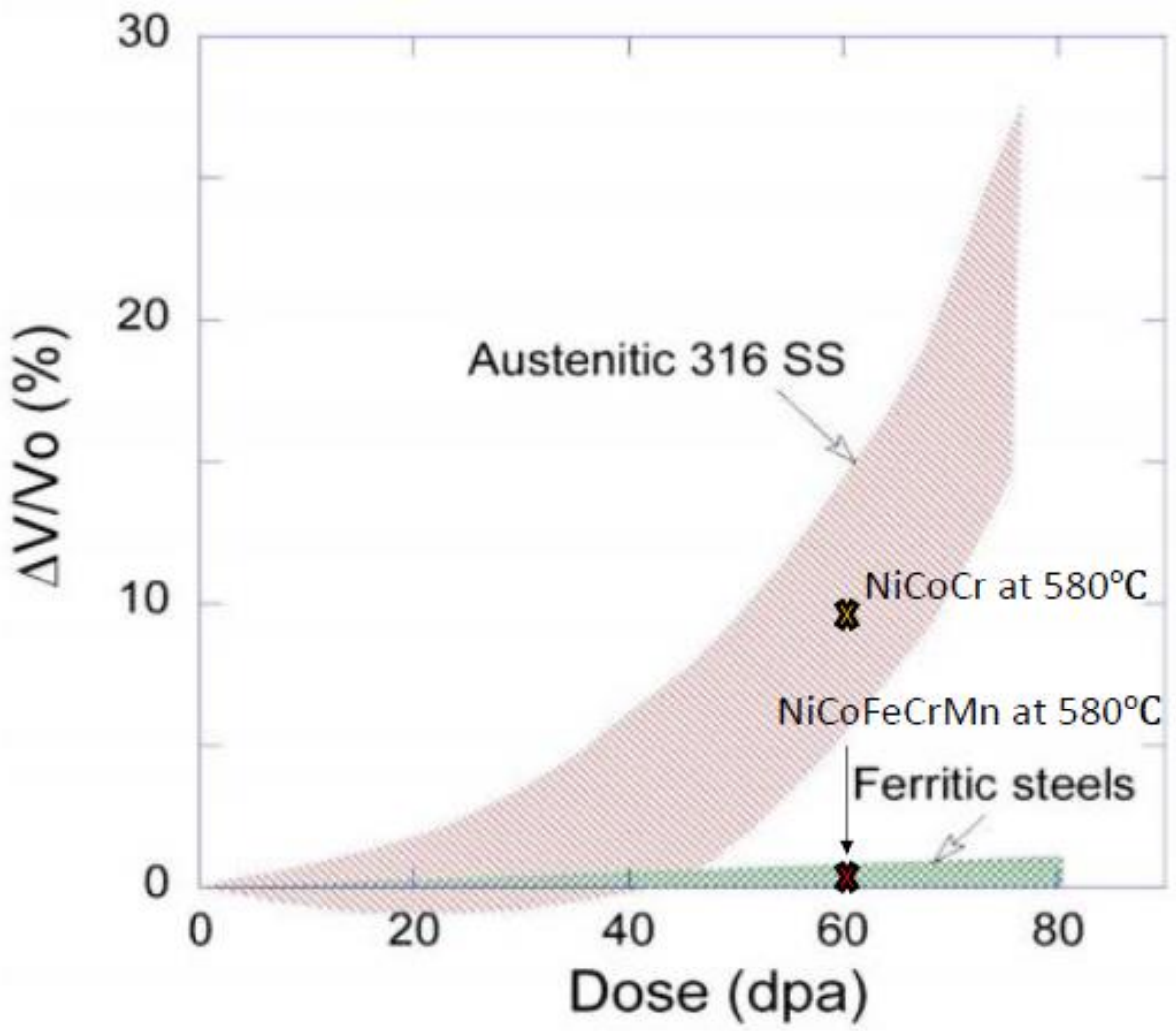

Figure 5.6 Comparison of swelling between austenitic 316 SS, ferritic steels, MEAs and HEAs. Modified from [121].

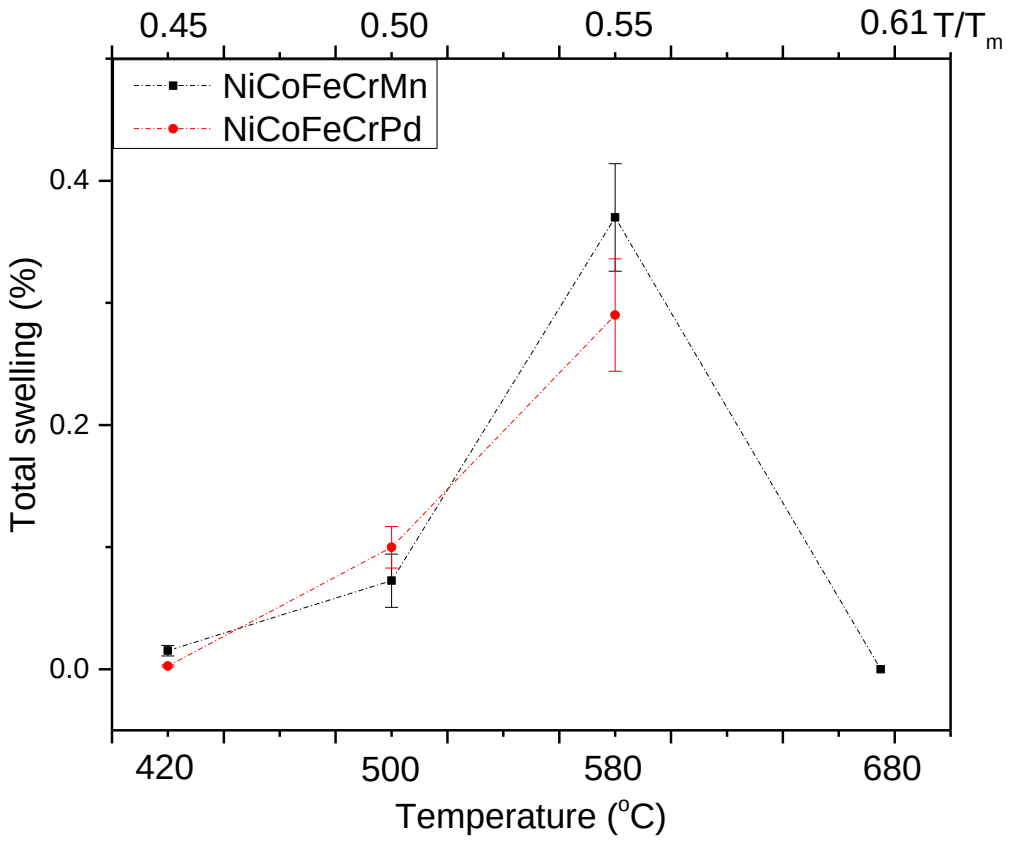

Figure 5.7 Temperature dependence of overall swelling in Mn-HEA and Pd-HEA irradiated by 3.0 MeV Ni^{2+} ions to ~60 dpa peak dose. Dotted lines are for guidance [17].

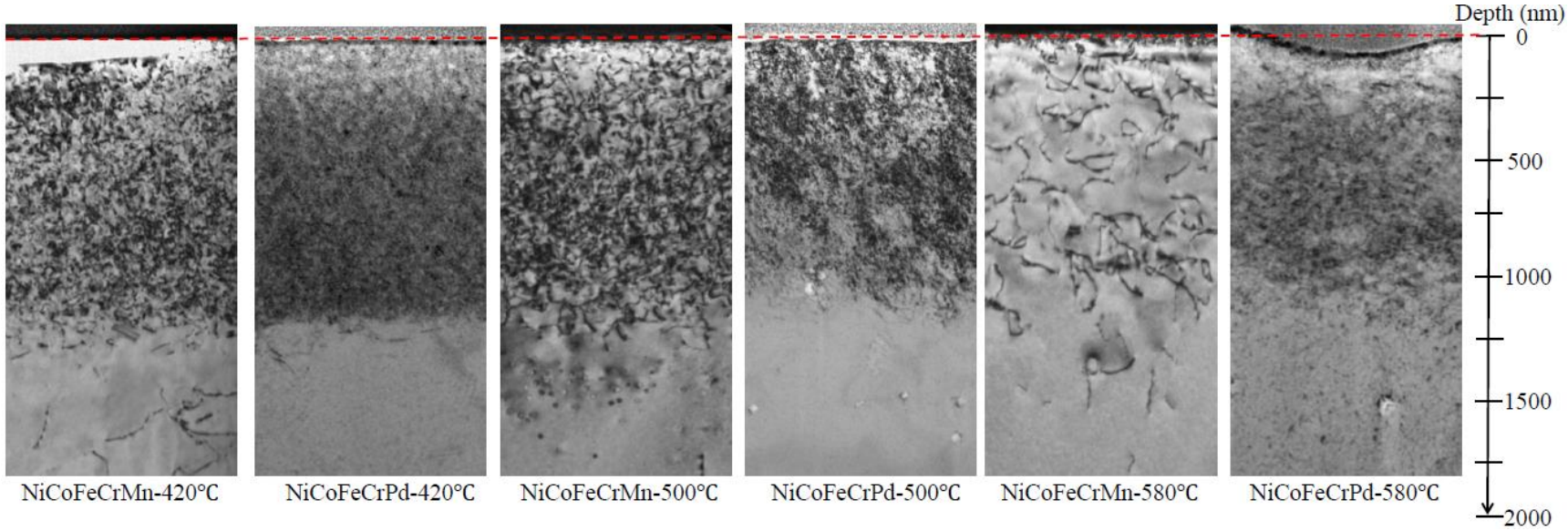

Figure 5.8 Distribution of dislocation loops at under-focus cross-sectional BF TEM images of Mn-HEA and Pd-HEA irradiated by 3.0 MeV Ni^{2+} ions to ~60 dpa at peak dose at 420, 500 and 580℃ [17].

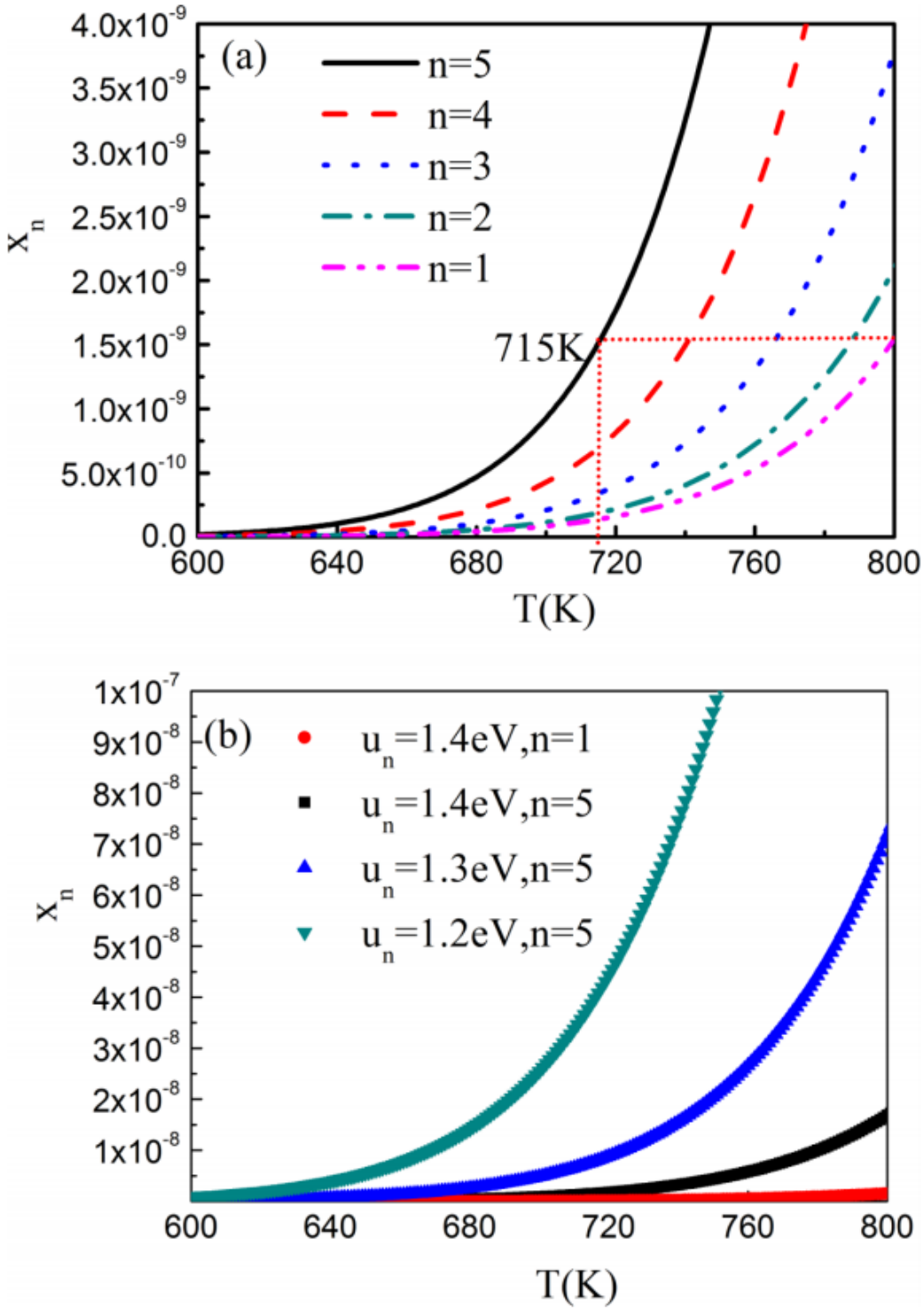

Figure 5.9 Equilibrium vacancy concentrations in alloys at different temperatures. (a) The change of vacancy concentration with configuration entropy for E_f^v=1.4 eV and (b) the change of vacancy concentration with vacancy formation energy [29].

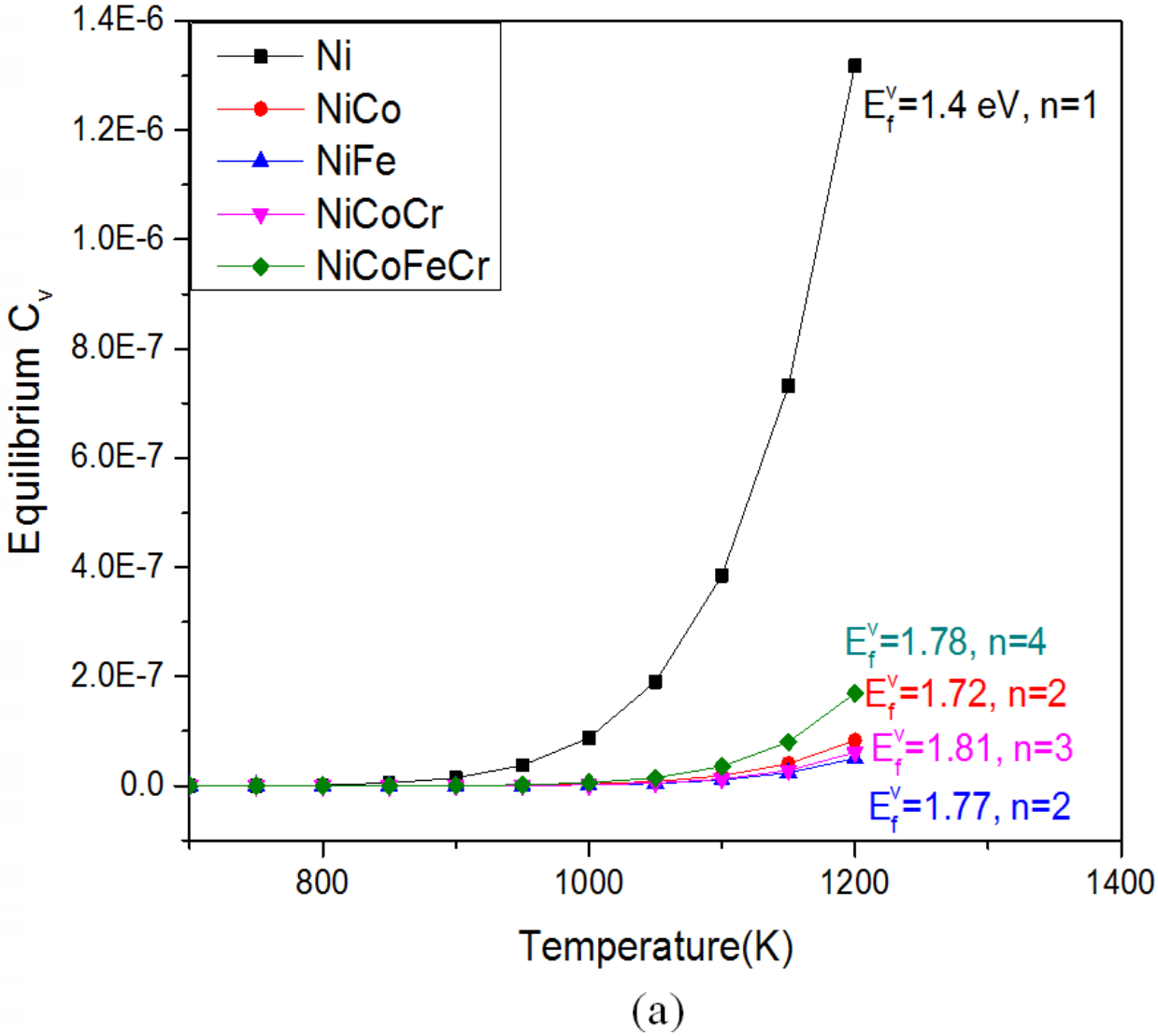

(a)

Figure 5.10 (a) Equilibrium vacancy concentrations in Ni, NiCo, NiFe, NiCoCr and NiCoFeCr as a function of temperature. The vacancy formation energy (E_f^v) used in the calculation is listed next to the number of elements in the alloy, with an unit of eV.

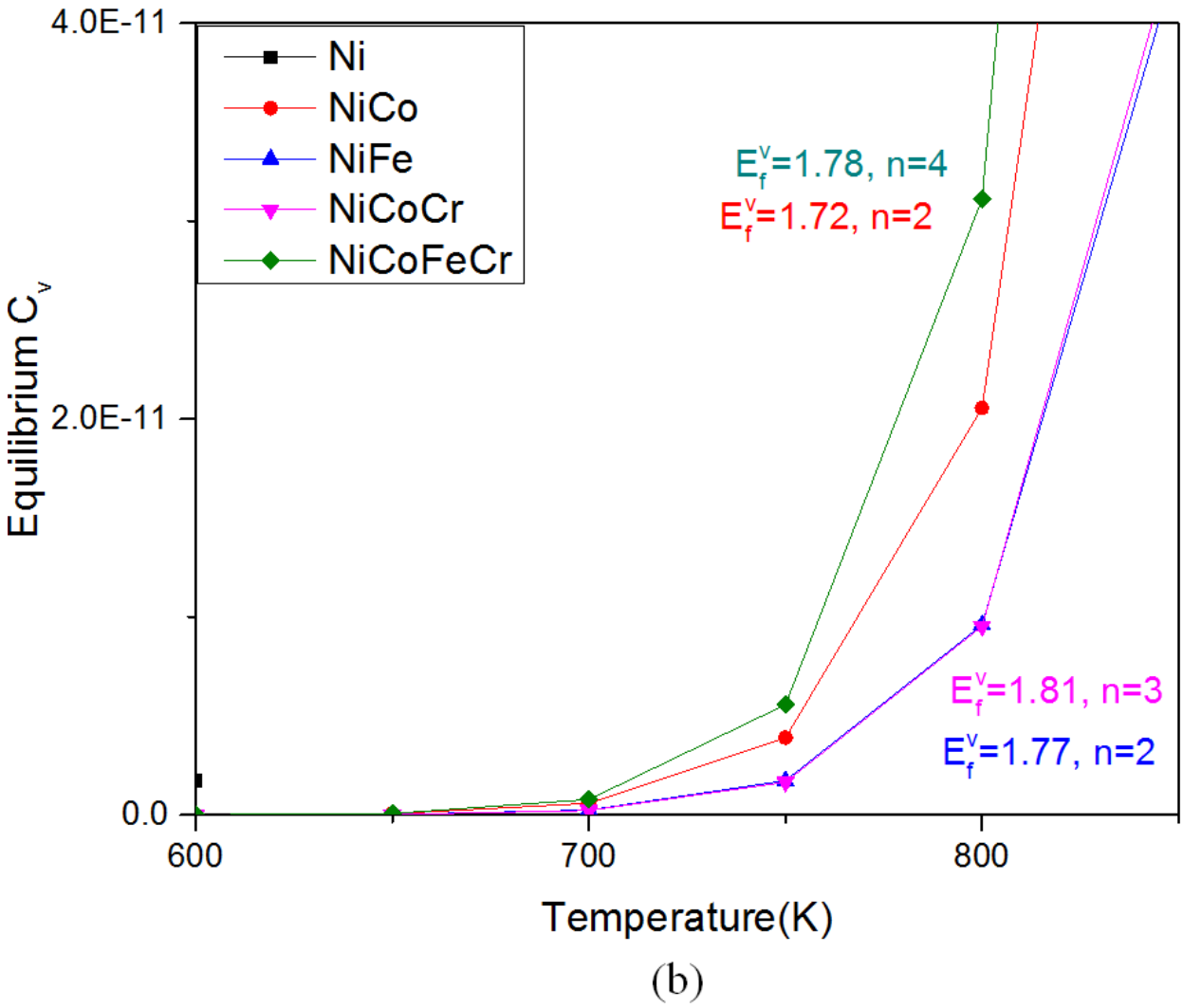

(b)

Figure 5.10 (b) Enlarged image of Figure 5.10 (a) from temperature range 600 to 800 K.

Chapter 6-Conclusions

Irradiation-induced void formation in nickel and Ni-containing equiatomic SP-CSAs at elevated temperature is controlled by the migration behaviors of interstitial clusters. It was initially found that the short-range, localized 3D motion of interstitial clusters dominates in the more chemically complex system, while the long-range 1D motion dominates in pure Ni. The relatively localized 3D migration mode can enhance defect recombination in the cascade region and effectively reduce the void swelling in materials.

The transition of 1D to 3D mode was quantitatively demonstrated using experimental and collaborated computational efforts in Ni-xFe binary alloys. The migration behavior of interstitial clusters shifted from 1D to 3D dominance with increasing iron concentration. The mean free path of interstitial clusters was used to characterize defect motions in the irradiated alloys. A relatively sharp drop on the mean free path was observed with increasing iron concentrations from 0% to 10%, followed by a slower decrease for higher iron concentrations. The increasing suppression of void swelling and delay of dislocation growth in more-concentrated Ni-Fe alloys was attributed to the decrease of the mean free path of interstitial clusters.

It has been demonstrated that when discussing defect dynamics induced by ion irradiation, the injected interstitial effect should be considered along with the 1D or 3D interstitial movement models to interpret the defect migration behaviors in different SP-CSAs. The injected interstitial effect was most pronounced in Ni and NiCo where the 1D migration mode was dominant. The effect was less significant in NiFe and NiCoFeCr where 3D migration mode is the dominating mechanism. The minor injected interstitial effect was attributed to the high density dislocation loops observed in the irradiated region and the insignificant number of injected interstitials.

In the study of varying irradiation temperatures, it has been demonstrated that the equiatomic Ni-based HEAs have superior swelling resistance than Ni-based MEAs over three irradiated homologous temperatures. Despite an order of magnitude increase on swelling with increasing temperature, the highest total swelling in Mn-HEA was still below 0.5% and comparable to the swelling exhibited in ferritic steels. It was concluded that the better swelling observed in HEAs can be attributed to the complex arrangement of different atomic species. This arrangement resulted in a highly-distorted lattice, a higher migration barrier for both defects and stronger solute-vacancy binding. Between the two HEAs studied, alloying with Pd was found to have a stronger suppression effect on void and dislocation loop growth than alloying with Mn. No significant increase was observed on the equilibrium vacancy concentration as the number of alloying components increased. This indicates that the main contribution to enhanced defect recombination and superior swelling resistance in HEAs comes from the interstitial migration mechanism and defect mobility, and it may have a relatively weak correlation to the equilibrium vacancy concentration.

Contrary to the 1D migration mode dominated in the well-studied dilute alloys, the 3D migration mode is identified to be the dominating migration mechanism for interstitial clusters in Ni-20X binary alloys. The results reveal that: (1) the average size of defect clusters decreases as the solute atomic volume size factor increases. Smaller void size in Ni-20Cr is attributed to faster vacancy mobility in the near surface region, and weaker vacancy binding energy beyond the irradiation peak than Ni-20Fe. The smaller voids observed in Ni-20Mn and Ni-20Pd beyond the damage peak are due to the stronger Mn/Pd-vacancy binding effect of largely oversized solute atoms. (2) Oversized magnetic solutes can act as strong trapping sites for interstitials. The larger the solute atomic volume factor, the stronger the trapping force. This leads to a more significantly sluggish interstitial migration and smaller dislocation loop size. The average dislocation loop size in Ni-20Fe was four times larger than Ni-20Pd (atomic volume factor is 10.6% and 41.3%) but an order of magnitude lower in density. The smaller dislocation loop size in Ni-20Cr is attributed to stronger interstitial binding of Cr-Ni. Overall, the alloying effect on defects is more significant in concentrated binary alloys than in dilute binary alloys, due to the concentration difference of alloying atoms and the interstitial dominant migration mechanisms in the main irradiation region.

In this study, the superior swelling resistance has been demonstrated on chemically complex alloys. However, this work also reveals that similar results on swelling resistance can be achieved in HEAs and well-designed binary alloys with increased concentration or atomic volume factor of alloying elements. The mechanical properties of concentrated binary alloys may not be comparable to HEAs, but the easy accessibility makes them desirable alternatives when applying in swelling sensitive environments.

Chapter 7-Future Work

The results and findings of this work provided considerable insight into understanding the radiation behaviors and controlling mechanisms of Ni-based SPCSAs. However, there are still many unanswered questions and areas which merit further study.

The determination of the mean free path of defect clusters in equiatomic SPCSAs. The ultimate goal of this is to provide a quantitative correlation between the defect distributions observed by TEM to the mean free path of defects calculated by MD simulations. The information is useful in the sense that it can be applied to a new material system and to predict its potential irradiation behavior.

Moving from fcc to bcc system and expand into non-equiatomic systems. All of the studied materials in this study have fcc crystal structure and are composed of mainly 3d transition alloy elements. Traditionally, materials with bcc crystal structure exhibit lower swelling than the ones with fcc structure. Conducting similar ion irradiation studies on bcc HEAs should provide important insight into its potential application. In addition, many non-equiatomic HEAs have shown superior mechanical properties compared to conventional alloys and should be included in the interest of future study.

The effect of pre-existed sinks on defect evolution. The main focus of the current study is on the defect recombination and extra measures have been taken to minimize the effect of sinks on defect evolution. However, the measure of introducing sinks to enhance the annihilation of irradiation-induced defects has been practiced for decades to improve material properties. Therefore, the study of sinks such as grain boundaries, the variation of grain sizes and pre-existing dislocation lines as well as secondary phases on defect evolution should be included in the future study.

The study of stacking fault tetrahedron (SFT) on Ni-based SPCSAs. While this study was able to characterize the swelling behavior and defect evolution of Ni-based SPCSAs, the studied irradiation temperature was limited to elevated temperatures and the state of defects created at room temperature could not be accessed. Stacking fault energy (SFE) is one of the irradiation-induced defects at room temperature, and it provides a way to measure the differences in deformation behavior of fcc alloys. The available studies are mainly characterized by Rutherford backscattering technique or insitu TEM observations. Both techniques have its merits and limitations such as missing the ability to detect larger defect size or being restricted to relatively low damage dose. Ex-situ TEM observation can study SFT directly without the restriction of low damage dose. In addition, the total defect migration range can serve as another indication of defect mobility.

The irradiation behavior of Ni SP-CSAs using neutron sources. Some of the main results reported in this thesis (i.e. 1D and 3D migration modes and the resulting defect distributions) are related to the unique depth dependent distribution of defect clusters in ion irradiated samples. To validate the irradiation behavior, neutron irradiation of a selected set of materials should be conducted to pave the way for potential applications in reactor environment.

The comparison of irradiation behavior in Ni SP-CSAs to the commercial Ni based Inconel Alloys. Some of the commercial Ni based Inconel alloys also have high concentration of alloying elements, such as 15-30% Cr and 5-11% Fe. The irradiation performance of Ni SP-CSAs and commercial Ni based Inconel Alloys should also be evaluated under similar conditions to provide a relative comparison.

The effect of minor impurity atoms. A more careful study on the effect of minor impurity atoms (for instance: C, O, N) introduced during the alloy preparation process should also be carried out. To better verify potential clusters formation and to confirm the material homogeneity, atom probe tomography (APT) study should be carried out on the pristine and irradiated samples.

REFERENCES

[1] A. Gali, E.P. George, Tensile properties of high and medium entropy alloys, Intermetallics, 39 (2013) 74.

[2] F. Otto, A. Dlouhy, Ch. Somsen, H. Bei, G. Eggeler, E.P. George, The influences of temperature and microstructure on the tensile properties of a CoCrFeMnNi high entropy alloy, Acta Mater. 61 (2013) 5743-5755.

[3] Z. Wu, H. Bei, G.M. Pharr, E.P. George, Temperature dependence of the mechanical properties of equiatomic solid solultion alloys with face centered cubic crystal structures, Acta Mater. 81 (2014) 428-441.

[4] G.S. Was, J.T. Busby, T. Allen, E.A. Kenik, A. Jenssen, S.M. Bruemmer, J. Gan, A.D. Edwards, P.M. Scott, P.L. Andresen, Emulation of neutron irradiation effects with protons : validation of principle, J. Nucl. Mater. 300 (2002) 198–216.

[5] G.S. Was, Z. Jiao, E. Getto, K. Sun, A.M. Monterrosa, S.A. Maloy, O. Anderoglu, B.H. Sencer, M. Hackett, Emulation of reactor irradiation damage using ion beams, Scr. Mater. 88 (2014) 33–36. doi:10.1016/j.scriptamat.2014.06.003.

[6] S.J. Zinkle, L.L. Snead, Opportunities and limitations for ion beams in radiation effects studies : Bridging critical gaps between charged particle and neutron irradiations, Scr. Mater. (2017). doi:10.1016/j.scriptamat.2017.06.041.

[7] I.L. Singer, Absorption of carbon from residual gases during Ti implantation of alloys, Appl. Phys. Lett. 43 (1983) 457. doi:10.1063/1.94387.

[8] J.G. Gigax, H. Kim, E. Aydogan, F.A. Garner, S. Maloy, J.G. Gigax, H. Kim, E. Aydogan, F.A. Garner, S. Maloy, Beam-contamination-induced compositional alteration and its neutron-atypical consequences in ion simulation of neutron-induced void swelling, Mater. Res. Lett. 0 (2017) 1–8. doi:10.1080/21663831.2017.1323808.

[9] H.W King, Quantitative Size-Factors for Metallic Solid Solutions, J. Mater. Sci. 1 (1966)79-90.

[10] K. Hamada, S. Kojima, Y. Ogasawara, T. Yoshiie, M. Kiritani, Role of solute atoms on microstructural evolution in neutron irradiated nickel, J. Nucl. Mater.212- 215 (1994) 270–274.

[11] T. Yoshiie, Q. Xu, Y. Satoh, H. Ohkubo, M. Kiritani, The effect of alloying elements on the defect structural evolution in neutron irradiated Ni alloys, J. Nucl. Mater. 283-287 (2000) 229–233.

[12] T. Yoshiie, T. Ishizaki, Q. Xu, Y. Satoh, M. Kiritani, One dimensional motion of interstitial clusters and void growth in Ni and Ni alloys, J. Nucl. Mater. 307-311 (2002) 924–929.

[13] K. Sato, D. Itoh, T. Yoshiie, Q. Xu, A. Taniguchi, T. Toyama, Effect of solute atom concentration on vacancy cluster formation in neutron-irradiated Ni alloys, J. Nucl. Mater. 417 (2011) 963–967.

[14] E. Wakai, T. Ezawa, J. Imamura, T. Takenaka, T. Tanabe, R. Oshima, Effect of solute atoms on swelling in Ni alloys and pure Ni under He+ ion irradiation, J. Nucl. Mater.

307–311 (2002) 367–373.
[15] C. Lu, L. Niu, N. Chen, K. Jin, T. Yang, P. Xiu, Y. Zhang, F. Gao, H. Bei, S. Shi, M. He, I.M. Robertson, W.J. Weber, L. Wang, Enhancing radiation tolerance by controlling defect mobility and migration pathways in multicomponent single-phase alloys, Nat. Commun. 7 (2016) 13564. doi:10.1038/ncomms13564.
[16] C. Lu, T. Yang, K. Jin, G. Velisa, P. Xiu, M. Song, Q. Peng, F. Gao, Y. Zhang, H. Bei, W.J. Weber, L. Wang, Enhanced void swelling in NiCoFeCrPd high entropy alloy by indentation induced dislocations, Mater. Res. Lett. 6 (2018) 584-591.
[17] T. Yang, C. Lu, G. Velisa, K. Jin, P. Xiu, Y. Zhang, H. Bei and L. Wang, Influence of irradiation temperature on void swelling in NiCoFeCrMn and NiCoFeCrPd, Scr. Mater. 158 (2019) 57-61.
[18] T. Yang, C. Lu, G. Velisa, K. Jin, P. Xiu, M. Crespillo, Y. Zhang, H. Bei and L. Wang, Effect of Alloying Elements on Defect Evolution in Ni-20X Binary Alloys, Acta Mater., 151 (2018) 159. doi: 10.1016/j.actamat.2018.03.054.
[19] K.H. Huang, J.W. Yeh. Master's thesis, National Tsing Hua University, 1996.
[20] C.Y. Hsu, J.W. Yeh, S.K. Chen, T.T. Shun, Wear resistance and high temperature compression strength of FCC $CuCoNiCrAl_{0.5}Fe$ alloy with boron addition, Metall. Mater. Trans. A, (2004) 35A, 1465.
[21] J.W. Yeh, S.K. Chen, S.J. Lin, J.Y. Gan, T.S. Chin, T.T. Shun, C.H. Tsau, S.Y. Chang, Nanostructured high entropy alloys with multiple principal elements: novel alloy design concepts and outcomes, Adv. Eng. Mater., 6 (2004) 299.
[22] J.W. Yeh, Ann Chim. Sci. Mater. 31, 633 (2006).
[23] K. Jin, H. Bei, Single phase concentrated solid solution alloys: Bridging intrinsic transport properties and irradiation resistance, Front. Mater. 5:26 (2018).
[24] M. Vaidya, S. Trubel, B.S. Murty, G. Wilde, S.V. Divinski, Ni tracer diffusion in CoCrFeNi and CoCrFeMnNi high entropy alloys, J. Alloy. Comp. 688 (2016) 994-1001.
[25] K. Jin, C. Zhang, F. Zhang, H. Bei, Influence of compositional complexity on interdiffusion in Ni-cotaining concentrated solid-solution alloys. Mater. Res. Lett. 6 (2018) 293-299.
[26] M. Vaidya, K.G. Pradeep, B.S. Murty, G. Wilde, S.V. Divinski, Bulk tracer diffusion in CoCrFeNi and CoCrFeMnNi high entropy alloys, Acta Mater. 146 (2018) 211-224.
[27] D.B. Miracle, O.N. Senkov, A critical review of high entropy alloys and related concepts, Acta Mater. 122 (2017) 448-511.
[28] G.S. Was, Fundamentals of Radiation Materials Science: Metals and Alloys, Springer, 2007.
[29] Z. Wang, C.T. Liu, P. Dou, Thermodynamics of vacancies and clusters in high entropy alloys, Phys. Rev. Mater. 1 (2017) 043601.
[30] C. Sun, S. Zheng, C.C. Wei, Y. Wu, L. Shao, Y. Yang, K.T. Hartwig, S.A. Maloy, S.J. Zinkle, T.R. Allen, H. Wang, X. Zhang, Superior radiation-resistant nanoengineered austenitic 304L stainless steel for applications in extreme radiation environments., Sci. Rep. 5 (2015) 7801.
[31] M. Song, Y.D. Wu, D. Chen, X.M. Wang, C. Sun, K.Y. Yu, Y. Chen, L. Shao, Y. Yang, K.T. Hartwig, X. Zhang, Response of equal channel angular extrusion processed ultrafine-grained T91 steel subjected to high temperature heavy ion irradiation, Acta Mater. 74 (2014) 285–295.
[32] A. Hirata, T. Fujita, Y.R. Wen, J.H. Schneibel, C.T. Liu, M.W. Chen, Atomic structure of

nanoclusters in oxide-dispersion-strengthened steels, Nat. Mater. 10 (2011) 922–926.
[33] G.R. Odette, M.J. Alinger, B.D. Wirth, Recent Developments in Irradiation-Resistant Steels, Annu. Rev. Mater. Res. 38 (2008) 471–503.
[34] M. He, S. Wang, S. Shi, K. Jin, H. Bei, K. Yasuda, S. Matsumura, K. Higashida, I.M. Robertson, Mechanisms of radiation-induced segregation in CrFeCoNi-based single-phase concentrated solid solution alloys, Acta Mater. 126 (2017) 182–193. doi:10.1016/j.actamat.2016.12.046.
[35] C. Lu, T. Yang, K. Jin, N. Gao, P. Xiu, Y. Zhang, F. Gao, H. Bei, W.J. Weber, K. Sun, Y. Dong, L. Wang, Radiation-induced segregation on defect clusters in single-phase concentrated solid-solution alloys, Acta Mater. 127 (2017) 98–107.
[36] A.J. Zaddach, C. Niu, C.C. Koch, D.L. Irving, Mechanical properties and stacking fault energies of NiFeCrCoMn high-entropy alloy, JOM 65 (2013) 1780-1789. doi: 10.1007/S11837-013-0771-4.
[37] S. Zhao, G.M. Stocks, Y. Zhang, Stacking fault energies of face-centered cubic concentrated solid solution alloys, Acta Mater. 134 (2017) 334-345.
[38] J.A. Sprague, J.E. Westmoreland, F.A. Smidt, P.R. Malmberg, The temperature dependence of nickel-ion damage in nickel, J. Nucl. Mater. 54 (1974) 286–298.
[39] T.D. Ryan, Heavy ion induced void formation in Ni, PhD dissertation, 1975, University of Michigan.
[40] N.A.P. Kiran Kumar, C. Li, K.J. Leonard, H. Bei, S.J. Zinkle, Microstructural stability and mechanical behavior of FeNiMnCr high entropy alloy under ion irradiation, Acta Mater. 113 (2016) 230-244. doi: 10.1016/j.actamat.2016.05.007.
[41] T. Yang, S. Xia, W. Guo, R. Hu, J. D. Poplawsky, G. Sha, Y. Fang, Z. Yan, C. Wang, C. Li, Y. Zhang, S.J. Zinkle, Y. Wang, Effects of temperature on the irradiation responses of Al 0.1 CoCrFeNi high entropy alloy., Scr. Mater. 144 (2018), 31–35. doi: 10.1016/j.scriptamat.2017.09.025.
[42] S.J. Zinkle, L.L. Snead, Microstructure of copper and nickel irradiated with fission neutrons near 230℃, J. Nucl. Mater. 225 (1995) 123-131.
[43] D.S. Gelles, Microstructural examination of commercial ferritic alloys at 200 dpa, J. Nucl. Mater. 237 (1996) 293–298.
[44] J.L. Brimhall, H.E. Kissinger, Void formation in irradiated copper, nickel and copper-nickel alloys, Radiat. Eff. 15 (1972) 259-272.
[45] Y. Yoshida, N. Muroga, T. Watanabe, H. Araki, K. Miyamoto, Effects of purity on damage evolution in Ni irradiated by 14 MeV neutrons, J. Nucl. Mater. 155–157 (1988) 1222–1226.
[46] M.A. Mitchell, F.A. Garner, Neutron-induced swelling of binary Ni-Al alloys, J. Mater. Sci. 187 (1992) 103–108.
[47] T. Yoshiie, M. Kiritani, Destination of point defects and microstructural evolution under collision cascade damage, J. Nucl. Mater. 271–272 (1999) 296–300.
[48] S.J. Zinkle, R. Dodd, G. Kulcinski, K. Farrell, Helium bubble formation in Cu, Ni and Cu-Ni alloys, J. Nucl. Mater. 117 (1983) 213–217.
[49] L.M. Wang, R.A.Dodd, G.L. Kulcinski, Effects of 14 MeV Nickel Ion Irradiation on Nickel-Copper Alloys Observed in Cross-section, J. Nucl. Mater. 155-157 (1988) 1241-1248.
[50] L.M. Wang, S.J. Zinkle, R.A. Dodd, G.L. Kulcinski, Effects of preinjected helium in heavy-ion irradiated nickel and nickel-copper alloys, Metall. Trans. A. 21 (1990)1847-

1851. doi:10.1007/BF02647231.
[51] Y. Zhang, G.M. Stocks, K. Jin, C. Lu, H. Bei, B.C. Sales, L. Wang, L.K. Béland, R.E. Stoller, G.D. Samolyuk, M. Caro, A. Caro, W.J. Weber, Influence of chemical disorder on energy dissipation and defect evolution in concentrated solid solution alloys, Nat. Commun. 6 (2015) 8736.
[52] M.H. Yoo and L.K. Mansur, Distributions of point defects in bounded media under irradiation, J. Nucl. Mater. 62 (1976)282-292.
[53] L.K. Mansur and M.H. Yoo, Advances in the theory of swelling in irradiated metals and alloys, J. Nucl. Mater. 85&86 (1979) 523-532.
[54] L. Shao, C.C. Wei, J. Gigax, A. Aitkaliyeva, D. Chen, B.H. Sencer, F.A. Garner, Effect of defect imbalance on void swelling distributions produced in pure iron irradiated with 3.5 MeV self ions, J. Nucl. Mater. 453 (2014)176-181.
[55] M.P. Short, D.R. Gaston, M. Jin, L. Shao, F.A. Garner, Modeling injected interstitial effects on void swelling in self ion irradiation experiments, J. Nucl. Mater. 471 (2016) 200-207.
[56] A.D. Marwick, Segregation in irradiated alloys: the inverse Kiekendall effect and the effect of constitution on void swelling, J. Phys. F. Met. Phys. 8 (1978) 1849.
[57] H. Wiedersich, P.R. Okamoto, N.Q. Lam, A theory of radiation-induced segregation in concentrated alloys, J. Nucl. Mater. 83 (1979) 98-108.
[58] L.E. Rehn, P.R. Okamoto, D.I. Potter, H. Wiedersich, Effect of solute misfit and temperature on irradiation induced segregation in binary Ni alloys, J. Nucl. Mater. 74 (1978) 242-251.
[59] R.L. Fleischer, Substitutional solution hardening, Acta Mater. 11 (1963).
[60] R. Labusch, Statistical theory of dislocation configurations in a random array of point obstacles, J. Appli. Phys. 48 (1977) 4550.
[61] Z. Wu, Y. Gao, H. Bei, Thermal activation mechanisms and Labusch type strengthening analysis for a family of high entropy and equiatomic solid solution alloys, Acta Mater. 120 (2016) 108-119.
[62] K. Jin, C. Lu, L.M. Wang, J. Qu, W.J. Weber, Y. Zhang, H. Bei, Effects of compositional complexity on the ion-irradiation induced swelling and hardening in Ni-containing equiatomic alloys, Scr. Mater. 119 (2016) 65. doi:10.1016/j.scriptamat.2016.03.030.
[63] J.W. Yeh, Alloy design strategies and future trends in high-entropy alloys, JOM 65, (2013) 1759-1771.
[64] H. Bei and K. Jin, Energy Dissipation to Defect Evolution 2017 Annual Meeting.
[65] Z. Wu, H. Bei, F. Otto, G.M. Pharr, E.P. George, Recovery, recrystallization, grain growth and phase stability of a family of FCC-structured multi-component equiatomic solid solution alloys, Intermetallics 46 (2014) 131–140. doi:10.1016/j.intermet.2013.10.024.
[66] J.H. Mooij, Structural and electrical properties of sputtered CrNi films, J. Vac. Sci. Tech., 9:446 (1972).
[67] S. Chakraborty, A.K. Majumdar, Electron transport studies in Ni-rich γ-NiFeCr alloys, J. Mag. Mag. Mater. 186 (1998) 357-372.
[68] M. Yamasaki, S. Kagao, Y. Kawamura, Thermal diffusivity and conductivity of Zr55Al10Ni5Cu30 bulk metallic glass. Scr. Mater. 53 (2005) 63-67.
[69] H. Chou, Y. Chang, S. Chen, J.W Yeh, Microstrecture, thermophysical and electrical properties in AlxCoCrFeNi ($0 \leq X \leq 2$) high-entropy alloys. Mater. Sci. Eng. B 163 (2009) 184-189.

[70] Y. Kao, S. Chen, T. Chen, P. Chu, J.W. Yeh, S. Lin, Electrical, magnetic and hall properties of AlxCoCrFeNi high entropy alloys, J. Alloy. Comp. 509 (2011) 1607-1614.
[71] J.I. Lee, S.H. Oh, E.S. Park, Manipulation of σy/k ratio in single phase fcc solid solutions, Appl. Phys. Lett. 109 (2016) 061906.
[72] K. Jin, B.C. Sales, G.M. Stocks, G.D. Samolyuk, M. Daene, W.J. Weber, Tailoring the physical properties of Ni-based single phase equiatomic alloys by modifying the chemical complexity, Sci. Rep. 6 (2016) 20159.
[73] K. Jin, S. Mu, K. An, W.D. Porter, G.D. Samolyuk, G.M. Stocks, Thermophysical properties of Ni-containing single phase concentrated solid solution alloys, Mater. Des. 117 (2017) 185-192.
[74] K.Y. Tsai, M.H. Tsai, J.W. Yeh, Sluggish diffusion in CoCrFeMnNi high entropy alloys, Acta. Mater. 61 (2013) 4887-4897.
[75] T. Nagase, P.D. Rack, J.H. Noh, T. Egami, In-situ TEM observation of structural changes in nanocrystalline CoCrCuFeNi multicomponent high entropy alloys (HEA) under fast electron irradiation by high voltage electron microscopy (HVEM), 59 Intermetallics, 32-42.
[76] J. Weertman, Elementary Dislocation Theory. Macmillian, London (1964).
[77] J.L. Brimhall, B. Mastel, Temperature dependence of void formation in neutron irradiated nickel, Scr. Met. 4, (1970) 51-54.
[78] N.M. Ghoniem, S. Sharafat, A numerical solution to the fokker-planck equation describing the evolution of the interstitial loop microstructure during irradiation, J. Nucl. Mater. 92 (1980) 121-135.
[79] Y. Zhang, M. L. Crespillo, H. Xue, K. Jin, C. H. Chen, C. L. Fontana, J.T. Graham, W. J. Weber, Nucl. New ion beam materials laboratory for materials modification and irradiation effects research, Nucl. Instrum. Methods Phys. Res. B 338 (2014)19-30. doi:10.1016/j.nimb.2014.07.028.
[80] J.F. Ziegler, M.D. Ziegler, J.P. Biersack, Nuclear Instruments and Methods in Physics Research B SRIM- The stopping and range of ions in matter (2010), Nucl. Inst. Methods Phys. Res. B. 268 (2010) 1818–1823. doi:10.1016/j.nimb.2010.02.091.
[81] R.E. Stoller, M.B. Toloczko, G.S. Was, A.G. Certain, S. Dwaraknath, F.A. Garner, On the use of SRIM for computing radiation damage exposure, Nucl. Instruments Methods Phys. Res. Sect. B Beam Interact. with Mater. Atoms. 310 (2013) 75–80.
[82] M. Rühle, M. Wilkens., Defocusing contrast of cavities, Crystal Lattice Defects, 6 (1975) 129-140.
[83] T. Malis, S.C. Cheng, R.F. Egerton, EELS Log-Ratio Technique for Specimen-Thickness Measurement in the TEM, J. Electron Microsc. Tech. (1988) 193–200.
[84] T. Yang, C. Lu, K. Jin, M.L. Crespillo, Y. Zhang, H. Bei, L. Wang, The effect of injected interstitials on void formation in self-ion irradiated nickel containing concentrated solid solution alloys, J. Nucl. Mater. 488 (2017) 328. doi:10.1016/j.jnucmat.2017.02.026.
[85] E. Getto, K. Sun, S. Taller, A.M. Monterrosa, Z. Jiao, G.S. Was, Methodology for determining void swelling at very high damage under ion irradiation, J. Nucl. Mater. 477 (2016) 273–279.
[86] E.M. Getto, The co-evolution of microstructure features in self-ion irradiated HT9 at very high damage levels, 2016, University of Michigan.
[87] C. Lu, K. Jin, L.K. Béland, F. Zhang, T. Yang, L. Qiao, Y. Zhang, H. Bei, H.M. Christen, R.E. Stoller, L. Wang, Direct Observation of Defect Range and Evolution in Ion-

Irradiated Single Crystalline Ni and Ni Binary Alloys, Sci. Rep. 6 (2016) 19994.
[88] M.L. Jenkins, M.A. Kirk, Characterization of radiation damage by transmission electron microscopy, Institute of Physics Publishing, Bristol and Philadelphia (2001).
[89] C. Lu, T. Yang, L. Niu, Q. Peng, K. Jin, M.L. Crespillo, G. Velisa, H. Xue, F. Zhang, P. Xiu, Y. Zhang, F. Gao, H. Bei, W.J. Weber, L. Wang, Interstitial migration behavior and defect evolution in ion irradiated pure nickel and Ni-xFe binary alloys, J. Nucl. Mater. 509 (2018) 237-244.
[90] S. Shi, H. Bei, I.M. Robertson, Impact of alloy composition on one-dimensional glide of small dislocation loops in concentrated solid solution alloys, Mater. Sci. Eng. A 700 (2017) 617-621.
[91] R.J. Olsen, K. Jin, C. Lu, L.K. Beland, L. Wang, H. Bei, E.D. Specht, B.C. Larson, Investigation of defect clusters in ion irradiated Ni and NiCo using diffuse X-ray scattering and electron microscopy, J. Nucl. Mater. 469 (2016) 153-161.
[92] F. Granberg, K. Nordlund, M.W. Ullah, K. Jin, C. Lu, H. Bei, L. Wang, F. Djurabekova, W.J. Weber, Y. Zhang, Mechanism of radiation damage reduction in equiatomic multicomponent single phase alloys, Phys. Rev. Lett. 116 (2016) 135504.
[93] S. Zhao, G.M. Stocks, Y. Zhang, Defect energetics of concentrated solid-solution alloys from ab initio calculations: Ni0.5Co0.5, Ni0.5Fe0.5, Ni0.8Fe0.2 and Ni0.8Cr0.2, Phys. Chem. Chem. Phys. 18 (2016) 24043–24056. doi:10.1039/C6CP05161H.
[94] Y.N. Osetsky, L.K. Beland, R.E. Stoller, Specific features of defect and mass transport in concentrated fcc alloys, Acta Mater. 115 (2016) 364-371.
[95] S. Zhao, Y. Osetsky, Y. Zhang, Preferential diffusion in concentrated solid solution alloys : NiFe, NiCo and NiCoCr, Acta Mater. 128 (2017) 391–399.
[96] Y. Zhang, S. Zhao, W.J. Weber, K. Nordlund, F. Granberg, F. Djurabekova, Atomic-level heterogeneity and defect dynamics in concentrated solid-solution alloys, Curr. Opin. Solid State Mater. Sci. Vol. 21 (2017) 221-237. doi:10.1016/j.cossms.2017.02.002.
[97] Y. Tong, G. Velisa, S. Zhao, W. Gao, T. Yang, K. Jin, C. Lu, H. Bei, J.Y.P. Ko, D.C. Pagan, Y. Zhang, L. Wang, F.X. Zhang, Probing local lattice distortion in medium and high entropy alloys, J. Mtla. 2 (2018) 73-81. doi:10.1016/j.mtla.2018.06.008.
[98] S. Zhao, W.J. Weber, Y. Zhang, Unique challenges for modeling defect dynamics in concentrated solid solution alloys, JOM 69,11 (2017) 2084-2091.
[99] J.B. Whitley, G.L. Kulcinski, P. Wilkes, H. V. Smith, J. Nucl. Mater. 79 (1979) 159–169.
[100] F.A. Garner, J. Nucl. Mater. 117 (1983) 177–197.
[101] D.L. Plumton, W.G. Wolfer, in: Damage Analysis and Fundamental Studies Quarterly Progress Report, DOE/ER-0046/12 (1983) 216.
[102] B.N. Singh, S.J. Zinkle, J. Nucl. Mater. 206 (1993) 212–229.
[103] J.F. Stubbins, F.A. Garner, J. Nucl. Mater. 191-194 (1992) 1295–1299.
[104] F.A. Garner, J. Nucl. Mater. 205 (1993) 98–117.
[105] L.K. Mansur and M.H. Yoo, The effects of impurity trapping on irradiation induced swelling and creep, J. Nucl. Mater. 74 (1978) 228.
[106] T. Kato, H. Takahashi and M. Izumiya, Effects of systematic modification with oversized elements on void formation in 316L austenitic stainless steel under electron irradiation, Mater. Trans. 32 (1991) 921-930.
[107] S. Shi, M. He, K. Jin, H. Bei, I.M. Robertson, Evolution of ion damage at 773K in Ni containing concentrated solid solution alloys, J. Nucl. Mater. 501 (2018) 132-142.
[108] S. Zhao, T. Egami, G.M. Stocks, Y. Zhang, Effect of d electrons on defect properties in

equiatomic NiCoCr and NiCoFeCr concentrated solid solution alloys, Phys. Rev. Mater. 2 (2018) 013602.
[109] K. Jin, W. Guo, C. Lu, M.W. Ullah, Y. Zhang, W.J. Weber, L. Wang, J.D. Poplawsky, H. Bei, Effects of Fe concentration on the ion-irradiation induced defect evolution and hardening in Ni-Fe solid solution alloys, Acta Mater. 121 (2016) 365-373. doi:10.1016/j.actamat.2016.09.025.
[110] G. Velisa, M.W. Ullah, H. Xue, K. Jin, M.L. Crespillo, H. Bei, W.J. Weber, Y. Zhang, Irradiation-induced damage evolution in concentrated Ni-based alloys, Acta Mater. 135 (2017) 54-60. doi:10.1016/j.actamat.2017.06.002.
[111] S.A. Briggs, C.M. Barr, J. Pakarinen, M. Mamivand, K. Hattar, D.D. Morgan, M.Taheri, K. Sridharan, Observations of defect structure evolution in proton and Ni ion irradiated Ni-Cr binary alloys, J. Nucl. Mater. 479 (2016) 48-58. doi: j.jnucmat.2016.06.046.
[112] D. Chakraborty, D.S. Aidhy, Cr- induced fast vacancy cluster formation and high Ni diffusion in concentrated Ni-Fe-Cr alloys, J. Alloys Compd. 725 (2017) 449-460. doi: 10.1016/j.jallcom.2017.07.140.
[113] J.D. Tucker, R. Najafabadi, T.R. Allen, D. Morgan, Ab initio -based diffusion theory and tracer diffusion in Ni – Cr and Ni – Fe alloys, J. Nucl. Mater. 405 (2010) 216–234. doi: 10.1016/j.jnucmat.2010.08.003.
[114] T. Egami, M. Ojha, O. Khorgolkhuu, D.M. Nicholson G.M. Stocks, Local electronic effects and irradiation resistance in high-entropy alloys, J. Nucl. Mater. 67 (2015) 2345–2349. doi: 10.1007/s11837-015-1597-1.
[115] T. Kato, H. Takahashi, M. Izumiya, Grain boundary segregation under electron irradiation in austenitic stainless steels modified with oversized elements, J. Nucl. Mater. 189 (1992) 167–174. doi: 10.1016/0022-3115(92)90529-T.
[116] D.J. Hepburn, E. MacLeod, G.J. Ackland, Transition metal solute interactions with point defects in fcc iron from first principles, Phys. Rev. B (2014) 1–22. doi: 10.1103/PhysRevB.92.014110.
[117] A.J. Zaddach, C. Niu, C.C. Koch, D.L. Irving, Mechanical properties and stacking fault energies of NiFeCrCoMn high-entropy alloy, JOM 65 (2013) 1780-1789. doi: 10.1007/S11837-013-0771-4.
[118] J.W. Yeh, Physical Metallurgy of High-Entropy Alloys, JOM 67 (2015) 2254-2261. doi: 10.1007/S11837-015-1583-5.
[119] M.W. Ullah, D.S. Aidhy, Y. Zhang, W.J. Weber, Damage accumulation in ion-irradiated Ni-based concentrated solid-solution alloys, Acta Mater. 109 (2016)17-22. doi:10.1016/j.actamat.2016.02.048.
[120] M.W. Ullah, H. Xue, G. Velisa, K. Jin, H. Bei, W.J. Weber, Y. Zhang, Effects of chemical alternation on damage accumulation in concentrated solid-solution alloys, Sci. Rep 7:4146 (2017)1–11. doi:10.1038/s41598-017-04541-8.
[121] Y. Chen, Irradiation effects of HT-9 martensitic steels, Nucl. Eng. Technol. 45(2013) 311-322.